UNIVERSITAT DE BARCELONA

Computational modeling of transition metals carbides with relevant to nanotechnology and catalysis

Juan José Piñero Vargas

ADVERTIMENT. La consulta d'aquesta tesi queda condicionada a l'acceptació de les següents condicions d'ús: La difusió d'aquesta tesi per mitjà del servei TDX (**www.tdx.cat**) i a través del Dipòsit Digital de la UB (**diposit.ub.edu**) ha estat autoritzada pels titulars dels drets de propietat intel·lectual únicament per a usos privats emmarcats en activitats d'investigació i docència. No s'autoritza la seva reproducció amb finalitats de lucre ni la seva difusió i posada a disposició des d'un lloc aliè al servei TDX ni al Dipòsit Digital de la UB. No s'autoritza la presentació del seu contingut en una finestra o marc aliè a TDX o al Dipòsit Digital de la UB (framing). Aquesta reserva de drets afecta tant al resum de presentació de la tesi com als seus continguts. En la utilització o cita de parts de la tesi és obligat indicar el nom de la persona autora.

ADVERTENCIA. La consulta de esta tesis queda condicionada a la aceptación de las siguientes condiciones de uso: La difusión de esta tesis por medio del servicio TDR (**www.tdx.cat**) y a través del Repositorio Digital de la UB (**diposit.ub.edu**) ha sido autorizada por los titulares de los derechos de propiedad intelectual únicamente para usos privados enmarcados en actividades de investigación y docencia. No se autoriza su reproducción con finalidades de lucro ni su difusión y puesta a disposición desde un sitio ajeno al servicio TDR o al Repositorio Digital de la UB. No se autoriza la presentación de su contenido en una ventana o marco ajeno a TDR o al Repositorio Digital de la UB (framing). Esta reserva de derechos afecta tanto al resumen de presentación de la tesis como a sus contenidos. En la utilización o cita de partes de la tesis es obligado indicar el nombre de la persona autora.

WARNING. On having consulted this thesis you're accepting the following use conditions: Spreading this thesis by the TDX (**www.tdx.cat**) service and by the UB Digital Repository (**diposit.ub.edu**) has been authorized by the titular of the intellectual property rights only for private uses placed in investigation and teaching activities. Reproduction with lucrative aims is not authorized nor its spreading and availability from a site foreign to the TDX service or to the UB Digital Repository. Introducing its content in a window or frame foreign to the TDX service or to the UB Digital Repository is not authorized (framing). Those rights affect to the presentation summary of the thesis as well as to its contents. In the using or citation of parts of the thesis it's obliged to indicate the name of the author.

Computational modeling of transition metals carbides with relevant to nanotechnology and catalysis.

Juan José Piñero

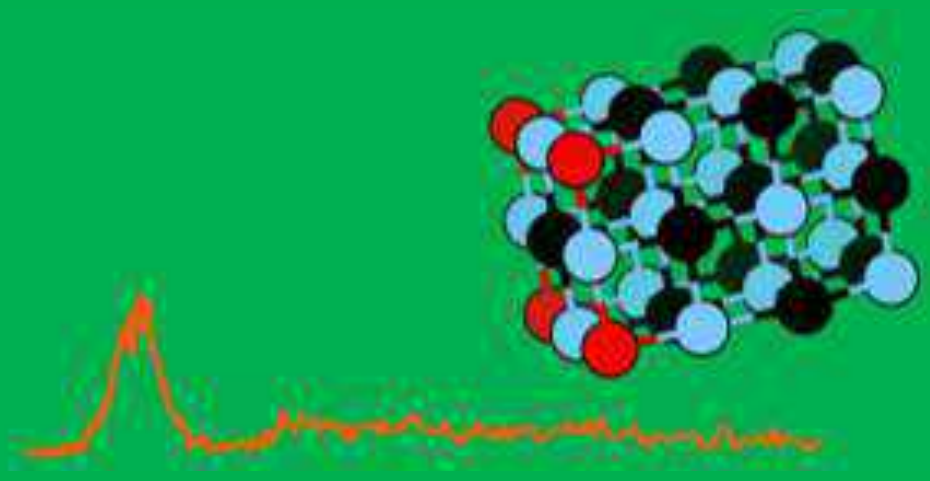

UNIVERSITAT DE BARCELONA

Programa de doctorat en Química Teòrica i Computacional

Memòria presentada per Juan José Piñero Vargas per a optar al grau de Doctor per la Universitat de Barcelona.

Computational modeling of transition metals carbides with relevant to nanotechnology and catalysis.

Dirigida per: Dr. Francesc Viñes Solana
(Universitat de Barcelona)

Dirigida per: Dr. Stefan Thomas Bromley
(Universitat de Barcelona)

UNIVERSITAT DE BARCELONA

UNIVERSITAT DE BARCELONA

FACULTAT DE QUÍMICA DEPARTAMENT DE CIÈNCIA DELS MATERIALS I QUÍMICA FÍSICA

INSTITUT DE QUÍMICA TEÒRICA I COMPUTACIONAL

Computational modeling of transition metals carbides with relevant to nanotechnology and catalysis.

Juan José Piñero Vargas

PhD Thesis

2021

„**Viele kleine Leute**, die an **vielen kleinen Orten viele kleine Dinge tun**, **können das Gesicht der Welt verändern**.“

(Afrikanisches Sprichwort)

“Many small people who in many small places do many small things that can alter the face of the world.”

(African proverb)

“Mucha gente pequeña que hace muchas cosas pequeñas en muchos lugares pequeños puede cambiar la faz del mundo.”

(Provervio africano)

The work presented in this doctoral thesis has been carried out at the Materials Science and Physical Chemistry Department of the Chemistry Faculty of the University of Barcelona (UB), and within the Institute of Theoretical and Computational Chemistry (IQTCUB).

This project has been possible in virtue of the financial support provided by the Spanish Ministerio de Economica y Competividad (Grant CTQ2015-64618R). Computer resources were provided by the Barcelona Supercomputing Center (Red Española de Supercomputación)

Agradecimientos

En primer lugar, me gustaría agradecer a mis directores de Tesis, Fransis y Stefan, así como a mi tutor Xino por estos 5 años de continuo aprendizaje. A Xino quiero agradecerle la gran oportunidad que me brindo hace cinco años de entrar en el mundo de la química computacional, hasta el momento era desconocido para mí y darme la oportunidad de participar en este proyecto que ha culminado en una Tesis Doctoral. A Fransis, que decir de él… muchas gracias por su paciencia sobre todo al principio donde tuvo que emplear mucho tiempo para enseñarme desde cero a enviar un cálculo. Recuerdo sus listas de cosas para hacer y los reports, si si, dos tonterías, pero es son tonterías que te ayudan a tener muy estructurado el trabajo y eso es fundamental, gracias por esas tonterías. Es cierto, que hemos tenido nuestras diferencias, pero eso es parte del trabajo y estoy muy agradecido por toda su dedicación hacía mí, una y mil veces, GRACIAS Fransis. En el caso de Stefan, ha sido algo diferente, también agradecerle su tiempo dedicado a mí, su eterna paciencia cuando los cálculos de nanopartículas no salían y dábamos palos de ciego, al final, se encontró el camino y el trabajo acabo saliendo con unos resultados satisfactorios. Con Stefan, no todo fue trabajo, quedan en el recuerdo, estas buenas tardes de bolera, cena y lo que surgía. Solo puedo daros las gracias a los 3 por haber hecho posible este trabajo.

También me gustaría agradecer a otros miembros del grupo, “Computational Materials Science Laboratory” (CMSL), empezando por Rosendo, mi primer compañero de despacho cuando empecé, Ángel morales, al cual cada vez que perdía el Madrid me gustaba visitar, Héctor Prats, con el cual he tenido el placer de colaborar en varios artículos y agradecerle todo lo que me enseño y con el cual realicé mi primer turno de laboratorio básico de QF, donde cada día de 16h a 17h fuimos abandonados por el gran escaqueado. También agradecer a Toni, sus consejos y explicaciones para enseñarme a utilizar LAMMPS. Tampoco puedo olvidarme en estas líneas de Isaac, y nuestros “piques” en los bolos, que buenos momentos se pasaban allí. Bueno, y por último todos los que en un momento u otro he compartido despacho con ellos, el 425, cuantos momentos vividos entre esas cuatro paredes. En primer lugar, agradecer a Christian Kunkel, mi predecesor en el sitio, no tuve la oportunidad de compartir despacho con él, pero sí, me facilito todo lo necesario para poder trabajar. Sergi Posada, que tío, el cual me ayudo en mis primeros pasos dentro del grupo y con los carburos… todo el día con las bromas, muchas gracias por tu ayuda, me llevo un gran recuerdo de ti, siempre estará en mi memoria la vigilancia del examen de ambientales. Oriol Lamiel, el turno de tarde, que momentos vividos en el despacho, junto a Sergi el alma del despacho. Lorena, que efímeramente también compartimos despacho, siempre guardare a “trompi” mi elefante que me regaló para mi cumpleaños. Marc Figueres, el gran ausente, pocas veces hemos coincidido en el despacho, pero las pocas veces que coincidimos, buenos momentos pasamos. Raúl morales, el gran Morales, me alegra haber visto su evolución completa dentro del grupo, empezando por alumno interno (que coñazo de tío para que le abriera cada día la puerta del despacho), continuando por el TFM, siguiendo por el TFM, y hasta llegar a Doctorando, ahora solo me queda ver (desde la distancia) como logra la su meta, ser Doctor, ánimo que ya va en camino. Oriol pique, jaque mate, puto Piqué que palizas me daba al ajedrez, un grande entre los grandes y no por su altura (que también se podría decir), gracias por todos los buenos momentos que me hiciste pasar a tu lado, pero que pon el aire que nos tienes a todos muertos de calor en el despacho. Martí, bueno, llegamos al Martí, reducte Hortenc, el relevo de tarde, heredero de Lamiel, gracias por hacer que los días muchos más llevaderos, el hombre de la fiesta. Como no acordarse de Joan M… Mariñoso, el hombre que de todo se queja, el cule más pesimista que conozco, siempre va a perder el Barça pero que finalmente ha conseguido que vuelva su presi, Laporta. También quiero recordarme de otros

compañeros con los cuales, en algún momento u otro también he compartido despacho: Helena, Alex, Biel y Anabel. Anabel, la última en llegar al despacho y revolucionarnos a todos, basta ya de ambientador. Para el gran recuerdo del 425, quedaran los éxitos Cartones y peces del sexteto: Piqué, Martí, Mariñoso, Morales, Jurado, y un servidor. Vaya risas con los villancicos, eso sí que son dos grandes temazos, queda pendiente ampliar el repertorio. Finalmente, se lograron las cortinas, la lucha del pueblo. Lástima de la covid, nos ha impedido estar un año juntos y no se pudo llevar a cabo la procesión del perchero. Chicos, la lucha debe de continuar y conseguir el perchero. Muchas gracias a todos por hacerme el trabajo más ameno.

También quiero dedicar unas palabras a Cristina Roncero, mi compi de laboratorio de Inorgánica, donde nuestros caminos se juntaron hasta el día de hoy, y espero que sigan unidos por mucho tiempo. No puedo dejar sin nombrar a Pablo Blanco, un gran compañero, mejor amigo, ha estado presente en el mejor día de mi vida y ahora lo está en los malos momentos. Mil gracias Pablo.

Miércoles, día de partido, venga chicos que el Dr. Cirera hace la convocatoria y todos para el futbol, que nivel más bueno hemos visto pasar por las pistas de la UPC, empezando por el mismo Cirera (CR7), Álex, Carlos, Linley, Aromí, Jorge, Coinas, Mariñoso, Biel, Martí y muchos más, muy buenos momentos los partidos de los miércoles que servían para conocernos más y sobretodo, romper la monotonía del trabajo.

En el ámbito personal quiero agradecer a la Dra. Garcia (Ledy), la cual fue de una ayuda vital en unos de los momentos más duro que pasé durante el grado, solo puedo decirte mil gracias muñeca, esa ayuda nunca te la podré devolver. Por otro lado, no puedo olvidarme de la Dra. Velasco (Vero) sin la cual no habría podido llegar hasta donde he llegado. Su ayuda con los cristales fue fundamental para poder presentar mi TFM, gracias Vero, eternamente agradecido. También quiero dedicarles unas palabras a mis compañeros de carrera, Laura Marics, mi gran amiga y mi apoyo en muchos momentos, buenos y malos con la cual espero poder trabajar algún día con ella y repetir momentos del pasado. Anna V. y Didac, dos compañeros y grandes amigos, gracias por vuestra ayuda, fue un placer coincidir en la carrera con vosotros. Anna C. y Jonathan M. Gracias a vosotros también, vuestra ayuda en los momentos finales ha hecho posible que culmine la Tesis. Una mención especial quiero dedicar a mi gran amigo, mi hermano, Jorge S. el chico que me solo me repetía que trabajara cada día, y que tanto odia las bolitas que tanto hago, que ha estado y está en los malos momentos, tantos momentos hemos pasado... Tampoco puedo olvidarme de su mujer, Laura G. gracias por estar ahí en los momentos difíciles y espero poder seguir muchos años a vuestro lado. Gracias a los dos.

La covid se llevó el buen ambiente del 425, pero me trajo una nueva familia, la familia REPSOL, mil gracias por hacer todas las tardes más amenas, han sido de gran ayuda a José G., Carmen M., Ángel (cal Minovas), Josep (ca l'esquerra), Josep (Cal Pere periques) y a las dos preciosas Carmen R. y Ada. Muchas gracias a todos, estas tardes de "misa" que nos quedaran para la perpetuidad.

Por último, agradecer a mi familia, a mi madre, a mi hermana y a mi Padre, que haya donde este seguro que me ha enviado fuerzas para poder acabar este trabajo. Antón, muchas gracias por todos los consejos y tu ayuda para poder llevar a cabo con éxito esta tesis, Pilar y pilarín. Una mención especial merece Lourdes, la cual ha aguantado cinco años día tras día esta tesis, gracias.

Gracias a todos, este trabajo no habría sido posible sin vosotros, eternamente agradecido.

Juanjo

Table of contents

List of definitions and abbreviations 19
1. Introduction 23
1.1. Catalysis **23**
1.2. Heterogeneous Catalysis **24**
1.3. Transitions Metals Carbides **25**
1.3.1. Catalytic properties 26
1.4. Hydrogen **26**
1.4.1 H_2 uses 27
1.4.2. H_2 as clean energy fuel 28
1.4.3. H_2 production 29
1.5. Motivation and outline of the Thesis **30**
1.6. References **31**
2. Theoretical Background 35
2.1. The Schrödinger equation **35**
2.1.1 The Born-Oppenheimer approximation 35
2.1.2. The Hartree-Fock method 36
2.2. Density functional theory (DFT) **37**
2.2.1. First Hohenberg-Kohn theorem 37
2.2.2. Second Hohenberg-Kohn theorem 39
2.2.3. Kohn-Sham method 39
2.3. Exchange-correlation functional **40**
2.3.1. Local density approximation (LDA) 40
2.3.2. Generalized Gradient Approximation (GGA) 40
2.3.3. Meta-GGA 41
2.3.4. Hybrid functionals 41
2.4. Basis functions **41**
2.4.1. Gaussian-Type Orbitals (GTOs) 42
2.4.2. Slater-Type Orbitals (STOs) 42
2.4.3. Numerical atomic orbitals 42
2.4.4. Plane wave functions 43
2.5. Core electrons and Pseudopotentials **43**
2.6. Solid state **44**
2.6.1. Periodic models for solids 44

2.6.2. The reciprocal lattice 45
2.6.3. Bloch's theorem 46
2.6.4. Miller indices 47
2.7. Models 48
2.7.1. Surfaces 48
2.7.2. Nanoparticles 49
2.8. Transitions States 50
2.8.1. NEB method 50
2.8.2. DIMER method 51
2.9. Vibrational frequencies 51
2.10. Zero-point energy 52
2.11. Infrared Spectroscopy 53
2.11.1. Harmonic IR Spectra 53
2.11.2. MD-Based IR Spectra 54
2.12. Computational details 55
2.12.1 VASP code 55
2.12.2. FHI-AIMS code 56
2.13. References 56
PART I: Surfaces 61
3. H_2 adsorption and dissociation on TiC 65
3.1. Introduction 65
3.2. Methodology 65
3.3. Low coverage H adsorption 66
3.4. High coverage H adsorption 67
3.5. H_2 adsorption at lower coverage 72
3.6. H_2 dissociation on the TiC (001) surface 73
3.7. H diffusion on TiC (001) surface 74
3.8. Experimental studies 75
3.9. Conclusions 78
3.10. Publication 79
3.11. References 86
4. H_2 adsorption and dissociation on TMCs (001) surfaces 91
4.1. Introduction 91
4.2. H absorption 91
4.3. H adsorption 92
4.4. H_2 adsorption 93

4.5. H_2 dissociation on TMCs (001) surfaces 94
4.6. Conclusions 95
4.7. Publication 97
4.8. References 100
5. CH_4 adsorption and dissociation on TiC (001) surface 105
5.1. Introduction 105
5.2. Methodology 105
5.3. CH_3 adsorption 105
5.4. CH_4 adsorption 107
5.5. CH_3 + H adsorption 108
5.6. Adsorption on TiC-supported Ni clusters 108
5.7. Adsorption on Ni clusters 109
5.7.1. CH_4 adsorption 109
5.7.2. CH_3 adsorption 110
5.7.3 H adsorption 111
5.7.4. CH_3 + H adsorption 111
5.8. CH_4 dissociation 112
5.8.1 CH_4 dissociation on bare TiC (001) surface 112
5.8.2 CH_4 dissociation on doped (001) surface. 113
5.9. Experimental study 113
5.10. Conclusions 115
5.11. Publication 116
5.12. References 127
PART II: Nanoparticles 129
6. Infrared vibrational spectra for TiC nanoparticles 133
6.1. Introduction 133
6.2. Methodology 134
6.3. Factors affecting the IR spectra of TiC NPs 135
6.3.1. Isomer effect 135
6.3.2. Functional effect 137
6.3.3. Charge effect 138
6.3.4. Temperature effect 140
6.4. Stability of $(TiC)_{18}$ based NPs 142
6.5. IR spectra of TiC larger NPs 147
6.5.1. Harmonic (0 K) IR Spectra 147
6.5.2. MD-based IR spectra 154

6.6. Conclusions 158
6.7. Publication 159
6.8. References 177
7. H_2 adsorption and dissociation on TiC NPs 181
7.1. Introduction 181
7.2. Methodology 181
7.3. H adsorption 182
7.4. H_2 adsorption 183
7.4.1. Size effect in the H_2 adsorption 184
7.4.2. Initial distance effect between NP and H_2 molecule in the H_2 adsorption 190
7.5. Adsorption Two H atoms 195
7.5.1. $(TiC)_{32}$ 195
7.5.2. $Ti_{18}C_{14}$ 197
7.5.3. $(TiC)_{18}$ and $(TiC)_{24}$ 199
7.6. H_2 adsorption and dissociation on TiC Nanoparticles 199
7.6.1. $(TiC)_{32}$ 200
7.6.2. $(TiC)_{18}$ 205
7.6.3. $(TiC)_{24}$ 206
7.7. Conclusions. 208
7.8. References 208
8. Global conclusions 211
9. List of publications 215
10. Summary in Spanish 219
10.1. Introducción 219
10.2.1. Adsorción y disociación de H_2 en la superficie (001) de TiC 222
10.2.2. Adopción y disociación de H_2 en la superficie (001) de diferentes TMCs 226
10.2.3. Adsorción y disociación de CH_4 en la superficie (001) de TiC 227
10.3. Espectros infrarrojos vibraciones para Nanopartículas de TiC 229
10.3.1. Factores que afectan los espectros de IR de las NP de TiC 230
10.3.2. Estabilidad de NP basadas en $(TiC)_{18}$ 236
10.3.3. Espectros infrarrojos basados en MD. 240
10.4. Adsorción de H_2 en NP de TiC 241
10.4.1. Adsorción de H sobre TiC NP 242
10.4.2. Disociación de H_2 en TiC NP 242
10.5. Conclusiones 243
10.6. Referencias 245

Appendix A: Supporting information to “Diversity of Adsorbed Hydrogen on the TiC (001) Surface at High Coverages” 247

Appendix B: Supporting information to “Assessing the usefulness of transition metal carbides for hydrogenation reactions” 257

Appendix C: Supporting information to “Room Temperature Methane Capture and Activation by Ni Clusters Supported on TiC(001): Effects of Metal-Carbide Interactions on the Cleavage of the C-H Bond” 273

List of definitions and abbreviations

1 electronvolt (eV) = 23.06035 kcal mol^{-1}

Angstrom (Å) = 10^{-10} m

k	rate
CI-NEB	Climbing Image - Nudged Elastic Band
DFT	Density Functional Theory
DFT-D3	Density Functional Theory with Grimme's D3 dispersion correction
$\mathbf{E_{abs}}$	Absorption Energy
$\mathbf{E_{ads}}$	Adsorption Energy
$\mathbf{E_{bulk}}$	Bulk Energy
$\mathbf{E_{slab}}$	Slab Energy
$\mathbf{E_{surf}}$	Surface Energy
FHI-aims	Fritz Haber Institute Ab Initio Molecular Simulations
GGA	Generalized Gradient Aproximation
HfC	Hafnium Carbide
HF	Hartree-Fock
IR	Infrared Spectroscopy
LCAO	Linear Combination of Atomic Orbitals
ML	Monolayer
δ-MoC	Molybdenum Carbide
NbC	Niobium carbide
NEB	Nudged Elastic Band
NP	Nanoparticle
PAW	Project Augmented Wave pseudopotentials
PBE	Perdew-Burke-Enzerhof functional
TaC	Tantalum Carbide

1.Introduction

TiC	Titanium Carbide
TMCs	Transition Metal Carbides
TS	Transition State
UHV	Ultra-High Vacuum
VC	Vanadium Carbide
vdW	Van der Waals dispersion
XPS	X-Ray Photoelectron Spectroscopy
ZPE	Zero Point Energy correction
ZrC	Zirconium Carbide
ΔE	Energy difference
CMSL	Computational Material Science Laboratory
IQTC	Institut de Química Teòrica i Computacional
IUPAC	International Union of Pure and Applied Chemistry
LAMMPS	Large-Scale Atomic/Molecular Massively Parallel Simulator

Chapter 1

Introduction

1. Introduction

1.1. Catalysis

A catalyst is defined by the International Union of Pure and Applied Chemistry (IUPAC) as *a substance that increases the rate of a reaction without modifying the overall standard Gibbs energy change in the reaction* Catalysis is defined as *the action of a catalyst*.[1] The role of a catalysts within a chemical reaction is to interact with the reactants, products, or intermediates to decrease the activation energy of the reaction (Figure 1.1). This decrease in most cases is due to the modification of the reaction mechanism. The catalyst only modifies the speed of the reaction, leaving the thermodynamic magnitudes unchanged. The catalyst does not affect the reactants or the products and at the end of the reaction it is not consumed. That is to say, in principle, all the catalyst can be recovered at the end of the chemical process.

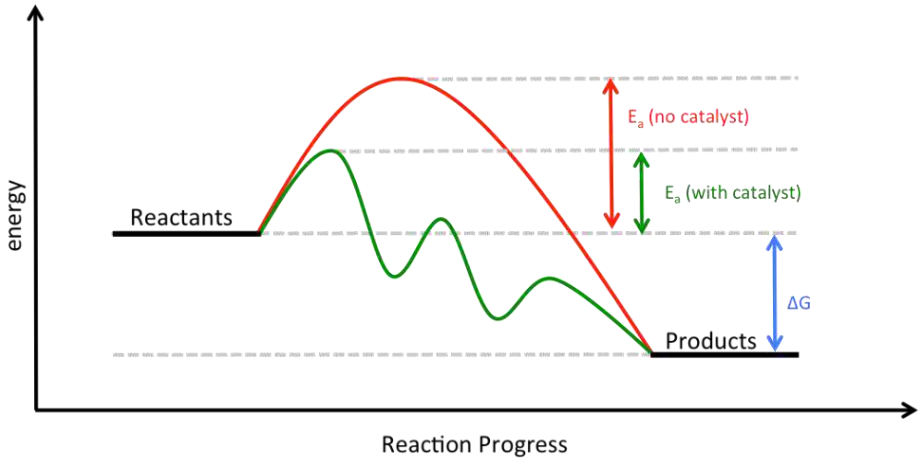

Figure 1.1. Representation of an arbitrary reaction profile for a catalysed reaction (green line) and non-catalysed reaction (Red line).

In a general sense, anything that increases the rate in a process is a "catalyst." This term comes from the Greek and means "to undo", "to untie", or "to gather". In principle a catalyst can also deactivate the catalysis, that is, in this case it would increase the activation energy so that the reaction does not take place. This type of catalyst is called an inhibitor.

The concept *catalyzed processes* was first coined by the Swedish chemist Jöns Jakob Berzelius in 1836 to describe reactions that are accelerated by substances that remain unchanged after the reaction. Other pioneers in catalysis were the chemist Alexander Mitscherlich who used the term *contact processes* and the chemist Johann Wolfgang Döbereiner who spoke of *contact action*. In the 1880s, Wilhelm Ostwald at the University of Leipzig began a systematic investigation of the reactions that were catalyzed by the presence of acids and bases. For this work, Ostwald was awarded the 1909 Nobel Prize in Chemistry.

1.2. Heterogeneous Catalysis

Catalysis can be classified into enzymatic, homogeneous, or heterogeneous catalysis. This classification is given by the nature of the catalyst and by the physical state in which the substances involved in the reaction are found. In enzymatic catalysis, biological reactions are catalysed by large complex molecules called enzymes. It is also worth mentioning that some synthetic molecules called artificial enzymes are capable of catalysing some biologically relevant chemical reactions. In homogeneous catalysis, the reactants and the catalyst are in the same physical state. As an example of this type of catalysis we have the Fenton process,[(2)] which consists in the elimination of the process of pollutants from the water by means of high-potential hydroxyl radicals and uses solubilized iron as a catalyst. The last family of catalysts are heterogeneous catalysts, where solid state catalysts catalyse reactions where the reactants are in the gas or liquid phase. One of the advantages of heterogeneous catalysts over homogeneous ones is the ease of separating the catalyst from the final products. The production of 90% of chemicals (by volume) is assisted by solid catalysts.[(3)] The chemical and energy industries rely heavily on heterogeneous catalysis. Different examples of heterogeneous catalytic reactions are shown in Table 1.1.

Table 1.1. Industrially important examples of heterogeneous catalysis.

Process	Catalyst	Reaction
Haber-Bosh	Iron	$N_{2(g)} + 3H_{2(g)} \rightarrow 2NH_{3(g)}$
Natural gas reforming	Nickel	$CH_{4(g)} + H_2O_{(g)} \rightarrow CO_{(g)} + 3H_{2(g)}$
Gas oil cracking	Zeolite	Products: • A gas: ethane, propane • A liquid: petrol • A residue: fuel oil
Naphtha reforming	Platinum and rhenium on alumina	$CH_3CH_2CH_2CH_2CH_2CH_3(g) \rightarrow$ $(g) + H_2(g)$
Epoxyethane synthesis	Silver on alumina	$C_2H_4(g) + \frac{1}{2}O_2(g) \rightarrow$ 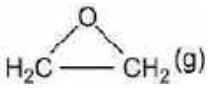
Sulfuric acid synthesis	Vanadium (V) oxide on silica	$2SO_{2(g)} + O_{2(g)} \rightarrow 2SO_{3(g)}$
Nitric acid synthesis	Platinum and rhodium	$4NH_{3(g)} + 5O_{2(g)} \rightarrow 4NO_{(g)} + 6H_2O_{(g)}$

Heterogeneous catalysts are extremely complex systems. In particular it is largely unknown where and how the catalytic process occurs on their surfaces. In this way, the study of their surfaces, within the field of Surface Science, becomes of primary importance. Apart from their characterization, there is a continuous search for new efficient catalysts, since most of the catalysts used in industry use expensive precious metal nanoparticles such as Pd or Pt as active phases, typically supported on either porous oxides or sulfides.[4] Increasingly, the study of new model catalysts is done through collaboration between experiments and computational calculations. Computational modelling has become a very useful tool not only to search for new catalysts, but also to better understand the reaction mechanisms that occur on their surfaces at the atomic level. In addition, this synergy has made it possible to reduce the number of experiments and focus the efforts on the appropriate planned materials with the consequent savings in economic costs involved in all the experimental trial and error studies. In this Thesis we will focus on a promising class of new heterogeneous catalysts: Transitions metal carbides (TMCs).

1.3. Transitions Metals Carbides

Transition metal carbides (TMCs) are obtainable by incorporating carbon atoms into the interstitial sites of their parent metals, which typically include all 3*d* elements and 4*d*/5*d* elements of groups III-VI early transition metals.[5] TMCs have physical and chemical properties that combine the characteristic features of three different classes of materials: First, TMCs show the extreme hardness and brittleness of covalent solids. Second, they have a high melting temperature and simple crystalline structures, typical of ionic crystals. Lastly, they also have electrical and magnetic properties, typical of transition metals.[5] Such TMCs were posed as catalytic materials already by Levy and Boudart,[6] TMC properties are also used for other purposes, from mechanical applications to coatings.

A clear indicator of the interest of this type of material is the large increase in publications that have been caused on this type of material. In the last year, more than 810 articles related to TMCs have been published, while 10 years ago the number of publications on these compounds was around 238 (2010) publications/year see Figure 1.2.

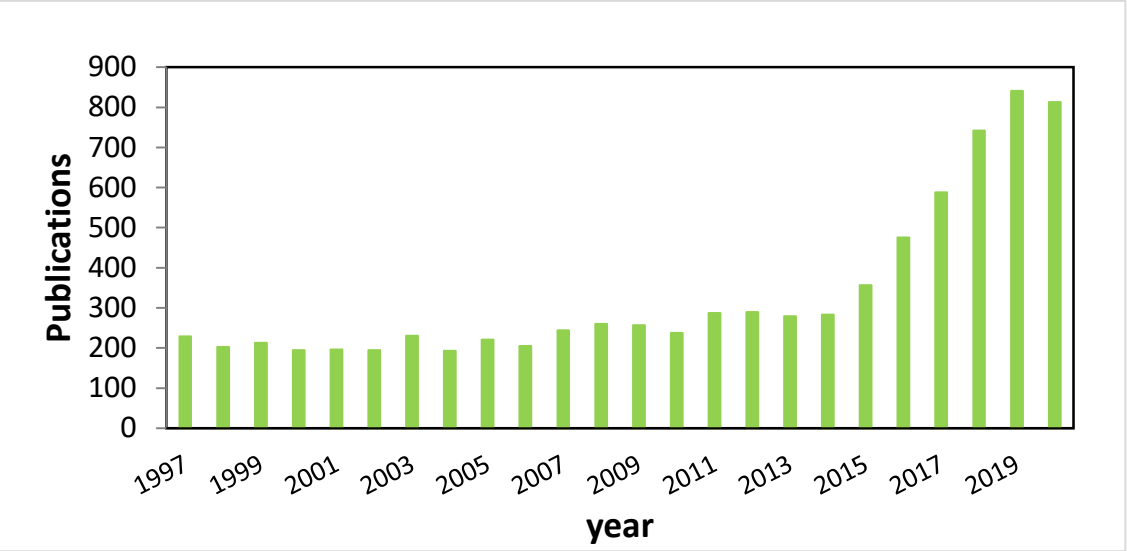

Figure 1.2. Number of published articles per year using the keyword "Transition metal Carbides" in Web of Science.

1.3.1. Catalytic properties

Some TMCs from early transition metals have been synthetized and tested as catalysts.[7] Many years have passed since Levy and Boudart in the 1970s showed that tungsten carbides could exhibit a behavior similar to Pt in various catalytic reactions such as hydrogenation, dehydrogenation, isomerization, and desulfurization reactions.[6] TiC is one of the family of carbide compounds that has recently attracted increased attention. This compound has been proposed as excellent catalyst for different reactions: H_2 dissociation,[8] CO oxidation,[9,10] and methane activation,[11] among others. The catalytic activity of this material has also been studied as a support for clusters of precious metals giving very promising catalytic results.

TMCs also present some advantages respect to precious metals (Ru, Rh, Pd, Os, Ir, and Pt). The first one is their cost; TMCs are cost-effective materials whereas noble metals are very expensive given their scarcity. The second advantage is that on TMCs the adsorption of molecules is less strong than on precious metals. This fact suggests that the dissociation of some products may be simpler. Finally, TMC catalysts are resistant against carbon or sulphur poisoning, although they can get poisoned with oxygen with the formation of oxycarbide reducing their catalytic activity. However, even in the last case there are recent studies where surface oxycarbide may retain chemical activity, as seen, e.g. in the CO_2 capture by group IV TMC oxycarbides.[12]

1.4. Hydrogen

Hydrogen is the most abundant chemical element, constituting approximately 75% of the visible matter in the universe.[13] Hydrogen is mainly found in stars in the plasma state. However, due

to its volatility, hydrogen is relatively rare on Earth, where it is found as part of minerals, oceans and all living beings.[13]

1.4.1 H_2 uses

Hydrogen is consumed in a multitude of processes.[14] Around 72% of hydrogen is used in the chemical and petrochemical industry (oil refining (37%), ammonia (50%), methanol (8%), etc.). The rest is used in metallurgy, electronics and in the propulsion of space vehicles (Figure 1.3).

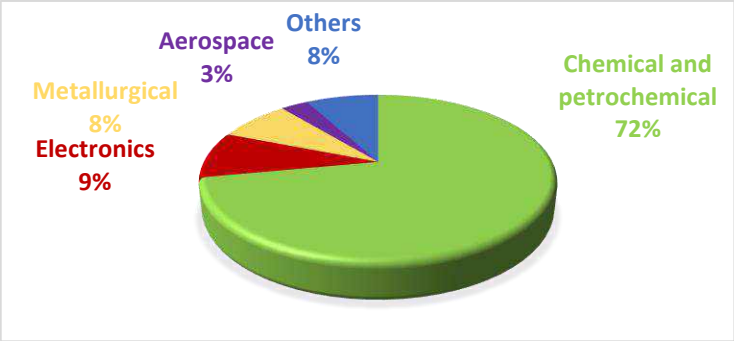

Figure 1.3. Chart of Industrial H_2 uses.

Within the chemical and petrochemical industry, the main use of hydrogen is in the manufacturing of ammonia through the Haber-Bosch process:[15]

$$N_{2(g)} + 3H_{2(g)} \rightarrow 2NH_{3(g)}$$

This process is fundamental for the fertilizer market, since it allows the use of atmospheric N_2 to obtain ammonia in the first step, up to nitrates in later synthesis stages. Other important uses of Industrial H_2 is in refineries where H_2 is employed to refine heavier, sour crudes, increase refinery yields and reduce emissions through the production of cleaner transportation fuels including ultra-low sulphur diesel fuel. In Figure 1.4, the main uses of industrial hydrogen are shown.

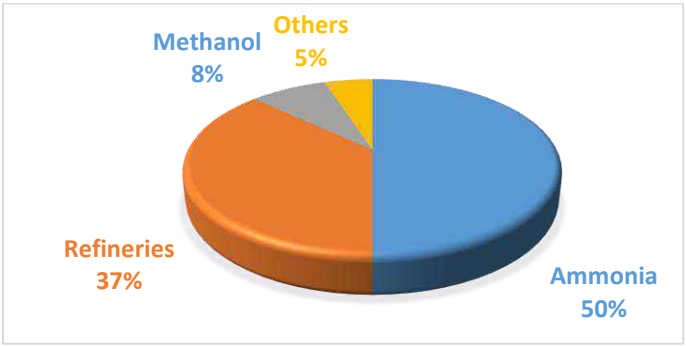

Figure 1.4. Chemical and petrochemical H_2 uses.

1.4.2. H_2 as clean energy fuel

Hydrogen is a green alternative to fossil fuels. Hydrogen is a zero-emission fuel when burned with oxygen. Hydrogen combustion only produces H_2O and does not produce CO_2 and NO_X, therefore, it non-polluting and does not contribute to global warming. This technology is used in electrochemical cells and internal combustion engines.

1.4.2.1 Electrochemical fuel cells

In an electrochemical fuel cell, that energy can be used with relatively high efficiency. In an electrochemical cell, hydrogen fuel is introduced in one part where oxidation is carried out, while in the other O_2 is reduced. In this case, the hydrogen is added at one catalytic surface of a proton exchange membrane in which it is dissociated giving place to two protons which cross the membrane and arrive to the other surface. On this side of the membrane, oxygen is added where it adsorbs and dissociates on the catalytic surface. Here protons from the hydrogen combine oxygen atoms forming water molecules. See Figure 1.5.

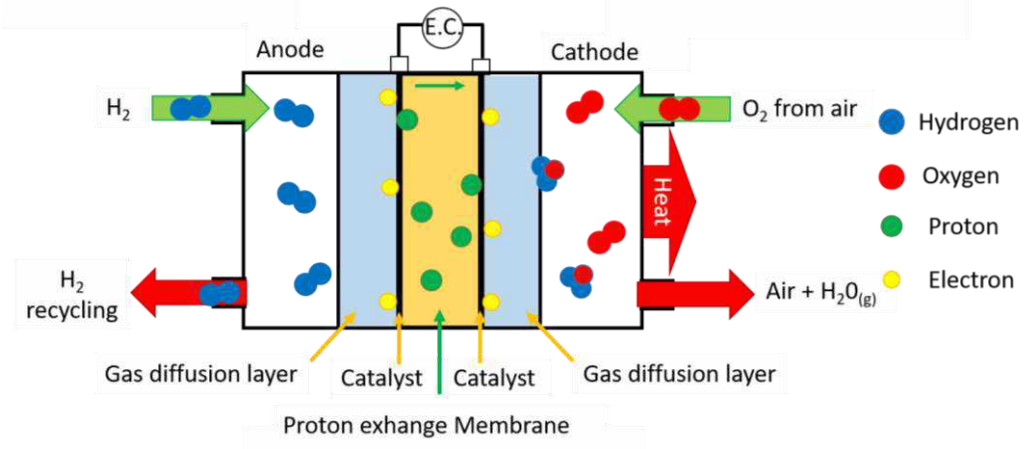

Figure 1.5. H_2 cell scheme.

The global reaction involved in this process is:

$$2H_{2(g)} + O_{2(g)} \rightarrow 2H_2O_{(g)}$$

In this case, the energy released in the water formation enables hydrogen to act as a fuel. In addition, using a similar technology to the hydrogen cell, the methanol cell increases the energy obtained. In this case, the global reaction involved is:

$$2CO_{2(g)} + 4H_2O_{(g))} \rightarrow 2CH_3OH_{(g)} + 3O_{2(g)}$$

The methanol (MeOH) cell has more benefits than the hydrogen fuel cell. On one hand, more energy is obtained; on the other hand, there is a possibility to use CO_2 to produce MeOH thus reducing amount in the atmosphere using carbon capture and storage technologies[16] and then

doing the water-gas shift reaction,[17] the CO_2 can be converted in MeOH. Even if MeOH is later on burned to produce CO_2, these steps helps at making C-economy circular, and so, sustainable over time.

Fuel cells have started to be used in commercial vehicles such as passenger cars, and have been used in buses for many years. Fuel cells are also used for the propulsion of spacecraft. In fact, nowadays fuel cells are being used in many different means of transport,[18] see Figure 1.6.

Figure 1.6. Left, Hydrogen train running test in Germany. Right, Hydrogen bus in Barcelona.

1.4.3. H_2 production

In 2018 the world production of H_2 reached a total of 60 million metric tons. This figure is expected to increase dramatically by 2030, reaching approximately around 300 million metric tons.[19] Currently, almost 96% of the World's hydrogen is produced from fossil fuels, mainly by reforming natural gas with water vapor,[20] according to the reaction:

$$CH_{4(g)} + H_2O_{(g)} \rightarrow CO_{(g)} + 3H_{2(g)}$$

Hydrogen production technologies using fossil fuels, especially natural gas, are proven technologies and widely applied. The main disadvantages of these processes are that CO_2 is also emitted in the hydrogen production process, and that exhaustible resources are being used as raw materials, of which there are limited and concentrated reserves in few places on the globe. Only 4% of the World's hydrogen is produced by electrolysis of water, which is for applications that require high gas purity.

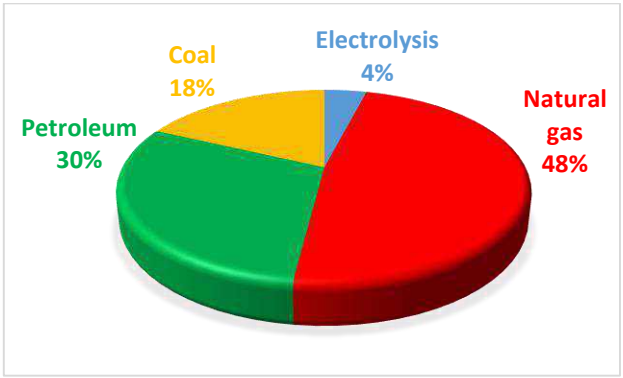

Figure 1.7. H_2 production

1.5. Motivation and outline of the Thesis

The reduction of greenhouse gases, especially two of the most harmful compounds, CO_2 and CH_4, is one of the main environmental goals nowadays. In addition, the transformation of these compounds into more valuable chemical compounds is sought, such as, for example, the transformation of carbon dioxide into methanol ($CO_{2(g)} + 3H_{2(g)} \rightarrow CH_3OH_{(g)} + H_2O_{(g)}$) or the procurement of hydrogen from methane "steam methane reforming" (SMR) ($CH_{4(g)} + H_2O_{(g)} \rightarrow 3H_{2(g)} + CO_{2(g)}$). Both CO_2 and CH_4 are two very thermodynamically stable molecules, therefore, for these reactions to take place, good catalysts are necessary. It is known that noble metals are good catalysts for this type of reaction, but the high cost of these metals and their low abundance in nature means that other alternative catalysts have to be investigated. TMCs catalysts are an alternative to these noble metal catalysts.

The research work in this thesis aims to study the structural and, chemical properties of catalytic materials formed by TMCs by means of computational modelling. In this thesis, the modelling is mainly focused on two aspects: *i)* the catalytic properties of TMC surfaces, and *ii)* the chemical and physical properties of Titanium Carbide (TiC) Nanoparticles (NPs). Chemically, these systems are studied with respect to hydrogen adsorption and dissociation. Hydrogen dissociation was studied on seven different TMCs with metals of groups IV, V, and one of group VI. The TMCs under study are shown in Figure 1.8.

group / series	IV	V	VI
3*d*	TiC	VC	
4*d*	ZrC	NbC	δ-MoC
5*d*	HfC	TaC	

Figure 1.8. The early TMCs under investigation in this Thesis.

My study specifically focused TiC based systems. On the TiC (001) surface we also studied methane dissociation. This reaction has been studied with the bare TiC surface and with the addition of small supported Ni clusters. I also studied the structure and vibrational spectra of a number of TiC-based nanoparticles (NPs)s with relation to understanding results from cluster beam experiments.

This Thesis has been carried out in the Computational Materials Science Laboratory (CMSL) of the *Institut de Química Teòrica i Computacional* (IQTC) at *Universitat de Barcelona*.

This Thesis is structured as follows:

- Chapter 2 describes the theoretical background with the models and the methodology employed to carry out the computational studies of the research realized in this Thesis.

- Chapter 3 reports the studies of H_2 adsorption and dissociation on TiC (001) surfaces. This study was performed in different steps. The first step consisted in finding the energetically favoured H adsorption positions between low coverage to over full coverage. In a second step, H_2 molecular adsorption was studied. The last step consisted in simulating the H_2 dissociation reaction. In addition, in this chapter the paper "**Diversity of Adsorbed Hydrogen on the TiC (001) Surface at High Coverages"** published in **the journal of Physical Chemistry C**, 2018, 122, 28013 is added. My contribution in this paper has consisted of making the computational part of the paper.
- Chapter 4 expands the study of chapter 3 but for the other of TMCs under study. These studies have served as a basis for later refining and publishing them in the paper added in this chapter: "**Assessing the usefulness of transition metal carbides for hydrogenation reactions"**, **Chem. Comm.,** 2019, 55, 12797.
- Chapter 5 is focused on the adsorption and dissociation of CH_4 on the bare TiC (001) surface and on the TiC (001) surface doped with Ni Clusters. The procedure used in this chapter is analogous to that followed in Chapter 3. In this chapter, the article "**Room Temperature Methane Capture and Activation by Ni Clusters Supported on TiC (001): Effects of Metal-Carbide Interactions on the Cleavage of the C-H Bond"** has been published on ***J. Am. Chem. Soc.*** **,**2019, 141, 5303 where I have contributed by carrying out studies on the surface of TiC without Ni clusters.
- Chapter 6 describes the stability and the characterization of TiC NPs. In particular, we model the infrared spectra of a wide range of TiC-based NPs and compare our results directly with results from cluster beam experiments. All theoretical studies of the paper ***Can Calculated Harmonic Vibrational Spectra Rationalize the Structure of TiC-based Nanoparticles?***, **Phys. Chem. Chem. Phys**. under review 2021 have been carried out for me.
- Chapter 7 reports the results of calculations the adsorption of H_2 molecular and its subsequent dissociation on TiC NPs of various sizes (this study is analogous to that reported in Chapter 3 on the TiC surface).
- Chapter 8 summarizes the general conclusions of this thesis.
- Chapter 9 reports the list of the publications obtained with the work of this Thesis.
- Chapter 10 resumes the Thesis in Castellano.
- Finally, 3 appendix show the supplementary information of the papers "**Diversity of Adsorbed Hydrogen on the TiC (001) Surface at High Coverages"** (Appendix A), "**Assessing the usefulness of transition metal carbides for hydrogenation reactions"** (Appendix B), and "**Room Temperature Methane Capture and Activation by Ni Clusters Supported on TiC (001): Effects of Metal-Carbide Interactions on the Cleavage of the C-H Bond"** (Appendix C).

1.6. References

1. A.D. McNaught and A. Wilkinson. IUPAC. Compendium of Chemical Terminology. 2nd ed (th. Vol. 2291, IUPAC Compendium of Chemical Terminology. Oxford: Blackwell Scientific Publications; **1997**. 2293 p.

2. A. Babuponnusami and K. Muthukumar. A review on Fenton and improvements to the Fenton process for wastewater treatment. *J. Environ. Chem. Eng.*, **2014**, 2, *1*, 557–572.
3. G. Rothenberg. *Catalysis: concepts and green applications*. Weinheim [Germany]: Wiley. **2008**. ISBN 9783527318247.
4. M. Fernández-García and J. A. Anderson, *Supported Metals in Catalysis, Catalytic Sciences Series*, Vol. 5, Imperial College Press, London, **2005**; A. Wieckowski, E. Savinova, and C. G. Vayenas, *Catalysis and Electrocatalysis at Nanoparticle Surfaces*, Marcel Dekker, New York, **2003**.
5. H.H. Hwu and J.G. Chen. Surface chemistry of transition metal carbides. *Chem. Rev.*, **2005**;105, *1*, 185–212.
6. R.B. Levy and M. Boudart. Platinum-Like Behavior of Tungsten Carbide in Surface Catalysis. *Science*, **1973**, 181, *4099*, 547–549.
7. A.P.E. York, J.B. Claridge, C. Márquez-alvárez, A.J. Brungs, and, S.C. Tsang, *Synthesis of Early Transition Metal Carbides and their Application for the Reforming of Methane to Synthesis Gas*. The Catalysis Centre, Inorganic Chemistry Laboratory, University of Oxford, South Parks, in: R.K. Grasselli, S.T. Oyama, A.M. Gaffney, J.E. Lyons (Eds.), 3rd World Congr. Oxid. Catal., Elsevier Science B. V., **1997**, pp. 711–720.
8. J.A. Rodriguez, P. Liu, F. Viñes, F. Illas, Y. Takahashi and K. Nakamura. Dissociation of SO_2 on Au / TiC (001): Effects of Au – C Interactions and Charge Polarization. *Angew. Chem. Int. Ed.*, **2008**; 129, *35*, 6685–6691.
9. J.A. Rodriguez, P. Liu, D.J. Stacchiola, S.D. Senanayake, M.G. White, and J.G.Chen. Hydrogenation of CO_2 to Methanol: Importance of Metal-Oxide and Metal-Carbide Interfaces in the Activation of CO_2. *ACS Catal.*, **2015**, 5, *11*, 6696–6706.
10. J.A. Rodriguez, J. Evans, L. Feria, A. B. Vidal, P. Liu, K. Nakamura, and, F. Illas. CO_2 hydrogenation on Au/TiC, Cu/TiC, and Ni/TiC catalysts: Production of CO, methanol, and methane. *J. Catal.*, **2013**, 307, 162–169.
11. C. Kunkel, F. Viñes, and, F.Illas. Biogas Upgrading by Transition Metal Carbides. *ACS Appl. Energy Mater.* **2018**, 1, *1*, 43–47.
12. C. Kunkel, F. Viñes, P.J. Ramirez, J.A. Rodriguez, and, F.Illas. Combining Theory and Experiment for Multitechnique Characterization of Activated CO on Transition Metal Carbide (001). *Phys. Chem. C* ,**2019**, 123, *13*, 7567–7576.
13. R.A. Alpher and R.C. Herman. Erratum: Theory of the origin and relative abundance distribution of the elements. *Rev Mod Phys.*, **1950**, 22, *4*, 153–212.
14. R. Ramachandran and R.K. Menon. An overview of industrial uses of hydrogen. *Int J Hydrog. Energy.*, **1998**, 23, *7*, 593–598.
15. J. Erisman, M. Sutton, J. Galloway, Z. Klimont and W. Winiwarter. How a century of ammonia synthesis changed the world. *Nat. Geosci.*, **2008**, 1, 636-639.
16. D.Y.C. Leung, G. Caramanna, and M.M. Maroto-Valer. An overview of current status of carbon dioxide capture and storage technologies. *Renew. Sust. Energ. Rev.*, **2014**,39,426–443.
17. D.S. Newsome. The Water-Gas Shift Reaction. *Catal Rev Sci Eng*, **1980**, 1, *2*, 275-318.
18. R. Cammack, M. Frey, and R. Robson, R. (Eds.). (2001). *Hydrogen as a Fuel: Learning from Nature* (1st ed.). CRC Press. London, **2001**. ISBN 9780429203978.
19. N. Sönnichsen (Jan 29, 2021). global hydrogen-production 2018-2030. https://www.statista.com/statistics/859104/hydrogen-production-outlook-worldwide-by-type/
20. M. Kayfeci, A. Keçebaş, and M. Bayat. *Hydrogen production*. F. Calise, M. D. D'Accadia, M. Santarelli, A. Lanzini, and, D. Ferrero (Eds),1st edition, Solar Hydrogen Production, Academic Press, 2019, pp. 45-83. ISBN 9780128148532.

Chapter 2

Theoretical Background

2. Theoretical Background

In this Chapter we will summarize the background theory needed to understand the simulations carried out in this Thesis.

2.1. The Schrödinger equation

The basis of quantum chemistry is the Schrödinger equation, developed by Erwin Schrödinger in 1926:[1]

$$\hat{H}\psi_n = E_n\psi_n \quad (2.1),$$

where $\hat{H}$ is the Hamiltonian operator, that, applied to the system wavefunction, ψ_n, delivers it multiplied by the system energy, E_n. This equation describes systems containing *n* particles, where the wavefunction is a function dependent on the R_n nuclear coordinates, and the r_n electron coordinates.

$$\hat{H}\psi(r_1, R_1 \dots r_n, R_n) = E\psi(r_1, R_1 \dots r_n, R_n) \quad (2.2).$$

In addition, the wavefunction also depends on the particle spin. The Hamiltonian can be decomposed as the sum of kinetic ($\hat{T}$) and potential ($\hat{V}$) energy operators;

$$\hat{H} = \hat{T} + \hat{V} = \left(\hat{T}_{el} + \hat{T}_{nuc}\right) + \left(\hat{V}_{ne} + \hat{V}_{ee} + \hat{V}_{nn}\right) \quad (2.3),$$

where $\hat{T}_{el}$ and $\hat{T}_{nuc}$ are the kinetic operators of the electrons and nuclei, respectively, $\hat{V}_{ne}$ is the columbic attraction between electrons and nuclei, $\hat{V}_{ee}$ represents the columbic repulsion between electrons, and $\hat{V}_{nn}$ corresponds to the columbic repulsion between nuclei.

Generally, exact solutions of the Schrödinger equation for polyelectronic systems are intractable. In order to simplify things, the Born-Oppenheimer approximation is often employed.

2.1.1 The Born-Oppenheimer approximation

The Born-Oppenheimer approximation[2] consists in uncoupling the nuclear and electronic motions. Since the mass of the nuclei are much larger compared to the that of electrons, this causes that the velocity of the nuclei is very small in comparison with the velocity of the electrons. As a consequence, the nuclear kinetic term ($\hat{T}_{nuc}$) can be neglected, considering the nuclei position fixed, which makes the nuclei repulsion ($\hat{V}_{nn}$) a constant. Taking into account these last considerations, the wave function can be expressed as the product of the electron and nuclear wavefunctions:

$$\psi_{tot}(R, r) = \psi_{el}(R, r) \cdot \psi_{nuc}(R) \quad (2.4).$$

Here one observes that the electronic wave function $\psi_{el}(R,r)$ takes into account the nuclear coordinates and, therefore, different nuclei configurations present different wavefunctions. This fact induces that the electronic energy term is complex to calculate. To solve this term, there are two main families of methods: i) wavefunction (WF) methods and ii) density functional theory (DFT) methods.

2.1.2. The Hartree-Fock method.

The Hartree-Fock (HF) method[1] can be regards as the most basic WF method used to solve the problem of electronic interactions in polyelectronic systems as described in the previous section. In order to solve this problem, the HF method calculates a single Slater determinant to describe all electrons of the system under study. The Slater determinant describes an antisymmetric electronic function (thus satisfying the fact that electrons are subject to exchange symmetry) for the ground electronic Hamiltonian. This fact is equivalent to considering each electron in the system as an independent electron with respect to the others. This last approximation is the main source of the method's errors, as it does not take into account electronic correlation (i.e. electron-electron coulombic interactions), that are not negligible. The HF method is based on the variational principle; because of this, the HF energy is above the real ground state energy (E_0). The difference between the real E_0 for the system and the HF energy is defined as the electronic correlation energy, see Figure 2.1.

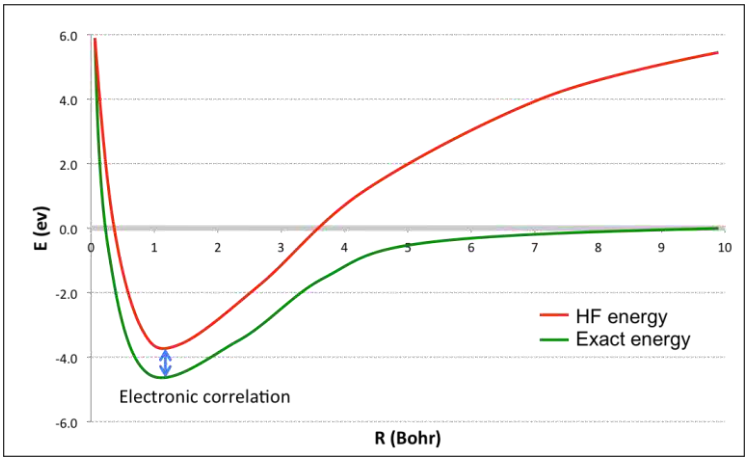

Figure 2.1. Comparison of HF and exact energy with respect the distance in between two atoms.

In order to improve the HF method, other methods have been developed to describe the electronic correlation and get closer to the real ground state energy. However, more sophisticated WF methods based on improvements to HF (post-HF methods) aimed at better describing the real ground state imply a significantly higher computational cost. In this thesis we do not use WF methods but employ DFT, which offers a good compromise between accuracy and computational efficiency.

2.2. Density functional theory (DFT)

Density Functional Theory (DFT)[3,4] offers an alternative way of treating the electronic Schrödinger equation and becomes useful to evaluate the energy and other properties of a polyelectronic system. The DFT method is based on a statistical model defined by Thomas and Fermi in 1927 for the electron gas model.[5,6] In this model, the energy of the system is established by electrons uniformly distributed under the influence of a nuclear field as a function only of the electron density. As previously explained, DFT is an alternative to WF methods, and requires less computational costs than other HF or post-HF methods, plus gives accurate results for the exchange and correlation energies.

The DFT method is thus based on using the electron density function *ρ(r)* of the ground state of a polyelectronic system. This method reduces the difficulty to calculate the electronic wavefunction (ψ_{el}), as, for a system with *N* electrons, the ψ depends on 3*N* spatial coordinates plus *N* spin ones, while ρ(r) depends only on three spatial coordinates (four with spin). The density function *ρ(r)* states the probability to find an electron in a certain volume. This function must fulfil two conditions:

- The integral of *ρ(r)* in all space must be equal the total number of electrons of the system.
- The value of the function at infinite distance must be equal to zero.

These conditions mathematically are translated into:

$$E_0 = E_0[\rho] \tag{2.5}$$

$$(\rho) = N \int \cdots \int |\psi(r_1, r_2, \dots, r_n)|^2 \, dr_1 dr_2 \dots dr_n \tag{2.6}$$

$$\int \rho(r) \, d_r = N \tag{2.7}$$

$$\rho \, (r \rightarrow \infty) = 0 \tag{2.8}$$

However, the DFT method was not widely used until Hohenberg and Kohn formulated their two theorems, explained next, based on which the modern DFT formalism was outlined. One year later, Kohn-Sham presented an implementation to optimize the electron density.

2.2.1. First Hohenberg-Kohn theorem

The first Hohenberg-Kohn theorem was described in 1964.[7] This theorem describes the (non-degenerate) ground state electronic energy as functional of the electron density. According to this theorem, the electron density is determined by the external potential (produced by the nuclei, $\hat{V}_{ne}$) and the inverse relation.

$$V_{ext} = V_{ne} \tag{2.9}$$

The main conclusion of this first theorem is that all properties of the ground state, including the energy, are defined by the functional of the electron density. The theorem is usually proven *ad absurdum*, assuming two different external potentials ($V_r$and $V_r^{'}$) that give the same ground state density ρ(r). Each external potential presents a different Hamiltonian with two fundamental functions, two wavefunctions, and two energies, also different:

$$\hat{H} = \left(\hat{T} + \hat{V}_{ext} + \hat{V}_{ee}\right) \qquad \hat{H}\psi = E_0\psi$$

$$\hat{H}^{'} = \left(\hat{T} + \hat{V}_{ext}^{'} + \hat{V}_{ee}\right) \qquad \hat{H}^{'}\psi^{'} = E_0^{'}\ \psi^{'} \qquad (2.10).$$

The variational principle establishes that, for a given system, the energy of a wavefunction is always higher than real energy of the system.

$$E_0 = \langle\psi|\hat{H}|\psi\rangle\ <\ \langle\psi^{'}\ |\hat{H}|\psi^{'}\ \rangle\ = \langle\psi^{'}\ |\hat{H}^{'}\ +\ \hat{V}_{ext}\ -\ \hat{V}_{ext}^{'}|\psi^{'}\ \rangle \qquad (2.11).$$

Simplifying one gets:

$$E_0 < E_0^{'}\ +\ \langle\psi^{'}\ |\ \hat{V}_{ext}\ -\ \hat{V}_{ext}^{'}|\psi^{'}\ \rangle \qquad (2.12),$$

and by employing the equation for the nuclei-electron and due to the multiplicative character of the potentials, one obtains:

$$V_{ext} = \int V_{ext}\,(r)\psi^{*}\,(r)\,\psi(r)\,dr\ =\ \int V_{ext}\,(r)\,\rho(r)\,dr \qquad (2.13).$$

When Eq. (2.12) is expressed in terms of the density, the resulting equation is:

$$E_0 < E_0^{'}\ +\ \int\left[V_{ext}(r) - V_{ext}^{'}(r)\right]\rho(r)dr \qquad (2.14).$$

When the procedure is repeated starting from the inverse relation, one gains:

$$E_0^{'}\ < E_0\ +\ \int\left[V_{ext}^{'}(r) - V_{ext}(r)\right]\rho(r)dr \qquad (2.15).$$

Now, when the equations (14) and (15) are added, one ends getting:

$$E_0\ + E_0^{'}\ <\ E_0^{'}\ + E_0 \qquad (2.16).$$

As one can simply see, the last equation is a contradiction, and so it is demonstrated that each density is associated with one potential.

Therefore, the ground state energy is a function of *ρ(r)* and, including the Born-Openheimer approximation, it can be expressed as:

$$E(\rho)\ = T(\rho) +\ V_{ee}(\rho) +\ V_{ne}(\rho) =\ F_{HK}[\rho] +\ \int\rho(r)V_{ne}\,(\rho)dr \qquad (2.17),$$

where $F_{HK}[\rho]$ is a universal functional, which is defined by the kinetic energy and the electron-electron repulsion potential, $\hat{V}_{ee}$ Unfortunately, the functional $F_{HK}[\rho]$ is unknown and there are great research endeavours to find an accurate mathematical expressions for $F_{HK}[\rho]$.

2.2.2. Second Hohenberg-Kohn theorem

The second theorem of Hohenberg-Kohn[7] enunciates that the energy in a non-degenerate ground state can be obtained by the variational method, and that the electronic density that minimizes the total energy is the exact electronic density of that state, so therefore defines correctly the external potential.

$$E_0 \leq E[\rho] \tag{2.18}.$$

When ρ_0 is known, in this case, the exact energy of the ground state is obtained. With these two theorems the variational principle is established, but one lacks a procedure to minimize the electron density, explained next.

2.2.3. Kohn-Sham method

In 1965 Kohn and Sham developed the last step for the modern DFT formalisms, the Kohn-Sham method.[3,4] This method focuses in obtaining an approximation of the universal functional $F_{HK}[\rho]$. The method proposes a fictional system with N non-interacting electrons. This means that the fictional system can be described by a Slater's determinant, whose elements are functions that represent each electron in the systems (orbitals, Φ_i). This implies that the total kinetic energy is the sum of the kinetic energy of each electron:

$$T_s[\rho] = \sum_{i=1}^{N} \left\langle \Phi_i \left| -\frac{1}{2}\nabla^2 \right| \Phi_i \right\rangle \tag{2.19}.$$

In this method, the universal functional, $F_{HK}[\rho]$, is also described as:

$$F_{HK}[\rho] = T_s[\rho] + J[\rho] + E_{xc}[\rho] \tag{2.20},$$

where $T_s[\rho]$ is the total kinetic energy of the system, $J[\rho]$ is a term that contains the classic repulsion between two electrons, and $E_{xc}[\rho]$ is the exchange-correlation functional. The $J[\rho]$ term is defined as:

$$J[\rho] = \frac{1}{2}\iint \frac{\rho(r_1)\rho(r_2)}{|r_1 - r_2|} dr_1 dr_2 \tag{2.21},$$

and the $E_{xc}[\rho]$functional is defined as:

$$E_{xc}[\rho] = T[\rho] - T_s[\rho] - J[\rho] + V_{ee}[\rho] \tag{2.22}.$$

To be considered a Kohn-Sham orbital, the orbital has to satisfy the Kohn-Sham equations:

$$\left(-\frac{1}{2}\nabla^2 + V_s(r_1)\right)\Phi_i(r) = \varepsilon_i\Phi_i(r) \quad (2.23),$$

$$V_s(r_1) = \int \frac{\rho(r_2)}{r_{12}} dr_2 + V_{XC} - V_{ne}(r_1) \quad (2.24),$$

where $V_s(r)$ contains the exchange-correlation interaction effects between electrons, $V_{ne}(r)$ is the external potential with *N* particles without interaction between, and V_{XC} is the only unknown term in the equation due to the exchange-correlation energy.

As the Kohn-Sham equation presents an unknown term, V_{XC}, the universal functional cannot have an exact solution, but finding a solution for this V_{XC} would imply an exact solution for the universal functional.

2.3. Exchange-correlation functional

A good choice of exchange-correlation functional is essential to perform DFT calculations. A poor choice can lead to absurd results in the simulations. Exchange-correlation functionals can be classified into four groups: Local density approximation (LDA), Generalized Gradient Approximation (GGA), meta-GGA, and Hybrid functionals.

2.3.1. Local density approximation (LDA)

LDA type of functionals were the first ones developed. This approximation is the simplest to be employed, as it assumes that the exchange-correlation energy at each point of the system exclusively depends on the density at that point.

$$E_{xc}^{LDA}[\rho] = f[\rho] \quad (2.25).$$

The exchange-correlation energy can be decomposed into a sum of the terms of exchange and correlation separately, that is:

$$E_{xc}[\rho] = E_x[\rho] + E_c[\rho] \quad (2.26).$$

LDA has an exchange component given by the Dirac Formula:

$$E_x[\rho] = -\frac{3}{4}\left(\frac{3}{\pi}\right)^{1/3}\rho^{1/3} \quad (2.27).$$

However, there is no analytical expression for the correlation part. Some examples of this type of functionals are the Vosko-Wilk-Nusair (VWN),[8] or the Cole-Perdew (CP) functional.[9]

2.3.2. Generalized Gradient Approximation (GGA)

This type of functional depends on the local density and also introduces on the gradient of the density.

$$E_{XC}^{GGA}[\rho(r)] = \int f_{xc}(\rho(r), |\nabla\rho(r)|)\rho(r)dr \quad (2.28).$$

These functionals provide better results than LDA for some system properties such as geometries, charge densities, energy of the ground state, and vibrational frequencies, although other system properties do not represent a substantial improvement. Two of most common GGA functionals are Perdew-Wang (PW91)[10] and Perdew-Burke-Ernzerhof (PBE).[11] The PBE was indeed the basis for better improvements, e.g. the revised version of PBE (RPBE)[12], developed to reproduce atomization energies of small molecules, but also performing well for adsorption energies on transition metal surfaces;[13] the PBEsol[14] (which exhibited improved performance from solids, or the Vega-Viñes (VV) and VVsol, which adjusted PBE and PBEsol, respectively, for describing transition metal bulks and surfaces.[15]

2.3.3. Meta-GGA

Meta-GGA functionals depend on the density, the gradient of the density, and also the Laplacian of the density (second derivate of the electron density);

$$E_{XC}^{mGGA}[\rho(r)] = \int f_{xc}(\rho(r), |\nabla\rho(r)|, |\nabla^2\rho(r)|)\rho(r)dr \qquad (2.29).$$

Some examples of this type of functionals are the Tao-Perdew-Staroverov-Scuseria (TPSS)[16], Perdew-Kurth-Zupan-Blaha (PKZB)[17], and M06L[18], among many others. In general meta-GGA deliver better thermochemistry estimates, particularly on molecular systems, but they are known to poorly describe metallic systems.[19]

2.3.4. Hybrid functionals

This last type of functional, as their name indicates, mix exact exchange from the HF method with different exchange-correlation contributions from the above mentioned LDA and GGA functionals, where the proportion of these different contributions is defined through empirical parameters.

The most popular hybrid functional is the three-parameter B3LYP functional,[20] which mixes 80% of LDA exchange with 20% of HF exchange. Another common hybrid functional is PBE0,[21] this functional mixes 25% of Hartree-Fock exchange and the other 75% of exchange belongs to the GGA functional PBE and also the correlation. Hybrid functionals are normally employed for the accurate description of molecular systems, and are also well-suited to simulate semiconducting or insulating materials.

2.4. Basis functions

System wavefunctions can be classified into two general types: atom-centred and periodic plane-wave-based. Usually these wavefunctions are represented as linear combination of simple basis functions in order to reduce the computational cost in the simulations. In computational chemistry there are four main functions used Three types are based on atom-centred functions and the fourth one is based in non-body centred plane-waves. The sets of bases for non-periodic

calculations are centred on nuclei and are based on the linear combination of atomic orbital (LCAO) approximations. Each atomic orbital is described, in turn, by a combination of nucleus-centred functions that can be chosen in different ways, resulting in different types of bases. The different types of bases are described below.

2.4.1. Gaussian-Type Orbitals (GTOs)

Gaussian-type functions are expressed as:

$$\eta^{GTO} = Nx^l y^m z^n exp^{[-\alpha r^2]} \quad (2.30),$$

where *N* is the normalization factor, *α* is the exponent which makes the function more compact or diffuse, and *l*, *m*, and *n* are the symbols that correspond to the Gaussian function with the *s*, *p*, *d,* or *f* orbitals.

2.4.2. Slater-Type Orbitals (STOs)

Another approach to GTO functions are the Slater-Type orbitals.[22] The main difference with GTOs is that in this case the functions are divided in two parts: a radial part and an angular part. These orbitals are expressed as:

$$\eta^{STO} = Nr^{n-1} e^{[-\zeta r]} Y_{ml}(\Theta\varphi) \quad (2.31),$$

where *N* is the normalization factor, *n* corresponds to the principal quantum number, *r* is the distance of the electron from atomic nucleus, ζ is a constant related to the effective charge of the nucleus, and Y_{ml} are spherical harmonics that describe the angular part of the function. A great disadvantage of the STO bases is that the integrals of many centres are much more difficult to calculate with the STO functions than with GTOs.

2.4.3. Numerical atomic orbitals

Numerical atomic orbitals (NAOs)[23] were recently developed with the goal to improve scalability of quantum mechanics calculations simulations in larger systems. NAOs have the form:

$$\varphi_{i[lm]} = \frac{u_i(r)}{r} \cdot Y_{ml}(\Omega) \quad (2.32),$$

where *ui(r)* is a numerically tabulated function obtained by calculating the numerical solution of the Kohn-Sham Hamiltonian for isolated pseudoatoms, Y_{ml} (Ω) denotes the real parts (m = 0, ...,l) and imaginary parts (m = −l,...,−1) of complex spherical harmonics, and *l, m* are implicit functions of the basis function index *i*. NAOs are fully optimized for different types of atoms and attempt to be compact as possible while maintaining high accuracy.

2.4.4. Plane wave functions

This type of function is commonly used in the description of periodic systems. The plane wave functions are expressed as:

$$\eta^{PW} = e^{[i\vec{k}\vec{r}]} \quad (2.33),$$

where *k* represents the crystal plane wave vector. The plane waves are not centered on the nuclei but are spread throughout the entire space, filling the entire box that repeats itself in one, two, or three dimensions, depending on the periodicity conditions of the system studied. The form of these functions is especially suitable for extended systems calculations. The great disadvantage of these functionals is the large number of wave functions necessary to achieve acceptable precision to describe the electrons in the nuclei. For this reason, effective core potentials (also known as pseudopotentials) were developed to reduce the amount of plane waves needed and consequently the computational cost to perform the simulations.

2.5. Core electrons and Pseudopotentials

It has been previously mentioned that system wavefunctions are usually represented as linear combination of functions in order to obtain better approximations to solve the Schrödinger equation and improve the calculation efficiency. Plane wave functions are suitable basis functions to describe periodic systems, but, as previously commented, a large number of plane waves are needed to describe the electrons. With the aim to avoid the use of so many plane waves, pseudopotentials are usually employed in practical calculations. This fact causes that the number of plane wave can be significantly reduced, and so makes the calculations more affordable.

Core electrons are considered not to participate in the chemical properties of the system. For this reason, core electrons are not considered in the calculations, where only valence electrons are taken into account, and where the core electrons are described by a pseudopotential.

There are different types of pseudopotentials. The most commonly used with plane wave are the norm-conserving pseudopotentials,[24] the ultrasoft pseudopotentials,[25] or the projected augmented wave (PAW) pseudopotentials. The latter ones are the ones employed in this Thesis, and were created by Blöchl in 1994.[26] Within the PAW method, the core electrons are treated as frozen functions while the valence electrons are treated as smooth wavefunctions. Then, this method provides a way to calculate all system electrons using a linear transformation relating valence functions and core electrons.

2.6. Solid state

2.6.1. Periodic models for solids

A solid is a macroscopic system formed by a large number of atoms which form a regular structure in all spatial directions.[27] For systems as large as solids, where their properties are intrinsically related to their structure, a computational methodology is used that allows taking into account the periodicity of the system to accurately describe all its properties with a small fraction of it. This methodology is known as the periodic model. Therefore, this model is a simplified system to study the electronic structure of solids. Solids can be periodic in 1D (nanotubes or nanowires), 2D (surfaces), or 3D (bulk structures).[28]

The models for periodic boundary conditions are built considering a piece of the solid (unit cell) that it is replicated in 3D directions to simulate the infinite solid, see Figure 2.2. Therefore, the unit cell is defined as the simplest portion of the solid structure that, when repeated by translation, reproduces the entire crystal.[29]

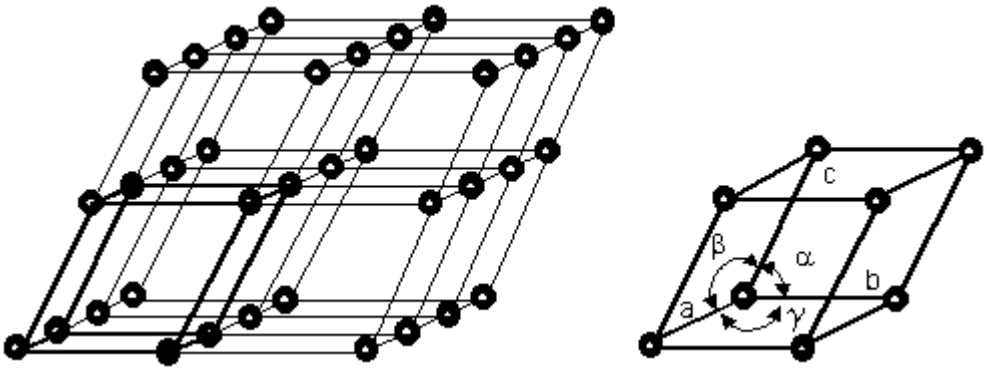

Figure 2.2. Solid representation. Left: 'entire' solid. Right: unit cell, defined by three cell vectors, a, b, and c, and three angles, α, β, and γ.

The periodic models work with the Bravais lattice.[30] The Bravais lattice is an infinite array of discrete points with an arrangement and orientation that looks exactly the same, independently from which point of the array is viewed. The Bravais lattice can be expressed as:

$$R = n_1 a_1 + n_2 a_2 + n_3 a_3 \qquad (2.34),$$

where n_i are integer numbers, *a*, *b*, and *c* are the cell vectors, and *R* represent any point of the periodic structure. Thus, working with periodic conditions enables generating an infinite solid model starting from the unit cell information. The other cells are exact reproductions of the unit cell, owing to the space translations defined by the lattice Bravais vectors. Therefore, the replicas present the same atoms as the unit cell and during the calculation, and they experience the same modifications as the unit cell.

Only 14 different possible lattices exist from a three dimensional periodicity. The lattices are defined by the a, b, c cell vectors, and the α, β, γ cell angles.[29] The 14 Bravais lattices are shown in Figure 2.3.

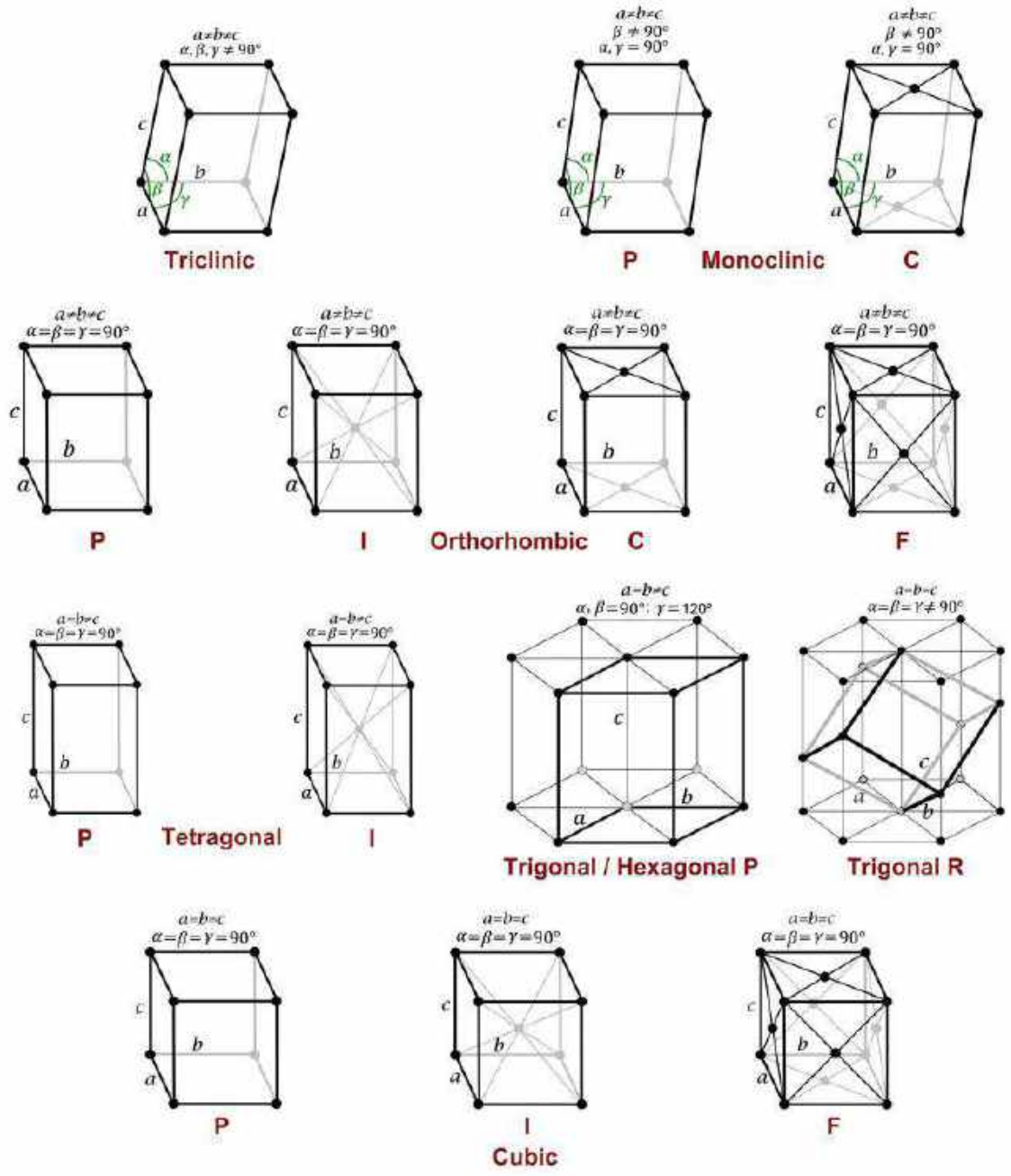

Figure 2.3. Representation of the 14 distinct Bravais lattices.

2.6.2. The reciprocal lattice

In periodic systems the calculations are carried out using a reciprocal space. The reciprocal space is a mathematical construction associated to the crystalline lattice, defined in the physical space, called real space.[32] Each one of the vectors on the real lattice (*a*, *b*, *c*) has it corresponding reciprocal lattice (*a**, *b**, *c**) vector defined as:

$$a^* = 2\pi\frac{b\times c}{a(b\times c)}\ ;\ b^* = 2\pi\frac{a\times c}{b(a\times c)}\ ;\ c^* = 2\pi\frac{a\times b}{c(a\times b)} \quad (2.35).$$

The reciprocal lattice presents a unique set of properties and special points, directly related with the periodicity and translational symmetry of the Bravais cells lattice in real space. Any vector that belongs to the reciprocal lattice can be represented as:

$$G = k_1a^* + k_2b^* + k_3c^* \quad (2.36),$$

where k_i are integer numbers equal that occurs in the direct cell. The reciprocal cell presents a 3D structured of parallelepiped formed by the three reciprocal vectors. The volume of the reciprocal cell is defined as:

$$V_{rec} = \frac{(2\pi)^3}{V_d} \quad (2.37),$$

where V_d is the volume of the direct cell. Thus, a large real unit cell implies small reciprocal cells and the opposite, small real unit cells represented a large reciprocal cell. The reciprocal lattice is defined as:

$$e^{ik(r+R)} = e^{ikr} \quad (2.38),$$

where e^{ikr} is a plane wave with the same periodicity as Bravais lattice and *R* are the different points of Bravais lattice which could be defined by means of the reciprocal space and the periodic conditions using plane waves, as is indicated by Bloch's theorem

2.6.3. Bloch's theorem

Bloch's theorem[33] describes the motion of electrons in a solid based on the idea that the solids present a periodic microscopic structure. Based on this hypothesis, the theorem sets how the wave functions of the electrons should be, and allows calculating the motion of all electrons by analyzing only the motion of a single electron.

Bloch's theorem describes the motion of the electrons in a solid based on three assumptions: First one says that the atoms in a crystal display a periodic structure, and have the periodicity of the points in the Bravais lattice denoted by vectors r. The second assumption is that, due to the order of the atoms, the crystal potential is a periodic function that satisfies

$$U(r+R) = U(r) \quad (2.39).$$

The last assumption mentions that the electrons are independent, *i.e.* they do not interact with each other, and each one satisfies the Schrödinger equation for a periodic potential.

The wavefunction to describe electrons of the system is then a product of a plane wave part and a periodic function part. Mathematically, this can been expressed as:

$$\Psi_i(r) = e^{ikr} v_i(r) \quad (2.40),$$

where e^{ikr} is the wave plane with the wave vector *k*, and $v_i(r)$ is the periodic function known as Bloch's function. The wave function can be expanded as a linear combination of plane waves:

$$\Psi_i(r) = \sum_G C_{i,k+G} e^{i(k+G)r} \quad (2.41),$$

where *G* is the reciprocal vector (Equation 2.36). Thus, the problem of correctly mapping all the electrons of the system is reduced to sampling the Brillouin zone at special set of *k*-points.

The plane wave on the real system is spread as a plane wave combination on the reciprocal space. Each plane wave is characterized by a kinetic energy $|k + G|\ 2h/2m$. Therefore, modulating the kinetic energy, it is possible to increase or decrease the set of plane wave basis functional, as commonly done in many computing packages.

2.6.4. Miller indices

The Miller indices form a notation system in crystallography for planes in Bravais lattices.[27] The Miller indices have the form (*hkl*) and they are defined as the reciprocal intersections between the plane and the coordinate axis. The Miller indices are defined as:

$$h = \frac{1}{a}\ ; k = \frac{1}{b}\ ; l = \frac{1}{c} \quad (2.42),$$

where *a*, *b*, and *c* are the vectors in the 3 coordinate axes. Miller indices are whole numbers, negative or positive, and they are prime numbers. Figure 2.4. shows different examples for the different Miller indices in a cubic structure.

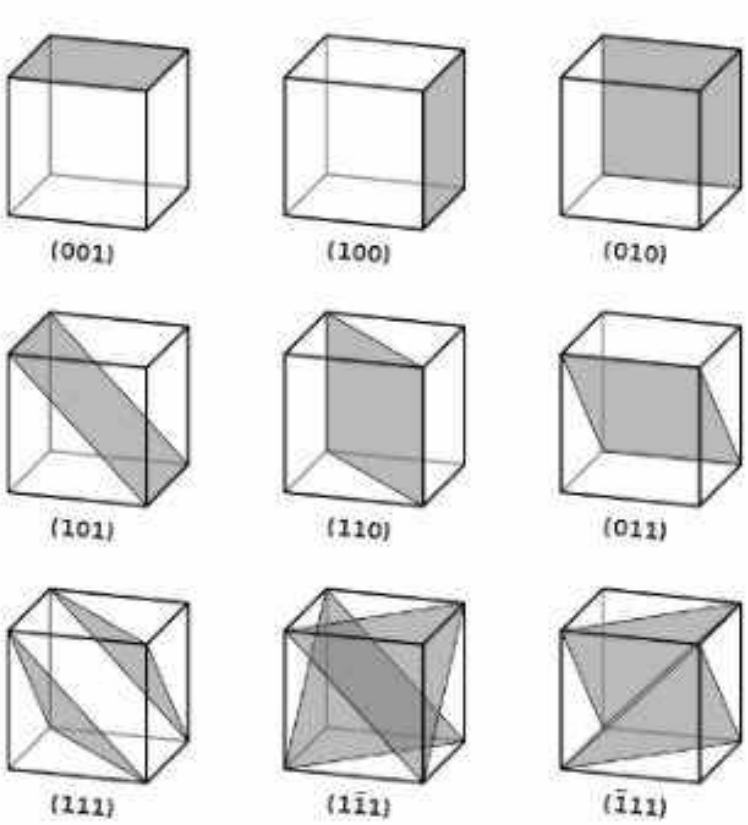

Figure 2.4. Different Miller indices for a cubic structure.

The Miller index presents three special cases:

- The Miller index is 0 when the plane has not intersection with an axis.
- The Miller index is negative when the intersection is in a negative zone. In this case, to indicate that this is a negative number, a symbol is put on top of the number, *e.g.* $(1\bar{1}1)$.
- The notation of Miller indices will be bracketed [*hkl*] when having a set of planes equivalent to (*hkl*) by lattice symmetry.

2.7. Models

This section deals with the simulation models employed in this thesis, and it is divided into two different sections: i) periodic slab models for surfaces, and ii) cluster models for isolated nanoparticles (NPs)

2.7.1. Surfaces

In is known in the literature that the (001) surface is the most stable one for TMCs.[34] In this Thesis this surface has been obtained from pre-optimized bulk solid TMCs, creating a supercell and adding vacuum in the direction normal to the surface, thus creating a slab model, see Figure 2.5.

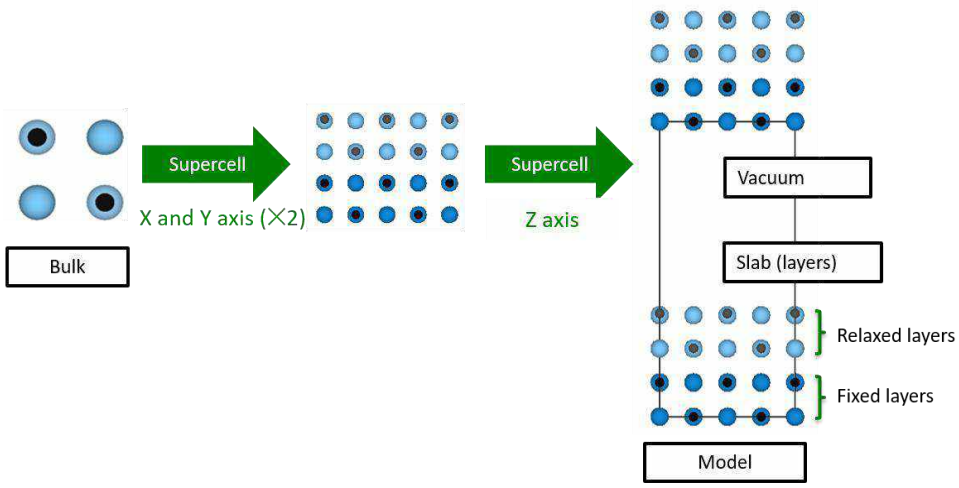

Figure 2.5. Representation of the steps followed to model the (001) surface.

Different tests were carried out to answer different questions to carry out the subsequent calculations to a converged level of accuracy: the number of needed layers, number of relaxed layers, and number of atoms. The result was that the model to be used for the calculations should contain at least four layers; where two layers were fixed (bottom) and two layers relaxed (top) with a vacuum of 10 Å and a total number of 64 total atoms, being a c(2x2) supercell. The model is shown in Figure 2.6. The same type of models were used for other TMC (001) surfaces.

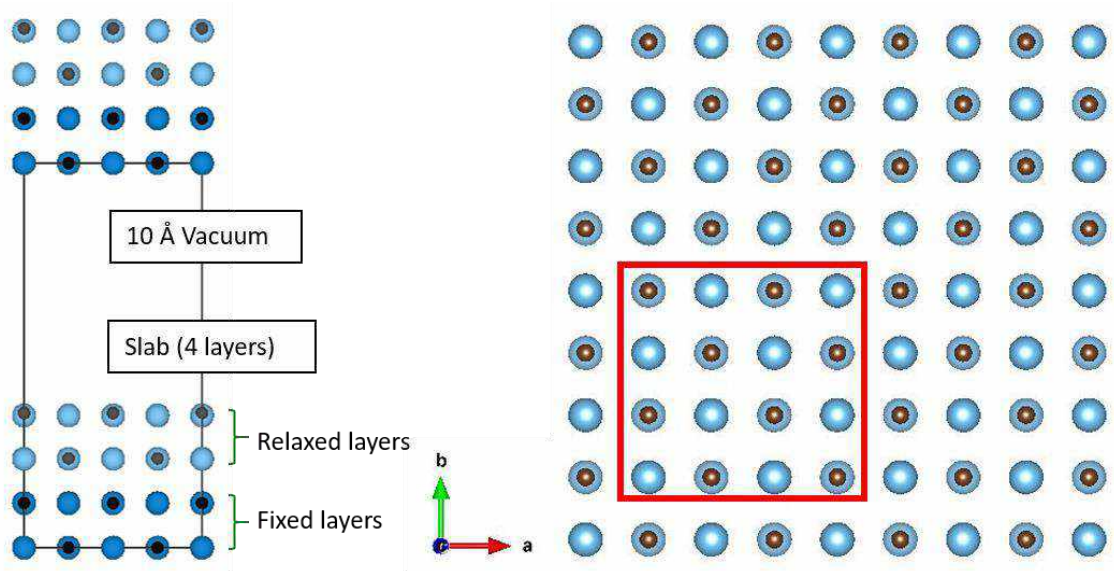

Figure 2.6. Side (left) and top (right) views of the employed slab model for TiC (001) surface.

All the calculations on TiC (001) surface will be made using Vienna *Ab Initio* Simulation Package (VASP) code.[35]

2.7.2. Nanoparticles

When simulating discrete systems, a periodic model introduces virtual images of the single system which have to be sufficiently separated in large unit cells incorporating vacuum spacing as to not interact. Another simpler model to investigate the properties of discrete system

employ the Cluster model.[31] In this model only a single finite number of atoms are studied in free space with open boundary conditions. The use of the cluster model to study discrete system reduces the computational cost with respect to a periodic approach and this allows the benchmarking of calculations with WF methods which are currently only implemented for isolated system. We employed the cluster model to calculate the properties of all NP systems in this Thesis.

The NP calculations were performed using the Fritz-Haber Institute *Ab Initio* Molecular Simulations package (FHI-AIMS) code.[36] Different sizes of TiC-based NP have been studied with atomic dimensions ranging from 2×2×2/$(TiC)_4$ to 6×6×6/$(TiC)_{108}$ based on cuts from the TiC parent rocksalt crystal structure. In addition to NPs based on these re cubic cuts, NPs with different atom removed were also considered. Figure 2.7 shows an example for the 4×4×4 NP employed in the studies in this Thesis.

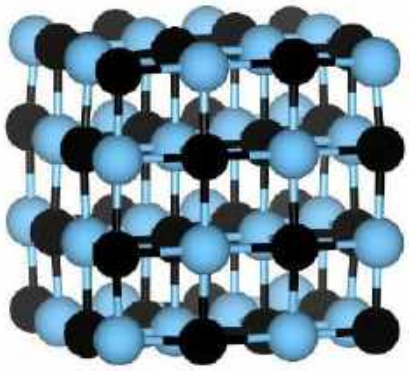

Figure 2.7. Cubic 4×4×4 TiC NP.

2.8. Transitions States

In order to find the barriers for chemical processes, transition states in between two minima (i.e. a saddle points on the potential energy surface between initial and final states) were calculated using two different methods: CI-NEB and Dimer methods.

2.8.1. NEB method

The nudge elastic band (NEB)[37] is a method which find saddle points and minimum energy paths between known reactants and products. This method is implemented in both VASP and FHI-aims codes. To use this method, a number of intermediate images between reactants and products along the reaction path are created. Then, the method optimizes these intermediate images and find the lowest energy possible for each image. In addition, the optimized images present equal spacing to neighbouring images. In order achieve this, spring forces are added along the band between images and by projecting out the component of the force due to the potential perpendicular to the band.

A small modification to the NEB method is the climbing image,[38] *i.e.* CI-NEB, in which the highest energy image is driven up to the saddle point. In this method the image does not feel the spring forces along the band. Instead, the true force at this image along the tangent is inverted. This way, the image tries to maximize and minimize the energy along the band in all directions. Finally, when the image converges, the exact saddle point for the system is found. The CI-NEB is only available in the VASP code.

Due to CI-NEB the highest image is moved to the saddle point and this image does not feel the spring forces, the spacing of the rest of images on either side of highest image is different. This phenomenon is shown in Figure 2.8.

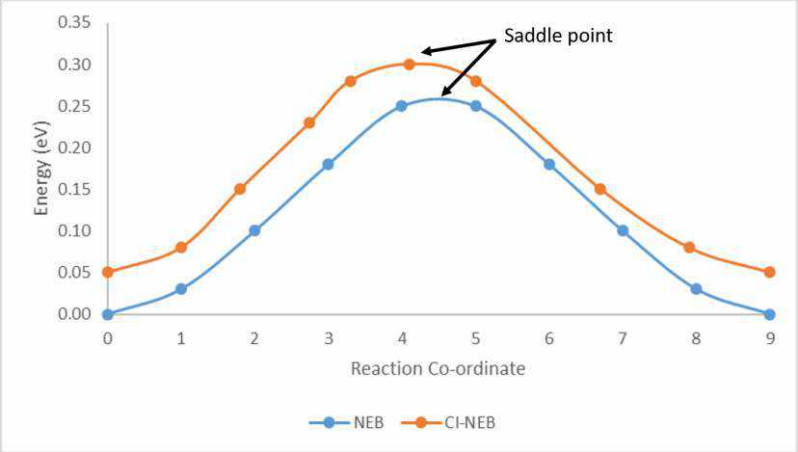

Figure 2.8. The graph shows an NEB calculation (Blue) and a CI-NEB calculation (orange).

Since in FHI-AIMS the CI-NEB is not available, one has to converge to the saddle point in the so-called adaptive NEB (ANEB), where a second (or third) NEB is done placing images in between two contiguous images close to the saddle point. Such a transition state has to be characterized by a vibrational analysis (see below).

2.8.2. DIMER method

The dimer method also allows finding a saddle point;[39,40] opposed to the NEB method, it allows the user to start from any initial configuration and search for a nearly saddle point. This method can also be used to start from a minimal basis and search in random directions for saddle points. In simple systems is easy to know that the reaction pathways and NEB method can be used, but in complex systems, the reactions often take place *via* unexpected mechanisms. In these cases, the Dimer method is designed to find the saddle points corresponding to unknown reactions mechanisms. This method is only availed in VASP code.

2.9. Vibrational frequencies

In any computational study exploring the potential energy landscape, it is customary to carry out vibrational frequencies to determine whether a minimum is so, or a transition state. In addition, such frequencies are useful to calculate the zero point energy correction (see below)

and vibrational partition functions, basic to obtain macroscopic properties such as enthalpy, entropy, Gibbs free energy and kinetic constants.[41,42]

The vibrational frequencies were thus obtained for the optimized geometries and transitions states, these are, stationary points of the potential energy forces, where the forces, first derivatives of the potential energy, are zero. Vibrational frequencies are related directly with the force constant (the second derivatives of the potential), and the mathematical analysis assures that stationary point is minima if the derivatives are real, and in a transition state one of them is imaginary.

2.10. Zero-point energy

Zero-point energy (ZPE) is the lowest possible energy that that a quantum mechanical system may have. The ZPE idea emerges from the Heisenberg uncertainty principle.[43] This energy is related with the nuclei vibration around the equilibrium position in the optimized geometry. The zero point energy correction is described as:

$$E_{corr}^{ZPE} = \sum_{i=1}^{MNV} \frac{1}{2} h\upsilon_i \qquad (2.43),$$

where, *h* is the Plank constant, and υ_i are all the frequencies for the Normal Mode of Vibration (NMV), excluding the imaginary frequencies. Finally, once the ZPE correction is calculated, the ZPE energy is obtained through the sum of the state energy and the ZPE energy, as can be seen in the equation 2.44.

$$E^{ZPE} = E + E_{corr}^{ZPE} \qquad (2.44).$$

It should be noted that frequencies less than 1000 cm^{-1} barely have a contribution to the ZPE. The frequencies higher than 1000 cm^{-1} begin to contribute to the ZPE values as shown in the graph in Figure 2.9.

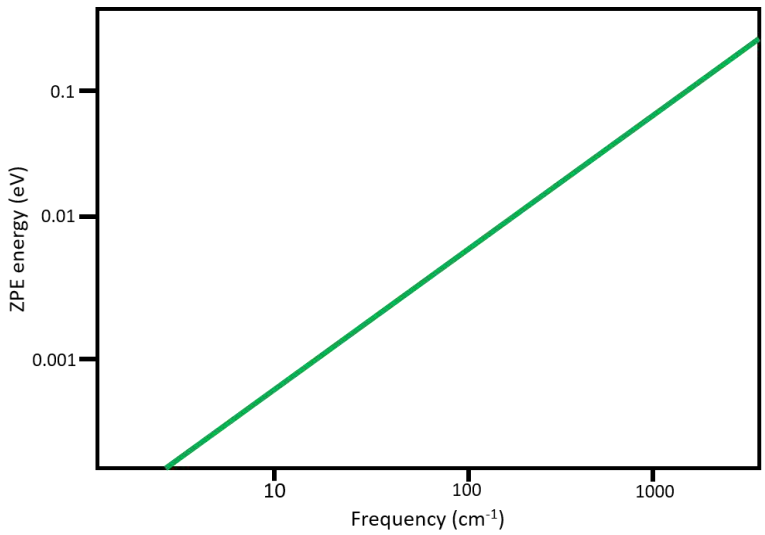

Figure 2.9. ZPE plotted as a function of vibrational frequency.[44]

2.11. Infrared Spectroscopy

2.11.1. Harmonic IR Spectra

One of the most common methods to simulated the IR spectra of a molecules is the harmonic approximation. Before calculating the Harmonic IR spectra, the geometry of the molecule has to be well optimized. This optimization can be carried out with any computational method. Once the structure has been optimized, the geometry corresponding to a minimum of the potential energy surface (PES) is available. To get the PES close to the equilibrium position, a Taylor series close to the minimum of the PES is employed. Taylor's series present the form:

$$U(q_1, \dots, q_{3N}) = U_e + \sum_{k=1}^{3N} \left(\frac{\partial U}{\partial q_k}\right)_e q_k + \frac{1}{2} \sum_{k=1}^{3N} \sum_{l=1}^{3N} \left(\frac{\partial^2 U}{\partial q_k q_l}\right)_e q_k q_l + \cdots \quad (2.45),$$

where:

$$q_1 = \left(X_1 - X_{1eq}\right)\sqrt{m_1}\,;\; q_2 = \left(Y_1 - Y_{1eq}\right)\sqrt{m_1}\,;\; q_3 = \left(Z_1 - Z_{1eq}\right)\sqrt{m_1}\,;\dots \quad (2.46).$$

Being an equilibrium position, U_e = 0 and the first derivative is also null, therefore, the harmonic oscillator approximation can be expressed as:

$$U(q_1, \dots, q_{3N}) = \frac{1}{2} \sum_{k=1}^{3N} \sum_{l=1}^{3N} \left(\frac{\partial^2 U}{\partial q_k q_l}\right)_e q_k q_l \quad (2.47).$$

Using this approximation, the PES obtained and the real PES match near the equilibrium region. However, the farther the molecule is from the PES minimum, the worse the approximation to the real PES is, Figure 2.10.

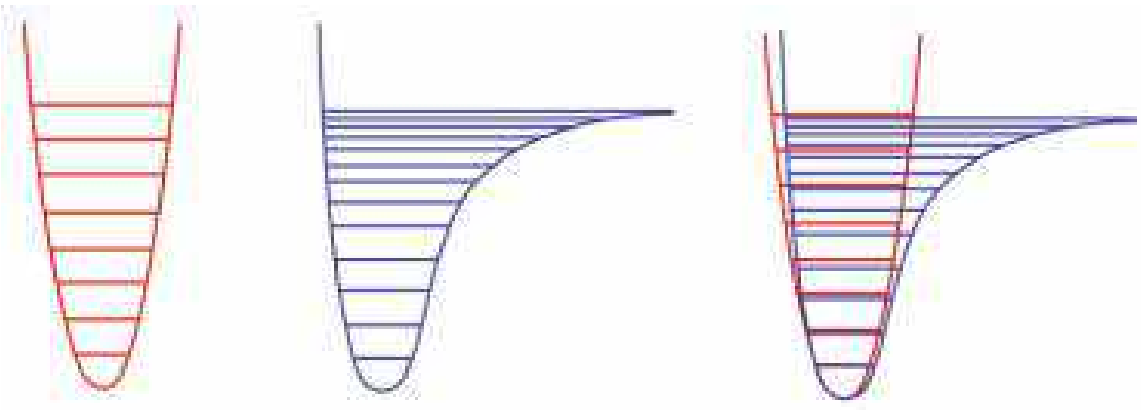

Figure 2.10. Comparison between harmonic (red) and real (blue) PES. Horizontal lines represent the vibrational levels.

The Hessian matrix can be obtained by the derivation of the equation (2.47). Diagonalizing the Hessian matrix, the harmonic frequencies of the system are obtained. When the matrix is diagonalized, one obtains 3*N* eigenvalues (λ_i), that are used to obtain the frequencies, employing the following equation:

$$v_i = \frac{\sqrt{\lambda_i}}{2\pi} \quad (2.48).$$

When the frequencies are calculated, 3*N* frequencies are obtained where only 3*N*-6 (or 3*N*-5 in the case of linear molecules) frequencies have to be taken into account because the rest correspond to translational and rotational movements.

This approximation possesses some limitations as only fundamental transitions are observed. Thus, the overtones are neglected. Another important limitation that is necessary to highlight in harmonic spectra is the fact that no information about the shape and broadening of the peaks is obtained. The usual procedure to obtain an IR spectrum similar to experimental IR is to apply a Gaussian or a Lorentzian function with a given width, in the positions in which the peaks are observed. In that way, a broadened peak that resembles the shape of the experimental ones is obtained.

2.11.2. MD-Based IR Spectra

In order to overcome the limitations of harmonic IR spectra, MD-Based IR can be obtained. While the harmonic oscillator expresses the transition probability between two vibrational states as polychromatic radiation,[45] MD-Based IR expresses this transition as the Golden Rule of time-dependent quantum-mechanical perturbation theory[46].

$$P(f \leftarrow i) = \frac{\pi F^2}{2\hbar^2} \left|\langle \phi_f | \hat{d} \phi_i \rangle\right|^2 \left[\delta(\omega_{fi} - \omega) + \delta(\omega_{fi} + \omega)\right] \quad (2.49),$$

where δ indicates a Dirac delta function. From this probability of transition, one can derive the expression for the absorption cross section $\alpha(\omega)$:[46]

$$\alpha(\omega) = \frac{4\pi^2}{\hbar c n} \omega\left(1 - e^{-\beta\hbar\omega}\right) \sum_f \sum_i p_i \left|\langle \phi_f | \hat{d} \phi_i \rangle\right|^2 (\omega_{fi} - \omega) \quad (2.50),$$

where pi is the probability that the system is found in the initial vibrational state, *c* is the lightspeed, *n* the refraction index of the medium, $\beta = K_b/T$. β is the Boltzmann's constant, and T the temperature of the system. From this absorption cross section is possible to define an absorption lineshape (equation 2.51) to express $\alpha(\omega)$ in a different way (equation 2.52):

$$I(\omega) = \frac{3\hbar c n \alpha(\omega)}{4\pi^2 \omega\left(1 - e^{-\beta\hbar\omega}\right)} = 3 \sum_f \sum_i p_i \left|\langle \phi_f | \hat{d} \phi_i \rangle\right|^2 (\omega_{fi} - \omega) \quad (2.51),$$

$$\alpha(\omega) = \frac{4\pi^2}{3\hbar c n} \omega\left(1 - e^{-\beta\hbar\omega}\right) I(\omega) \quad (2.52).$$

Thus, only one term is necessary calculate $I(\omega)$. In addition, it can be proved[46] that this absorption lineshape can also be calculated from the Fourier transform of the dipole autocorrelation function:

$$I(\omega) = \frac{1}{2\pi} \int_{-\infty}^{+\infty} e^{-i\omega t}\, C_\mu(t) dt \quad (2.53),$$

where

$$C_\mu(t) = \langle \mu(0) \cdot \mu(t) \rangle \quad (2.54),$$

where $\mu(t)$ is the total dipole moment of the system in a given time, that is directly obtained from the charge distribution of the system at each step of the MD simulation, and ⟨ ⟩ indicates an average. During the MD simulation is necessary to keep track of the total dipole moment of the system at each step of the simulation. From the time evolution of the dipole moment then one can compute the dipole auto-correlation function, and therefore obtain the MD-based IR spectrum.

2.12. Computational details

In this Thesis, all calculations were carried out using DFT employing two different codes to carry out the calculations: VASP and FHI-AIMS. The VASP code has been used to perform as well the surfaces calculations while the FHI-aims code has been employed to carry out the TiC-based NPs calculations. The GGA PBE functional[11] has been used in all calculations.

2.12.1 VASP code

Within the VASP code different tests were made to find the optimal parameters to carry out the calculations. In addition, these tests were made so as to reduce the computational time. In all cases, 9×9×1 k-points meshes were used, with a cut-off energy of 415 eV, and optimizations were considered converged when forces acting on atoms were below 0.01 eV $Å^{-1}$.

After optimizations, the adsorption or absorption energies were calculated using the equation:

$$E_{ads}^{X} = E_{X/TMC} - (E_X - E_{TMC}) \quad (2.45),$$

where $E_{X/TMC}$ is the total energy obtained for every position/coverage under study, E_x is the energy of one isolated atom or isolated molecule under study, and E_{TMC} is the energy of the surface to the coverage that is being studied but without the last species atom adsorbed (e.g. when only one H atom adsorption is considered, this energy corresponds of the bare surface). E_x is obtained by placing the atom or molecule in broken symmetry unit cell of 9×10×11 Å dimensions and carrying out a Γ-point optimization. As the adsorption energy has been defined, the more negative is the adsorption energy value, the greater is the adsorption.

To find the TS, four intermediate images have used with the CI-NEB method,[38] except in some cases that a higher number of the intermediate images have been employed. In all cases,

the TS was later confirmed using a vibrational frequency study, where the Hessian matrix was built and diagonalized after displacements of 0.03 Å length.

2.12.2. FHI-AIMS code

In the calculations on TiC NPs with the FHI-AIMS code, the PBE GGA functional was employed. In addition, all calculations were treated non-spin polarized because the results obtained in the test realized in the same calculation employing spin polarized and non-spin polarized show the same results. In addition, in the previous literature, has already been shown that the TMCs do not present magnetism,[47] for this reason, the calculations can do using non-spin polarized. The electronic density was expanded using a Light-Tier-1 basis of NAOs, providing results of a similar or higher quality to those obtained with valence triple-zeta plus polarization Gaussian type orbitals.[48-50]

All relative energies pertain to NP structures which have been optimized using the above DFT method and the Broyden-Fletcher-Goldfarb-Shanno (BFGS) algorithm[51] until the residual force component per atom was less than 10^{-2} eV/Å. Harmonic frequencies were then calculated using these optimized NP structures by calculating the second derivatives of the energy from the numerical changes in the forces arising from small finite atomic displacements (0.0025 Å). A 10 cm^{-1} full width at half maximum Gaussian broadening was applied to all reported harmonic IR peaks for better approximating the finite width of the experimental peaks.

In order to search for alternative NP structures, a classical molecular dynamics (MD) simulated annealing approach was used employing modified embedded-atom method interatomic potentials[52] as implemented in the LAMMPS code.[53] Specifically, a series of contiguous NVT MD simulations were run starting first from a high temperature (2500-3000 K) and reducing the temperature in a step-wise manner by 500 K until a temperature of 1000 K was reached. Low energy NP structures were then extracted and optimized using the above-described DFT approach.

To look for the TS using this code, NEB calculations with 8 intermediate images were carried out and checked using vibrational frequencies.

2.13. References

1. A. Szabo and N.S. Ostlund. Modern quantum chemistry: introduction to advanced electronic structure theory. Dover Publications, **1996**.
2. M. Born and R. Oppenheimer. Zur Quamtentheorie der Molekeln. *Ann. Phys*. **1927**, 389, *20*, 457–484.
3. W. Kohn and L.J. Self-Consistent Equations Including Exchange and Correlation Effects. Phys Rev. **1965**, 140, A1133–A1138.
4. R.G. Parr and W. Yang. Density-functional theory of atoms and molecules. Oxford University Press, **1989**.

5. E. Fermi. Eine statistische Methode zur Bestimmung einiger Eigenschaften des Atoms und ihre Anwendung auf die Theorie des periodischen Systems der Elemente. Z. Physik, **1928**, 48, 73–79.
6. L.H. Thomas. The calculation of atomic fields. Math. Proc. Cambridge Philos. Soc. 23, 542 (**1927**).
7. P. Hohenberg and W. Kohn. Inhomogeneous Electron Gas. Phys Rev., **1964**, 136, B864– B871.
8. S.H. Vosko, L. Wilk, and M. Nusair. Accurate spin-dependent electron liquid correlation energies for local spin density calculations: a critical analysis. Can J Phys., **1980**; 58, *8*, 1200–1211.
9. A.Lee and J.P.P. Cole. Calculated electron affinities of the elements. *Phys Rev* A. **1982**, 1265.
10. J.P. Perdew, J.A. Chevary, S.H. Vosko, K.A. Jackson, M.R. Pederson, D.J. Singh DJ, and C. Fiolhais. Atoms, molecules, solids, and surfaces: Applications of the generalized gradient approximation for exchange and correlation. Phys Rev B., **1992**; 46, 6671.
11. J.P. Perdew, K. Burke, and M. Ernzerhof. Generalized gradient approximation made simple. Phys Rev Lett., **1996**, 77, *18*, 3865–3868.
12. Y. Zhang and W. Yang. Comment on "generalized gradient approximation made simple." Phys Rev Lett., **1998**, 80, 890.
13. B. Hammer, L.B. Hansen, and J.K. Nørskov. Improved adsorption energetics within density-functional theory using revised Perdew-Burke-Ernzerhof functionals. Phys Rev B - Condens Matter Mater Phys., **1999**, 59, *11*, 7413–7421.
14. J.P. Perdew, A. Ruzsinszky, G.I. Csonka, O.A. Vydrov, G.E. Scuseria, L.A. Constantin, X. Zhou, and K. Burke. Restoring the density-gradient expansion for exchange in solids and surfaces. *Phys Rev Lett*., **2008**, 100, 136406.
15. L. Vega and F. Viñes. Generalized gradient approximation adjusted to transition metals properties: Key roles of exchange and local spin density. J Comput Chem., **2020**, 41, *30*, 2598–2603.
16. J. Tao, J.P. Perdew, V.N. Staroverov, and G.E. Scuseria. Climbing the Density Functional Ladder: Nonempirical Meta – Generalized Gradient Approximation Designed for Molecules and Solids. Phys Rev Lett., **2003**, 93, 146401.
17. J.P Perdew, S. Kurth, A. Zupan, and P. Blaha. Accurate Density Functional with Correct Formal Properties: A Step Beyond the Generalized Gradient Approximation. Phys Rev Let., **1999**, 82, 12, 2544–2547.
18. Y. Zhao, N.E. Schultz, and D.G. Truhlar. Exchange-correlation functional with broad accuracy for metallic and nonmetallic compounds, kinetics, and noncovalent interactions. J. Chem. Phys., **2005**, 123, 161103.
19. P. Janthon, S. Luo, S.M. Kozlov, F. Viñes, J. Limtrakul, D.G. Truhlar, and F. Illas. Bulk properties of transition metals: A challenge for the design of universal density functionals. J Chem Theory Comput., **2014**, 10, 9, 3832–3839.
20. P. J. Stephens, F.J. Devlin, C.F. Chabalowski, and M.J. Frisch. Ab Initio Calculation of Vibrational Absortion and Circular Dichroism Spectra Using Density Functional Force Fields. J. Phys. Chem., **1994**, 98, 45, 11623–11627.
21. J.P. Perdew and M. Ernzerhof. Rationale for mixing exact exchange with density functional approximations. J. Chem. Phys., **1996**, 105, 22, 9982–9985.
22. J.C. Slater. Atomic shielding constants. Phys. Rev., **1930**, 36, 57–64.
23. V. Blum, R. Gehrke, F. Hanke, P. Havu, V. Havu, X. Ren, K. Reuter, and M. Scheffler. Ab initio molecular simulations with numeric atom-centered orbitals. *Comput Phys Commun*., **2009**, 180, 11, 2175–96.
24. D.R. Hamann, M. Schlüter, and C. Chiang. Norm-Conserving Pseudopotentials. *Phys Rev Lett*., **1979**, 43, *20*, 1494–1497.
25. D. Vanderbillt. Soft self-consistent pseudopotentials in a generalized eigenvalue formalism. *Phys Rev* B., **1990**, 41, 7892.
26. P.E. Blöchl. Projector augmented-wave method. Phys. Rev. B. **1994**, 50, 24, 17953–17979.

27. Ashcroft NW, Mermin ND. Solid State Physics Description. ISBN: 0030839939
28. J.N. Tiwari, R.N. Tiwari, and K.S. Kim. Zero-dimensional, one-dimensional, two-dimensional and three-dimensional nanostructured materials for advanced electrochemical energy devices. *Prog. Mater. Sci*., **2012**, 57, *4*, 724–803
29. Ashcroft N, Mermin N. Solid state Physics. Publishing SC, editor. **1976**.
30. Friedrich J, Hessel C, Friedrich W, Knipping P. Historical introduction. Vol. I. **2006**. 2–5 p
31. Z.H. Stachurski. *On structure and Properties of amorphous materials*. Vol. 4, Materials. **2011**. 1564–1598.
32. «Reciprocal lattice». Online Dictionary of Crystallography (en inglés). Unión Internacional de Cristalografía. 25 de mayo de 2007. Consulted the 12th september 2021.
33. F. Bloch. Über die Quantenmechanik der Elektronen in Kristallgittern. Z. Phys., 1929, 52, 555–600.
34. M.G. Quesne, A. Roldan, N.H. De Leeuw, and C.R.A. Catlow. Bulk and surface properties of metal carbides: Implications for catalysis. Phys. *Chem. Chem. Phys*., **2018**, 20, *10*, 6905–6916.
35. G. Kresse and J. Furthmüller. Efficient iterative schemes for ab initio total-energy calculations using a plane-wave basis set. *Phys. Rev.* B., **1996**; 54, *16*, 11169–11186.
36. V. Blum, R. Gehrke, F. Hanke, P. Havu, V. Havu, X. Ren, K. Reuter, and M. Scheffler. Ab initio molecular simulations with numeric atom-centered orbitals. Comput Phys Commun. **2009**, 180, *11*, 2175–96.
37. G. Henkelman. A Climbing image nudged elastic band method for finding saddle points and minimum energy paths. J Chem. Phys., **2000**, 113, 9901–9904.
38. G. Henkelman and H. Jónsson. Improved tangent estimate in the nudged elastic band method for finding minimum energy paths and saddle points. J Chem Phys., **2000**, 113, *22*, 9978–9985.
39. G. Henkelman and H. Jónsson H. A dimer method for finding saddle points on high dimensional potential surfaces using only first derivatives. J Chem Phys., **1999**; 111, *15*, 7010–7022.
40. R.A. Olsen and G.J. Kroes. Comparison of methods for finding saddle points without knowledge of the final states. J Chem Phys., **2004**, 121, *20*, 9776–9792.
41. M.W. Wong. Vibrational frequency prediction using density functional theory. *Chem. Phys. Lett*., **1996**, 256, *4–5*, 391–399.
42. A.A El-Azhary and H.U. Suter. Comparison between optimized geometries and vibrational frequencies calculated by the DFT methods. *J. Phys. Chem.*, **1996**, 100, *37*, 15056–63.
43. Sciama DW. The Physical Significance of the Vacuum State of a Quantum Field. **1991**.
44. J.K. Nørskov, F. Studt, F. Abild-Pedersen, and T. Bligaard. Fundamental Concepts in Heterogeneous Catalysis Wiley, New Jersey, **2014**.
45. J.C. Paniagua and P. Alemany. Química quàntica. 1st editio. Barcelona, **2000**.
46. D.A. McQuarrie. Statistical Mechanics. 1st editio. University Science Books, **2000**.
47. H.H. Hwu and J.G. Chen. Surface chemistry of transition metal carbides. *Chem. Rev.*, **2005**;105, *1*, 185–212.
48. O. Lamiel-Garcia, K.C. Ko, J.Y. Lee, S.T. Bromley, and F. Illas. When Anatase Nanoparticles Become Bulklike: Properties of Realistic TiO_2 Nanoparticles in the 1-6 nm Size Range from All Electron Relativistic Density Functional Theory Based Calculations. *J. Chem. Theory Comput*., **2017**, 13, *4*, 1785–1793.
49. F. Viñes and F. Illas. Electronic structure of stoichiometric and reduced ZnO from periodic relativistic all electron hybrid density functional calculations using numeric atom-centered orbitals. *J. Comput. Chem*., **2017**, 38, *8*, 523–529.
50. S.R. Jensen, S. Saha, J.A. Flores-Livas, W. Huhn, V. Blum, S. Goedecker, and L. Frediani. The Elephant in the Room of Density Functional Theory Calculations. *J. Phys. Chem. Lett.*, **2017**, 8, *7*, 1449–1457.
51. J. Nocedal and S.J. Wright. Numerical optimization. 2 edition. Springer, editor.

52. H.K. Kim, W.S. Jung, and B.J Lee BJ. Modified embedded-atom method interatomic potentials for the Fe-Ti-C and Fe-Ti-N ternary systems. *Acta Mater.*, **2009**, 57, 11, 3140–3147.

53. S. Plimpton. Fast Parallel Algorithms for Short-Range Molecular Dynamics. *J. Comp. Phys*., **1995**, 117, *1*, 1–19.

PART I: Surfaces

Chapter 3

H_2 adsorption and dissociation on TiC

3. H_2 adsorption and dissociation on TiC

3.1. Introduction

The interaction of molecular hydrogen with titanium carbide (TiC) is an important topic in catalysis, solid-state chemistry, and materials science.[1–9] TiC displays high activity for the hydrogenation of various compounds such as ethylene and CO_2.[1,3,4] To perform these reactions in an efficient way, it is important to know the interaction of H with the carbide surface. In this way, the study of this system can help to understand better the reaction mechanism to these reactions. In principle, hydrogen can be present at different TiC sites: On the surface,[3,4] in the bulk,[5–9] in interstitial positions,[10] physisorbed,[11] and forming a *Kubas* structure.[12,13] In this aspect, TiC can be regarded as a textbook example within the family of transition metal carbide (TMC) materials.[12,14]

The goal of this Chapter is to study whether TiC (001) surfaces are good candidates to adsorb and dissociate H_2, so as to envision them as catalysts for hydrogenation activities. This study implied a detail study on the Hydrogen atom adsorption preference at low coverage, the surface filling by H adatoms, and the stability of H_2 moieties, the possible H_2 dissociation, even the possibility of H incorporation in the TiC lattice as an absorbed moiety.

This work has been published in **the journal of Physical Chemistry C** with the name "**Diversity of Adsorbed Hydrogen on the TiC (001) Surface at High Coverages"**, 2018, 122, 28013.

3.2. Methodology

VASP code[15] has been used to carry out the calculations using PBE[16] Grimme's D3 correction[17] for dispersive forces. A two-step optimization procedure has been followed, in which moieties were initially optimized with looser optimization criteria, while most promising situations were reoptimized with tighter thresholds. The adsorption (or absorption) energies were estimated as:

$$E^{H}_{ads/abs} = E_{H/TMC} - (\mathrm{E_H} - \mathrm{E_{TMC}}) \qquad (3.1),$$

where $E_{H/TMC}$ is the total energy of the TiC surface with the H atom, E_H the total energy of an isolated Hydrogen atom in vacuum, and E_{TMC} the total energy of the pristine TiC (001) surface. Notice that the same equation is used when calculating consecutive H adsorption, but considering as E_{TMC} the surface with a given H coverage, on which an extra H is adsorbed. Notice that E_H is obtained by placing the H atom in broken symmetry unit cell of 9×10×11 Å dimensions and carrying out using a Γ-point optimization. In a similar way, the H_2 energy adsorption is calculated with the same equation, but using the energy of an isolated H_2 molecule instead of E_H.

For the H_2 dissociation, Dimer[18] and CI-NEB[19] methods (see Chapter 2) have been used to locate the sought TS, and characterized as so by vibrational analysis. The last step was to add the Zero Point Energy (ZPE) to the energy system. ZPE is calculated through the equation:

$$E_{corr}^{ZPE} = \sum_{i=1}^{MNV} \frac{1}{2} h\upsilon_i \quad (3.2),$$

where *h* is the Plank constant, and υ_i are all the frequencies for the Normal Modes of Vibration (NMV), excluding the imaginary frequency in the TS. This energy is added up to the system minima and TS, so that the dissociation energy barrier is corrected as:

$$E_{barr}^{ZPE} = E_{barr} + E_{corr,TS}^{ZPE} - E_{corr,IS}^{ZPE} \quad (3.3),$$

where the ZPE corrections are applied to the TS and the initial state (IS).

3.3. Low coverage H adsorption

The H atom was tested at six different high-symmetry sites on the TiC (001) surface, all belonging to a coverage of 0.125 monolayers (ML), defining a ML as having the same number of H atoms as the number of surface metal (or carbon) atoms. Figure 3.1 shows the six different explored sites; (1) Top metal (M-Top), (2) Top Carbon (C-Top), (3) Bridge between vicinal Carbon and metal atoms, (4) 4-fold hollow , (5) 3-fold hollow formed by 2 metal and 1 Carbon atoms (MMC), and (6) 3-fold hollow formed by 2 Carbon and 1 metal atoms (CCM).

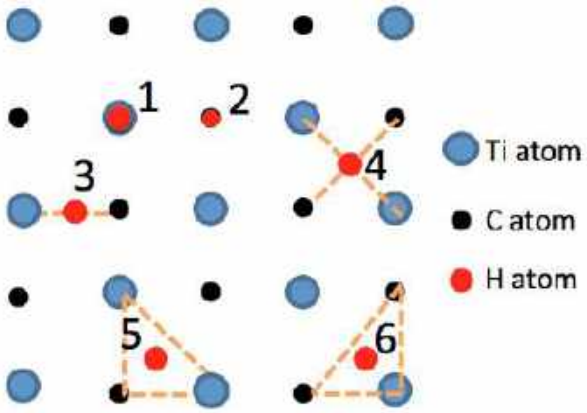

Figure 3.1. Schematic top view of a TiC (001). The image shows C atoms (black), metallic atoms (blue), and H atoms (red) in the six initials positions under study. Dashed orange lines are guides to the eyes.

The optimizations for the initial positions showed that only two final positions were stable. Either with H adsorbed on C-Top, or the 4-fold hollow, see Figure 3.2.

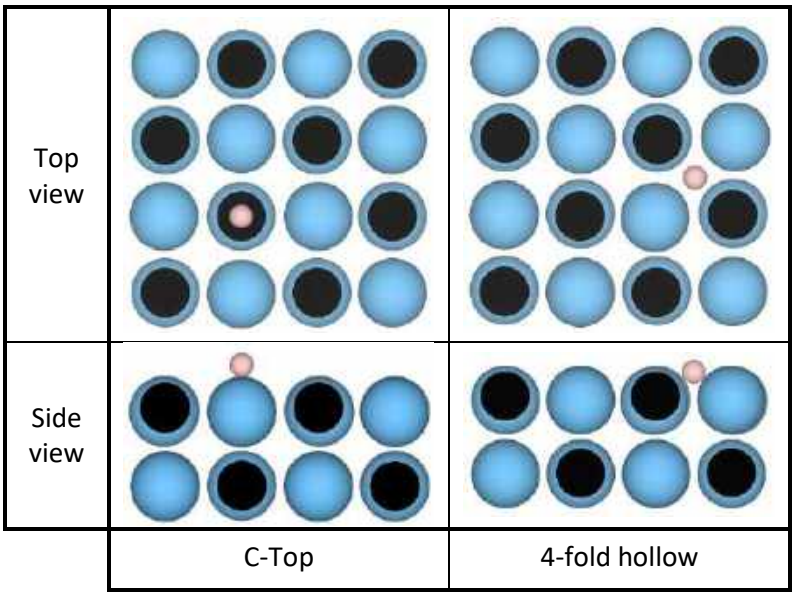

Figure 3.2. Final positions for H adsorbed on the TiC (001) surface. Left: C-Top. Right: 4-fold hollow. Top (top) and side (bottom) views are shown. Colour coding as in Figure 3.1.

The E_{ads} on C-Top is stronger than on 4-fold hollow, -2.83 *vs*. -1.89 eV, respectively, as obtained at a PBE-D3 level, with dispersive forces representing an almost negligible contribution to the adsorption (PBE E_{ads} values are -2.73 and -1.77 eV, respectively).

3.4. High coverage H adsorption

Based on the results of the previous section, the adsorption of more than a single H atom on the TiC (001) surface was addressed, considering two H atoms (0.25 ML), five H atoms (0.65 ML), and finally a full coverage (1 ML) situation.

For the 0.25 ML situation, different mutual positions were explored departing from one H atom on C-Top and the second H atom adsorbed nearly on C-Top or Ti-Top, either close or far; see Figure 3.3. The most stable cases are C-Top sites, with a nearly identical E_{ads} of -2.83 eV, succinctly implying no repulsion in between neighbouring H adatoms, and so, that all C-Top sites are basically identical. Ti-Top sites are less stable, with E_{ads} values ranging from -0.83 to -1.20 eV.

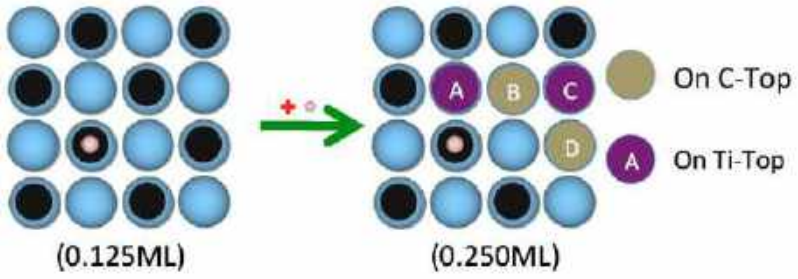

Figure 3.3. Top view scheme of the sampled sites around a C-Top H. Colour coding as in Figure 3.2.

Even if the above results seem to point to a negligible interaction in between neighbouring H adatoms, the reality is not this. The relatively low coverage offers a flexibility to accommodate H atoms. For instance, neighbouring H adatoms on C-Top sites separate from each other to a distance of 3.20 Å (see Figure 3.4). However, when one H atom is on C-Top and the other H atom is on Ti-Top, the distance between both H atoms is 1.55 Å (see Figure 3.4), in this sense, closer to an elongated H_2 *Kubas* situation.[20] Based on these results, one can assume that the rest of the adsorbed H atoms up to 0.5 ML would occupy C-Top positions, see Figure 3.5.

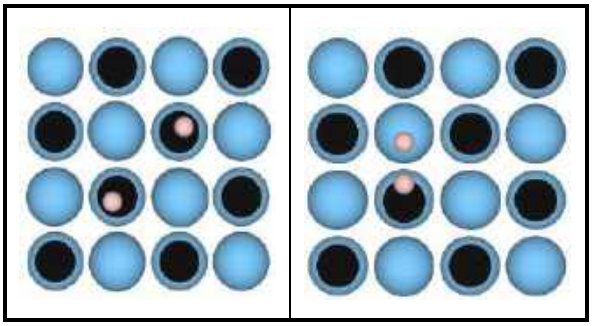

Figure 3.4. Top views of H atoms adsorbed in C-Top and Ti-top. Left: Two H atoms adsorbed on C-Top. Right: Two H atoms adsorbed, one on Ti-Top and another in C-Top.

From this situation, one may sample the position of a fifth H adatom. Three different Ti-top places were sampled: In the middle of the four H atoms (A), on Ti near two H atoms (B), or far away (C). In addition, it may be adsorbed on another C-Top. All possibilities are depicted in Figure 3.5. Again, most stable site is C-Top, with an E_{ads} of -2.35 eV. Notice the reduction in the E_{ads} with coverage, as a result of lateral interactions. Notice however that the Ti-Top surrounded by C-Top has an E_{ads} of -2.03 eV, approaching the farther C-Top sites, see Figure 3.5.

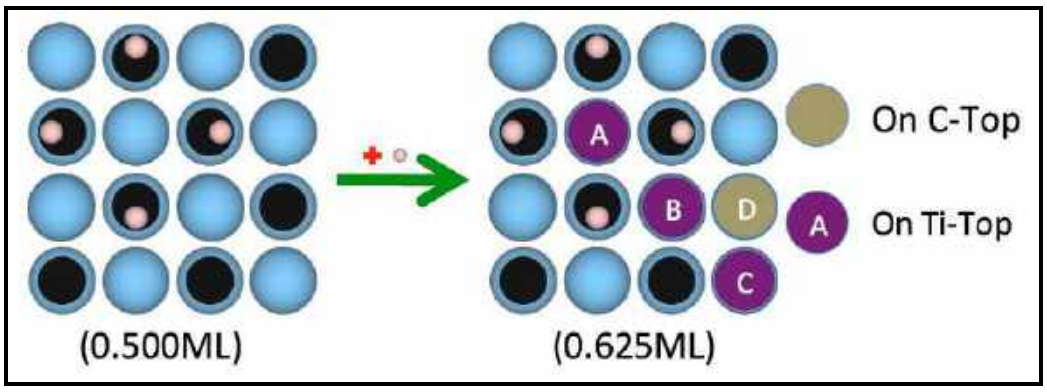

Figure 3.5. Top view scheme of a fifth added H adatom.

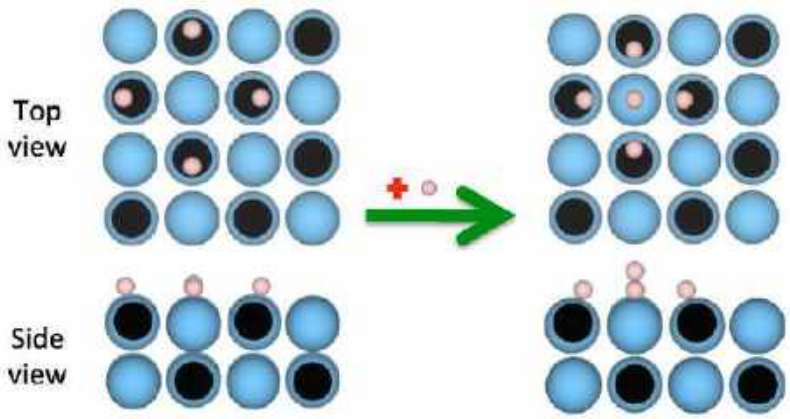

Figure 3.6. Fifth added H on Ti-Top in the middle of four hydrogen atoms adsorbed on C-Top, forming a sort of pyramidal H.

Notice as well in Figure 3.6 that the addition of the fifth H implies a change of orientation of the neighbouring H adatoms, which, before, had H moving away from each other. However, now, are oriented towards the H at Ti-top. In this sense, regardless where is the position on fifth H is added, the interaction between H atoms change the initial position of the hydrogen atoms in C-Top. As nearer the fifth H atom is from the four cubic H atoms, the stronger the interaction is, and for this reason the adsorption energy is higher for the fifth atom. According with the scheme in Figure 3.5, the adsorption energy on Ti-Top decreases when moving away from the pyramid, see Figure 3.7.

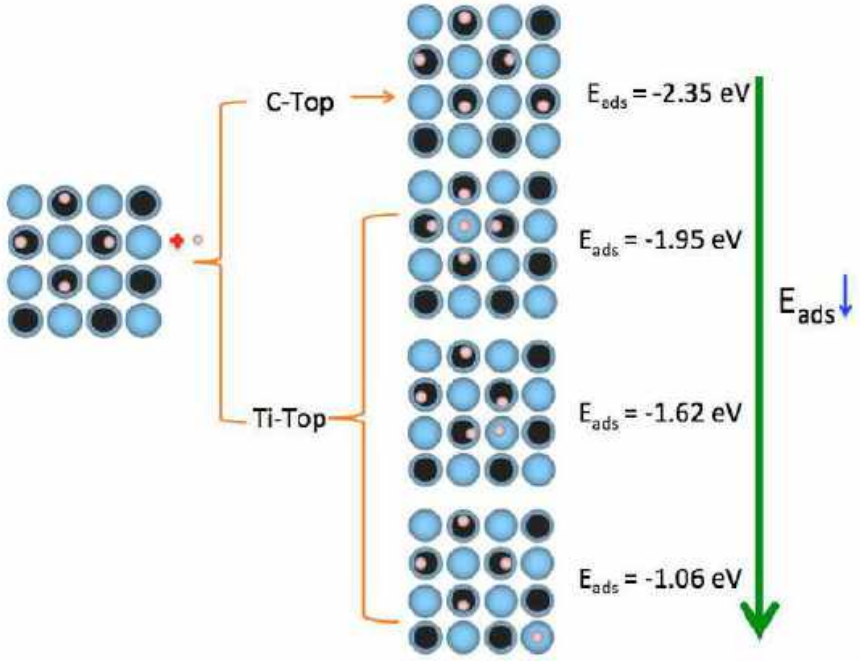

Figure 3.7. Top views of E_{ads} variation for the 5th on C-Top and Ti-Top sites.

Up to this point, results suggest that 1 ML coverage would be attainable by occupying all C-Top sites. The stepwise filling of the sites has been explored considering random, or driven by the results shown in Figure 3.7, see Figure 3.8. The results are encompassed in Table 3.1

revealing how E_{ads} decays as the coverage increases, getting overall reduced by 0.8 eV in total from lowest to highest coverage.

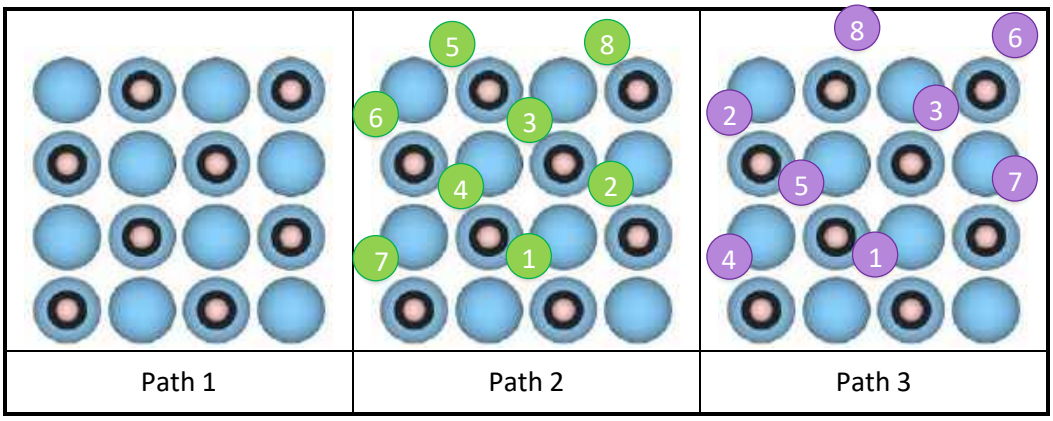

Figure 3.8. Top view scheme of the H filling of surface C-Top sites on Tic (001) sites. Number tags imply the order of addition, except for Path 1, which is random.

Table 3.1. H adsorption energy, E_{ads} in eV, on TiC (001) surface at different coverages.

E_{ads} (eV)		Nº of adsorbed H atoms							
		1 H	2 H	3 H	4 H	5 H	6 H	7 H	8 H
Path 1	PBE-D3	-2.83	-2.81	-2.64	-2.61	-2.61	-2.41	-2.21	-2.02
Path 2	PBE-D3	-2.83	-2.81	-2.64	-2.61	-2.61	-2.41	-2.21	-2.02
Path 3	PBE-D3	-2.83	-2.81	-2.63	-2.37	-2.58	-2.36	-2.30	-2.02

As far as the filling sequence is considered, one can plot the Eads of Paths 1-3 *versus* the number of H added atoms, see Figure 3.9 revealing, in general terms, the same trend.

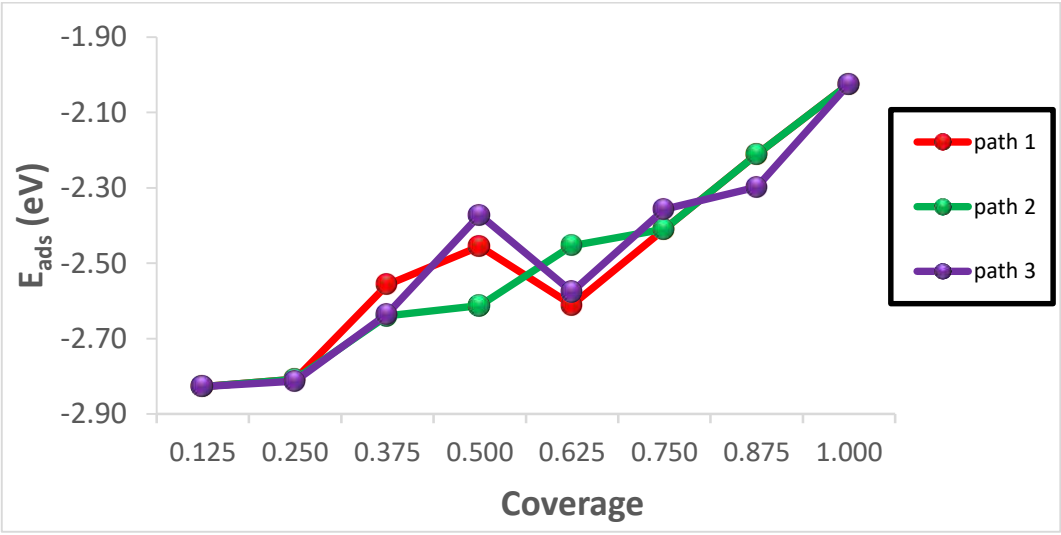

Figure 3.9. E_{ads} variation with respect the number of H atoms according to the filling patterns shown in Figure 3.8.

Furthermore, one can evaluate the sequential adsorption energy variation, *versus* the number of added H, see Figure 3.10. There, one immediately appreciates that the fifth H features a particular stabilization with respect the other stages.

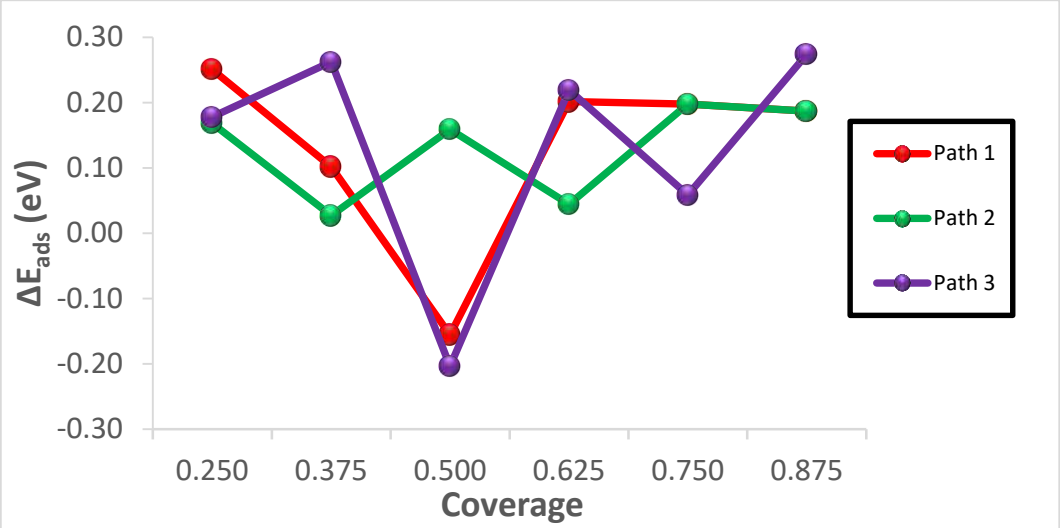

Figure 3.10. E_{ads} difference, ΔE_{ads}, in eV, with respect the number of added H on TiC (001) surface.

Once the full coverage situation is explained, we regarded other possibilities to correlate our findings with the experiments. Firstly, we explored the possible H incorporation, *i.e.* absorption, initially, on the pristine TiC (001) model. To this end, H was placed between first and second layers (subsurface), in the six positions described in Figure 3.1. The most stable site was found for the 4-fold hollow site, with an E_{abs} of -1.79 eV, thus, much smaller compared to the adsorption value of -2.83 eV.

As a final limit, we studied the possibility of subsurface H being stabilized when H adatoms get destabilized. To this end, we investigated H absorption on the 4-fold hollow site on the nearly fully H-covered TiC (001) model, and, as well, when having a fully H-covered TiC (001) surface, this is, adding the 8^{th} or 9^{th} H atoms, respectively. In the case of being the 8^{th}, the absorption energy is -1.37 eV, still, smaller than the adsorption energy of -2.02 eV. In the case of the 9^{th} H atom, the comparison is made in between the subsurface H, with an E_{abs} of -1.28 eV, and the H on a pyramidal Ti-Top site, see above and Figure 3.11, with an E_{ads} of -2.54 eV.

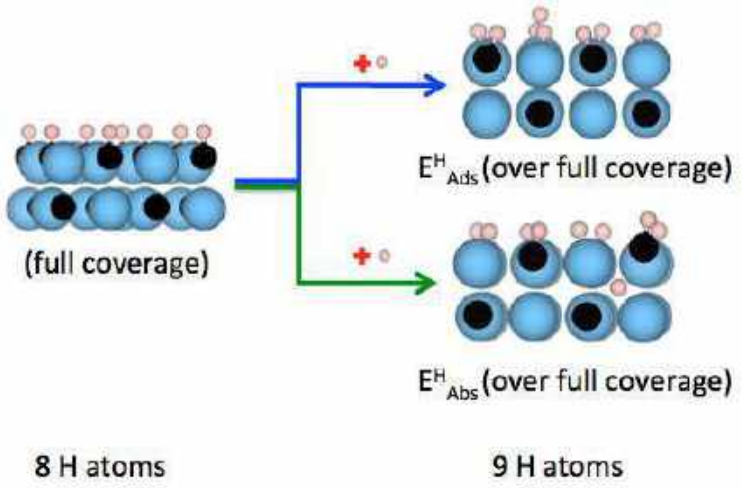

Figure 3.11. Scheme with the two possibilities studied for the 9th H atom.

The present study reveals that H absorption does not seem to be a worrying phenomenon, as other surface H species may exist above the 1 ML limit. In particular, the pyramidal H on Ti-Top, which, indeed, has a larger E_{ads} than the highest coverage C-Top situations. Notice as well that the C-H bonds feature some lability, affected by the presence or absence of neighbours. See different orientations when having 7, 8, or 9 H adatoms in Figure 3.12.

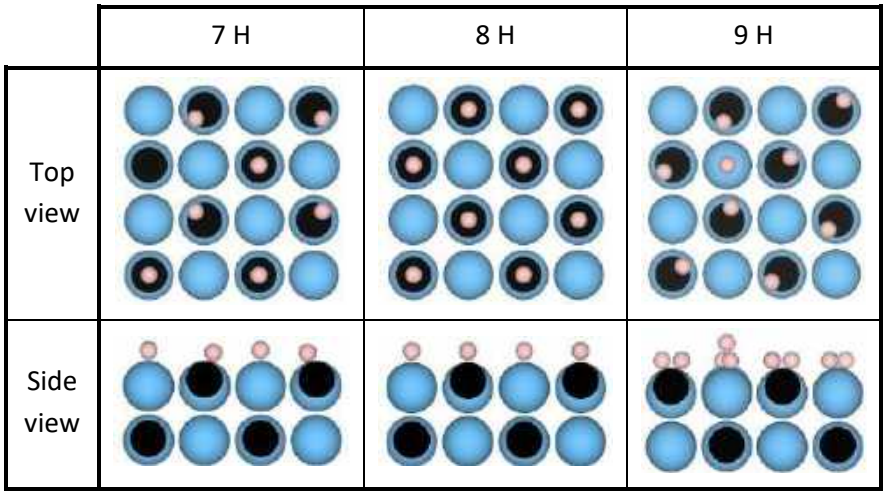

Figure 3.12. Top (top) and side (bottom) views for most stable situations when having 7, 8, or 9 H adatoms on the TiC (001) Surface.

3.5. H_2 adsorption at lower coverage

In this section, we study the adsorption of molecular H_2 on the TiC (001) surface. 19 different sites were studied for the H_2 molecular adsorption, including six vertical orientations and 13 parallel H_2 molecules; see Figure 3.13.

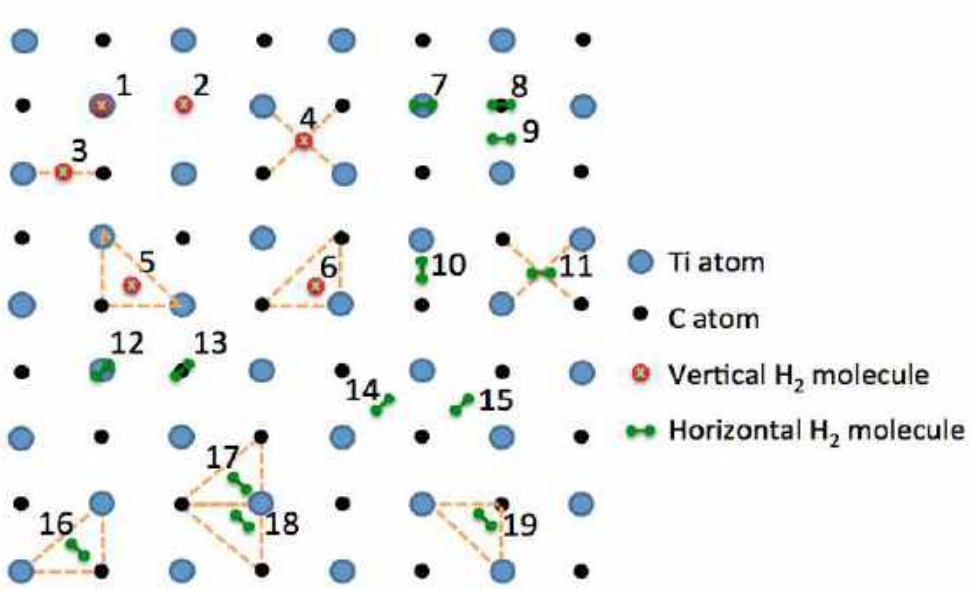

Figure 3.13. Schematic top view of a TiC (001) surface and the 19 studied H_2 adsorption positions. The image shows C atoms (black), metallic atoms (blue), and H_2 molecules. Dashed orange lines are guides to the eyes.

The optimizations revealed that a possible minimum for H_2 is a *Kubas* mode on top of a surface C atom, with an E_{ads} of -0.66 eV, see Figure 3.14. The rest of the found minima feature E_{ads} of *ca*. -0.21 eV, responding to a physisorption situation, found as well on top of a C atom, with an E_{ads} of -0.41 eV, being a non-*Kubas* adsorption. In all cases except the *Kubas* type adsorption, the dispersive interaction energy contribution, ranging from 0.14 - 0.22 eV, is dominant.

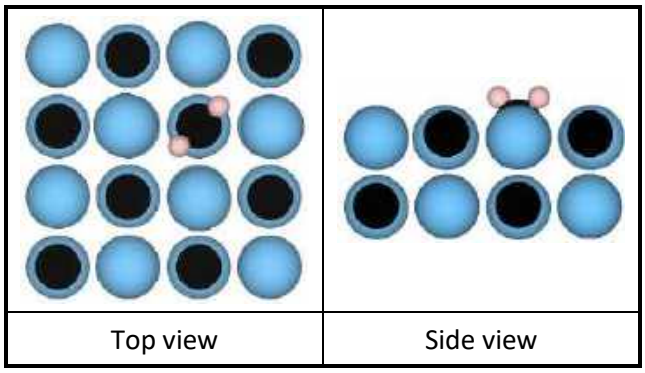

Figure 3.14. Top (left) and side (right) views of H_2 adsorption on a *Kubas* mode on TiC (001).

3.6. H_2 dissociation on the TiC (001) surface

From the previous information, one can start exploring the H_2 dissociation as catalysed by the TiC (001) surface. Notice that a strong interaction with the surface is sought, able to compensate the dissociation energy (DE) of H_2, ΔE_{dis}, here estimated to be -4.53 eV, and so, quite similar to the experimental value of -4.48 eV.[21]

Before searching for the TS, one has to have clear that one will depart from the *Kubas* mode with E_{ads} -0.66 eV, going to a final point with two vicinal H adatoms in C-Top sites, with a DE energy of -0.44 eV. Thus being an exothermic step. The TS has been acquired either using CI-NEB or Dimer methodologies, and TS characterized as so by a vibrational analysis, showing only one imaginary frequency. Figure 3.15 shows the reaction energy profile, displaying an energy barrier of 0.46 eV, which is relatively small, but not negligible. When one accounts for ZPE, the profile basically shifts up in energy. The E_{ads} is -0.03 eV, the barrier reduces up to 0.34 eV, and the reaction is a bit more exothermic by -0.13 eV.

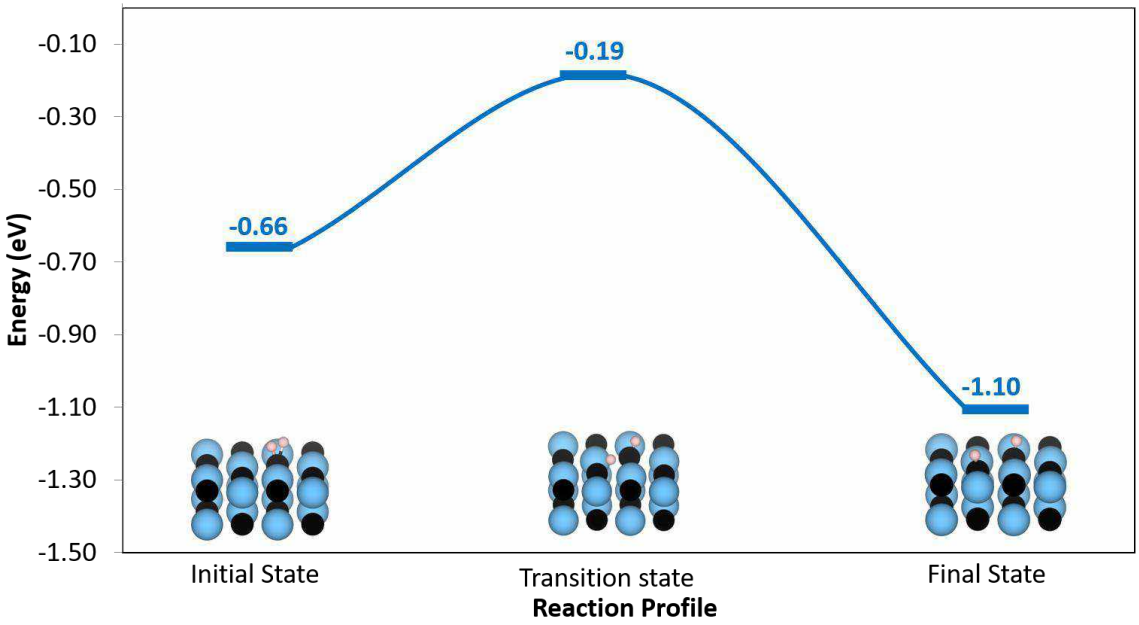

Figure 3.15. H_2 dissociation reaction energy profile on TiC (001) surface.

3.7. H diffusion on TiC (001) surface

As seen before, the H_2 adsorption and dissociation seems to be feasible on TiC (001) surfaces. The last question is whether such H adatoms would stay rigid on when generated, or would be mobile over the surface otherwise. The latter would favour the hydrogenation processes or achieving the high coverage patterns shown above. To this end, H diffusion has been evaluated through two paths starting from C-Top position; H diffusing to vicinal C atom (green arrow) or H diffusing to a farther C atom (orange arrow) in Figure 3.16.

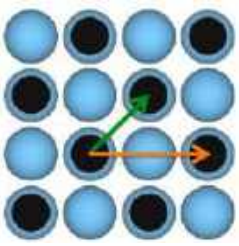

Figure 3.16. The two paths explored in H atom diffusion.

The energy barriers revealed that the shortest path, *i.e.* to a vicinal C-Top through a bridge in between two surface Ti atoms, featured a diffusion energy barrier of 0.90 eV. Furthermore, the path across a Ti-Top site implied a much larger energy barrier of 2.01 eV. Thus, from these first preliminary results, it seems as H adatoms are movable, but not easily.

3.8. Experimental studies

The experimental studies belonging to this Chapter have been carried out by Dr. Rodriguez's group at the Brookhaven National Laboratory, in the USA. In the experimental studies, when a clean TiC (001) surface is exposed to molecular H_2 at different pressures; 5, 50, and 150 Langmuir (L), and 1 Torr of H_2, hydrogen is molecularly adsorbed on the TiC (001) surface. This fact is corroborated by means of H_2-thermal desorption spectra (Figure 3.17.), obtained through Temperature Programmed Desorption (TPD) studies. The three lower spectra of the figure correspond to UHV exposures, where H_2 desorbs at temperatures between 320 and 430 K. The experimental investigators assigned these peaks to different surface situations. A weak peak is shown around 410 K and could come from adsorption and dissociation of H_2 on defect sites of the TiC (001) surface. The peaks at 370 and 340 K are probably associated with hydrogen bound to ideal terrace sites of TiC (001). For doses under UHV conditions, saturation in the H coverage of 0.6 - 0.7 ML was seen upon H_2 exposures above 100 L.[22] When the TiC (001) surface is exposed at 300 K to 1 Torr of H_2 for 5 minutes in a micro-reactor, the H_2-thermal desorption spectrum is observed a higher H coverage of 1.4-1.6 ML and led to a hydrogen desorption peak at 320 - 330 K.

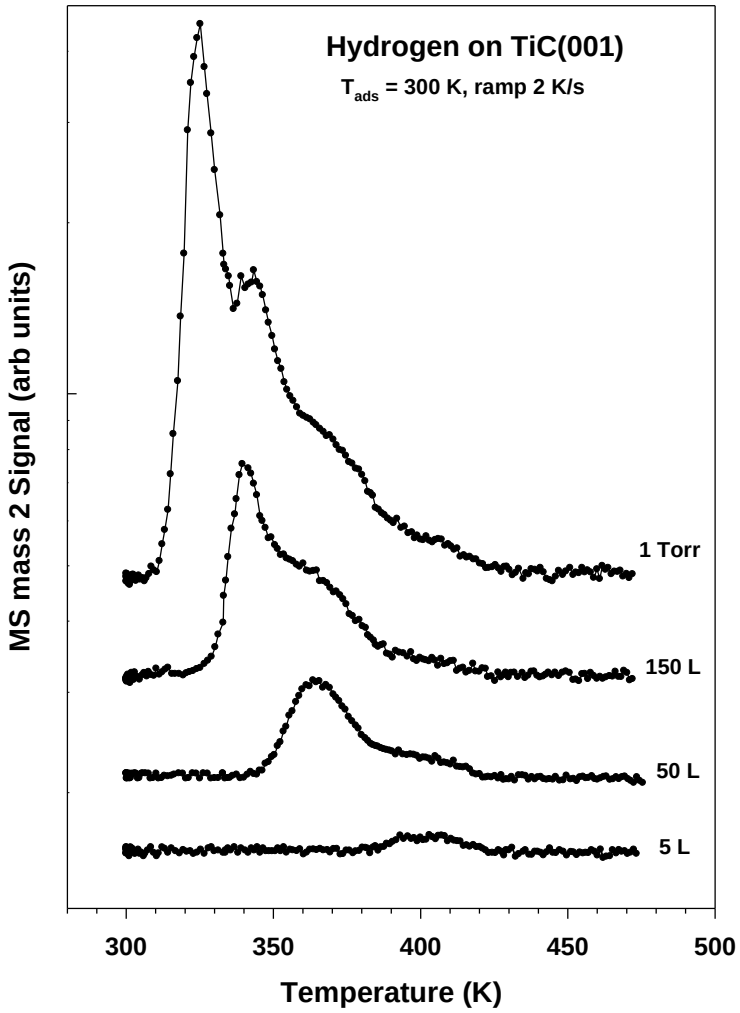

Figure 3.17. H_2-thermal desorption spectra collected after dosing molecular hydrogen with 5, 50, and 150 Langmuir (L) to a TiC (001) surface at 300 K. The top spectrum corresponds to a surface.[21]

When the TiC (001) surface is exposed at large adsorbate coverages (> 1 ML), signals are observed that are probably associated with the formation of compounds on the surface of the sample. Figure 3.18 shows C 1*s* X-ray Photoemission Spectroscopy (XPS) experiments collected before and after exposing a TiC (001) surface to 1 Torr of H_2 at 300 K. The results show that a C 1*s* peak is obtained for the clean surface, undoubtedly associated with the C on the TiC surface.[23] Upon contact with 1 Torr of H_2, a new peak appears at near 283.5 eV, which indicates the formation of CH_x groups on the surface of the carbide. In addition, this peak is not found for UHV doses of H_2. Under a high pressure of H_2, the surface of the carbide appears to generate the CH_x groups and accommodate an extra amount of hydrogen not bound to C. The CH_x decomposed when the surface was heated to 500 K. Thus, the data point to a reversible mechanism for the storage of hydrogen on the surface of the carbide.

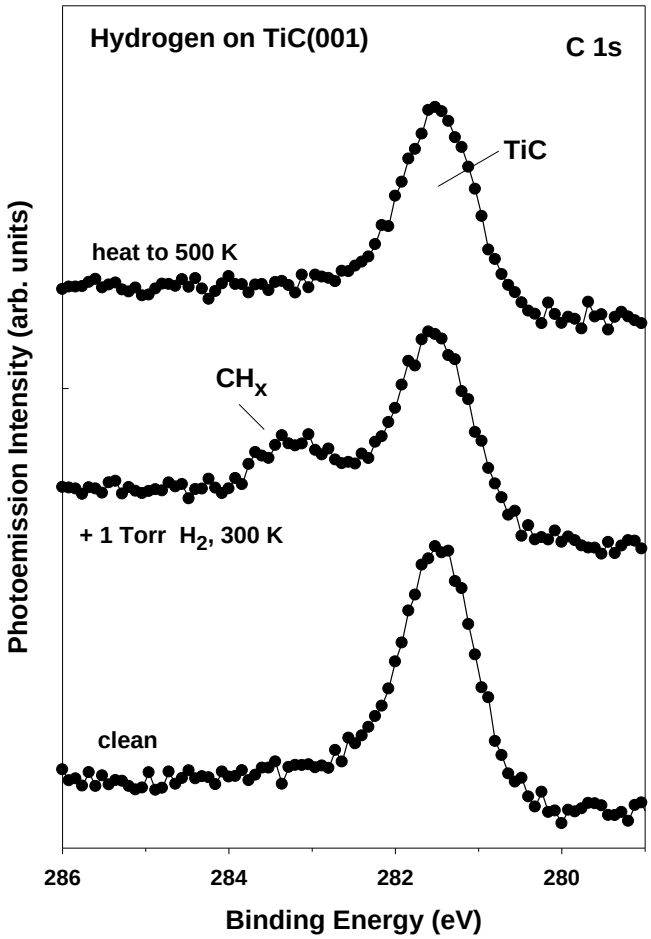

Figure 3.18. C 1s XPS spectra for clean TiC(001), bottom, a surface exposed at 300 K to 1 Torr of H_2 for 5 minutes, middle, and the H_2/TiC(001) system heated to 500 K, top.[21]

The results obtained from DFT-based calculations have made it possible to clarify these experimental results. The results show that the most stable adsorption positions for H atomic and H molecular is on C-Top. In addition, the H_2 molecule adsorbs forming *Kubas* mode. The calculations results have revealed that the H molecule adsorbs on C-Top until full coverage. The adsorption energy for the H atom decreases as the coverage increases as can be seen in Figure 3.9 and Table 3.2. This fact matches with the H atoms desorbed at lower temperature as Figure 3.17. Experimental studies also indicate that the H coverage is 1.4 - 1.6 ML. With the simulations, it has been found that hydrogen is adsorbed on Ti-Top beyond a full monolayer, see Figure 3.7.

Finally, the experimental peaks have been assigned with the help of the calculations. In the TPD spectra, the peak that appears at 320-330 K likely corresponds to weakly adsorbed H_2 molecules, physisorbed on the TiC (001) surface. This conclusion can be justified because the experiment was carried out to 1 Torr of H_2 (high doses of H_2) and the desorption of low temperature indicates a weak adsorption. That is, the lower the adsorption, the lower the desorption temperature. When the surface is exposes at a lower hydrogen dosage of 150 L, two peaks can be observed, one at 340 K and another at 365 K. The first peak would correspond to the H adsorption atoms on Ti-top sites, since its adsorption is only favourable when all the

surface C atoms are occupied by H, and, also, the adsorption on the Ti is weaker than on the C-top sites. This conclusion can be supported through the H_2 exposition of dose of 50 L, where the first peak disappears from the TPD spectra while the second peak continues to appear. This second peak would be assigned to the H adsorption on C-Top. Finally, when the sample is exposed to only 5 L of hydrogen, a peak appears at about 400 K with low intensity, in this case, the H would be adsorbed on surface defects, where the adsorption of H is stronger than on C-Top.

3.9. Conclusions

According to the above results, it is clear that there is a preference for H atoms to occupy C-Top positions on the TiC (001) surface. The filling sequence up to full coverage has also been obtained, finding that H atom prefers to be adsorbed on the surface rather than to be absorbed between the layers. Even if C-Top H adatoms stabilize neighboring H adatoms on Ti-Top sites, there is a preference towards occupying all surface C-Top sites. However, Ti-Top sites can be occupied when surrounded by C-Top sites, forming sort of pyramidal H moieties, particularly occupied when going over a 1 ML situation. H_2 adsorption is also preferred on C-Top sites, but in the form of an elongated H_2 moiety, called a *Kubas* model. Such H_2 is physisorbed, but can be easily dissociated into H adatoms, being the process exothermic and has a small energy barrier. The as generated H adatoms may diffuse over the TiC (001) surface, but with moderate energy barriers. Such results suggest the use of TiC as a possible hydrogenation catalyst. The theoretical results in the chapter made it possible to understand experimental studies, allowing the assignment of the peaks obtained in the experimental TPD.

3.10. Publication

THE JOURNAL OF PHYSICAL CHEMISTRY C

Article

Cite This: J. Phys. Chem. C 2018, 122, 28013−28020

pubs.acs.org/JPCC

Diversity of Adsorbed Hydrogen on the TiC(001) Surface at High Coverages

Juan José Piñero,[†] Pedro J. Ramírez,[‡] Stefan T. Bromley,[†,§] Francesc Illas,[†] Francesc Viñes,*[,†] and José A. Rodriguez*[,∥]

[†]Departament de Ciència de Materials i Química Física & Institut de Química Teòrica i Computacional (IQTCUB), Universitat de Barcelona, c/Martí i Franquès 1-11, Barcelona 08028, Spain

[‡]Facultad de Ciencias, Universidad Central de Venezuela, Apartado 20513, Caracas 1020-A, Venezuela

[§]Institució Catalana de Recerca i Estudis Avançats (ICREA), Passeig de Lluís Companys, 23, Barcelona 08010, Spain

[∥]Chemistry Department, Brookhaven National Laboratory, Upton, New York 11973, United States

Supporting Information

ABSTRACT: The catalyzed dissociation of molecular hydrogen on the surfaces of diverse materials is currently widely studied due to its importance in a broad range of hydrogenation reactions that convert noxious exhaust products and/or greenhouse gases into added-value greener products, such as methanol. In the search for viable replacements for expensive late-transition-metal catalysts, TiC has been increasingly investigated as a potential catalyst for H_2 dissociation. Here, we report on a combination of experiments and density functional theory calculations on the well-defined TiC(001) surface, revealing that multiple H and H_2 species are available on this substrate, with different binding configurations and adsorption energies. Our calculations predict an initial occupancy of H atoms on the surface C atom sites, which then enables the subsequent stabilization of H atoms on top of the surface Ti atoms. Further H_2 can be also molecularly adsorbed over Ti sites. These theoretical predictions are in full accordance with information extracted from X-ray photoemission spectroscopy and temperature-programmed desorption experiments. The experimental results show that at high coverages of hydrogen, there is a reconstruction of the TiC(001) surface, which facilitates the binding of hydrogen.

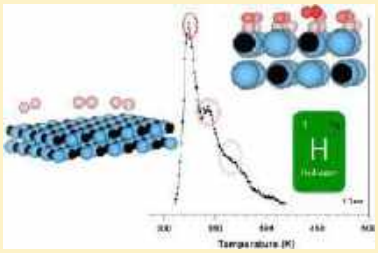

INTRODUCTION

The interaction of molecular hydrogen with titanium carbide (TiC) is an important topic in catalysis, solid-state chemistry, electrochemistry, and materials science.[1−9] TiC displays a high activity for the hydrogenations of ethylene and CO_2.[1,3,4] In principle, ethylene and CO_2 molecules are preferentially adsorbed on the carbon sites of TiC,[3,10] leaving the Ti sites free for the dissociation of H_2 and subsequent hydrogenation reactions. In the case of CO_2, an attack of H to form a HOCO intermediate is a key step that precedes the formation of CO and its subsequent hydrogenation to methanol.[3,4] To carry out these reactions in an efficient way, hydrogen atoms must be present on the TiC surface while displaying high activity and mobility. Therefore, it is important to study the interaction of H with the carbide surface as a function of coverage and to establish how much hydrogen a nearly stoichiometric TiC system can adsorb and/or absorb. In principle, hydrogen can be present at different TiC sites: on the surface,[3,4] in the bulk,[5−9] in interstitial positions,[11] physisorbed,[12] and adoption of a Kubas adsorption mode.[13,14] In this aspect, TiC can be regarded as a textbook example within the family of transition-metal carbide (TMC) materials.[14,15]

It has also been shown that TiC can be useful as a material for hydrogen storage, although the low gravimetric content prevents its technological use.[6−9] Under electrochemical conditions, H is found to be absorbed on defective TiC_x compounds.[6,7] As the TiC_x composition progressively deviates from a 1:1 stoichiometry, the insertion of H and/or H_2 into the substrate lattice increases linearly, where H/H_2 species occupy carbon vacancies,[7,8] a situation that also occurs in heterogeneous catalysis working conditions.[16,17] Studies using X-ray diffraction[6,7] have shown that TiC allows the insertion of hydrogen within its structure but only under two conditions. First, the carbide should have a high concentration of C vacancies with a composition in the range of $TiC_{0.6-0.7}$, thus likely containing C vacancies in the bulk matrix. Second, carbon vacancies must be ordered, leaving the (111) planes as empty as possible, as disordered carbide structures do not allow significant hydrogen insertion. Results of calculations based on density functional theory (DFT) suggest that

Received: July 30, 2018
Revised: November 9, 2018
Published: November 15, 2018

ACS Publications © 2018 American Chemical Society

DOI: 10.1021/acs.jpcc.8b07340
J. Phys. Chem. C 2018, 122, 28013−28020

nanoparticles of titanium carbide, such as Ti_8C_{12} and $Ti_{14}C_{13}$, have potential for hydrogen storage at near-ambient conditions.[5] The titanium atoms in these systems catalyze the dissociation of H_2 and are capable of coordinating with multiple hydrogen ligands.[5] Inelastic and elastic neutron scatterings have shown the presence of molecular hydrogen trapped in two-dimensional layered titanium-carbide-based MXenes ($Ti_3C_2T_x$, where T_x represents a surface-terminating species, including H, O, OH, and F).[9] The trapped H_2 occupies small cavities in the structure of the MXenes and exhibits a high mobility.[9] Previous studies have shown that H_2 adsorption occurs on TiC, but the H_x species present on this carbide, or how the surface becomes covered as the H_2 pressure increases have not been reported. In general, H_2 and/or H species are particularly important species in heterogeneously catalyzed processes,[18] such as fossil fuel refinement, hydrogenation of alkenes,[19] and the production of other diverse chemical compounds.

Herein, surface and subsurface H_x species are systematically studied on TiC by both theory and experiments. Note that TiC is a system that is representative of TMCs with 1:1 stoichiometry. Specifically, we sample H_2 on the TiC(001) surface with increasing hydrogen doses and pressures by combining both X-ray photoelectron spectroscopy (XPS) and temperature-programmed desorption (TPD) with DFT-based calculations. Hereby, the interaction of H_2 with the well-defined TiC(001) surface is determined by considering a wide range of molecular and atomic adsorption scenarios. The desorption of adsorbed H_2 molecules are observed over a broad range of temperatures (~150 K), consistent with a large variation in the H adsorption energy with respect to coverage, as predicted by the DFT-based simulations. At room temperature, more than a monolayer (ML) of hydrogen can adsorb on the stoichiometric TiC(001) surface. Moreover, our experimental and theoretical studies point to a H-induced reversible reconstruction of the carbide surface that facilitates the dissociation of H_2 and the binding of hydrogen in diverse ways.

EXPERIMENTAL AND THEORETICAL METHODS

TPD and XPS Studies. The TiC(001) single crystal was cleaned following the procedures reported in the literature.[20−22] The cleaning methodology led to a clear (1 × 1) diffraction pattern by low-energy electron diffraction (LEED) and no surface impurities detected by photoemission or XPS. The crystal growers estimated a $TiC_{0.95-0.98}$ stoichiometry for the bulk of the sample, and, after cleaning, our quantitative XPS results showed surfaces with essentially a Ti/C ratio of one.[22] For the surfaces prepared in this way, images of scanning tunneling microscopy gave a square crystal lattice with terraces that were 400−650 Å wide, separated by single and double step heights. For a sample with these characteristics, no penetration of H_2 or H into the bulk is to be expected.[8]

The experiments were carried out in an ultrahigh-vacuum (UHV) chamber that has a high-pressure cell or a batch reactor attached.[3,4] The sample could be transferred between the reactor and the UHV chamber without exposure to air. The UHV chamber (base pressure 1 × 10^{-10} Torr) was equipped with instrumentation for XPS, LEED, ion-scattering spectroscopy, and TPD.[3,4] The TiC(001) was exposed to H_2 (>99.999% purity) at 300 K in the UHV chamber or in the high-pressure reactor. After exposure to hydrogen, the TPD spectra were acquired with a heating rate of 2 K s^{-1}. The amount of hydrogen under each TPD peak was calibrated using the TPD data for a saturation coverage of hydrogen on Pt(111).[23] Coverages of hydrogen are reported with respect to the total number of Ti and C atoms on a TiC(001) surface. In the TPD experiments, at a nominal coverage of 1 ML, all of the atoms of the carbide surface are bound to one H atom.

DFT-Based Calculations. Periodic DFT-based calculations using suitable supercell models representing the systems of interest were carried out to investigate the role of the TiC surface on atomic (H) and molecular hydrogen (H_2) adsorption. Only the TiC(001) surface was considered, as previous studies have already demonstrated that this surface is the most stable one for TiC and other TMC compounds.[24] This surface was modeled by periodically repeated two-dimensional slabs with a separating vacuum region of 10 Å, which was large enough to avoid spurious interactions between the slabs periodically repeated perpendicular the surface direction.[13,15] The slab was constructed using the lattice parameter taken from the optimized bulk TiC crystal.[25] The slab contained four atomic layers; the two outermost ones were allowed to fully relax, whereas the two bottom layers were fixed at bulk positions to simulate the bulk. To represent the (001) surface, a $(2\sqrt{2} \times 2\sqrt{2})R45°$ supercell was employed. The supercell contained a total of 64 (32 C and 32 Ti) atoms.

All calculations were carried out using the Vienna ab initio simulation package code.[26] The Perdew−Burke−Ernzerhof (PBE)[27] exchange−correlation functional was chosen, and the effect of dispersive forces was described by the D3 dispersion correction developed by Grimme (PBE-D3).[28] The effect of core electrons on the valence electron density was taken into account through the projected augmented wave method of Blöchl,[29] as implemented by Kresse and Joubert, with $2s^2\ 2p^2$ and $3p^6\ 3d^3\ 4s^1$ for C and Ti atoms, respectively.[30] The valence electron density was expanded in a plane wave basis set with a kinetic energy cutoff of 415 eV. Monkhorst−Pack **k**-point schemes[31] of 9 × 9 × 1 dimensions were used for bulk and surface slab calculations. A conjugated-gradient algorithm was employed for the atomic structure optimization, together with a force convergence criterion of 0.01 eV $Å^{-1}$. The tetrahedron smearing method with Blöchl corrections with a smearing width of 0.2 eV was used to determine the partial occupancies for each orbital, and total energies were then extrapolated to 0 K (no smearing). The electronic relaxation convergence criterion was set to 10^{-5} eV.

The sequential adsorption energy (E_{ads}) of a nth adsorbed H atom was calculated as

$$E_{ads} = (E_{n\cdot H/TiC} - (E_H - E_{(n-1)\cdot H/TiC})) \quad (1)$$

where $E_{n\cdot H/TiC}$ is the energy of the n·H atoms adsorbed on the surface, E_H is the energy of an isolated H atom, n is the number of H atoms in the system, and $E_{(n-1)\cdot H/TiC}$ is the energy of the relaxed TiC surface containing $(n - 1)$·H atoms, each in its optimal position. With this definition, a more negative E_{ads} value indicates a stronger adsorption. E_H is obtained by placing the atom in a broken symmetry unit cell of 9 × 10 × 11 $Å^3$ dimensions and carrying out a **Γ**-point optimization. Notice that when 1/2·H_2 is used as an energy reference, i.e., using E_{H_2} instead of E_H and calculating adsorption energies likewise, the obtained E_{ads} are systematically reduced by 2.26 eV both at PBE and PBE-D3 levels.

DOI: 10.1021/acs.jpcc.8b07340
J. Phys. Chem. C 2018, 122, 28013−28020

To ascertain whether the TiC(001) surface is suitable to dissociate H_2, the transitions state for the H_2-splitting reaction step was obtained by using the climbing image nudged elastic band[32] procedure. To characterize the thus obtained candidate transition state (TS), an analysis of the vibrational frequencies was performed. Here, in the construction and diagonalization of the Hessian matrix built from finite difference displacements of 0.03 Å, only the degrees of freedom of the adsorbed H_x were considered. A well-defined TS was confirmed when only a single imaginary frequency was obtained.

To study the desorption process, one could use statistical thermodynamics coupled to transition state theory (TST) to obtain the adsorption and desorption rate estimates.[33,34] However, the prediction of the TPD peak is more involved because it corresponds to the temperature at which the desorption rate is maximum. Therefore, temperature of the maximum desorption rate, T_d, of the adsorbed H atoms has been estimated by using the broadly employed Redhead equation.[35] The desorption is assumed to be a second-order reaction, given that H adatoms have to diffuse to recombine into a H_2 molecule prior to desorption. Thus, the employed Redhead equation is

$$E_{des} = RT_d^2\left(\frac{\theta A}{\beta}\exp^{-(E_{des})/RT_d}\right) \quad (2)$$

where R is the ideal gases constant, θ is the surface coverage, A is a rate pre-exponential factor, which can be estimated from TST and has values in a range between 10^8 and 10^{13} under the general validity of Redhead equation, β is the heating rate of 2 K s^{-1} in accordance with TPD spectra, and E_{des} is the desorption activation energy, here quantified as minus the E_{ads}. In the present work, the pre-exponential factor is chosen to cover a broad range, and thus to minimize the possible effects coming from the approximations involved in TST.

RESULTS AND DISCUSSION

Binding and Desorption of Hydrogen: TPD and XPS Spectra. Figure 1 shows a set of TPD spectra recorded after different exposures of molecular hydrogen to a clean TiC(001) surface at 300 K. The uppermost spectrum in Figure 1 was recorded after exposing the sample at 300 K to 1 Torr of H_2 for 5 min in a microreactor. The three lower spectra of the figure correspond to the UHV exposures of 5, 50, and 150 Langmuir (L). Desorption of hydrogen is observed at temperatures between 320 and 430 K. A weak peak is observed around 410 K and could come from the adsorption and dissociation of H_2 on the defect sites of the TiC(001) surface. The peaks at 370 and 340 K are probably associated with hydrogen bound to the ideal terrace sites of TiC(001). For doses under UHV conditions, saturation in the H coverage of 0.6−0.7 ML was seen upon H_2 exposures above 100 L. As we will see below, this saturation coverage for UHV dosing is in good agreement with the corresponding coverage calculated using DFT for H on a perfect TiC(001) surface at 300 K. A higher H coverage of 1.4−1.6 ML was seen upon exposure of the sample to 1 Torr of H_2 and led to a hydrogen desorption peak at 320−330 K. This much higher coverage of hydrogen is probably associated with the reconstruction of the carbide surface.[36,37]

Desorption spectra collected after trapping H_2 in rough powders of TiC show evolution of H_2 in a medium-temperature (330−573 K) and a high-temperature range

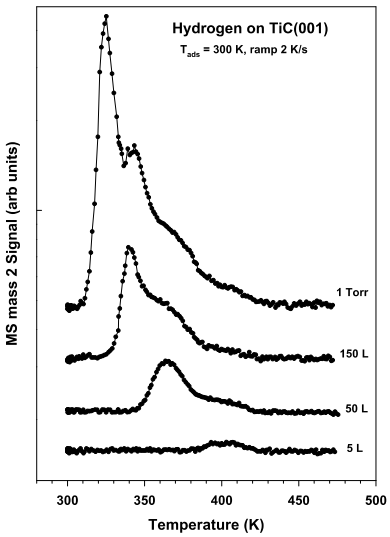

Figure 1. H_2 thermal desorption spectra collected after dosing molecular hydrogen with 5, 50, and 150 Langmuir (L) to a TiC(001) surface at 300 K. The top spectrum corresponds to a surface exposed to 1 Torr of H_2 for 5 min.

(723−1000 K).[36,37] The high-temperature desorption features are usually assigned to the hydrogen trapped inside the titanium carbide and/or bound to highly defective sites of the substrate. We did not observe these high-temperature features in our TPD studies. On a TiC(001) substrate with a 1:1 stoichiometric ratio, no significant penetration of hydrogen into the bulk of the sample is expected.[8] Furthermore, the theoretical calculations, to be discussed in the next section, show that hydrogen atoms or molecules are not stable in the interstitial sites of a perfect TiC(001) lattice. However, a reconstruction in the lattice of the carbide could produce sites where hydrogen binds well.[36,37]

The large adsorbate coverages (>1 ML) seen in the experiments for Torr doses of H_2 are probably associated with the formation of compounds on the surface of the sample. Figure 2 shows the C 1s XPS spectra collected before and after exposing the TiC(001) surface to 1 Torr of H_2 at 300 K. In a clean sample, one sees the C 1*s* peak expected for titanium carbide.[22] Upon contact with 1 Torr of H_2, a new peak appears at near 283.5 eV, which indicates the formation of CH_x groups on the surface of the carbide.[38] This peak was not seen for the UHV doses of H_2. Under a high pressure of H_2, the surface of the carbide appears to generate the CH_x groups and accommodate extra amount of hydrogen not bound to C. The CH_x is decomposed when the surface was heated to 500 K. Thus, the data point to a reversible mechanism for the storage of hydrogen on the surface of the carbide.

Hydrogen Adsorption: DFT-Based Calculations. First, atomic H adsorption on the TiC(001) surface was studied by considering the adsorption of a single H atom on the above-described slab model. This model system implies a small H

DOI: 10.1021/acs.jpcc.8b07340
J. Phys. Chem. C 2018, 122, 28013−28020

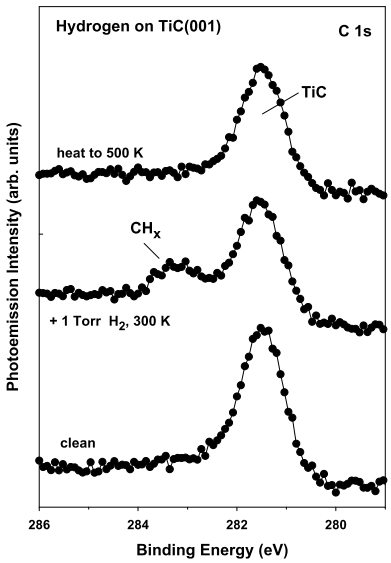

Figure 2. C 1*s* XPS spectra for clean TiC(001), bottom, a surface exposed at 300 K to 1 Torr of H_2 for 5 min, middle, and the H_2/TiC(001) system heated to 500 K, top.

coverage of 0.125 ML. Notice that, at variance with the Pt(111) reference for H coverage, here a monolayer is defined according to the number of surface titanium atoms (or equally well to the same number of surface carbon atoms). H adsorption was explored on six different sites of the TiC(001) surface; see Figure S1 of the Supporting Information.

The results from the DFT-based calculations show that the most stable adsorption configuration is the C-top site with an adsorption energy of −2.73 eV predicted by the PBE functional and −2.83 eV by the calculations using PBE-D3; see Table S1 in the Supporting Information. In a second step, H_2 adsorption was explored considering two different orientations with respect to the surface, with the molecular axis either vertical or horizontal with respect to the surface. Thus, H_2 adsorption was considered by exploring 19 configurations, in which six positions were vertical and 13 were horizontal; see Figure S2 in the Supporting Information. In accordance with the previous reports in the literature,[13] the most energetically favorable position for H_2 adsorption is the C-top position, adopting a so-called Kubas mode of adsorption.[13,14] This situation corresponds to a noticeable elongation of the H−H bond length, although with no bond breaking, and with a PBE adsorption energy value of −0.46 eV (−0.66 eV at PBE-D3). The adsorption energy values thus obtained are similar to those reported in a previous study on TiC(001) using the PW91 functional[39] with a H adsorption energy of −2.60 eV and a H_2 adsorption energy of −0.48 eV.[13] The other less energetically favorable minima are shown in Tables S1 and S2 of the Supporting Information.

The H_2 dissociation kinetics for a H_2 C-top Kubas bonding on TiC(001) has been examined by searching for the reaction step transition state and the associated activation energy barrier. To this end, the reaction path, shown in Figure 3, is

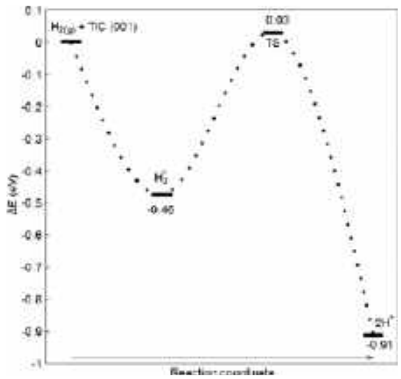

Figure 3. Reaction profile of H_2 adsorption and scission on the TiC(001) surface.

sketched with H_2 being initially molecularly adsorbed on a C-top and then breaking into two H atoms, both of which are adsorbed on the neighboring C-top sites. The reaction profile reveals an energy barrier of only 0.49 eV, whereas the effective energy barrier with respect to the energy reference of non-interacting TiC(001) and H_2 is negligible (0.03 eV).

The TS has only one imaginary frequency of 1377 cm^{-1}, corresponding to a H_2 separation mode, thus confirming its true saddle point nature. These results confirm that H_2 dissociation is possible and likely under catalytic working conditions, thus, no rate-limiting step of H adsorption on TiC(001) surface is expected.

The diffusion of H atom was also studied with respect to two different situations: when H diffuses to a vicinal C atom or when H diffuses to more distant C atoms; see Figure 4.

The results obtained show that the energy barrier for H atoms to diffuse toward a vicinal C atom (0.86 eV) is much lower than diffusion to more distant C atoms (2.11 eV).

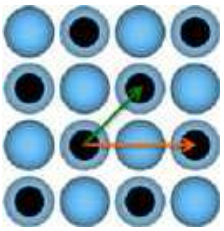

Figure 4. H diffusion studies. Blue balls represent Ti atoms and black balls are C atoms. The green arrow indicates the diffusion path to a vicinal C atom, whereas the orange arrow shows the path to a more distant C atom.

DOI: 10.1021/acs.jpcc.8b07340
J. Phys. Chem. C 2018, 122, 28013−28020

Considering these values, when H_2 dissociation occurs, the H atoms are predicted to be adsorbed on two vicinal C atoms.

Next, the adsorption energy at different H coverages, from 0.125 to 1 ML, was studied. For each H coverage considered, placements of many H atoms were examined, including vicinal and remote situations. In all cases, the H adsorption is energetically favorable, as can also be seen in Figure 5. Figure S3 of the Supporting Information shows the sequence of H atom filling on the TiC(001) surface.

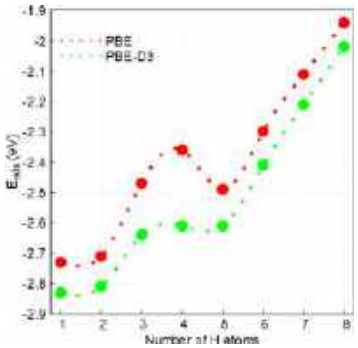

Figure 5. Adsorption energies (E_{ads}, in eV) for different H atom coverages on the TiC(001) surface.

The results show that the sequential E_{ads} per H atom decreases as more H atoms are added to the surface. These values reduce by 2.26 eV when using half the energy of a H_2 molecule as a reference; see Table S4. Taking this into consideration, most of the H adsorptions are thermodynamically favorable, but a full occupancy of all the surface C positions would be only achievable under a certain H_2 partial pressure.

The observed decrease of E_{ads} with coverage is as expected because the electronic repulsion between the adsorbed atoms increases at this higher coverage situation, thus causing the adsorption energy to decrease. An interesting feature of Figure 5 is that the adsorption energy does not monotonically decrease along the explored H coverage range. Attention is drawn to Figure 5, which shows that adding the fifth H lends extra stability to the system. This phenomenon may be related to the key role of electrostatic forces of the system and, hence, it has been further studied. To further evaluate this situation, four H atoms were adsorbed on the vicinal C-top sites and a fifth H atom was added at diverse positions, either on the Ti-top in three different places or on a nearby C atom; see the sites in Figure 6.

Here, incremental adsorption energies are obtained as

$$E_{ads} = (E_{H/TiC} - (E_H - E_{TiC+4H}))$$

where $E_{H/TiC}$ is the energy of the surface with five H atoms and E_{TiC+4H} is the energy of the surface with four H atoms adsorbed on vicinal C atoms. The results for the adsorption energy values for the fifth H atom are reported in Table 1.

Results show that the fifth H prefers to adsorb on the C-top than on the Ti-top, with the adsorption energies being −2.49 and −1.95 eV, respectively. Not all Ti-top positions are

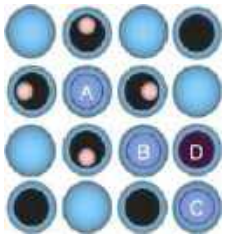

Figure 6. Top view of the tested adsorption sites (A−D) of a fifth H atom when four H are simultaneously adsorbed on the vicinal C-top sites. Blue balls represent Ti atoms and black balls are C atoms.

Table 1. Adsorption Energies for the Fifth H Atom on TiC(001) on Different Sites as Shown in Figure 6[a]

	Ti-top			C-top
E_{ads}^{H}	situation A	situation B	situation C	situation D
PBE	−1.95	−1.62	−1.06	−2.49
PBE-D3	−2.03	−1.69	−1.12	−2.61

[a]All values are given in eV.

equivalent, and the adsorption energy may vary by up to ∼0.9 eV. The central Ti-top position (A), for example, has a much larger adsorption energy than other two Ti-top positions (B and C); see Figure 6.

The presence of the previously adsorbed H atoms on the surface causes a change in the site stability in such a way that the adsorption energy on Ti noticeably increases from a value of −0.73 to −1.95 eV when all surrounding four C-top sites are occupied by H. The H atoms adsorbed in such a resulting pyramidal-like configuration exhibit two different heights above the surface: for the four H atoms on the C-top positions, the height is 1.17 Å, whereas for the central Ti-top position, the height of the H atom is 1.85 Å; see Figure 7.

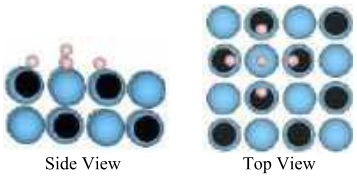

Figure 7. Pyramidal adsorption configuration formed by five adsorbed H atoms. Left: side view. Right: top view. Blue balls represent Ti atoms, black balls are C atoms, and pink balls are H atoms.

We also consider this mode of H adsorption for higher coverages. Specifically, the adsorption of a ninth H atom is evaluated when adsorbing on a full coverage of all four Ti-top and all four C-top sites of the supercell model of the TiC(001) surface. Here, we compare the pyramidal Ti-top mode with two other different positions for the subsequent H atom: on C-top forming a Kubas mode and subsurface; see Figure 8.

The results of the three hydrogen adsorption modes evaluated show that the adsorption of the ninth H atom is again most favorable on a pyramidal Ti-top site; see Table 2.

DOI: 10.1021/acs.jpcc.8b07340
J. Phys. Chem. C 2018, 122, 28013−28020

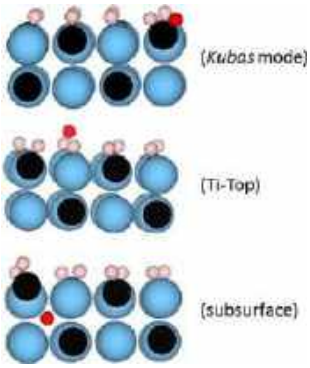

Figure 8. Side view of the three final positions evaluated where a ninth H atom is added to a slab that is precovered with eight adsorbed H atoms (color code as in Figure 7; the added H atom is indicated in red).

Table 2. Adsorption Energies of the Ninth H Atom on TiC(001) on Different Sites as Shown in Figure 8[a]

E_{ads}^{H}	Kubas mode	Ti-top	subsurface
PBE	−1.94	−2.43	−1.12

[a]All values are given in eV.

Notice that such a situation favors the occupancy of Ti atoms by H atoms with respect to H_2 molecule in the gas phase, with an adsorption energy of −0.28 eV as obtained at the PBE-D3 level.

Another possibility to fill the surface is by direct molecular H_2 physisorption, once all surface C atoms are covered by H adatoms, thus achieving the H coverage of over 1 ML as found when exposing the sample to 1 Torr of H_2. To analyze this situation, four physisorbed H_2 molecules have been optimized on separated surface Ti atoms;[13] see Figure 9. These species

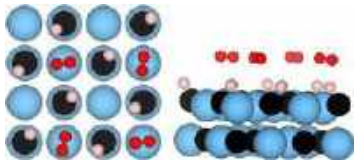

Figure 9. H_2 molecules physisorbed on surface Ti-top situations from top (left) and side (right) views. Blue balls represent Ti atoms, black balls are C atoms, and pink/red balls refer to H adatoms on the surface C-top or Ti-top H_2 physisorbed positions, respectively.

have a mean adsorption energy of −0.24 eV (PBE-D3) with respect to the H_2 reference and are located 2.89 Å above the surface plane, with an elongated H_2 bond length d(H−H) of 0.76 Å.

Altogether, the results allow us to provide an explanation of the experimental results. For the physisorbed H_2 molecules, using the Redhead equation, we estimate a TPD desorption range of 92−146 K, which is much lower than the temperature range examined in the experiments in Figure 1, 320−420 K. Thus, the very high coverages of hydrogen seen in the experiments at temperatures above 300 K cannot be generated on a perfect surface of TiC(001) and must be associated with the reconstruction of the carbide. The exact nature of this reconstruction is unknown and, according to the XPS results in Figure 2, it involves the formation of CH_x groups. In Figure 5, one can see the desorption peaks for H_2 at 325, 340, 365, and 405 K. The feature at 405 K is small and probably associated with the binding of hydrogen to the defect sites of TiC(001). As mentioned above, the peak at 325 K is linked to the reconstruction of the carbide surface. Thus, only the peaks at 340 and 365 K may be associated with the binding of hydrogen to an ideal TiC(001) surface. The calculations show that at small and medium coverages of H, there is a sequential population of C and Ti atoms. In qualitative terms, the peak at 365 K probably corresponds to the binding of H to C sites, whereas the peak at 340 K could involve binding of H to Ti sites. Our predicted desorption temperatures (212−325 K on Ti, 334−510 K on C), estimated using the calculated adsorption energies and the Redhead equation for limiting cases of pre-exponential factor of 10^{13}−10^{8}, respectively, can be somewhat smaller than the desorption temperatures in Figure 1, especially with the 10^{13} limit of the pre-exponential factor. This is expected due to the approximations in the DFT calculations and the Redhead equation. We note that, although our models provide insight into the relative static energetics of the hydrogen adsorption modes, in such a loosely bound and dynamic system, different adsorption situations can coexist and convert into each other, even in the course of the desorption process. Finally, the low-intensity peak appearing at about 400 K can be associated with the H atom adsorption on the defects on the surface such as steps or vacancies. In these positions, not considered here, the adsorption is assumed to be stronger and the peak height small due to the low concentration of defects.

The TPD assignments are further supported by the experimental C 1*s* XPS data shown in Figure 2, where a peak at 283 eV is visible when the clean surface is annealed at a temperature of 500 K, which indicates that the peak corresponds to Ti−C bonding. When the surface is exposed to H_2 under UHV conditions at 300 K, the TPD peaks at 365 and 340 K are observed to produce an extra feature in the C 1*s* XPS, with a small shift of 0.1−0.2 eV in the main peak. This result has been analyzed by estimating the core-level shift values obtained using the initial state model as well as the Janak−Slater model, as described in previous work.[40,41] The present estimates reveal that a C−H configuration has a C 1*s* binding energy only 0.27 eV higher than that of the bare surface C in the carbide, in agreement with the observed trend shown in the XPS measurements for low coverages of H on TiC(001). Thus, the extra peak near 283.5 eV in Figure 2 can be assigned to the CH_x groups on the basis of their binding energy,[36] and previously proposed as H_2 molecules trapped in the interstitial sites of the reconstructed TiC powders.[34,35] On a flat TiC(001) surface, we found a very low adsorption energy for H_2, but the C−H_2 species displayed a C 1s energy difference of 1.23 eV higher than that of the bare surface C atoms. Thus, in the future, when dealing with a reconstructed TiC(001), one must consider the possibility of H_2 bound inside or on the modified carbide lattice.

DOI: 10.1021/acs.jpcc.8b07340
J. Phys. Chem. C 2018, 122, 28013−28020

CONCLUSIONS

Here, we demonstrate, both experimentally and theoretically, that H_2 dissociation is possible on the TiC(001) surface. In addition, we reveal the nature of adsorbed H species once H_2 has been dissociated. First, the H_2 molecules are adsorbed on surface carbon atoms to form Kubas modes. Then, the H_2 molecule dissociates through a small energy barrier of 0.49 eV. The dissociated H atoms are adsorbed first on top of the C atoms on the surface. Once H atoms adsorb and occupy all the surface C atoms, further H atoms can be stabilized adsorbed on the surface Ti atoms. Moreover, H_2 molecules can be weakly adsorbed on the surface of titanium atoms, giving rise to a third type of adsorbed hydrogen. The sequence of occupation explains the TPD spectra at low coverage and is consistent with the XPS spectra, which show the existence of only one type of H_x species on the surface C atoms. A reconstruction of the TiC(001) surface makes possible the adsorption of large coverages of hydrogen. The present work provides a detailed description of the evolution of adsorbed H on TiC, which is likely to hold for other TMCs with the same M:C ratio.

ASSOCIATED CONTENT

Supporting Information

The Supporting Information is available free of charge on the ACS Publications website at DOI: 10.1021/acs.jpcc.8b07340.

Explored positions for H adsorption on the TiC(001) surface (Figure S1), H adsorption energies (Table S1), explored positions for H_2 adsorption on the TiC(001) surface (Figure S2), H_2 adsorption energies (Table S2), order of addition of hydrogen atoms on the TiC(001) surface (Figure S3), adsorption energies for different H atoms coverage (Tables S3 and S4) (PDF)

AUTHOR INFORMATION

Corresponding Authors

*E-mail: francesc.vines@ub.edu (F.V.).
*E-mail: rodrigez@bnl.gov (J.A.R.).

ORCID

Stefan T. Bromley: 0000-0002-7037-0475
Francesc Illas: 0000-0003-2104-6123
Francesc Viñes: 0000-0001-9987-8654
José A. Rodriguez: 0000-0002-5680-4214

Notes

The authors declare no competing financial interest.

ACKNOWLEDGMENTS

The research carried out at Brookhaven National Laboratory was supported by the U.S. Department of Energy, Office of Science and Office of Basic Energy Sciences under contract No. DE-SC0012704. P.J.R. is grateful for financial support by BID and EN-SCN. The work was supported by Spanish MINECO/FEDER Grant CTQ2015-64618-R and in part by Generalitat de Catalunya Grants 2017SGR13 and XRQTC and by the NOMAD Center of Excellence Project receiving funding from the European Union Horizon 2020 Research and Innovation Programme, Grant Agreement 676580. F.V. thanks the Spanish MINECO for a Ramón y Cajal research contract (RYC-2012-10129), F.I. acknowledges additional support through the ICREA Academia Award for Excellence in Research, and J.J.P. thanks the Spanish MINECO for ayuda para la formación de doctores contract (BES-2016-78816). Financial support from Spanish MICIUN through the Excellence María de Maeztu program (grant MDM-2017-0767) is fully acknowledged.

REFERENCES

(1) Kojima, I.; Miyazaki, E.; Inoue, Y.; Yasumori, I. Catalytic Activities of TiC, WC, and TaC for Hydrogenation of Ethylene. *J. Catal.* **1979**, *59*, 472−474.

(2) Fan, G.; Xiaojing, L.; Xu, C.; Jiang, W.; Zhang, Y.; Gao, D.; Bi, J.; Wang, Y. Palladium Supported on Titanium Carbide: A Highly Efficient, Durable, and Recyclable Bifunctional Catalyst for the Transformation of 4-Chlorophenol and 4-Nitrophenol. *Nanomaterials* **2018**, *8*, 141−154.

(3) Vidal, A. B.; Feria, L.; Evans, J.; Takahashi, Y.; Liu, P.; Nakamura, K.; Illas, F.; Rodriguez, J. A. CO_2 Activation and Methanol Synthesis on Novel Au/TiC and Cu/TiC Catalysts. *J. Phys. Chem. Lett.* **2012**, *3*, 2275−2280.

(4) Rodriguez, J. A.; Evans, J.; Feria, L.; Vidal, A. B.; Liu, P.; Nakamura, K.; Illas, F. CO_2 Hydrogenation on Au/TiC, Cu/TiC, and Ni/TiC Catalysts: Production of CO, Methanol, and Methane. *J. Catal.* **2013**, *307*, 162−169.

(5) Zhao, Y.; Dillon, A. C.; Kim, Y.; Heben, J.; Zhang, S. B. Self-Catalyzed Hydrogenation and Dihydrogen Adsorption on Titanium Carbide Nanoparticles. *Chem. Phys. Lett.* **2006**, *425*, 273−277.

(6) Nguyen, J.; Glandut, N.; Jaoul, C.; Lefort, P. Electrochemical Hydrogen Insertion in Substoichiometric Titanium Carbide $TiC_{0.6}$: Influence of Carbon Vacancy Ordering. *Langmuir* **2013**, *29*, 12036−12042.

(7) Nguyen, J.; Glandut, N.; Jaoul, C.; Lefort, P. Hydrogen Insertion in Substoichiometric Titanium Carbide. *Int. J. Hydrogen Energy* **2015**, *40*, 8562−8570.

(8) Khidirov, I. Neutron Diffraction Study of Titanium Carbide TiC_x Prepared from Hydrogen-Containing Titanium Powder. *Russ. J. Inorg. Chem.* **2015**, *60*, 1263−1266.

(9) Osti, N. C.; Naguib, M.; Tyagi, M.; Gogotsi, Y.; Kolesnikov, A. I.; Mamontov, E. Evidence of Molecular Hydrogen Trapped in Two-Dimensional Layered Titanium Carbide-Based MXene. *Phys. Rev. Mater.* **2017**, *1*, No. 024004.

(10) Jimenez-Orozco, C.; Florez, E.; Moreno, A.; Liu, P.; Rodriguez, J. A. Systematic Theoretical Study of Ethylene Adsorption on δ-MoC(001), TiC(001), and ZrC(001) Surfaces. *J. Phys. Chem. C* **2016**, *120*, 13531−13540.

(11) Estreicher, S. K.; McAfee, J. L.; Fedders, P. A.; Pruneda, J. M.; Ordejón, P. The Strange Behavior of Interstitial H_2 Molecules Si and GaAs. *Phys. B* **2001**, *308*−*310*, 202−205.

(12) Costanzo, F.; Silvestrelli, P. L.; Ancilotto, F. Physisorption, Diffusion, and Chemisorption Pathways of H_2 Molecule on Graphene and on (2,2) Carbon Nanotube by First Principles Calculations. *J. Chem. Theory Comput.* **2012**, *8*, 1288−1294.

(13) Florez, E.; Gomez, T.; Liu, P.; Rodriguez, J. A.; Illas, F. Hydrogenation Reactions on Au/TiC(001): Effects of Au-C Interactions on the Dissociation of H_2. *ChemCatChem* **2010**, *2*, 1219−1222.

(14) Skipper, C. V. J.; Hamaed, A.; Antonelli, D. M.; Kaltsoyannis, N. The Kubas Interaction in M(II) (M = Ti, V, Cr) Hydrazine-Based Hydrogen Storage Materials: a DFT Study. *Dalton Trans.* **2012**, *41*, 8515−8523.

(15) Posada-Pérez, S.; Viñes, F.; Valero, R.; Rodriguez, J. A.; Illas, F. Adsorption and Dissociation of Molecular Hydrogen on Orthorhombic β-Mo_2C and Cubic δ-MoC (001) Surfaces. *Surf. Sci.* **2017**, *656*, 24−32.

(16) Ding, H.; Fan, X.; Li, C.; Liu, X.; Jiang, D.; Wang, C. First-Principles Study of Hydrogen Storage in non-Stochiometric TiC_x. *J. Alloys Compd.* **2013**, *551*, 67−71.

(17) Ding, H.; Fan, X.; Chu, K.; Du, B.; Wang, J. The Influence of Stacking Faults on Hydrogen Storage in TiC_x. *Int. J. Hydrogen Energy* **2014**, *39*, 9262−9266.

DOI: 10.1021/acs.jpcc.8b07340
J. Phys. Chem. C 2018, 122, 28013−28020

(18) Hagen, J. *Industrial Catalysis: A Practical Approach*; Wiley-VCH Verlag GmbH & Co: Weinheim, Germany, 2015.
(19) Spielmann, J.; Buch, F.; Harder, S. Early Main-Group Metal Catalysts for the Hydrogenation of Alkenes with H_2. *Angew. Chem.* **2008**, *120*, 9576−9580.
(20) Rodriguez, J. A.; Liu, P.; Takahashi, Y.; Nakamura, K.; Viñes, F.; Illas, F. Desulfurization of Thiophene on Au/TiC(001): Au-C Interactions and Charge Polarization. *J. Am. Chem. Soc.* **2009**, *131*, 8595−8602.
(21) Frantz, P.; Didziulis, S. V. Detailed Spectroscopic Studies of Oxygen on Metal Carbide Surfaces. *Surf. Sci.* **1998**, *412*−*413*, 384−396.
(22) Rodriguez, J. A.; Liu, P.; Dvorak, J.; Jirsak, T.; Gomes, J.; Takahashi, Y.; Nakamura, K. The Interaction of Oxygen with TiC(001): Photoemission and First-Principles Studies. *J. Chem. Phys.* **2004**, *121*, 465−474.
(23) Christmann, K.; Ertl, G.; Pignet, T. Adsorption of Hydrogen on a Pt(111) Surface. *Surf. Sci.* **1976**, *54*, 365−392.
(24) Quesne, M. G.; Roldan, A.; Leeuw, N. H.; Catlow, C. R. A. Bulk and Surface Properties of Metal Carbides: Implications for Catalysis. *Phys. Chem. Chem. Phys.* **2018**, *20*, 6905−6916.
(25) Kunkel, C.; Viñes, F.; Illas, F. Transition Metal Carbides as Novel Materials for CO_2 Capture, Storage, and Activation. *Energy Environ. Sci.* **2016**, *9*, 141−144.
(26) Kresse, G.; Furthmüller, J. Efficient Iterative Schemes for Ab Initio Total Energy Calculations Using a Plane-Wave Basis Set. *Phys. Rev. B* **1996**, *54*, 11169−11186.
(27) Perdew, J. P.; Burke, K.; Ernzerhof, M. Generalized Gradient Approximation Made Simple. *Phys. Rev. Lett.* **1996**, *77*, 3865−3868.
(28) Grimme, S.; Antony, J.; Ehrlich, S.; Krieg, S. A Consistent and Accurate Ab Initio Parametrization of Density Functional Dispersion Correction (DFT-D) for the 94 Elements H-Pu. *J. Chem. Phys.* **2010**, *132*, No. 154104.
(29) Blöchl, P. E. Projector Augmented-Wave Method. *Phys. Rev. B* **1994**, *50*, 17953.
(30) Kresse, G.; Joubert, D. From Ultrasoft Pseudopotentials to the Projector Augmented-Wave Method. *Phys. Rev. B* **1999**, *59*, 1758.
(31) Monkhorst, H. J.; Pack, J. D. Special Points for Brillouin-Zone Integrations. *Phys. Rev. B* **1976**, *13*, 5188.
(32) Henkelman, G.; Uberuaga, B. P.; Jónsson, H. A Climbing Image Nudged Elastic Band Method for Finding Saddle Points and Minimum Energy Paths. *J. Chem. Phys.* **2000**, *113*, 9901.
(33) Reuter, K.; Scheffler, M. First-Principles Kinetic Monte Carlo Simulations for Heterogeneous Catalysis: Application to the CO Oxidation at RuO_2(110). *Phys. Rev. B* **2006**, *73*, No. 045433.
(34) Reuter, K.; Frenkel, D.; Scheffler, M. The Steady State of Heterogeneous Catalysis, Studied by First-Principles Statistical Mechanics. *Phys. Rev. Lett.* **2004**, *93*, No. 116105.
(35) Redhead, P. A. Thermal Desorption of Gases. *Vacuum* **1962**, *12*, 203−211.
(36) Pérez Escobar, D.; Wallaert, E.; Duprez, L.; Atrens, A.; Verbeken, K. Thermal Desorption Spectroscopy Study of the Interaction of Hydrogen with TiC Precipitates. *Met. Mater. Int.* **2013**, *19*, 741−748.
(37) Wei, F. G.; Tsuzaki, K. Quantitative Analysis on Hydrogen Trapping of TiC Particles in Steel. *Metall. Mater. Trans. A* **2006**, *37*, 331−353.
(38) Rodriguez, J. A.; Dvorak, J.; Jirsak, T. Chemistry of Thiophene on Mo(110), MoC_x and MoS_x Surfaces: Photoemission Studies. *Surf. Sci.* **2000**, *457*, L413−L420.
(39) Tsuzuki, S.; Lüthi, H. P. Interaction Energies of Van der Waals and Hydrogen Bonded Systems Calculated Using Density Functional Theory: Assessing the PW91 Model. *J. Chem. Phys.* **2001**, *114*, 3949−3957.
(40) Kunkel, C.; Viñes, F.; Ramírez, P. J.; Rodriguez, J. A.; Illas, F. Combining Theory and Experiment for Multitechnique Characterization of Activated CO_2 on Transition Metal Carbide (001) Surfaces. *J. Phys. Chem. C* **2018**, DOI: 10.1021/acs.jpcc.7b12227.
(41) Viñes, F.; Sousa, C.; Illas, F. On the Prediction of Core Level Binding Energies in Molecules, Surfaces and Solids. *Phys. Chem. Chem. Phys.* **2018**, *20*, 8403−8410.

DOI: 10.1021/acs.jpcc.8b07340
J. Phys. Chem. C 2018, 122, 28013−28020

3.11. References

1. I. Kojima, E. Miyazaki, Y. Inoue, and I. Yasumori. Catalytic activities of TiC, WC, and TaC for hydrogenation of ethylene. *J. Catal.*, **1979**, 59, *3*, 472–474.
2. G. Fan, X. Li, C. Xu, W. Jiang, Y. Zhang, J. Bi, and Y. Wang. Palladium Supported on Titanium Carbide: A Highly Efficient, Durable, and Recyclable Bifunctional Catalyst for the Transformation of 4-Chlorophenol and 4-Nitrophenol. *Nanomaterials*, **2018**, 8, *3*, 141.

3. A.B. Vidal, L. Feria, J. Evans, Y. Takahashi, P. Liu, K. Nakamura, F. Illas, and J.A. Rodriguez. CO_2 Activation and Methanol Synthesis on Novel Au/TiC and Cu/TiC Catalysts. *J. Phys. Chem. Lett.*, **2012**, 3, *16*, 2275–2280.
4. J.A. Rodriguez, J. Evans, L. Feria, A.B. Vidal AB, P. Liu, K. Nakamura, and F. Illas. CO_2 hydrogenation on Au/TiC , Cu/TiC , and Ni/TiC catalysts : Production of CO, methanol , and methane. *J. Catal.*, **2013**, 307, 162-169.
5. Y. Zhao, A.C. Dillon, Y. Kim, M.J. Heben, and S.B. Zhang. Self-catalyzed hydrogenation and dihydrogen adsorption on titanium carbide nanoparticles. *Chem. Phys. Lett.*, **2006**, 425 ,273–277.
6. J. Nguyen, N. Glandut, C. Joaul, and P. Lefort. Electrochemical Hydrogen Insertion in SubstoichiometricTitanium Carbide $TiC_{0.6}$: Influence of Carbon Vacancy Ordering. *Langmuir*, **2013**, 29, *38*, 12036–12042.
7. J. Nguyen, N. Glandut, C. Joaul, and P. Lefort. Hydrogen insertion in substoichiometric titanium carbide. *Int. J. Hydrog. Energy*, **2015**, 40, *27*, 8562-8570.
8. I. Khidirov. Neutron Diffraction Study of Titanium Carbide TiC_x Prepared from Hydrogen Containing Titanium Powder. *Russ. J. Inorg. Chem.*, **2015**, 60, *10*, 1381–1384.
9 N.C. Osti, M. Naguib, M. Tyagi, Y. Gogotsi, A.I. Kolesnikov, and E. Mamontov. Evidence of molecular hydrogen trapped in two-dimensional layered titanium carbide-based MXene. *Phys. Rev. Materials*, **2017**, 1, 024004.
10. S.K. Estreicher, J.L. McAfee, P.A. Fedders, J.M. Pruneda, and P. Ordejón. The strange behavior of interstitial H_2 molecules Si and GaAs. *Phys B Condens Matter.*, **2001**; 308–310, 202–205.
11. F. Costanzo, P.L. Silvestrelli, and F. Ancilotto. Physisorption, diffusion, and chemisorption pathways of H_2 molecule on graphene and on (2,2) carbon nanotube by first principles calculations. *J. Chem. Theory Comput*., **2012**, 8, *4*, 1288–1294.
12. C.V.J. Skipper, A. Hamaed, D.M. Antonelli, and N. Kaltsoyannis. The Kubas interaction in M(II) (M = Ti, V, Cr) hydrazine-based hydrogen storage materials: a DFT study. *Dalt Trans.*, **2012**, 41, *28*, 8515–8523.
13. E. Florez, T. Gomez, P. Liu, J.A. Rodriguez, and F. Illas. Hydrogenation reactions on Au/TiC(001): Effects of Au-C interactions on the dissociation of H_2. *ChemCatChem.*, **2010**, 2, *10*, 1219–1222.
14. S. Posada-pérez, F. Viñes, and R. Valero. Adsorption and dissociation of molecular hydrogen on orthorhombic β-Mo_2C and cubic δ-MoC (001) surfaces. *Surf Sci*, **2017**, 656, 24–32.
15. G. Kresse and J. Furthmüller. Efficient iterative schemes for ab initio total-energy calculations using a plane-wave basis set. *Phys Rev B.*, **1996**; 54, *16*, 11169–11186.
16. J.P. Perdew, K. Burke, and M. Ernzerhof. Generalized gradient approximation made simple. *Phys Rev Lett.*, **1996**, 77, *18*, 3865–3868.
17. S. Grimme, J. Antony, S. Ehrlich, and H. Krieg H. A consistent and accurate ab initio parametrization of density functional dispersion correction (DFT-D) for the 94 elements H-Pu. *J. Chem. Phys.*, **2010**, 132, 154104.
18. G. Henkelman and H. Jónsson H. A dimer method for finding saddle points on high dimensional potential surfaces using only first derivatives. *J Chem Phys*., **1999**; 111, *15*, 7010–7022.
19. G. Henkelman and H. Jónsson. Improved tangent estimate in the nudged elastic band method for finding minimum energy paths and saddle points. *J Chem Phys.*, **2000**, 113, *22*, 9978–9985.
20. G.J. Kubas. Dihydrogen complexes as prototypes for the coordination chemistry of saturated molecules. *PNAS*, **2007**, 104, *17*,6901-6907.
21. G. Herzberg. The dissociation energy of the hydrogen molecule. *J. Mol. Spectrosc.*, **1970**, 33, *1*, 147–68.
22. J.J. Piñero, P.J. Ramírez, S.T. Bromley,F. Illas, F. Viñes, and J.A. Rodriguez. Diversity of Adsorbed Hydrogen on the TiC(001) Surface at High Coverages. *J. Phys. Chem.* C., **2018**, 122, *49*, 28013–28020.

23. J.A. Rodriguez, P. Liu, Y. Takahashi, K. Nakamura, F. Viñes, and F. Illas. Desulfurization of Thiophene on Au/TiC (001): Au-C Interactions and Charge Polarization. *J. Am. Chem. Soc.*, **2009**, 131, *24*, 8595–8602.

Chapter 4

H_2 adsorption and dissociation on TMCs (001) surfaces

4. H_2 adsorption and dissociation on TMCs (001) surfaces

4.1. Introduction

In the previous Chapter it was mentioned that titanium carbide (TiC) is an attracting a lot of interest in field ranging through catalysis, solid-state chemistry, and materials science. This wide-ranging importance is confirmed by the many studies that have been and are being carried out on this material. TiC, despite being one of the most studied TMC, is one example of a family of materials that have also aroused scientific attention. In the literature, there are an increasing number of publications on various properties of these TMCs, such as the electronic structure[1,2] and electrical conductivity,[3] among other properties.[4,5] Most relevant to this Thesis are the various adsorption studies on different TMCs such as: adsorption of molecular hydrogen,[6] molecular oxygen,[7] carbon monoxide,[8,9] carbon dioxide ,[10] methane,[11,12] ethylene,[13,14] among many other compounds. These studies have been carried out on all TMCs of the early transitions metals in groups IV-VI as for example the Ethylene Hydrogen on TaC.[15]

Similarly to what was reported for TiC (001) in Chapter 3, in this chapter we address the possible H_2 adsorption sites and the eventual dissociation of H_2 into two H adatoms on another six different TMCs: ZrC, HfC, VC, NbC, TaC, and δ-MoC - the rocksalt polymorph of MoC. The methodology followed is exactly the same as the one employed in Chapter 3, including the generation of surface slab models, and so, we refer to it for details. Notice that H_2 adsorption and dissociation has been regarded only at low coverage, avoiding the influence of lateral inter-hydrogen interactions. All DFT calculations have been performed at the PBE[16] and PBE-D3[17] level. For finding TS states we employed the CI-NEB[18] methods for PBE calculations and the Dimer[19] method where D3 corrections were implemented.

This work has served as the basis for the communication published in "**Chemical Communications** under the name **Assessing the usefulness of transition metal carbides for hydrogenation reactions"**, 2019, 55, 12797.

4.2. H absorption

Before addressing H_2 adsorption and dissociation, atomic H adsorption and absorption has been explored. Table 4.1 summarizes the calculated E_{ads} and E_{abs} values on the seven explored TMCs, at the PBE level (i.e. not considering dispersive forces). Notice that, systematically, H prefers to adsorb on C-Top positions, except for TaC, which prefers Ta-Top. The absorption situations, on the four-fold hollow site, are systematically less favourable, by at least, 1 eV. In the case of δ-MoC, no energy minimum was found for H absorption, as the H emerged to be on the surface. Due to its relatively low energetic satbilty H absorption is not considered further in the remainder of this chapter.

Table 4.1. Adsorption (E_{ads}) and absorption (E_{abs}) energies for all TMC (001) surfaces. PBE estimates are given in eV.

	TiC	VC	ZrC	NbC	δ-MoC	HfC	TaC
E_{ads}	-2.73	-2.13	-2.83	-2.01	-2.93	-2.77	-2.30
E_{abs}	-1.66	-0.55	-1.90	-0.55	-2.78	-1.75	-0.43

4.3. H adsorption.

In this section different H adatoms are investigated at a nominal coverage of 0.125 eV. The H E_{ads} values, obtained at a PBE-D3 level, are listed in Table 4.2. Notice that energetic contribution E_{ads} due to dispersive interactions, again, is marginal, (ranging between -0.01 (δ-MoC) and -0.13 eV (VC)).

Table 4.2. H E_{ads} values, in eV, obtained at a PBE-D3 level on TMCs (001) surfaces.

	TiC	VC	ZrC	NbC	δ-MoC	HfC	TaC
E_{ads}	-2.83	-2.26	-2.91	-2.05	-2.94	-2.84	-2.35

Since δ-MoC, aside from TiC, are one of the most popular carbides used in catalysis, a further work was carried out to study the E_{ads} trend with increasing H coverage, mimicking that of TiC in Chapter 3. Figure 3.8 shows the evolution of E_{ads} on δ-MoC compared to TiC. An important difference between both is that even if E_{ads} in δ-MoC decreases a little, it has a fairly constant value, particular from the fourth H onwards, at variance with TiC, where there is a gradual reduction in the magnitude of the E_{ads}. Test calculations on the possible absorption at high coverage revealed E_{abs} values smaller than E_{ads} by more than 1.5 eV. Thus, in general terms, H adsorption is quite similar in between TiC and δ-MoC, except for the fact that the C-H bond strength is less affected by the coverage in the latter system.

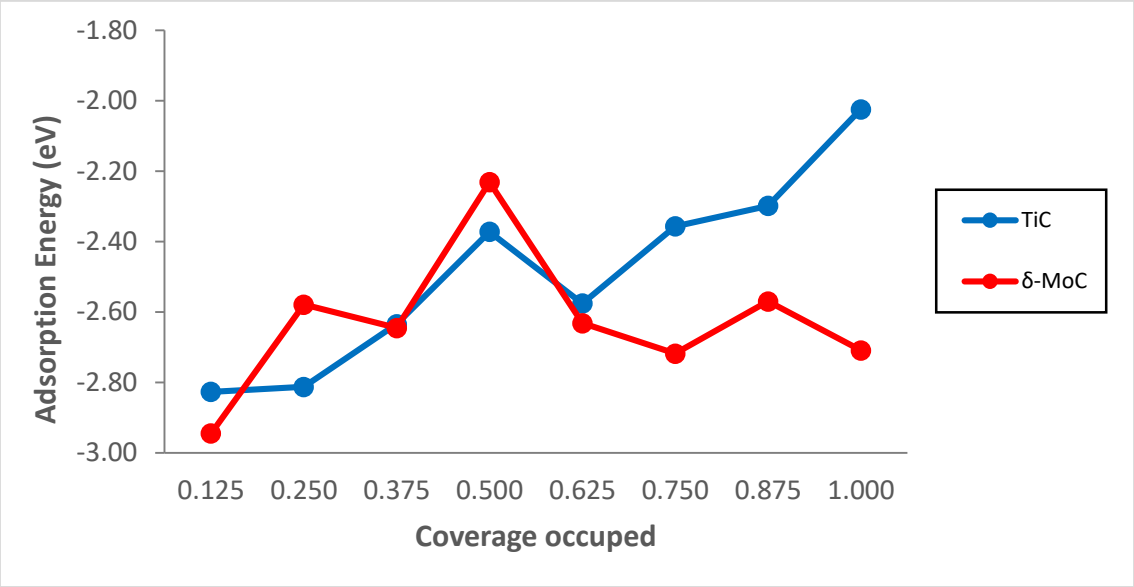

Figure 4.1. E_{ads} evolution as a function of the number of H atoms, for both TiC and δ-MoC.

4.4. H_2 adsorption

H_2 adsorption was studied similarly as for the TiC (001) surface, but, instead of exploring the 19 different situations, only the six most stable sites were studied for the rest of TMCs. The respective calculated E_{ads} values are reported in Table 4.3. The results show that the most energetically favourable position to adsorb H_2 is position 13, which is C-Top with H atoms pointing to vicinal C surface sites. There, the H_2 is found to be partially dissociated (d_{H-H}= 1.60 Å, i.e. a *Kubas* mode). A similar distance is obtained on position 8, which is again C-Top, but now with H atoms pointing towards vicinal Ti surface atoms. From this data, it seems that the most favourable TMC for adsorption and subsequent dissociation of H_2 is δ-MoC.

Table 4.3. H_2 adsorption values, E_{ads}, in eV, obtained by PBE-D3 calculations on different TMC (001) surfaces.

Site	TiC	VC	ZrC	NbC	δ-MoC	HfC	TaC
1	-0.21	-0.09	-0.07	-0.07	-0.10	-0.07	-0.08
7	-0.21	-0.19	-0.20	-018	-0.15	-0.21	-0.25
8	-0.41	0.03	-0.51	0.06	-0.86	-0.26	0.36
10	-0.21	-0.19	-0.20	-0.18	-0.55	-0.21	-0.25
12	-0.20	-0.19	-0.20	-0.18	-0.15	0.21	-0.25
13	-0.66	0.04	-0.77	0.02	-1.27	-0.57	0.33

The results obtained with vdW interactions are essentially the same to those without vdW interactions, although some sites become slightly more energetically favourable (by <0.05 eV) with vdW interactions.

In addition, *Kubas* modes are exhibited for all TMCs except in TaC, where this mode adsorption has not been found. This adsorption mode is the energetically most favourable for the TMC of group IV and δ-MoC. In the rest of TMC of group V, the *Kubas* modes exits but it is not the most favourable adsorption.

4.5. H_2 dissociation on TMCs (001) surfaces

As done for TiC in Chapter 3, the first step of H_2 dissociation has been evaluating the final dissociated state, with two vicinal H adatoms on C-top sites (Ta-top sites for TaC). The final energy states with respect H_2 in vacuum have been identified, and the H_2 dissociation energies are listed in Table 4.4, revealing that H_2 dissociation is generally exothermic, except for group V TMCs (VC, NbC, and TaC), where it is basically isoenergetic, or slightly endothermic, as found in the case of NbC.

Table 4.4. Estimated energy values of the H_2 dissociation, gained PBE-D3 and given in eV.

E_{diss} (eV)	TiC	VC	ZrC	NbC	δ-MoC	HfC	TaC
PBE-D3	-1.12	0.01	-1.29	0.43	-1.36	-1.15	-0.16

Having defined the initial and final states of H_2 dissociation, the TS of the process have been acquired either using CI-NEB or Dimer methodologies. Thus, a reaction energy profile is found for each TMC; see example in Figure 4.2 for ZrC (001), departing from H_2 C-Top in a *Kubas* mode, with an energy barrier of 0.72 eV.

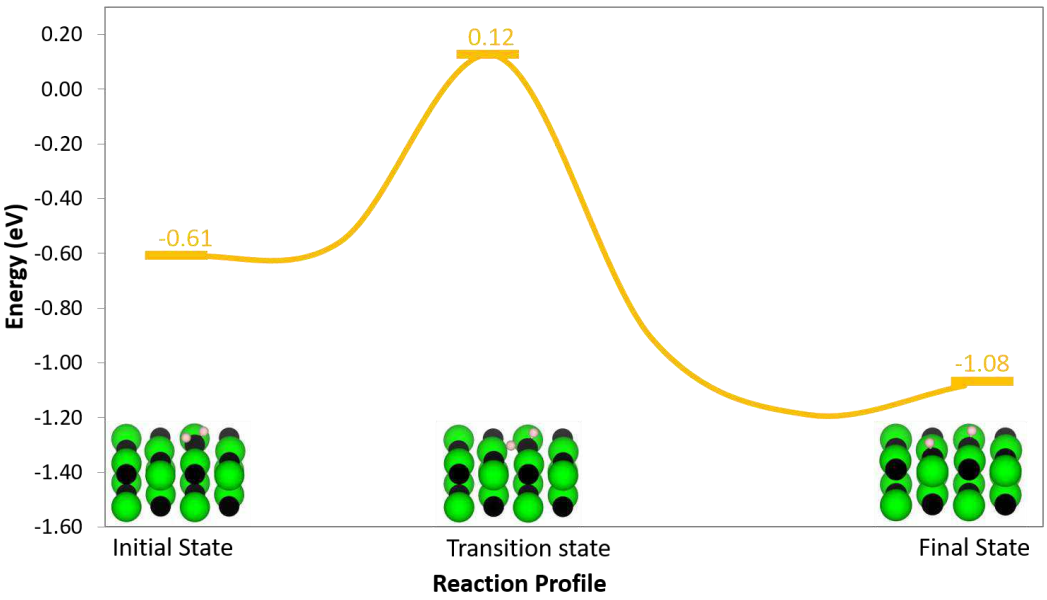

Figure 4.2. H_2 dissociation energy profile.

A summary of the barriers calculated at the PBE-D3 level and considering ZPE is found in Table 4.5, and the overall profiles shown in Figure 4.3.

Table 4.5. H_2 dissociation energy barriers, E_b, calculated at a PBE-D3 level including ZPE, given in eV.

	TiC	VC	ZrC	NbC	δ-MoC	HfC	TaC
E_b (eV)	0.35	1.08	0.59	0.86	0.90	0.46	1.11

The results show two types of TMCs concerning H_2 adsorption; group IV and V TMCs show H_2 E_{ads} that are moderate, up to -0.36 eV (HfC), with the sole exception of δ-MoC, where a stronger adsorption of -0.85 eV is found. When it comes to the H_2 dissociation, group IV TMCs feature an exothermic process, see above, while group V TMCs (VC, NbC, and TaC) and δ-MoC feature it as an isoenergetic process (NbC and δ-MoC) or slightly endothermic (VC and TaC). This directly affects the energy barriers, which are of about 1 eV for such cases, and much smaller (below 0.6 eV) for group IV TMCs, see Figure 4.3.

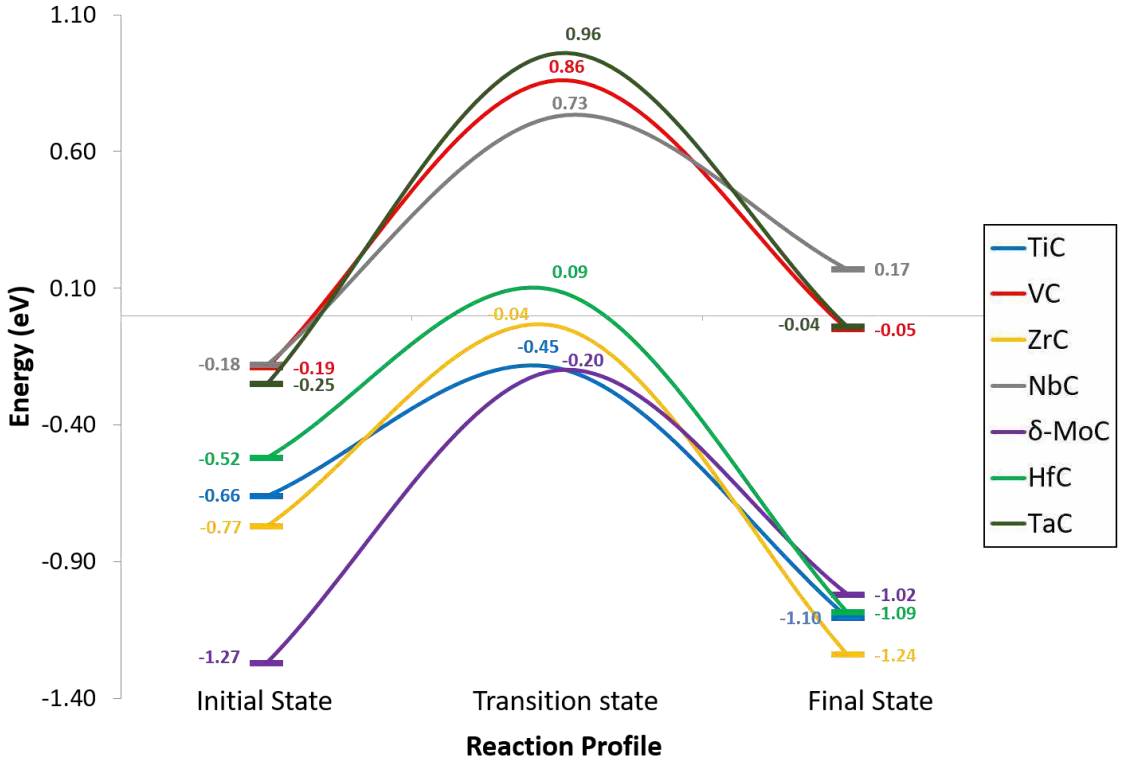

Figure 4.3. H_2 adsorption and dissociation reaction energy profiles calculated at a PBE-D3 level for all the studied TMC (001) surfaces.

4.6. Conclusions

The main conclusions of this Chapter are described below. The first one is that H_2 molecules preferably physisorb on C-Top sites for Group IV TMCs and δ-MoC, but on M-Top for group V TMCs (VC, NbC, and TaC). When a H_2 molecule adsorbs on C-Top, the H_2 molecule adopts a *Kubas* mode adsorption, where the H_2 bond is slightly elongated. Once adsorbed, the H_2 molecule is thermodynamically driven to dissociate on group IV TMCs (TiC, ZrC, and HfC), where H adatoms occupy vicinal C-Top sites, and, in all cases, the H_2 dissociation energy barriers are easily

surmountable, being, at most, of the order of *ca.* 0.60 eV. On Group V TMCs, the physisorption and the generally endothermic dissociation step is translated into somewhat larger E_b values, of *ca.* 1 eV, making it more difficult to have H adatoms on the surface. Finally, δ-MoC features a strong H_2 adsorption, but a somewhat high E_b value of 0.90 eV, making it a viable hydrogenating catalyst, but at temperatures large enough so as to overcome this reaction step energy barrier.

4.7. Publication

ChemComm

COMMUNICATION

View Article Online
View Journal | View Issue

Cite this: *Chem. Commun.*, 2019, **55**, 12797

Received 8th August 2019,
Accepted 30th September 2019

DOI: 10.1039/c9cc06084g

rsc.li/chemcomm

Assessing the usefulness of transition metal carbides for hydrogenation reactions†

Hector Prats, [a] Juan José Piñero,[a] Francesc Viñes, *[a] Stefan T. Bromley, [ab] Ramón Sayós [a] and Francesc Illas [a]

Transition Metal Carbides (TMCs) are proposed as replacements for and expensive late Transition Metals (TMs) as heterogeneous catalysts, often implying hydrogenation reactions or steps. Present density functional theory based calculations support using group IV TMCs and δ-MoC as viable TM alternatives, given the moderate exoergicity and affordable reaction step energy barriers.

Transition Metal Carbides (TMCs) have been attracting much interest over the last few decades for diverse technological applications in many fields, including heterogeneous catalysis, solid state chemistry, and materials science.[1–5] A primary reason for this attention is the unique combination of physicochemical properties arising from the different degrees of ionic/covalent/metallic bonding exhibited in TMCs. In addition, some TMCs display catalytic activities that are similar to, or even better than those of noble and Pt-group metals[6] for a considerable number of reactions including alkene hydrogenation,[4,7] ammonia synthesis *via* the Haber–Bosch process,[8] the water gas shift reaction,[9] methanol synthesis from CO_2,[10] fossil fuel refinement,[11] and the production of other diverse chemicals compounds.[12] Most of the aforementioned reactions have in common that they imply elementary hydrogenation steps which, to be carried out in an efficient fashion, require highly active and mobile (available) hydrogen atoms to be present on the TMC catalyst surface.

Hence, factors such as the types of hydrogen species and their stabilities play a central role in such hydrogenation reactions, ultimately determining the catalyst performance. Previous literature on the interaction of H_2 on materials point for to the presence of diverse atomically chemisorbed H species,[3,4] although other studies highlight the stability of molecularly physisorbed H_2,[13] surface Kubas H_2 structures (*i.e.*, chemisorbed H_2 with an elongated bond),[14,15] as well as H moieties present in the bulk, placed in defects or at interstitials.[16] This blend of situations seems to back up a rich adsorptive landscape of H_2 on TMC surfaces, but, regardless of its central role in a plethora of catalyzed reactions, the adsorption, desorption, dissociation, Kubas formation, and H and H_2 mobilities on TMCs remain hitherto understudied, and consequently, poorly understood. Note that the present study focuses in heterogeneous catalysis applications, although the results can be of guidance for TMCs utilization as electrocatalysts for the Hydrogen Evolution Reaction (HER).[17]

Herein, we supply this necessary and lacking knowledge cornerstone by a thorough Density Functional Theory (DFT) based computational study of the interaction of atomic (H) and molecular (H_2) hydrogen species on seven rocksalt TMCs. Their (001) surface has been considered, as previous studies have already demonstrated that this surface is the most stable.[6] By considering a very wide range of molecular and atomic adsorption scenarios, we are able to establish the most energetically favorable H_2 adsorption sites and dissociation pathways. The DFT based calculations have been carried out using the Perdew–Burke–Ernzerhof (PBE)[18] exchange–correlation functional with the contribution of dispersion terms added through the D3 approach, as proposed by Grimme *et al.* (PBE-D3).[19] The system total energy has been obtained by self consistently solving the Kohn–Sham equations with the valence electron density expanded in a plane wave basis set of 415 eV of kinetic energy limit, and using periodic slab surface models. The Vienna *Ab Initio* Simulation Package (VASP) code has been used for all the optimizations.[20] All other necessary computational details are provided in the ESI.† This computational approach has been proven to be accurate when correlating simulations with experimental data on a number of de/hydrogenation reactions and/or interaction of H or H_2 interactions with TMC-based catalysts.[4,5,21,25,27]

The H_2 dissociation Transition States (TSs) have been located through the Climbing-Image Nudged Elastic Band (CI-NEB) method,[22] employing five intermediate images between reactants—initial state—and products—final state. These images were generated using the Atomic Simulation Environment (ASE)[23]

[a] *Departament de Ciència dels Materials i Química Física & Institut de Química Teòrica i Computacional (IQTCUB), Universitat de Barcelona, c/Martí i Franquès 1–11, 08028 Barcelona, Spain. E-mail: francesc.vines@ub.edu*
[b] *Institució Catalana de Recerca i Estudis Avançats (ICREA), Passeig de Lluís Companys 23, 08010 Barcelona, Spain*

† Electronic supplementary information (ESI) available. See DOI: 10.1039/c9cc06084g

This journal is © The Royal Society of Chemistry 2019

Table 1 Calculated adsorption energy values (ΔE_{ads}) for H_2, H, and $H_{2,Kubas}$ on the (001) surface of the studied TMCs. All values include the ZPE term

	ΔE_{ads} (eV)						
Site	TiC	ZrC	HfC	VC	NbC	TaC	δ-MoC
$H_2^{*(top-M)}$	−0.10	−0.11	−0.11	−0.05	−0.06	−0.13	−0.42
$H_2^{*(top-C)}$	−0.05	−0.04	−0.04	−0.04	−0.01	−0.05	−0.60
$H^{*(top-M)}$	1.51	1.33	1.20	0.60	0.35	−0.06	0.21
$H^{*(top-C)}$	−0.52	−0.61	−0.54	0.10	0.18	0.17	−0.55
$H_{2,Kubas}^{*(top-C)}$	−0.40	−0.51	−0.26	0.24	0.26	0.47	−0.98

and applying the Image Dependent Pair Potential (IDPP) procedure.[24] The gained TSs were characterized by frequency analysis ensuring they exhibit only one imaginary frequency. Note that favourable adsorption energies, ΔE_{ads}, are defined here negative, and, so, the more negative the ΔE_{ads}, the stronger the bonding. All reported energy values include the Zero Point Energy (ZPE) term, with frequencies estimated within the harmonic approximation.

The H_2 molecular adsorption on each TMC (001) surface has been exhaustively sampled by considering three molecular conformations on the different high-symmetry, non-equivalent sites over the TMC surfaces. The results show that the H_2 molecule ends up being physisorbed on top of either a surface metal atom (top-M) or a surface C atom (top-C), with top-M being the preferred site in almost all the studied TMCs, see Table 1. The physisorption energy values range −0.01 to −0.13 eV, thus, mostly due to dispersive forces between H_2 and the TMC surfaces; see ΔE_{ads} gained only at PBE level in Table S1 of the ESI.† The δ-MoC behaves different than the other TMCs, with a stronger adsorption of the H_2 molecule on both top-M and top-C adsorption sites; the latter being the most stable one, with an ΔE_{ads} of −0.60 eV. The Kubas mode for adsorbed H_2, previously described in the literature for a number of the TMCs studied herein,[14,25–27] corresponds to an almost dissociated H_2 molecular state where both atomic H species are adsorbed on the same C atom, with H_2 bond lengths ranging 1.68 to 1.80 Å, see Table S2 of the ESI,† and having a non-negligible interaction between them, estimated to be in between −0.55 to −0.92 eV, see Table S2 of the ESI.†

The adsorption energies reported in Table 1 show that the formation of the Kubas mode is actually thermodynamically favorable on group IV TMCs and δ-MoC, with adsorption energies stronger than those of molecular H_2 adsorption on top-C or top-M, yet Kubas H_2 is not thermodynamically favored on group V TMCs. Interestingly, on TaC and δ-MoC(001) surfaces the Kubas H_2 leads to an elevation of the surface carbon atom, resulting in a final structure resembling a CH_2 species adsorbed on a C-vacancy site, see Fig. S1 of the ESI.† However, the strong interaction of surface C atoms with neighbouring surface metal atoms[28] prevents considering the CH_2 group as a carbene-type intermediate. Furthermore, although the formation of such H_2 Kubas modes is typically assumed to be barrierless in the literature,[14,25–27] we found that it actually involves a high energy barrier, as later discussed. Note that, in order to establish the existence of a Kubas formation barrier, one should first indeed find a stable physisorbed H_2 state. However, finding this physisorbed site is elusive and very sensitive to the initial conditions of the geometry optimization; for instance, the H_2 adsorbed on top-C requires an initial guess with the H_2 molecule at least at 1.50 Å above the C atom, and when initial conditions had the H_2 closer to the surface, the adsorption directly evolved to the Kubas mode, giving the wrong impression that the process is non-activated. This could well be the reason why this barrier was not found in previous studies in the literature, yet it is crucial for providing a correct description of the ability of TMC surfaces to adsorb and dissociate H_2, *vide infra*.

Atomic H adsorption was also studied considering six different non-equivalent sites on the TMC surfaces. Results show that, once again, top-M and top-C are the only stable adsorption sites for H adatoms, with top-C being the preferred site on all TMCs with ΔE_{ads}, when stable, ranging from −0.52 eV to −0.61 eV. The sole exception to this is TaC, for which the top-M site is energetically preferred, see Table 1, thus introducing itself as an appealing hydrogenating catalyst whenever the target molecule prefers to interact with a surface C atom. An interesting feature along group IV TMCs compared to group V is that the former leads to a much stronger adsorption of H on top-C compared to top-M sites, which in turn yields ΔE_{ads} differences between sites of up to 2.03 eV on TiC, while this difference reduces to solely 0.17 eV in NbC. Results for atomic H adsorption also confirm a behaviour of δ-MoC similar to group IV with respect to ΔE_{ads} values on top-C and top-M sites, respectively, but with a reduced difference of ΔE_{ads} between sites of 0.76 eV. The effect of an adsorbed H on other adsorbed species is expected to be negligible, as both experimentally and theoretically proven on metallic surface systems.[29,30] The optimized geometries for H_2 and H adsorption on all the studied TMC surfaces are shown in Fig. S1 of the ESI.†

The dissociative H_2 landscape over TMC (001) surfaces is more complex and richer than one could anticipate from chemical intuition. For instance, a H_2 molecule landing on a TMC surface can physisorb on a top-M site, $H_2^{*(top-M)}$, and then dissociate into two vicinal chemisorbed H, $H^{*(top-M)}$, species, or, alternatively, the H_2 could physisorb on a top-C site, $H_2^{*(top-C)}$, and, subsequently, form a $H_{2,Kubas}$ mode, $H_{2,Kubas}^{*(top-C)}$, to finally dissociate into two chemisorbed H atoms, $H^{*(top-C)}$. A graphical scheme including all the possible adsorption configurations and elementary steps connecting the diversity of adsorbing situations is shown in Fig. 1. In total, eight elementary steps have been investigated, including

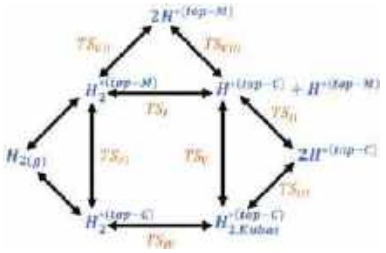

Fig. 1 Graphical scheme showing the possible elementary steps connecting all adsorption minima and their corresponding transition states.

 This journal is © The Royal Society of Chemistry 2019

Table 2 Calculated TS energy barriers for several steps involving adsorbed H_2 and H species on the (001) surface of the studied TMCs. All values are given in eV and include the ZPE term

	Forward (reverse) energy barrier						
Step	TiC	ZrC	HfC	VC	NbC	TaC	δ-MoC
$H_2^{*(top\text{-}M)} \xrightleftharpoons{TS_I} H^{*(top\text{-}C)} + H^{*(top\text{-}M)}$	0.68 (0.00)	0.52 (0.06)	0.48 (0.06)	0.65 (0.00)	0.60 (0.04)	0.47 (0.11)	0.39 (0.31)
$H^{*(top\text{-}C)} + H^{*(top\text{-}M)} \xrightleftharpoons{TS_{II}} 2H^{*(top\text{-}C)}$	0.10 (1.72)	0.03 (1.60)	0.12 (1.50)	0.14 (0.53)	0.38 (0.52)	—	0.19 (0.95)
$2H^{*(top\text{-}C)} \xrightleftharpoons{TS_{III}} H_{2,Kubas}^{*(top\text{-}C)}$	1.11 (0.47)	1.42 (0.71)	1.44 (0.63)	0.66 (0.62)	0.82 (0.92)	—	1.07 (0.96)
$H_{2,Kubas}^{*(top\text{-}C)} \xrightleftharpoons{TS_{IV}} H_2^{*(top\text{-}C)}$	2.13 (1.78)	2.22 (1.75)	2.17 (1.95)	1.57 (1.85)	1.59 (1.86)	0.40 (0.92)	1.92 (1.53)
$H^{*(top\text{-}C)} + H^{*(top\text{-}M)} \xrightleftharpoons{TS_V} H_{2,Kubas}^{*(top\text{-}C)}$	0.13 (1.11)	0.04 (0.90)	0.12 (0.68)	0.22 (0.58)	0.39 (0.63)	0.45 (0.45)	0.36 (1.01)
$H_2^{*(top\text{-}M)} \xrightleftharpoons{TS_{VI}} H_2^{*(top\text{-}C)}$	0.06 (0.01)	0.07 (0.00)	0.08 (0.00)	0.01 (0.00)	0.05 (0.00)	0.08 (0.00)	0.00 (0.18)
$H_2^{*(top\text{-}M)} \xrightleftharpoons{TS_{VII}} 2H^{*(top\text{-}M)}$	—	—	—	—	—	0.82 (0.81)	—
$2H^{*(top\text{-}M)} \xrightleftharpoons{TS_{VIII}} H^{*(top\text{-}C)} + H^{*(top\text{-}M)}$	—	—	—	—	—	0.77 (0.42)	—

H_2 and H diffusion, and H_2 dissociation. The corresponding $TS_{I–VIII}$ values of these elementary steps are reported in Table 2 and the structures shown in Fig. S2 of the ESI.† Our results suggest that the formation of a $H_{2,Kubas}$ from a physisorbed H_2 molecule on top-C is very unlikely, due to the high predicted TS energy barriers, which range from 1.53 to 1.95 eV in all TMCs except for TaC, where the barrier is reduced to 0.92 eV, yet still fairly high. Instead, we found that the most feasible path for the

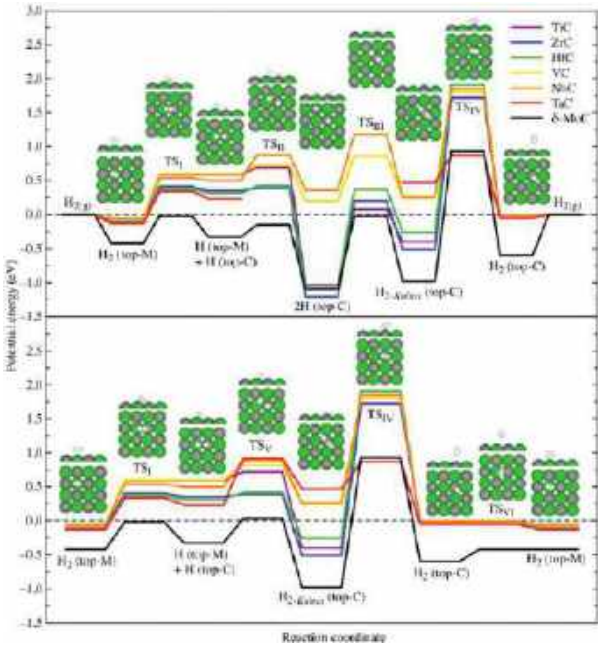

Fig. 2 Energy profiles (PBE-D3 values including the ZPE term) for H_2 adsorption, desorption, and dissociation on the (001) surface of the studied TMCs. The top diagram includes TSs I–IV, while the bottom diagram includes TSs I and IV–VI. The optimized geometries for all adsorption minima and transition states on HfC are also displayed. Hf, C, and H atoms are shown as green, grey, and white spheres, respectively.

$H_{2,Kubas}$ formation starts from a physisorbed H_2 molecule on a top-M site, followed by a dissociation through TS_I to produce two coadsorbed H species on neighboring top-M and top-C sites, finally followed by the formation of the $H_{2,Kubas}$ through the TS_V saddle point, TS_I being the rate limiting step, with energy barriers ranging 0.39 to 0.68 eV. However, once the two coadsorbed H species are formed, the diffusion of H species adsorbed on the top-M site towards another neighboring top-C site, resulting in two H species adsorbed on two separate top-C sites (TS_{II} in Fig. 1), would compete with the Kubas formation. The only exception to this general behavior is TaC. As previously stated, this carbide adsorbs H species more strongly on top-M sites than on top-C sites. Therefore, on TaC, the most likely scenario is H_2 adsorption leading to two H adatoms on two separate top-M sites. This configuration can be reached from a physisorbed H_2 molecule on a top-M site in a single step, *i.e.*, through TS_{VII}, with an energy barrier of 0.82 eV, or in two consecutive steps, *i.e.*, through TS_I followed by TS_{VIII}, the latter barrier being 0.42 eV, as shown in Fig. 1. The optimized geometries for TSs on all studied TMC (001) surfaces are shown in Fig. S2 of the ESI.†

Interestingly, for all TMCs in a given group, the energy barrier for H_2 dissociation through TS_I decreases when descending along a group of the periodic table. Fig. 2 shows the energy profiles for the full H_2 dissociation scenario except for the two processes involving TS_{VII} and TS_{VIII}, as these are only important for TaC, and shown in Fig. S3 of the ESI.† As deduced from Fig. 2, clearly, the most stable configuration for all group IV TMCs and δ-MoC is the coadsorption of two H species adsorbed on top-C, while H_2 adsorbed on either top-C or top-M exhibit the lowest energy configuration on group V TMCs. Note also that, on all TMCs except for NbC, the $H_{2,Kubas}$ configuration is higher in energy than that for the coadsorption of two H species both on top-C; on NbC, the $H_{2,Kubas}$ is 0.10 eV lower. However, it is on δ-MoC that H adsorbed on top-C sites can be regarded as competitive with the H_2 Kubas situation.

In summary, the present work demonstrates that group V TMCs are probably not the best candidates for efficient hydrogenation reactions, given the very low physisorption energies of H_2 and the endoergicity of $H_{2,Kubas}$ formation and of the H_2 dissociation. In fact, for group V, the only dissociated state which is lower in energy than H_2 in the gas-phase is the coadsorption of two H species on two top-M sites in TaC. On the other hand, group IV TMCs are likely to be good candidates to replace noble metals as heterogeneous catalysts for hydrogenation reactions, see comparison of energy barriers in Table S3 in ESI.† Although group IV TMCs also exhibit very low H_2 physisorption energies, the adsorption energies for dissociated H states or the $H_{2,Kubas}$ configuration are much stronger. Finally, among the seven studied TMCs, δ-MoC emerges as the best candidate since it exhibits moderate adsorption energies for molecular H_2, $H_{2,Kubas}$, and atomic H entities, plus features the lowest energy barrier for H_2 dissociation on top-M sites. Additionally, our results show that group IV TMCs and δ-MoC are predicted as good candidates for hydrogenation reactions, since the coadsorption of two H species on two separate top-C sites is always preferred compared to the formation of $H_{2,Kubas}$. Moreover, the direct formation of $H_{2,Kubas}$ modes from physisorbed H_2 on top-C is energetically hindered. To summarize, present results show that, for hydrogenation reactions, TMCs can outperform late transition metals featuring comparable or even smaller energy barriers for H_2 dissociation, see comparison in ESI.†

Conflicts of interest

There are no conflicts to declare.

Notes and references

1 I. Kojima, E. Miyazaki, Y. Inoue and I. Yasumori, *J. Catal.*, 1979, **59**, 472–474.
2 G. Fan, X. Li, C. Xu, W. Jiang, Y. Zhang, D. Gao, J. Bi and Y. Wang, *Nanomaterials*, 2018, **8**, 141–154.
3 A. B. Vidal, L. Feria, J. Evans, Y. Takahashi, P. Liu, K. Nakamura, F. Illas and J. A. Rodriguez, *J. Phys. Chem. Lett.*, 2012, **3**, 2275–2280.
4 J. A. Rodriguez, J. Evans, L. Feria, A. B. Vidal, P. Liu, K. Nakamura and F. Illas, *J. Catal.*, 2013, **307**, 162–169.
5 H. Prats, R. A. Gutierrez, J. J. Piñero, F. Viñes, S. T. Bromley, P. J. Ramirez, J. A. Rodriguez and F. Illas, *J. Am. Chem. Soc.*, 2019, **141**, 5303–5313.
6 M. G. Quesne, A. Roldán, N. H. de Leeuw and C. R. A. Catlow, *Phys. Chem. Chem. Phys.*, 2018, **20**, 6905–6916.
7 J. Spielmann, F. Buch and S. Harder, *Angew. Chem., Int. Ed.*, 2008, **120**, 9576–9580.
8 S. T. Oyama, *Catal. Today*, 1992, **15**, 179–200.
9 S. Posada-Pérez, R. A. Gutiérrez, Z. Zuo, P. J. Ramírez, F. Viñes, P. Liu, F. Illas and J. A. Rodríguez, *Catal. Sci. Technol.*, 2017, **7**, 5332–5342.
10 J. A. Rodríguez, P. Liu, D. J. Stacchiola, S. D. Senanayake, M. G. White and J. G. Chen, *ACS Catal.*, 2015, **5**, 6696–6706.
11 K. Aydin and R. Kenanoğlu, *Int. J. Hydrogen Energy*, 2018, **26**, 14047–14058.
12 M. J. Burk, Y. M. Wang and J. R. Lee, *J. Am. Chem. Soc.*, 2018, **21**, 5142–5143.
13 F. Costanzo, P. L. Silvestrelli and F. Ancilotto, *J. Chem. Theory Comput.*, 2012, **8**, 1288–1294.
14 E. Florez, T. Gomez, P. Liu, J. A. Rodriguez and F. Illas, *ChemCatChem*, 2010, **2**, 1219–1222.
15 C. V. J. Skipper, A. Hamaed, D. M. B. Antonelli and N. Kaltsoyannis, *Dalton Trans.*, 2012, **41**, 8515–8523.
16 S. K. Estreicher, J. L. McAfee, P. A. Fedders, J. M. Pruneda and P. Ordejón, *Phys. B*, 2001, **308**, 202–205.
17 G.-Q. Yu, B.-Y. Huang, X. Chen, D. Wang, F. Zheng and X.-B. Li, *J. Phys. Chem. C*, 2019, **123**, 21878–21887.
18 J. P. Perdew, K. Burke and M. Ernzerhof, *Phys. Rev. Lett.*, 1996, **77**, 3865–3868.
19 S. Grimme, J. Antony, S. Ehrlich and H. Krieg, *J. Chem. Phys.*, 2010, **132**, 154104.
20 G. Kresse and J. Furthmüller, *Phys. Rev. B: Condens. Matter Mater. Phys.*, 1996, **54**, 11169–11186.
21 H. Prats, S. Posada-Pérez, J. A. Rodriguez, R. Sayós and F. Illas, *ACS Catal.*, 2019, **9**, 9117–9126.
22 G. Henkelman, B. P. Uberuaga and H. Jónsson, *J. Chem. Phys.*, 2000, **113**, 9901–9904.
23 A. H. Larsen, J. J. Mortensen, J. Blomqvist, I. E. Castelli, R. Christensen, M. Dułak, J. Friis, M. N. Groves, B. Hammer, C. Hargus, E. D. Hermes, P. C. Jennings, P. B. Jensen, J. Kermode, J. R. Kitchin, E. L. Kolsbjerg, J. Kubal, K. Kaasbjerg, S. Lysgaard, J. B. Maronsson, T. Maxson, T. Olsen, L. Pastewka, A. Peterson, C. Rostgaard, J. Schiøtz, O. Schütt, M. Strange, K. S. Thygesen, T. Vegge, L. Vilhelmsen, M. Walter, Z. Zeng and K. W. Jacobsen, *J. Phys.: Condens. Matter*, 2017, **29**, 273002.
24 S. Smidstrup, A. Pedersen, K. Stokbro and H. Jónsson, *J. Chem. Phys.*, 2014, **140**, 214106.
25 A. A. Koverga, E. Flórez, L. Dorkis and J. A. Rodriguez, *J. Phys. Chem. C*, 2019, **123**, 8871–8883.
26 F. Silveri, M. G. Quesne, A. Roldán, N. H. de Leeuw and C. R. A. Catlow, *Phys. Chem. Chem. Phys.*, 2019, **21**, 5335–5343.
27 J. J. Piñero, P. J. Ramírez, S. T. Bromley, F. Illas, F. Viñes and J. A. Rodríguez, *J. Phys. Chem. C*, 2018, **122**, 28013–28020.
28 F. Viñes, C. Sousa, P. Liu, J. A. Rodriguez and F. Illas, *J. Chem. Phys.*, 2005, **122**, 174709.
29 B. Hammer, *Phys. Rev. B: Condens. Matter Mater. Phys.*, 2011, **63**, 205423.
30 A. Groß, *J. Chem. Phys.*, 2011, **135**, 174707.

 This journal is © The Royal Society of Chemistry 2019

4.8. References

1. F. Viñes and C. Sousa. A systematic density functional theory study of the electronic structure of bulk and (001) surface of transition-metals carbides. *J. Chem. Phys.*, **2005**, 122, *17*, 4709.
2. J. Häglund, G. Grimvall, T. Jarlborg T, and A.F. Guillermet. Band structure and cohesive properties of 3d-transition-metal and nitrides with the NaC1-type structure carbides. *Phys Rev*. B., **1991**, 43, *18*, 400–408.
3. R.H. Willens, E. Buehler, and B.T. Matthias. Superconductivity of the Transition-Metal Carbides. *Phys. Rev*., **1967**, 159, 327.

4. A.F. Guillermet and G. Grimvall. Cohesive properties and vibrational entropy of 3d-transition metal carbides. *J. Phys. Chem. Solids*, **1992**, 53, *1*, 105-125.
5. A.F. Guillermet, J. Higlund, and Grimvall G. Cohesive properties of 4d-transition-metal carbides and nitrides in the NaCl-type structure. *Phys Rev B*. **1992**, 45, *20*, 11557–11567.
6. S. Posada-pérez, F. Viñes, and R. Valero. Adsorption and dissociation of molecular hydrogen on orthorhombic β-Mo_2C and cubic δ-MoC (001) surfaces. *Surf Sci*, **2017**, 656, 24–32.
7. F. Viñes, C. Sousa, F. Illas, P. Liu, and J. A. Rodriguez. A Systematic Density Functional Study of Molecular Oxygen Adsorption and Dissociation on the (001) Surface of Group IV - VI Transition Metal Carbides.*J. Phys. Chem. C*, **2007**, 111, *45*, 16982–16989.
8. C. Kunkel, F. Viñes, P.J. Ramirez, J.A. Rodriguez, and F. Illas. Combining Theory and Experiment for Multitechnique Characterization of Activated CO on Transition Metal Carbide (001) Surfaces. *J. Phys. Chem. C*, **2019**, 123, *13*, 7567–7576.
9. P.V. Kamath, D.D. Sarma, and C.N.R. RAO. Adsorption of carbon monoxide and oxygen on transition metal surfaces : A comparative study of the results from electron spectroscopy and theoretical calculationst. *Proe Indian Acad SCi*. **1984**, 93, *3*, 335–355.
10. C. Kunkel, F. Viñes, and F. Illas. Surface Activity of Early Transition Metal CO_2 Adsorption Case Study. *J. Phys. Chem. C*, **2019**, 123, *6*, 3664–3671.
11. T. Christofoletti, J.M. Assaf, and E.M Assaf. Methane steam reforming on supported and non-supported molybdenum carbides. *Chem. Eng. J.,* **2005**, 106, *2*, 97–103.
12. M. Figueras, R.A Gutiérrez, H. Prats, F. Viñes, P.J. Ramírez, F. Illas, and J.A. Rodriguez. Boosting the activity of transition metal carbides towards methane activation by nanostructuring. Phys Chem Chem Phys. **2020**;19.
13. I. Kojima, E. Miyazaki, Y. Inoue, and I. Yasumori. Catalytic activities of TiC, WC, and TaC for hydrogenation of ethylene. *J. Catal.*, **1979**, 59, *3*, 472–474.
14. C. Jimenez-Orozco, E. Florez, A. Moreno, P. Liu, and J.A. Rodriguez. Systematic Theoretical Study of Ethylene Adsorption on δ-MoC(001), TiC(001), and ZrC(001) Surfaces. *J. Phys. Chem. C*, **2016**, 120, *25*, 13531–13540
15. I. Kojima, E. Miyazaki, Y. Inoue, and I. Yasumori. Catalysis by transition metal carbides. IV. Mechanism of ethylene hydrogenation and the nature of active sites on tantalum monocarbide. *J Catal*., **1982**, 73, *1*, 128–135.
16. J.P. Perdew, K. Burke, and M. Ernzerhof. Generalized gradient approximation made simple. *Phys Rev Lett.*, **1996**, 77, *18*, 3865–3868.
17. S. Grimme, J. Antony, S. Ehrlich, and H. Krieg H. A consistent and accurate ab initio parametrization of density functional dispersion correction (DFT-D) for the 94 elements H-Pu. *J. Chem. Phys.*, **2010**, 132; 154104.
18. G. Henkelman and H. Jónsson. Improved tangent estimate in the nudged elastic band method for finding minimum energy paths and saddle points. *J Chem Phys.*, **2000**, 113, *22*, 9978–9985.
19. G. Henkelman and H. Jónsson H. A dimer method for finding saddle points on high dimensional potential surfaces using only first derivatives. *J Chem Phys*., **1999**; 111, *15*, 7010–7022.

Chapter 5

CH_4 adsorption and dissociation on TiC (001) surface

5. CH_4 adsorption and dissociation on TiC (001) surface

5.1. Introduction

Methane (CH_4) is the most abundant and stable alkane molecule.[1] This compound, together with carbon dioxide (CO_2), are the two main greenhouse gases contributing to the global warming and climate change. Although CH_4 emissions are five times less than CO_2, the CH_4 greenhouse effect is 23 times greater and, therefore, its contribution to climate change is comparable to that of CO_2.[2] Nowadays different strategies oriented towards reducing the content of greenhouse gases in the atmosphere are applied. One of the most promising strategies to reduce the emission of these molecules into the atmosphere is the carbon capture and storage (CCS) technologies,[3] where the CO_2 or CH_4 molecules are sequestered, adsorbed in a viable material. Even more interesting are the carbon capture and use (CCU) technologies, where the sequestered CO_2 or CH_4 are converted into other valuable chemicals.[4] Towards this end, a viable material is needed, which has to act as a catalyst to dissociate these strongly bound molecules.

In this work the TiC (001) surface is studied as a possible catalyst. Particularly, two options will be studied, either the clean TiC (001) surface, or its use as a support for small Ni clusters as the latter have been proposed as viable catalysts for desulfurization reactions.[5] The idea here was to inspect the dissociation of methane, limiting step to convert it into other chemicals, such as methanol.

This work was carried out in collaboration with other researchers. The CH_4 adsorption part on Nickel clusters was carried out by Dr. Prats while the experimental part was carried out by Dr. Rodriguez's group at Brookhaven National Laboratory. Finally, this work has been published in **the *Journal of the American Chemical Society* (JACS)** with the name "**Room Temperature Methane Capture and Activation by Ni Clusters Supported on TiC (001): Effects of Metal-Carbide Interactions on the Cleavage of the C-H Bond",** 2019, 141, 5303**.**

5.2. Methodology

The followed methodology is exactly the same as the one employed in Chapter 3, including the surface slab models, and so, we refer to it for further details. The only difference between Chapter 3 was that, in this Chapter, the transition states (TSs) have found using the CI-NEB,[6] but with the intermediate images generated by means of the Atomic Simulation Environment (ASE)[7] Image Dependent Pair Potential (IDPP)[8] tool, instead of a direct, linear interpolation.

5.3. CH_3 adsorption

Having analysed the H adsorption in Chapter 3, the other possible fragment of the CH_4 dissociation is investigated here. The CH_3 moiety can be adsorbed on TiC (001) with different

orientations with respect to the surface. In this Thesis only two orientations were tested: Either parallel or perpendicular with respect to the surface, knowing that CH_3 is a flat moitety.[9–11] For the parallel orientation, 14 different conformations have been tested, see Figure 5.1.

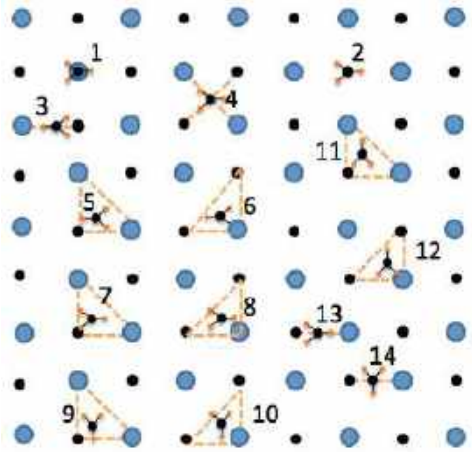

Figure 5.1. Schematic top view of a (001) surface of a TMC with the CH_3 adsorption positions studied having CH_3 parallel to surface. The image shows C atoms (black), metallic atoms (blue), and CH_3 molecules in 14 initial positions. Dashed orange lines are guides for the eyes.

In addition, when the CH_3 is perpendicular to the surface, 13 different sites were tested for the adsorption of the CH_3 molecular species. These positions are shown in Figure 5.2.

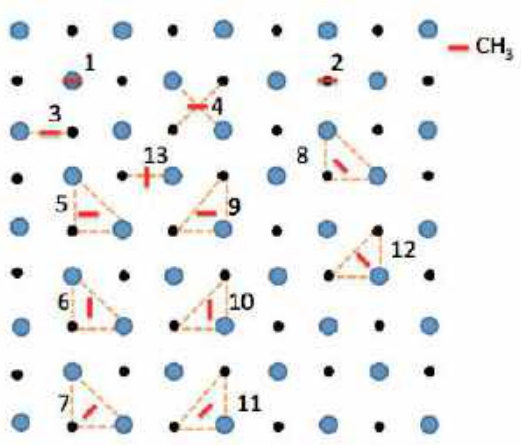

Figure 5.2. Schematic top view of a (001) surface of a TMC with the CH_3 adsorption positions studied when CH_3 is perpendicular to surface. Colour coding as in Figure 5.1.

The most favourable adsorption energy position for CH_3 molecule is the same position found for the H adatoms, shown and discussed in Chapter 3, the C-Top, with an adsorption energy of -2.93 eV as obtained at a PBE-D3 level; see Figure 5.3.

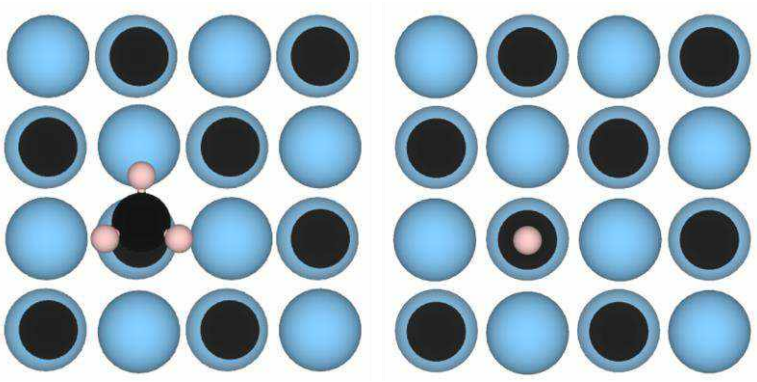

Figure 5.3. Final geometry for the CH_3 molecule and H atoms once these molecules are adsorbed on TiC (001) surface. Ti, C, and H atoms are shown here as dark grey, light grey, and white spheres, respectively.

5.4. CH_4 adsorption

The CH_4 adsorption on TiC (001) surface was studied previously.[12] where the three most stable adsorption positions were found; see Figure 5.4.

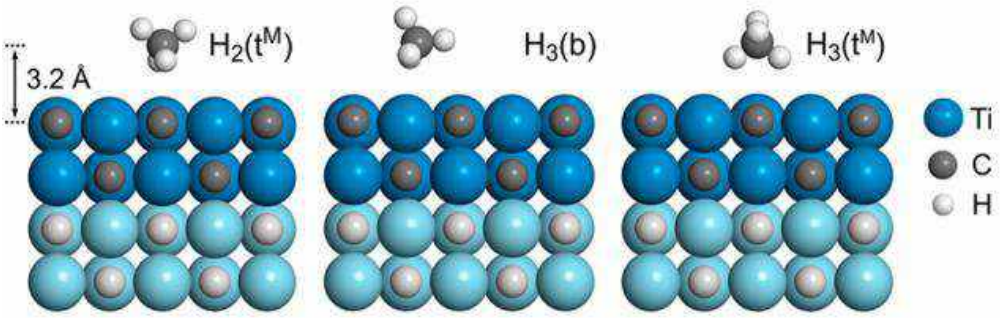

Figure 5.4. Side views of CH_4 adsorbed on TiC (001) in the three different considered cases.[12]

The adsorption positions in ref. 12 were recalculated at a PBE-D3 level and the adsorption energy values are shown in Table 5.1.

Table 5.1. Adsorption energies, in eV, of CH_4 on the TiC (001) surface, in eV.

E_{ads} (eV)	PBE-D3[12]
$H_2(t^M)$	-0.23
$H_3(b)$	-0.23
$H_3(t^M)$	-0.23

There one can see that in all cases small adsorption energies are found, implying a physisorption. Since these adsorption energies are small, everything indicates that the CH_4 dissociation on TiC (001) surface under the studied conditions would hardly occur unless molecular beams of CH_4 were used.[13]

5.5. CH_3 + H adsorption

The final CH_3 and H moieties upon co-adsorption has been addressed. Since both compete for the same C-Top surface site, different mutual sites have been regarded, even including less stable Ti-Top sites for H sites; see Figure 5.5.

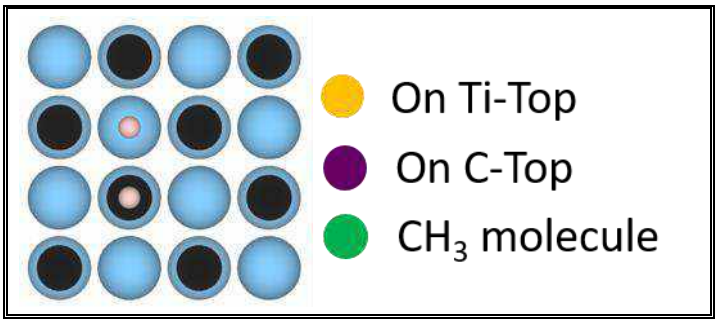

Figure 5.5. Top view of where H atoms have been added (A-C) having CH_3 on a C-Top site (M).

The results showed that the most stable configuration for the co-adsorption of CH_3 and H is when H atoms are in position A. That is, both molecules are adsorbed on vicinal C-Top atoms as can be seen in Figure 5.6, with an E_{ads} of -0.43 eV for the adduct.

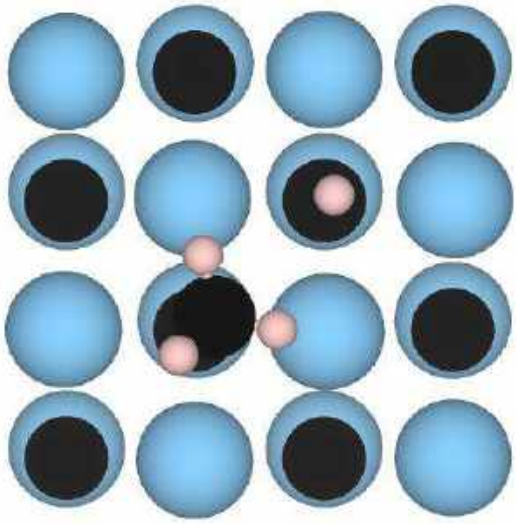

Figure 5.6. Top view of the optimized geometry for CH_3 + H adsorbed on TiC (001) surface; colour coding as in Fig. 5.1.

5.6. Adsorption on TiC-supported Ni clusters

Three Ni clusters sizes have been studied to be supported on TiC (001): Ni_4, Ni_9, and Ni_{13}. For these Ni clusters, the unit cell used for the TiC (001) surface was extended, to be a *c*(4×4) for the largest clusters. The optimized geometries for the Ni clusters adsorbed on TiC (001) surface are shown in Figure 5.7. These supported cluster structures were based on Ni being more stable again on C-Top site, and past studies showing a preference towards having a 3D truncated pyramidal structure instead of planar, extended Ni clusters.[14,15]

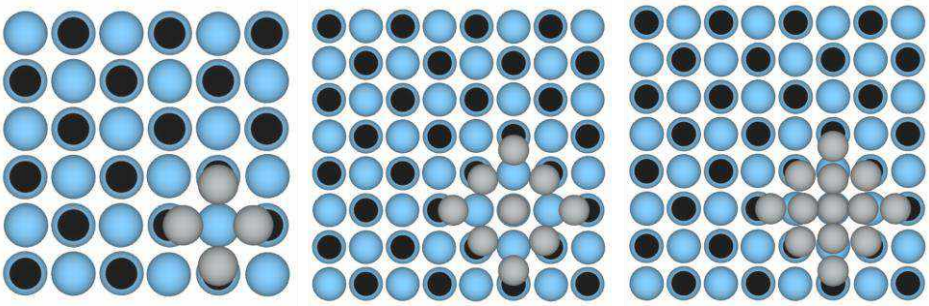

Figure 5.7. Most stable optimized geometries found for Ni_4/TiC, Ni_9/TiC, and Ni_{13}/TiC. Ni atoms are shown as grey spheres, and Ti and C atoms as light and blue and black spheres, respectively. The unit cell is shown by black dotted lines.

5.7. Adsorption on Ni clusters

5.7.1. CH_4 adsorption

The CH_4 adsorption energy on TiC (001) containing Ni_n clusters was systematically studied, including different adsorption modes and sites. Results showed that the CH_4 molecule prefers to adsorb on Top-Ni vertex Ni atom. Both Ni_4/TiC and Ni_9/TiC cases can be seen in Figure 5.8.

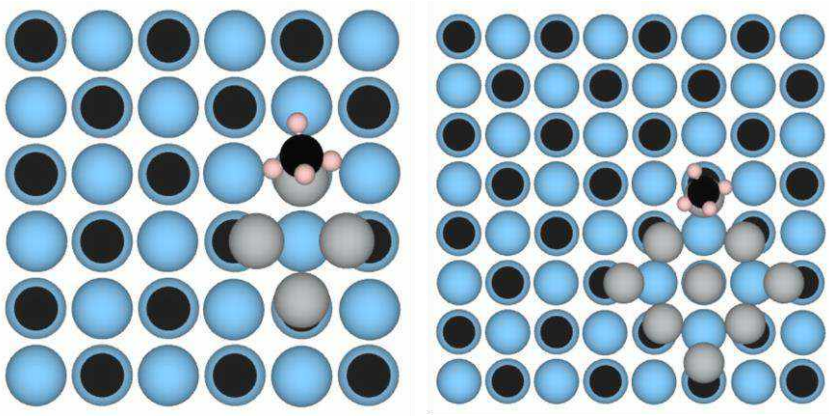

Figure 5.8. Top view of most stable CH_4 position on Ni_4/TiC (left) and Ni_9/TiC (right).

The Ni_{13}/TiC case is a little different. The CH_4 molecule adsorb in the Ni vertex atom but in this case, the CH_4 is located on the Ni-edge; see Figure 5.9.

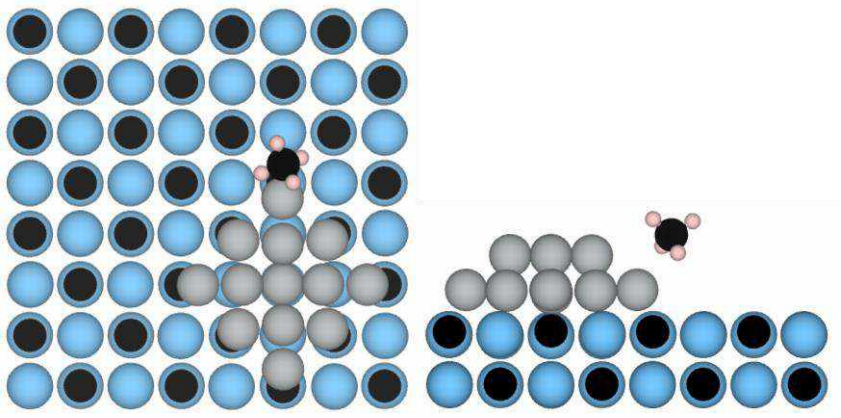

Figure 5.9. Top (left) and side (right) views of CH_4 adsorbed on Ni_{13}/TiC.

The adsorption energies found for the different sizes are contained in Table 5.2. In addition, the CH_4 adsorption energy on the bare TiC (001) surface and on Ni (111) are listed for comparison.

Table 5.2. CH_4 adsorption energies, in eV on Ni_n/TiC, TiC (001) and Ni (111) Ref. 16 (PBE-D2).

Catalyst	Ni_4/TiC	Ni_9/TiC	Ni_{13}/TiC	TiC (001)	Ni (111)[16]
CH_4 E_{ads}	-0.57	-0.64	-0.36	-0.23	-0.24

The results for CH_4 adsorption show that, on the Ni_n/TiC systems, the CH_4 adsorption energy is 1.5-2.5 times stronger than on the clean TiC (001) surface, which is indeed similar to Ni (111). Among them, the one with the highest adsorption energy is Ni_9/TiC.

5.7.2. CH_3 adsorption

Similarly to CH_4, the CH_3 moiety adsorbs in the same place on Ni_4/TiC and Ni_9/TiC cases and a little bit different on Ni_{13}/TiC. On Ni_4/TiC and Ni_9/TiC the CH_3 fragment adsorb in the 3-fold hollow Ni. Both Ni_4/TiC and Ni_9/TiC cases can be seen in Figure 5.10. The CH_3 moiety on Ni_{13}/TiC adsorbs on Ni-Top of the first slab as can be seen in Figure 5.11.

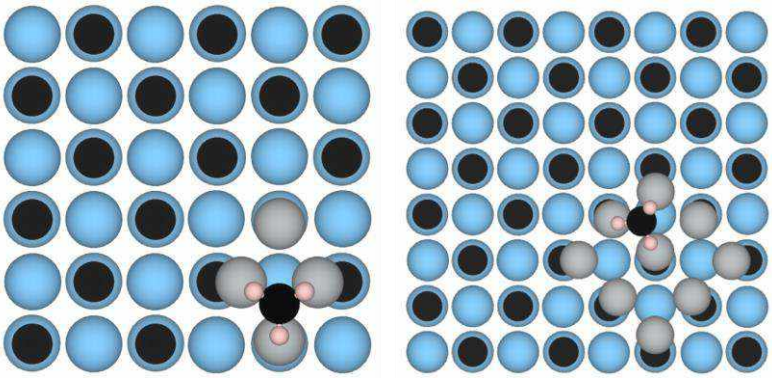

Figure 5.10. Top views of the adsorption position for CH_3 on Ni_4/TiC (left) and Ni_9/TiC (right).

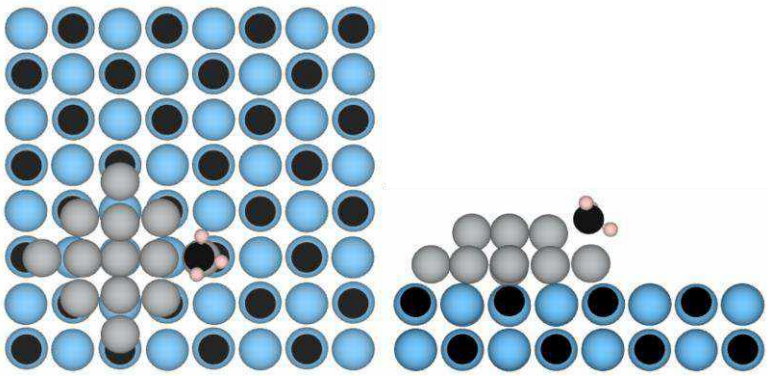

Figure 5.11. Top (left) and side (right) views of CH_3 adsorption position on Ni_{13}/TiC.

5.7.3 H adsorption

The final adsorption position of the H atom on the Ni cluster depends on the Ni Cluster size. The adsorbed position for the atomic H on Ni_4 cluster is a 3-fold follow Ni atoms while on Ni_9, the adsorption occurs on 4-fold hollow Ni atoms. Both cases are represented in Figure 5.12.

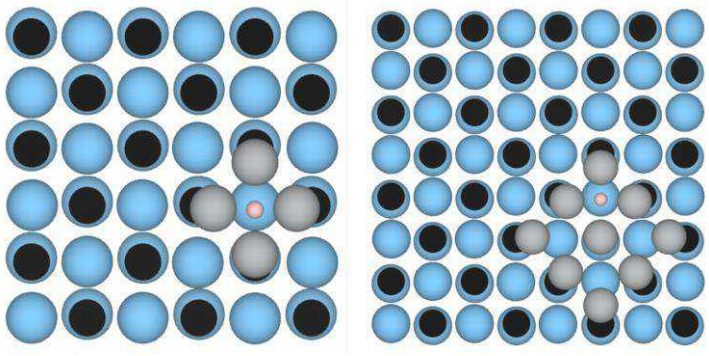

Figure 5.12. Top views of H adsorption on Ni_4/TiC (left) and Ni_9/TiC (right).

Finally, the H atom is also studied on Ni_{13}/TiC. In this case, the H adsorbs on a middle of one three-fold hollow, on a Ni (111) resembling facet. This position is shown in Figure 5.13.

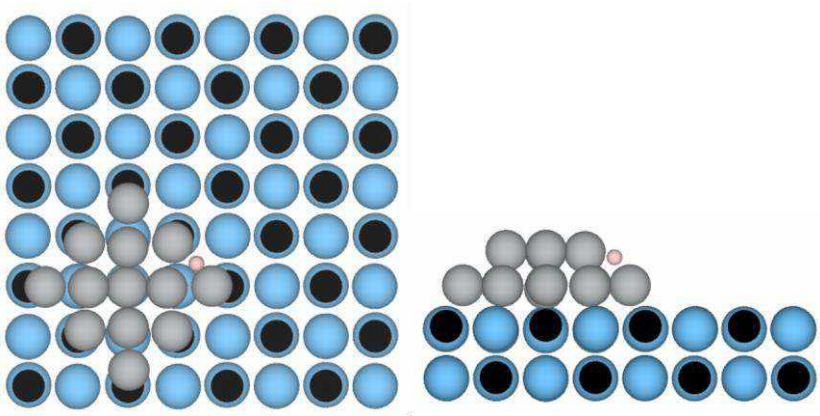

Figure 5.13. Top (left) and side (right) views of H adsorption on Ni_{13}/TiC.

5.7.4. CH_3 + H adsorption

As on bare TiC (001), CH_3 + H co-adsorption configuration is studied on the Ni_n clusters supported on TiC (001), so as to get a final state situation for the CH_4 dissociation. The optimized positions in each case are a little bit different. For Ni_4/TiC case, in the final position, both the CH_3 molecule and the H atom are adsorbed on the bridge between two Ni atoms and the CH_3 molecule opposite the H atom. For Ni_9/TiC case, the CH_3 molecule is adsorbed on the bridge between two Ni atoms and the H atom in vicinal a four-fold hollow Ni atoms. In the last size under study, Ni_{13}/TiC the CH_3 molecule is located on the vertex of the cluster, and the released H adatom adsorbs on a three-fold hollow site of small (111) Ni supported cluster. The optimized adsorption position for three Ni_n/TiC cluster are shown in Figure 5.14, and the adsorption energies for the adducts are listed in Table 5.3.

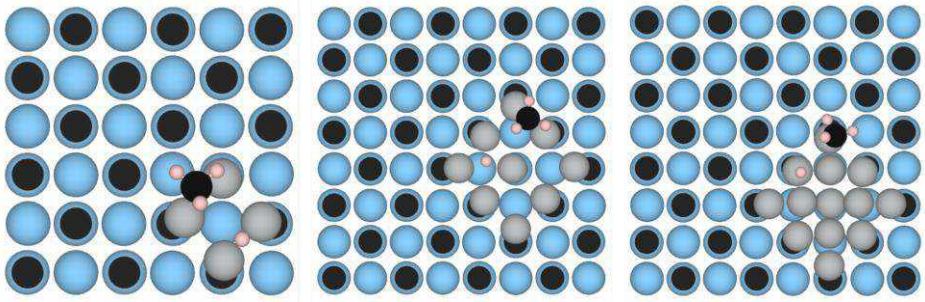

Figure 5.14. Optimized CH_3 + H co-adsorption position for the three Ni_n/TiC cluster systems. Left: Ni_4/TiC. Center: Ni_9/TiC. Right: Ni_{13}/TiC.

Table 5.3. CH_3 + H co-adsorption energies, in eV, on the different Ni_n/TiC.

	Ni_4/TiC	Ni_9/TiC	Ni_{13}/TiC
CH_3 + H E_{ads}	-1.32	-1.69	-1.05

5.8. CH_4 dissociation

5.8.1 CH_4 dissociation on bare TiC (001) surface

CH_4 transition states were studied for the three initial positions described in Figure 5.4, but only for one of the initial positions the barrier dissociation was obtained H_3 (t^M), while the other two did not converge. The reaction profile obtained with ZPE correction is shown in Figure 5.15.

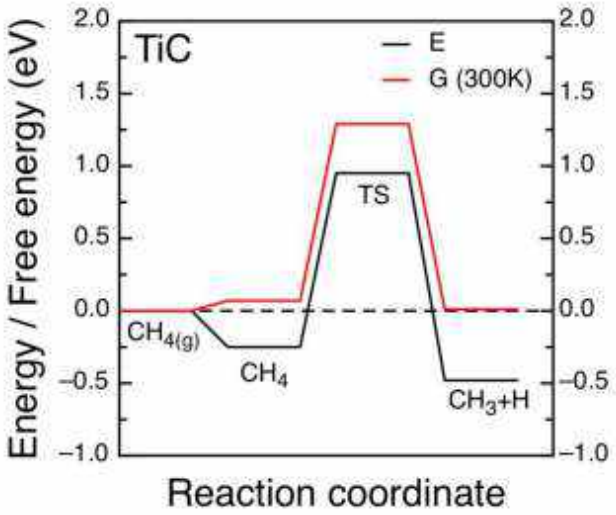

Figure 5.15. Reaction profile for CH_4 first C-H bond scission, obtained using PBE-D3 and accounting for ZPE.

The results obtained for the CH_4 dissociation show a barrier energy of 1.32 eV when PBE-D3, and reduces to 1.23 eV when the ZPE is added. Figure 5.16 also shows the Gibbs free energy profile when having 1 atm of CH_4 and 300 K of temperature, revealing that reaction step energy barriers are barely affected by the working conditions.

5.8.2 CH_4 dissociation on doped (001) surface.

The CH_4 dissociation on doped TiC (001) surface with Ni_n clusters have also obtained using CI-NEB method for the three Ni clusters. The reactions profiles for all cases are shown in Figure 5.9. The results obtained for the three cases are shown on Table 5.4. These values are obtained using PBE-D3 and applying a ZPE correction. As one can clearly see, Ni_n clusters feature much reduced energy barriers when compared to the TiC (001) support and the extended Ni (111) surface, implying that such low-coordinated sites in Ni_n are key in CH_4 activation by catalysing first C-H bond scission.

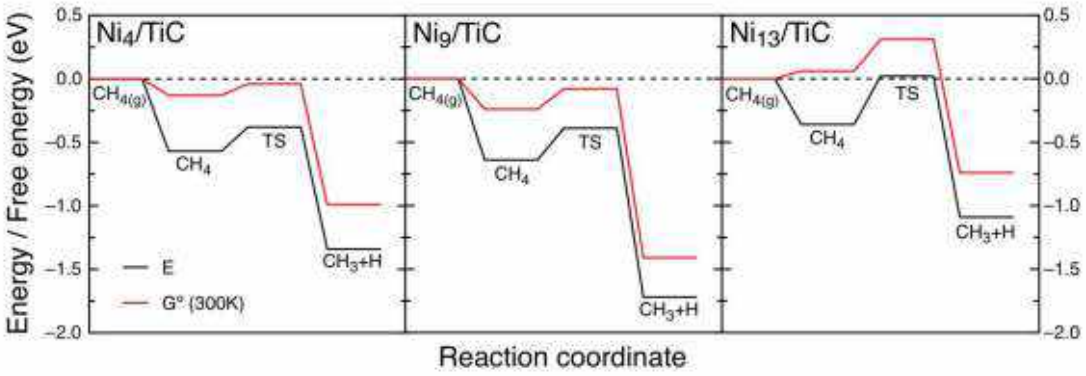

Figure 5.9. Reaction profiles for CH_4 dissociation reaction on TiC (001) surface when having Ni_4, Ni_9, or Ni_{13} clusters.

Table 5.4. Reaction step energy barriers (E_b) for the CH_4 dissociation on different Ni_n supported on TiC (001) surfaces Note that present E_b values account for the ZPE, but this is not the case for the Ni (111) value in Ref. 17

Catalyst	Ni_4/TiC	Ni_9/TiC	Ni_{13}/TiC	TiC (001)	Ni (111)[17]
CH_4 E_b	0.18	0.25	0.38	1.22	1.18

5.9. Experimental study

In a similar fashion as done in Chapter 3, the experimentalists of the Dr. Rodriguez's group at Brookhaven National Laboratory, USA, carried out the experiments, and computational simulations helped finding an explanation. In this case, they used XPS spectra collected before and after dosing methane to Ni/TiC (001) and Ni (111) surfaces at 300 K (Figure 5.17) where one can see that the CH_4 only adsorbs on Ni/TiC (001) when the CH_4 is exposed at 300K 1 Torr for 5 minutes.

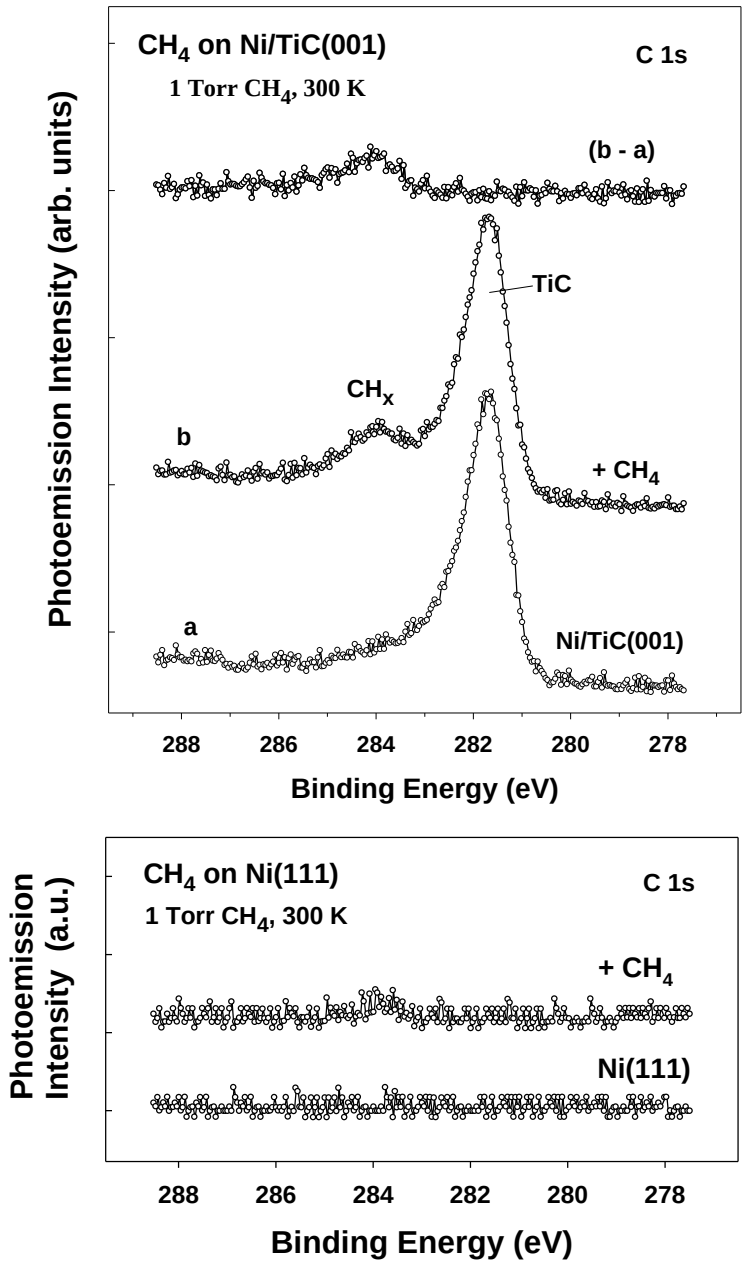

Figure 5.10. C 1s XPS spectra collected before and after dosing methane to Ni/TiC (001) and Ni (111) surfaces at 300 K (top and bottom panels, respectively). The dosage of methane was 1 Torr for 5 minutes. The coverage of Ni on the TiC (001) substrate was 0.2 ML.[18]

The simulations helped understanding the interaction of CH_4 with Ni_x clusters supported on TiC (001) surface, which tend to favour the CH_4 adsorption. This adsorption is 1.5-2.5 times stronger than on the clean TiC (001) surface as can see in Tables 5.2. The computational study made it possible to know how the size of the Ni cluster affects adsorption. The Ni_4 cluster is the most favourable for the adsorption of CH_3 and H and the Ni_9 cluster is the most favourable for the adsorption of CH_4. The synergy of Ni clusters and the TiC support material not only favours the adsorption of the molecules, but also increases their reactivity. Evidence for this is that the dissociation barriers values obtained for methane supported in Ni clusters are relatively small, only 0.18eV for Ni_4/TiC, while the same barriers for the clean surface are around 1 eV larger.

This difference in the C-H bond scission energy barriers values, aside from the best adsorption on Ni_x/TiC systems, helped understanding better the experimental studies and why in this cases the methane can dissociated at room temperature, while this does not occur on the TiC (001) surface or on the Ni (111) surface.

5.10. Conclusions

The CH_4 molecule on TiC (001) surface has a low adsorption energy. The dissociation study for this molecule shows that, as far as the TiC (001) surface is concerned, this dissociation will hardly occur, since the CH_4 adsorption is very weak, and the molecule would likely desorb before breaking into CH_3 and H, as this features a very large energy barrier. On the other hand, when the surface supports Ni clusters, the CH_4 adsorption energy increases 1.5-2.5 times with respect that on the clean TiC (001) surface, depending on the size of the Ni clusters. Furthermore, the activation energy decreases considerably, going from 1.22 eV on the clean surface to 0.18 eV in the best case studied (Ni_4/TiC). It seems plausible that a combination of low coordination and particular electronic structure of Ni clusters provokes that CH_4 activation can occur more easily.

5.11. Publication

JACS
JOURNAL OF THE AMERICAN CHEMICAL SOCIETY
Article
Cite This: J. Am. Chem. Soc. 2019, 141, 5303−5313
pubs.acs.org/JACS

Room Temperature Methane Capture and Activation by Ni Clusters Supported on TiC(001): Effects of Metal−Carbide Interactions on the Cleavage of the C−H Bond

Hèctor Prats,[†] Ramón A. Gutiérrez,[‡,×] Juan José Piñero,[†] Francesc Viñes,[†] Stefan T. Bromley,[†,§] Pedro J. Ramírez,[×] José A. Rodriguez,*[,‡] and Francesc Illas*[,†]

[†]Departament de Ciència de Materials i Química Física & Institut de Química Teòrica i Computacional (IQTCUB), de la Universitat de Barcelona, Martí i Franquès 1-11, 08028 Barcelona, Spain
[‡]Chemistry Department, Brookhaven National Laboratory, Upton, New York 11973, United States
[×]Facultad de Ciencias, Universidad Central de Venezuela, Caracas 1020-A, Venezuela
[§]Institució Catalana de Recerca i Estudis Avançats (ICREA), 08010 Barcelona, Spain

Supporting Information

ABSTRACT: Methane is an extremely stable molecule, a major component of natural gas, and also one of the most potent greenhouse gases contributing to global warming. Consequently, the capture and activation of methane is a challenging and intensively studied topic. A major research goal is to find systems that can activate methane, even at low temperatures. Here, combining ultrahigh vacuum catalytic experiments, X-ray photoemission spectra, and accurate density functional theory (DFT) based calculations, we show that small Ni clusters dispersed on the (001) surface of TiC are able to capture and dissociate methane at room temperature. Our DFT calculations reveal that two-dimensional Ni clusters are responsible for this chemical transformation, confirming that the lability of the supported clusters appears to be a critical aspect in the strong adsorption of methane. A small energy barrier of 0.18 eV is predicted for CH_4 dissociation into adsorbed methyl and atomic hydrogen species. In addition, the calculated reaction free energy profile at 300 K and 1 atm of CH_4 shows no effective energy barriers in the system. Comparison with other reported systems which activate methane at room temperature, including oxide and zeolite-based materials, indicates that a different chemistry takes place on our metal/carbide system. The discovery of a carbide-based surface able to activate methane at low temperatures paves the road for the design of new types of catalysts which can efficiently convert this hydrocarbon into other added-value chemicals, with implications in climate change mitigation.

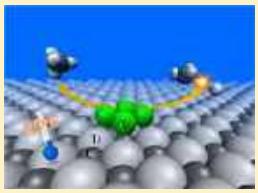

INTRODUCTION

Although carbon dioxide (CO_2) is the main greenhouse gas, in terms of its overall contribution to global warming, methane (CH_4), the simplest, most abundant, and stable alkane molecule, immediately follows.[1] Even though CH_4 emissions are five times smaller than CO_2, its greenhouse effect is 23 times larger, and therefore, its contribution to climate change is comparable to that of CO_2. The Earth's atmospheric methane content has oscillated between 350 and 800 volumetric parts per billion (ppb) during the last glacial and interglacial periods,[2] with main release sources being wetlands, living organisms, and permafrost melting processes.[3] However, since the industrial revolution, CH_4 levels have risen to the present value of 1770 ppb,[4,5] mostly from anthropogenic sources, including unsustainable landfills, livestock farming, and fossil fuels used for energy production and transportation.[6−8]

Different combined strategies oriented toward reducing the content of greenhouse gases in the atmosphere include reducing emissions, more efficient use of fossil fuel sources of energy, and using alternative renewable, green sources of energy. A particularly appealing strategy is to use carbon capture and storage (CCS) technologies,[9] where appropriate materials are used as CO_2 or CH_4 scrubbers. Even more interesting are carbon capture and usage (CCU) technologies, where the corresponding molecules, once adsorbed, are converted and ideally catalyzed by the same substrate material into other valuable chemicals.[10] In the case of captured methane, this is a real challenge because of the high 4.5 eV C−H bond strength, the absence of low-energy empty orbitals, and the presence of high energy occupied orbitals.[7] An ideal transformation process would involve the production of synthesis gas (syngas for short), a gas stream mixing carbon monoxide (CO) and hydrogen (H_2). This syngas can be used as feedstock for Fischer−Tropsch synthesis, after H_2 enrichment or diminution, to obtain long-chain hydrocarbons.[11] The syngas stream formation can pass through different reactions, including methane dry reforming (eq 1),[12−14] methane steam reforming (eq 2),[11,15,16] or methane partial oxidation (eq 3).[17−19]

Received: December 19, 2018
Published: March 8, 2019

ACS Publications © 2019 American Chemical Society

DOI: 10.1021/jacs.8b13552
J. Am. Chem. Soc. 2019, 141, 5303−5313

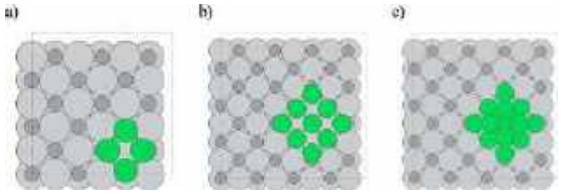

Figure 1. Most energetically stable PBE-D3 optimized geometries found for: (a) Ni_4/TiC, (b) Ni_9/TiC, and (c) Ni_{13}/TiC. Ni atoms are shown as green spheres and Ti and C atoms as light and dark gray spheres, respectively. The unit cell in each case is indicated by a black dotted line.

$$CH_4 + H_2O \rightarrow CO + 3H_2 \quad (\Delta_r H^\circ = 206 \text{ kJ mol}^{-1}) \tag{1}$$

$$CH_4 + CO_2 \rightarrow 2CO + 2H_2 \quad (\Delta_r H^\circ = 247 \text{ kJ mol}^{-1}) \tag{2}$$

$$CH_4 + \frac{1}{2}O_2 \rightarrow CO + 2H_2 \quad (\Delta_r H^\circ = -36 \text{ kJ mol}^{-1}) \tag{3}$$

The common limiting steps for such processes are first, methane adsorption, and second, its subsequent activation. These steps are intimately related to the first hydrogen abstraction from CH_4, which is regarded as the rate-determining step of the overall mechanism.[20−22] In addition, methane also can be transformed directly into commodity chemicals such as methanol, ethylene, or benzene.[7] An optimal catalyst for CH_4 capture and conversion would be one that simultaneously meets two criteria, namely, (i) it must adsorb CH_4, ideally even at room temperature, and (ii) it must feature a low energy barrier for C−H bond scission, preferably to be overcome at room temperature as well. On a reaction free energy profile, these criteria would imply that the first dehydrogenation reaction step transition state would be lower than the molecular desorbed state.

There is an ongoing search for materials that can accomplish the activation of methane at low temperatures to enable the direct conversion of CH_x fragments into commodity chemicals.[7] Most of the studies dealing with the activation of methane have focused their attention on metals, bulk oxides, homo- and heteronuclear oxide clusters, zeolites, and also on biomimetic materials.[7,21−25] On metal surfaces, methane binds weakly and the probability for dissociation is low.[26] The reactions in eqs 1−3 above are nowadays carried out at elevated temperatures on Ni-based catalysts.[11,20] A previous DFT study regarding the Ni(111) surface explains this fact in the sense that the first C−H bond scission is endothermic by 0.36 eV and involves an energy barrier (E_b) of 1.07 eV.[27] Similar calculations for CH_4 on Pt(111) show the process to be energetically uphill by 0.17 eV with a slightly reduced energy barrier of 0.93 eV. This result is in line with the experimental observation of a barrier reduction of 0.29 ± 0.06 eV when comparing CH_4 reactivity on Pt(111) to that exhibited by Ni(111).[28] Nevertheless, metals are not, in general, very efficient for promoting C−H bond cleavage.[24−30]

A few oxide and metal/oxide systems can activate methane at low temperature.[21,22,31,32] On these materials, it has been found that cooperative interactions between a cation and an oxide center can lead to a cleavage of the first C−H bond in methane with energy barriers that are below 0.5 eV. In this aspect, these oxide-based systems are more efficient than metals or metal alloys. In this study, we move in a different direction and, by combining X-ray photoemission spectroscopy (XPS) experiments with state-of-the-art DFT based calculations, we show that small Ni particles in contact with a metal carbide such as TiC can also trigger the cleavage of C−H bonds at 300 K. This is a remarkable finding since both bulk Ni and TiC exhibit very low activity toward methane activation. Clearly, there is a synergy in the Ni/TiC(001) system that facilitates the activation of methane. In this way, the present work points to a new approach for developing a novel family of materials that would be active for CH_4 activation under mild conditions.

EXPERIMENTAL DETAILS

The reactivity of Ni/TiC(001) surfaces toward methane was studied in a system which combines an ultrahigh-vacuum (UHV) chamber (base pressure ~7×10^{-10} mbar) and a batch reactor.[33−36] Within this system, the sample could be transferred between the reactor and UHV chamber without exposure to air. The UHV chamber was equipped with instrumentation for X-ray and ultraviolet photoelectron spectroscopies (XPS and UPS), low-energy electron diffraction (LEED), ion scattering spectroscopy (ISS), and temperature-programmed desorption (TPD).

The TiC(001) single crystal was cleaned following methodologies reported in the literature.[36,37] Nickel was vapor-deposited on the TiC(001) surface at 300 K.[36] The admetal doser consisted of a resistively heated tungsten basket with a drop of ultrapure Ni inside.[36] Initially, the flux of the doser was calibrated by the acquired thermal desorption spectra for the desorption of Ni from a Mo(100) substrate.[34,38] This information was then used to calibrate admetal coverages estimated by means of XPS.[34]

In the tests of methane activation, the Ni/TiC(001) samples were transferred to the reactor at ~300 K, then 1.33 mbar (1 Torr) of methane was introduced for a period of 5 min. After this exposure, the methane gas was removed and each sample was transferred back to the UHV chamber for surface characterization. Maximum activity was found for small coverages, 0.2−0.3 monolayers (ML), of nickel on the carbide substrate.

COMPUTATIONAL METHODS

As explained above, both Ni(111) and TiC(001) surfaces are inactive whereas maximum conversion of CH_4 is observed for small dosages of 0.2−0.3 ML of Ni over the TiC(001) surface. This suggests that small supported Ni clusters are the main players, in accordance with previous studies of Au and Cu clusters on TMCs.[39−41] Consequently, CH_4 activation on Ni/TiC(001) was assessed by modeling different types of TiC-supported Ni clusters using periodic DFT based calculations. Specifically, the pristine TiC(001) surface, three different Ni_n/TiC(001) (n = 4, 9, 13) clusters (see Figure 1), and a Ni supported nanorod model (see Figure 2) featuring low coordinated sites were investigated. These particular Ni clusters sizes have been selected as representative models as they feature compact high symmetry structures, thus maximizing the atomic coordination, which

DOI: 10.1021/jacs.8b13552
J. Am. Chem. Soc. 2019, 141, 5303−5313

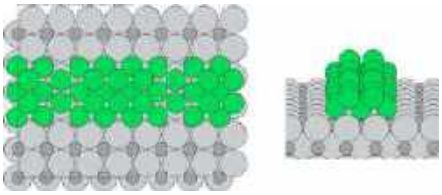

Figure 2. Optimized geometries (top and near-side views) of the Ni rod. Ni atoms are shown as green spheres and Ti and C atoms as light and dark gray spheres, respectively. The unit cell is indicated by a black dotted line.

makes them particularly likely to be energetically stable. The calculations employed the Perdew–Burke–Ernzerhof (PBE)[42] exchange-correlation (xc) functional, and the contribution from dispersive interactions was included through the D3 correction as proposed by Grimme (PBE-D3).[43] For the systems containing Ni nanoclusters, as well as for gas phase CH_3 and H (see below), spin polarization was taken explicitly into account. The transition states (TS) were located using the Climbing-Image NEB (CI-NEB) method.[44] Initial guesses for the five employed intermediate images were generated by means of the Atomic Simulation Environment (ASE)[45] using the Image Dependent Pair Potential (IDPP).[46] The energy reaction profiles were obtained at 0 K and in vacuum but also at working conditions of temperature and CH_4 partial pressure by using the atomistic thermodynamics approach.[47] All calculations were carried out using the Vienna Ab Initio Simulation Package (VASP) code.[48] Further computational details are provided in the Supporting Information. Favorable adsorption energies, E_{ads}, have a negative sign.

RESULTS AND DISCUSSION

Experiments. In our experiments, surfaces of Ni/TiC(100), TiC(001), and Ni(111) were exposed to methane in a batch reactor. Figure 3 shows C 1s XPS spectra collected after exposing to methane a TiC(001) surface precovered with 0.2 ML of nickel (top panel) and bare Ni(111) (bottom panel). In agreement with previous studies,[26] we found no adsorption of methane after exposing Ni(111) and TiC(001) to 1.33 mbar (1 Torr) of the molecule at 300 K. The adsorption and dissociation of methane on Ni/TiC(001) produces a peak at ~284 eV that can be attributed to adsorbed CH_3 or CH_2 species.[32] We estimate that 0.2–0.3 ML of CH_x are deposited on the surface as a consequence of dissociation of methane on the Ni particles or the nickel–carbide interface. The ratio of CH_x species to Ni adatoms was in the range of 1–1.5. Figure 4 shows Ni $2p_{3/2}$ XPS spectra recorded for a Ni/TiC(001) surface before and after adsorption of the CH_x species produced by the dissociation of CH_4 at 300 K. Reaction with methane induced an attenuation in the signal of nickel (36%) and a positive shift of ~0.4 eV in the Ni $2p_{3/2}$ peak. Thus, the CH_x deposited on the Ni/TiC(001) surface is in direct contact with the nickel.

We also found that the amount of Ni present on the carbide surface had a strong effect on the reactivity of the surface toward methane. Figure 5 displays the change of the CH_x intensity (peak at ~284 eV) as a function of Ni coverage in Ni/TiC(001). In these experiments, all the surfaces were exposed to 1 Torr of methane for 5 min at 300 K. A maximum of activity is seen at Ni coverages of 0.2–0.3 ML. Under these conditions, small particles of nickel interact strongly with the TiC substrate.[33] An increase in the Ni coverage increases the

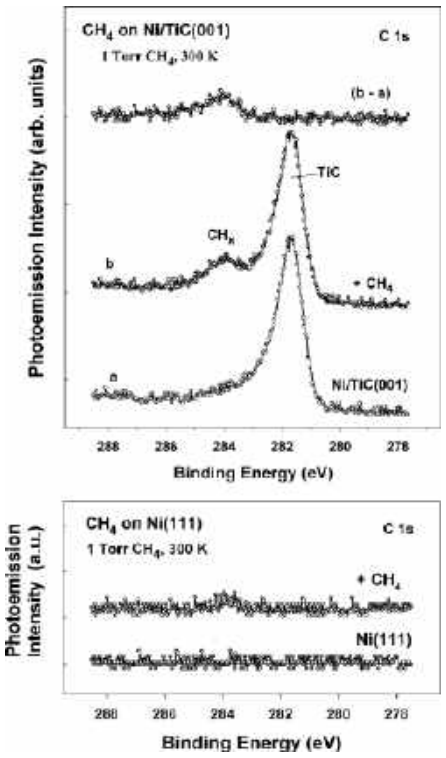

Figure 3. C 1s XPS spectra collected before and after dosing methane to Ni/TiC(001) and Ni(111) surfaces at 300 K (top and bottom panels, respectively). The dosage of methane was 1 Torr for 5 min. The coverage of Ni on the TiC(001) substrate was 0.2 ML.

size of the Ni particles, favoring Ni–Ni interactions over Ni–TiC interactions, and the admetal nanoparticles slowly acquire the chemical properties of bulk nickel losing their reactivity toward methane. At large coverages of nickel, the dissociation of methane was negligible as seen on plain Ni(111).[21,26]

Temperature had a strong effect on the stability of the adsorbed CH_x groups. In the XPS experiments, we observed the gradual disappearance of the CH_x species when the temperature was raised from 320 to 420 K, see Figure 6. Using a mass spectrometer we detected mainly the evolution of CH_4 from the CH_x/Ni/TiC(001) surface between 340 and 410 K, with weaker signals for C_2H_6 and C_2H_4 (see Figure 7). Thus, it is clear that the species produced by dissociation of methane are chemically active and can be used for producing more complex hydrocarbons. Relatively weak interactions between CH_x and Ni are reflected in the Ni 2p XPS results shown in Figure 4 where the intensity and position of the Ni $2p_{3/2}$ peak are recovered after desorbing the CH_x groups by heating to 450 K. We did not observe any decrease in the reactivity of the surface after five cycles of adsorption–desorption. In CH_x/Ni/

DOI: 10.1021/jacs.8b13552
J. Am. Chem. Soc. 2019, 141, 5303–5313

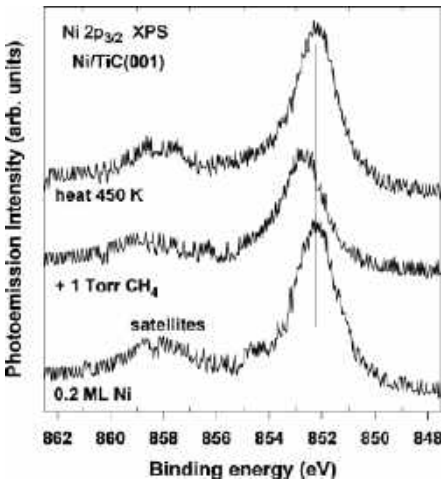

Figure 4. Ni $2p_{3/2}$ XPS spectra collected before and after adsorbing methane on a TiC(001) surface precovered with 0.2 ML of nickel. In the first step the surface was exposed to 1 Torr of methane at 300 K for 5 min in a batch reactor. After pumping the gas and recording the spectrum in the middle of the figure, the CH_x/Ni/TiC(001) system was heated to 450 K to induce the desorption of the adsorbed CH_x species.

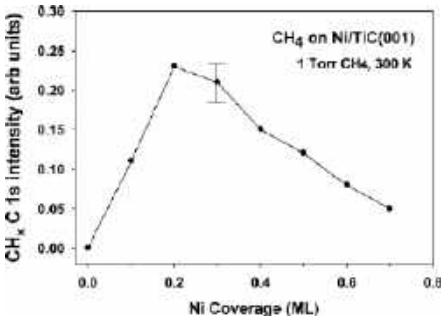

Figure 5. Variation of the CH_x intensity as a function of Ni coverage in Ni/TiC(001). In all cases the surface was exposed to 1 Torr of methane for 5 min at 300 K. This type of experiment was done three times, and average values are reported with the typical variation for the measurements in the CH_x C 1s intensity.

TiC(001), one has strong Ni↔TiC interactions and moderate Ni↔CH_x interactions when the Ni coverages are below 0.3 ML.

Computational Study. To better understand the above-described experiments for the Ni/TiC(001) systems, CH_4 adsorption and dissociation were studied on three Ni_n clusters (representing small to medium coverages of the admetal) and over a nanorod (representing a large coverage of the admetal), all supported on a slab model of TiC(001). For comparison,

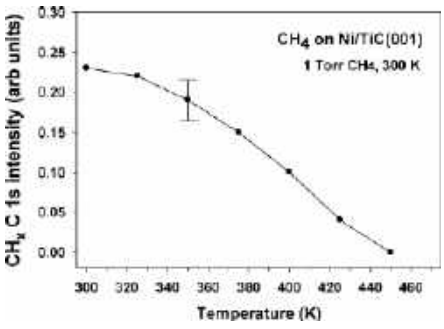

Figure 6. Effect of temperature on the C 1s signal for the CH_x species obtained after dosing methane to Ni/TiC(001) (θ_{Ni} of ~0.2 ML). Initially, the Ni/TiC(001) surface was exposed to 1 Torr of methane for 5 min at 300 K. The gas was pumped out and the temperature of the sample was ramped up under ultrahigh vacuum conditions. This type of experiment was done five times, and average values are reported with the typical variation for the measurements in the CH_x C 1s intensity. In these experiments, we did no observe signs for deactivation of Ni/TiC(001).

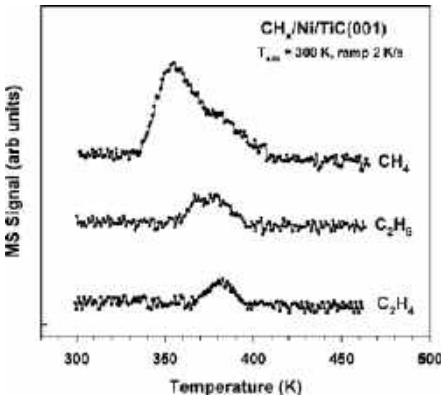

Figure 7. Temperature-programmed desorption (TPD) spectra for the evolution of methane, ethane, and ethylene from a CH_x/Ni/TiC(001) surface. A TiC(001) surface precovered with 0.2 ML of Ni was exposed to 1 Torr of methane at 300 K in a microreactor. The gas was pumped out, and the sample was transferred to a UHV chamber for a TPD study (heating ramp 2 K/s).

CH_4 adsorption and dissociation on the pristine TiC(001) surface was also considered. In the latter reference case, a previous study reported a CH_4 adsorption energy of −0.25 eV,[49] similar to the value of −0.24 eV for the Ni(111) surface obtained using DFT calculations employing the PBE functional with the Grimme D2 correction.[50] The C−H bond scission of CH_4 on TiC(001) is energetically downhill although it features a large E_b of 1.5 eV (Figure 6); a similar value of 1.07 eV has been reported for the case of CH_4 dissociation on the Ni(111) surface.[27] The most stable CH_3 and H adsorption sites and

DOI: 10.1021/jacs.8b13552
J. Am. Chem. Soc. 2019, 141, 5303−5313

modes are reported in section S2 of the Supporting Information (SI) are the TS structures for CH_4 dissociation on the clean TiC(001) are reported in section S3 of the SI. Both, TiC(001) and Ni(111) are able to adsorb methane but both feature a high C−H bond breaking energy barrier well above that of the desorption limit, thus inhibiting any further reaction as inferred from the energy (E) and Gibbs free energy (G) profiles in Figure 8.

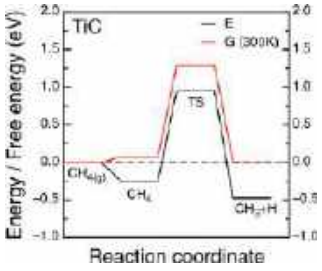

Figure 8. ZPE corrected energy profiles (E, black lines) and Gibbs free energy profiles (G) at 300 K, 1 atm of CH_4 (red lines) for CH_4 adsorption and subsequent dissociation on the clean TiC(001) surface.

With respect to the bare TiC(001) and Ni(111) surfaces, the CH_4 dissociation reaction profile on the TiC(001)-supported Ni_n clusters completely changes. The smallest Ni_4/TiC cluster features a high degree of lability since it easily stretches or contracts upon interaction with CH_4, CH_3, or H. Such easiness of deformation gradually vanishes for the larger Ni_9 and Ni_{13} clusters. The structure of Ni_4 and Ni_9 clusters is planar whereas Ni_{13} exhibits a three-dimensional capped pyramid structure which allows us to assess the effect of dimensionality on the CH_4 adsorption and dissociation.

On the TiC-supported Ni_n clusters, the surface sites that interact most strongly with CH_4, CH_3, and H moieties have been identified by a systematic computational screening carried out within the PBE-D3 approach. Results show that CH_4 adsorbs on all supported Ni optimized structures with adsorption energy (E_{ads}) of ∼0.3 eV, whereas CH_3 and H exhibit larger E_{ads} values of ∼2.5 eV. The most favorable adsorption situations and corresponding E_{ads} values are collected in Table 1. The structure of all considered sites, the adsorption energy values and optimized geometries for the most stable cases can be found in sections S3 and S4 of the Supporting Information. Results show that on the Ni_n/Ti(001)—Ni_n/TiC in the following—systems, the CH_4 adsorption energy is 1.5−2.5 times stronger than on the clean TiC(001) surface. Notice that CH_4 prefers to adsorb on low coordinated Ni atoms (i.e., on the vertices of the clusters, see Figure S4), rather than on the TiC substrate near the Ni cluster boundary region. Furthermore, CH_4 adsorption on the 3D supported Ni_{13} cluster is noticeably weaker than for the planar 2D Ni_4 and Ni_9 cases. As the size of the Ni cluster increases, its reactivity toward CH_4 and CH_3 decreases, in agreement with the experimental trend seen in Figure 5. The highest reactivity is found on the Ni_4/TiC(001) system, where all the Ni adatoms are in contact with the carbide surface and have a few metal neighbors. At this point one may wonder about the origin of such enhanced activity of the Ni_4 clusters when supported on TiC(001) and whether this is instigated by a particular electronic structure. Such enhanced activity and reactivity observed on Ni_4 clusters supported on TiC(001) has been observed in the past in similar systems, such as Au_4 clusters supported on TiC(001) catalysts, active in desulfurization reactions,[39,51,52] as well as Cu_4, Ni_4, and Au_4 clusters supported on TiC(001) which exhibit activity toward CO_2 hydrogenation reactions.[36] Detailed experiments and theoretical modeling have shown that the underlying chemistry of transition metal clusters supported on carbides such as TiC arises from the substrate induced electron density polarization of the supported metal clusters, with no evidence of net charge transfer. This is in agreement with experimental and computational evidence confirming that the enhanced activity/reactivity is larger for small flat metal clusters and tends to vanish in larger, three-dimensional metal clusters and nanoparticles.[53,54]

Table 1. PBE-D3 Adsorption Energies (ZPE Corrected, E_{ads}, in eV) of CH_4, CH_3, and H on the Clean TiC(001) and Ni(111) Surfaces and on Several Ni_n/TiC Surfaces (n = 4, 9, 13)

	E_{ads} /eV		
	CH_4	CH_3	H
Ni(111)	−0.24[a]	−1.81[b]	−2.77[b]
TiC(001)	−0.25	−2.26	−2.77
Ni_4/TiC	−0.57	−3.12	−3.42
Ni_9/TiC	−0.64	−3.04	−3.32
Ni_{13}/TiC	−0.36	−2.83	−3.21

[a]Value taken from ref 50 (PBE-D2); note that it does not include ZPE. [b]Values taken from ref 55 (PBE).

However, aside from the electron density polarization reported for other related systems, the relatively high lability of the smallest Ni_4 supported cluster deserves some additional comments. The cluster elongates in the direction where one Ni atom interacts with CH_4 and contracts in the perpendicular direction, adopting a rhombus-like shape with, with a ratio between major and minor diagonals (r_D) of 1.34. The same effect is observed for CH_3 and H adsorption, with an r_D values of 1.52 and 1.43, respectively. In both cases, the Ni atom rearrangement allows the formation of Ni_3 3-fold hollow sites, where both CH_3 and H species adsorb. Lability is not observed either for methane or H adsorbed on the Ni_9/TiC cluster, yet the Ni_3 3-fold hollow site emerges when CH_3 is adsorbed, with an r_D of 1.30, hence smaller than the value of 1.52 for Ni_4/TiC. Finally, on the 3D Ni_{13}/TiC cluster, the different species energetically prefer to adsorb at the edges of the cluster.

The CH_4 dissociation on Ni_4/TiC appears to be facilitated when starting from a vertex site with CH_3 + H going to bridge sites with a calculated E_b of 0.18 eV only (see TS1 in Figure 9); a drastic reduction when compared to the case of Ni(111) implying an E_b of 1.07 eV.[27] This significant E_b lowering is related to the overall reaction energy going from 0.35 eV (endothermic) on the Ni(111) surface to −0.76 eV (exothermic) on Ni_4/TiC. This is as expected from the Brønsted−Evans−Polanyi (BEP)[56,57] relationship applied to heterogeneously catalyzed reactions, as suggested by Pallasana and Neurock[58] and popularized by Nørskov et al.[59] Indeed, for CH_4 dissociation on the Ni_4, Ni_9 and Ni_{13} clusters supported on TiC(001) and Ni(111), a quantitative, BEP relationship

DOI: 10.1021/jacs.8b13552
J. Am. Chem. Soc. 2019, 141, 5303−5313

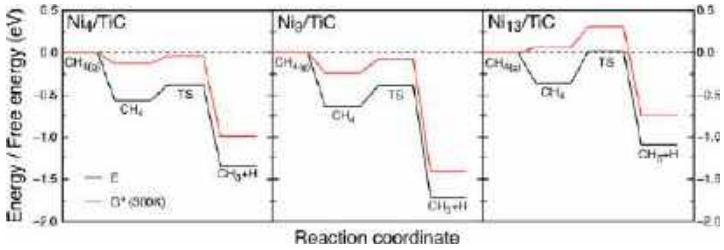

Figure 9. Total (ZPE corrected) energy profile (black lines, equivalent to the Gibbs free energy profiles at 0 K and zero CH_4 partial pressure) and at 300 K and 1 atm of CH_4 (red lines) on the three studied Ni_n/TiC(001) systems.

emerges when plotting E_b in front of the reaction energy as discussed in detail below.

As illustrated in Figure S9, the lability effect of the small Ni_4 cluster supported on TiC is evident. To investigate its possible effect on the CH_4 first dehydrogenation step reaction energy profile, calculations have been carried out by freezing both TiC surface and Ni cluster atoms in the most stable configuration. The resulting constrained energy profile show a significant increase of the E_b from 0.18 eV up to 0.42 eV (see Figure S10 in the Supporting Information), highlighting the important role of the lability of such small clusters in the course of CH_4 adsorption and dissociation. Interestingly, we note that r_D lowers along the reaction coordinate, from 1.34 for adsorbed CH_4, 1.19 for TS2, and 1.00 for CH_3 + H products. Finally, we note that the spin properties of Ni clusters are not negligible during the catalytic process. While the total magnetic moment for the reactant configuration (i.e., CH_4−Ni_4/TiC) is close to 1, it becomes quenched down to zero for both the TS and the product configurations. This is a clear fingerprint of the multiconfigurational character of the electronic structure of these systems that is, nevertheless, sufficiently well described by spin polarized DFT.[60] These differences in the total magnetization along the CH_4 dissociation pathway are also observed for larger Ni clusters and have been shown to be a key point in other catalytic processes using magnetic metal clusters, as in the course of ammonia synthesis by supported Fe clusters.[61]

For the larger Ni_9 supported cluster, the most favorable path corresponds to the direct dissociation from the CH_4 molecule located on top of a vertex Ni atom to a CH_3 + H configuration where CH_3 is placed on a bridge site and the H on a 4-fold hollow site (see Figure S11). On this Ni_9/TiC system, E_b is just 0.25 eV, only 0.07 eV higher than corresponding value for Ni_4/TiC (0.18 eV). Interestingly, this energy barrier is still much lower than the −0.64 eV CH_4 adsorption energy on Ni_9/TiC (Table 1).

Finally, on the largest Ni_{13} supported cluster, CH_4 and the CH_3 preferentially adsorb on a vertex of the cluster, and the released H adatom adsorbs on a 3-fold hollow site of small (111) facets of the supported cluster, as shown in Figure S12. Here E_b becomes 0.38 eV, noticeably higher than the energy barriers for the smaller clusters (0.18 and 0.25 eV for Ni_4/TiC and Ni_9/TiC, respectively). Nevertheless, this value is already slightly higher than the methane adsorption energy of 0.36 eV on this Ni_{13}/TiC model system. This implies that the CH_4 dissociation criteria would not be completely fulfilled, indicating that on such larger 3D clusters the dissociation process becomes unfavorable, in agreement with the experimental observations. Note that the most stable arrangement for the CH_4−Ni_n/TiC system coincides with the most stable arrangement for the bare Ni_n/TiC clusters in all three models. Only some elongations or contractions between the Ni atoms are observed in the two-dimensional Ni_4/TiC and Ni_9/TiC models.

The synergic effect between Ni particles and the TiC(001) support becomes more evident when comparing CH_4 adsorption energies and first dehydrogenation energy barriers to equivalent values calculated for the pristine Ni(111) and TiC(001) extended surfaces reported in Table 2. Clearly, only

Table 2. CH_4 Adsorption Energies, E_{ads}, and First Dehydrogenation Energy Barriers, E_b, on Ni_n/TiC, TiC(001), and Ni(111)[a]

catalyst	CH_4 E_{ads}	E_b
Ni_4/TiC	−0.57	0.18
Ni_9/TiC	−0.64	0.25
Ni_{13}/TiC	−0.36	0.38
TiC(001)	−0.25	1.22
Ni(111)	−0.24[b]	1.18[c]

[a]All values are given in eV. [b]Reference 50 (PBE-D2). [c]Reference 55 (PBE). Note that present E_b values account for the ZPE, which is not the case for the value for Ni(111) in ref 50; the average ZPE decreases the energy barrier by 0.15 eV.

2D Ni clusters supported on TiC exhibit E_{ads} values larger than E_b energy barriers. This conclusion is further supported from total energy and Gibbs free energy profiles in Figure 9; the latter corresponding to 300 K and 1 atm (1.01325 bar) of CH_4 partial pressure. The Gibbs free energy profiles indicate that on all the studied Ni_n/TiC clusters both adsorption and dissociation processes are exergonic, contrary to the situation corresponding to Ni(111). Moreover, the smaller Ni_4/TiC and Ni_9/TiC clusters present no effective free energy barrier for CH_4 dissociation at normal conditions, confirming that small Ni particles are particularly active to trigger CH_4 dissociation at room temperature, in agreement with the experimental findings. Note also that room temperature is actually the temperature where the highest conversion is achievable, given that a rise in temperature would only place the effective energy barrier above the reactant energy limit, in accordance with experiment.

At this stage, one may wonder whether the effect of the TiC support consists in stabilizing adsorbed methane, decreasing

DOI: 10.1021/jacs.8b13552
J. Am. Chem. Soc. 2019, 141, 5303−5313

the dissociation energy barrier, or both. The support effect has been qualitatively studied by comparing the full energy profile of the dissociation reaction computed in two different ways: (i) with the surface atoms and the cluster Ni atoms frozen to the most stable configuration for the clean supported cluster (black line in Figure 10) and (ii) for the same clean cluster molecular structure but removing the TiC support (blue line in Figure 11). Obviously, in the case of CH_4 interacting with the unsupported Ni_4 cluster with the frozen structure, the ZPE corrections have not been included. The results of this computational experiment indicate that, while the energy barrier for CH_4 dissociation on the unsupported or supported Ni_4 cluster is quite similar (0.43 versus 0.50 eV), CH_4 adsorption on Ni_4 is no longer favored when the TiC support is not present, a clear demonstration of the key role of the interaction between the Ni cluster and the support. The effect seems also to be linked to the planar structure of such small Ni_n clusters adopted upon interaction with the TiC(001) surface. This is agreement with the results reported for CH_4 adsorption and dissociation on tetrahedral Ni_4 and icosahedral Ni_{13} gas phase clusters where E_{ads} of 0.39 and 0.40 eV are smaller and E_b values of 0.44 and 0.43 eV are larger than for the supported clusters, respectively.[62]

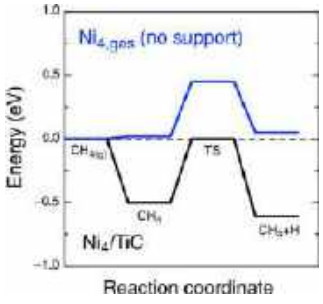

Figure 10. Energy profiles (non ZPE corrected) for CH_4 adsorption and subsequent dissociation on frozen Ni_4 cluster supported on TiC (black line) and unsupported (blue line).

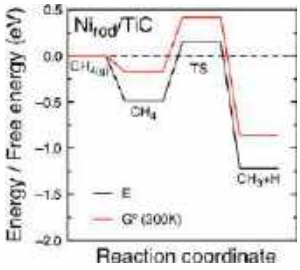

Figure 11. Total ZPE corrected energy (black lines) and Gibbs free energy at 300 K and 1 atm of CH_4 (red lines) profiles for CH_4 adsorption and dissociation on the Ni nanorod supported on TiC(001).

Finally, we focus on the finite size effects of the three supported Ni clusters by comparing E_{ads} and E_b values with respect to an infinite array of Ni atoms forming a supported nanorod, as shown in Figure 2. The nanorod shape resembles that of a Ni_{13}/TiC cluster expanded in one [010] direction so as to generate a periodic structure with bulk-like properties. The incommensurability of the periodic Ni nanorod structure and the TiC(001) surface leads to clustering of Ni atoms and a degree of lability of the second layer of Ni atoms. On this supported nanorod model, E_{ads} is −0.49 eV, slightly smaller than the corresponding values on Ni_4/TiC and Ni_9/TiC (Table 1), yet highlighting the importance of low coordinated Ni atoms on methane adsorption as well as the effect of the support. Note, however, that the E_{ads} value for the supported nanorod is larger than that computed for the Ni_{13}/TiC cluster (−0.36 eV), which is attributed to the above-stated lability of the Ni rod compared to the rigidity of the Ni_{13}/TiC cluster. However, the important aspect is that, on the supported nanorod, the CH_4 dissociation energy barrier is 0.64 eV, much higher than the corresponding values for the finite supported clusters and also higher than the desorption energy. The latter kinetically inhibits CH_4 dissociation, with an even more unfavorable free energy profile at working conditions of temperature and pressure (see Figure 11).

Unravelling Trends in C−H Activation. To further investigate the chemistry involved in the activation of the C−H bond in CH_4 through its interaction with the Ni/TiC systems studied in the present work, as well as to attempt to obtain appropriate simple descriptors, we analyze in detail the relationship between the calculated values of the energy barrier for C−H activation and the corresponding energy reaction with adsorbed CH_3 and H as products. For convenience and also for a possible practical use of the resulting BEP relationship,[58,59] the values not corrected by the ZPE have been used. Note, however, that the main influence of ZPE is in the adsorption energy of CH_4, which leads to an average systematic reduction of the calculated energy barriers of ~0.15 eV. Besides, the values corresponding to the Ni(111) extended surface have been included as this provides an appropriate model for the limiting case of very large supported particles. The resulting BEP plot thus constructed is presented in Figure 12 and shows a clear, linear trend. This is an interesting result since it would allow one to estimate the energy barrier for similar systems by simple interpolation and without the need to compute the vibrational frequencies of the adsorbed products. More importantly, the BEP relationship in Figure 12 shows that the low energy barrier for the systems used in the experiments comes from the fact that the underlying carbide stabilizes the dissociation products when the supported particles are small enough. The effect gradually disappears for larger particles and almost vanishes for the supported nanorod model, where the decrease in the energy barrier with respect to Ni(111) is clearly due to the presence of the low coordinated Ni atoms.

At this point one may wonder whether the chemistry governing C−H scission in these systems bears some similarity to that exhibited by oxides and zeolites, some of which are able to dissociate CH_4. In a recent paper, Latimer et al.[21] studied trends in C−H activation for several hydrocarbons on a broad family of materials containing O atoms including, among others, oxides, zeolites, metal organic frameworks, and

DOI: 10.1021/jacs.8b13552
J. Am. Chem. Soc. 2019, 141, 5303−5313

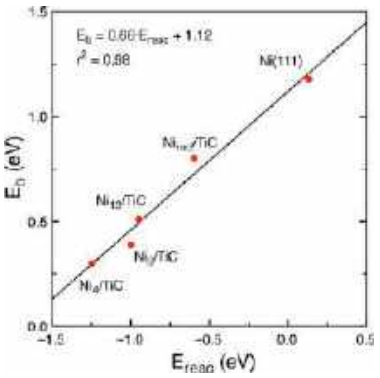

Figure 12. Energy barrier (E_b) for CH_4 to CH_3 + H dissociation on the Ni/TiC systems and on Ni(111) versus the reaction energy (E_{reac}). The values used to construct the plot are reported in Table S2 and, for convenience, do not include the ZPE term.

graphene. Interestingly, they argue that the overall chemistry is governed by hydrogen affinity (E^f_H) defined as the formation energy of adsorbed hydrogen with respect to gas phase H_2O and O_2. More specifically, these authors found that E^f_H can be used as a descriptor for predicting the formation energy of the transition state for C–H scission (E^f_{TS}) in a variety of O containing catalysts; i.e., that E^f_{TS} goes linear E^f_H. Moreover, they postulate that the origin of this behavior lies in the radical-like TS character involving one site on the catalyst surface only and, therefore, is supposed to be rather independent of the particular catalyst geometry.[21]

Inspired by this work, we adapted the definition of E^f_H and E^f_{TS} to the Ni/TiC systems studied in the present work. To this end, we define the formation energy of adsorbate i, E^f_i, referenced to the clean surface and to gas-phase H_2 and CH_4 as

$$E^f_i = U_{i+slab} - U_{slab} - \sum_j (n_j R_j) \quad (4)$$

where U_{i+slab} is the raw DFT energy of the slab with adsorbate i, U_{slab} is the raw DFT energy of the slab, n_j is the number of atomic species j in i, and R_j is the reference energy of that atomic species with the reference energies R_j for each atomic species defined as

$$R_H = \frac{1}{2} U_{H_2(g)} \quad (5)$$

$$R_C = U_{CH_4(g)} - 4R_H \quad (6)$$

where again $U_{i(g)}$ is a "raw" energy directly taken from the DFT based calculation. We note that one interesting feature of the formation energy approach (as opposed to the use of pure DFT energies) is that it does not distinguish between thermodynamic minima (adsorbed states) and saddle points (transition-states). Thus, it is possible to define the formation energy of the CH_3–H dissociation transition state, E^f_{TS}, as

$$E^f_{TS} = U_{CH_3-H+slab} - U_{slab} - R_C - 4R_H \quad (7)$$

which is related to the DFT calculated energy barrier for CH_3–H dissociation, E_b, as

$$E_b = E^f_{TS} - E^f_{CH_4} \quad (8)$$

The analysis of the E^f_{TS} versus E^f_H plots (Figure S15) shows that while the main trend in the formation energy of the TS is well captured by hydrogen affinity E^f_H descriptor, there is a considerable deviation from linearity implying that the chemical mechanism for CH_4 activation by Ni/TiC is different and does not involve the same type of radical like TS. Interestingly, plotting the natural logarithm of the raw DFT energy barrier with respect to the adsorbed hydrogen formation energy results in an almost perfect straight line as shown in Figure 13, indicating a somehow different chemistry.

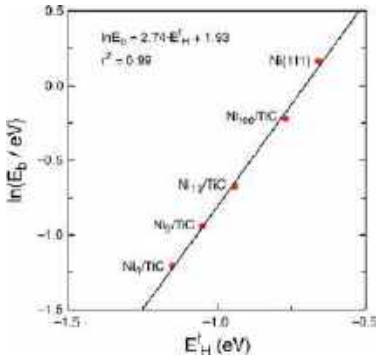

Figure 13. Logarithm of the energy barrier (E_b) for CH_4 to CH_3 + H dissociation on the Ni/TiC systems and on Ni(111) versus the E^f_H. For convenience, the values used to construct the plot do not include the ZPE term.

In the case of low-temperature methane dissociation on $IrO_2(110)$[31] and $Ni/CeO_2(111)$,[63] a concerted mechanism has been reported where the cleavage of the first C–H bond involves simultaneous bonding interactions with a metal cation and an oxygen anion. This type of interaction cannot take place on a metal/carbide system where the C centers do not have the very high negative charge present in the O centers of an oxide (i.e., carbides have a lower degree of ionicity than oxides).[64,65] Nevertheless, the C centers in the carbide can be involved in the activation of methane by enhancing the reactivity of a supported metal or by accommodating the H and CH_3 produced by the dissociation of the hydrocarbon.

CONCLUSIONS

The interaction of methane with pristine Ni(111) and TiC(001) surfaces is very weak. In contrast, a series of XPS experiments for 0.2 ML of Ni supported on a TiC(001) single crystal point to CH_4 adsorption and decomposition at room temperature and low partial pressures of the hydrocarbon. This unexpected, exciting, and technologically relevant result has been explained by means of DFT based calculations on models of Ni clusters and nanorods supported on TiC(001) surface. These calculations confirm that small 2D supported Ni clusters are responsible for the observed catalytic behavior featuring

DOI: 10.1021/jacs.8b13552
J. Am. Chem. Soc. 2019, 141, 5303–5313

adsorption energies up to −0.64 eV, thus allowing for CH_4 adsorption at room temperature. At the same time, on the supported clusters, C−H bond scission energy barriers become smaller than the CH_4 adsorption energies and can be as low as 0.18 eV. The lability of such 2D few-atom Ni clusters, together with the interaction with the support, appear to promote methane adsorption and low-energy barrier decomposition into CH_3 and H. These features are lost for larger 3D supported Ni clusters indicating that the mere existence of low coordinated sites is not sufficient to trigger C−H scission before desorption takes place.

Our results for a range of Ni/TiC systems, including extended Ni(111) surface as a limiting case, show that a BEP relationship holds for the C−H scission. This indicates that the interaction between the metal and the underlying carbide support stabilizes the dissociation products with a concomitant decrease of the energy barrier involved in this elementary step. Moreover, it is found that the adsorbed hydrogen formation energy E^f_H constitutes a very good descriptor for methane activation on these Ni-based catalysts. However, E^f_H appears to be directly related to the logarithm of the raw energy barrier E_b for CH_4 dissociation and not to the TS formation energy (E^f_{TS}) as in the case of oxides and zeolites,[21] implying that a different chemistry is involved. The present results open the way for the preparation of a new family of active materials for methane activation and conversion under mild conditions, thus widening the applications of existing natural gas resources.

■ ASSOCIATED CONTENT

Supporting Information

The Supporting Information is available free of charge on the ACS Publications website at DOI: 10.1021/jacs.8b13552.

Computational details, adsorption energies on clean TiC, transition state for CH_4 dissociation on clean TiC, adsorption energies on supported Ni clusters, transition states for CH_4 dissociation on supported Ni clusters, adsorption energies on the supported Ni nanorod, transition state for CH_4 dissociation on the supported Ni nanorod, kinetic parameters and free energies, and details on the calculation of descriptors for C−H activation (PDF)

■ AUTHOR INFORMATION

Corresponding Authors

*rodriguez@bnl.gov.
*francesc.illas@ub.edu.

ORCID

Francesc Viñes: 0000-0001-9987-8654
Stefan T. Bromley: 0000-0002-7037-0475
José A. Rodriguez: 0000-0002-5680-4214
Francesc Illas: 0000-0003-2104-6123

Notes

The authors declare no competing financial interest.

■ ACKNOWLEDGMENTS

This manuscript has been authored by employees of Brookhaven Science Associates, LLC under Contract No. DE-SC0012704 with the U.S. Department of Energy. The research carried out at the Universitat de Barcelona was supported by the Spanish MINECO/FEDER Grant CTQ2015-64618-R and, in part, by Generalitat de Catalunya (Grants 2017SGR13 and XRQTC). H.P. acknowledges financial support from Generalitat de Catalunya predoctoral FI-DGR-2015 Grant. J.J.P. thanks the Spanish MINECO for Ayuda para la formación de doctores contract (Grant BES-2016-78816). F.V. thanks the MINECO for a postdoctoral Ramón y Cajal (RyC) research contract (Grant RYC-2012-10129), and F.I. acknowledges additional support from the 2015 ICREA Academia Award for Excellence in University Research. Financial support from Spanish MINECO through the Excellence María de Maeztu Program (Grant MDM-2017-0767) is also fully acknowledged. Authors are thankful for the computational time provided at Marenostrum-IV supercomputer at the Barcelona Supercomputing Centre (BSC) through the Grants QCM-2018-2-0006 and QCM-2018-1-0032 awarded by the Red Española de Supercomputacion (RES).

■ REFERENCES

(1) Feichter, J.; Schurath, U.; Zellner, R. Luftchemie und Klima. *Chem. Unserer Zeit* **2007**, *41*, 138−150.
(2) Spahni, R.; Chappellaz, J.; Stocker, T. F.; Loulergue, L.; Hausammann, G.; Kawamura, K.; Flückiger, J.; Schwander, J.; Raynaud, D.; Masson-Delmotte, V.; Jouzel, J. Atmospheric Methane and Nitrous Oxide of the Late Pleistocene from Antarctic Ice Cores. *Science* **2005**, *310*, 1317−1321.
(3) Grunwald, M.; Dellwig, O.; Beck, M.; Dippner, J. W.; Freund, J. A.; Kohlmeier, C.; Schnetger, B.; Brumsack, H.-J. Methane in the Southern North Sea: Sources, Spatial Distribution and Budgets. *Estuarine, Coastal Shelf Sci.* **2009**, *81*, 445−456.
(4) Denman, K. L.; Brasseur, G.; Chidthaisong, A.; Ciais, P.; Cox, P. M.; Dickinson, R. E.; Hauglustaine, D.; Heinze, C.; Holland, E.; Jacob, D.; Lohmann, U.; Ramachandran, S.; da Silva Dias, P. L.; Wofsy, S. C.; Zhang, X. Couplings Between Changes in the Climate System and Biogeochemistry. In *Climate Change 2007: The Physical Science Basis. Contribution of Working Group I to the Fourth Assessment Report of the Intergovernmental Panel on Climate Change*; Solomon, S., Qin, D., Manning, M., Chen, Z., Marquis, M., Averyt, K. B., Tignor, M., Miller, H. L., Eds.; Cambridge University Press, Cambridge, U.K., 2007.
(5) Loulergue, L.; Schilt, A.; Spahni, R.; Masson-Delmotte, V.; Blunier, T.; Lemieux, B.; Barnola, J.-M.; Raynaud, D.; Stocker, T. F.; Chappellaz, J. Orbital and Millennial-Scale Features of Atmospheric CH_4 over the Past 800,000 Years. *Nature* **2008**, *453*, 383−386.
(6) Thornton, P. K. Livestock Production: Recent Trends, Future. *Philos. Trans. R. Soc., B* **2010**, *365*, 2853−2867.
(7) Tang, P.; Zhu, Q.; Wu, Z.; Ma, D. Methane Activation: The Past and Future. *Energy Environ. Sci.* **2014**, *7*, 2580−2591.
(8) Bousquet, P.; Ciais, P.; Miller, J. B.; Dlugokencky, E. J.; Hauglustaine, D. A.; Prigent, C.; Van der Werf, G. R.; Peylin, P.; Brunke, E.-G.; Carouge, C.; Langenfelds, R. L.; Lathière, J.; Papa, F.; Ramonet, M.; Schmidt, M.; Steele, L. P.; Tyler, S. C.; White, J. Contribution of Anthropogenic and Natural Sources to Atmospheric Methane Variability. *Nature* **2006**, *443*, 439−443.
(9) Leung, D. Y. C.; Caramanna, G.; Maroto-Valer, M. M. An Overview of Current Status of Carbon Dioxide Capture and Storage Technologies. *Renew. Sust. Energ. Rev.* **2014**, *39*, 426−443.
(10) Markewitz, P.; Kuckshinrichs, W.; Leitner, W.; Linssen, J.; Zapp, P.; Bongartz, R.; Schreiber, A.; Müller, T. E. Worldwide Innovations in the Development of Carbon Capture Technologies and the Utilization of CO_2. *Energy Environ. Sci.* **2012**, *5*, 7281−7305.
(11) Besenbacher, F.; Chorkendoff, I.; Clausen, B. S.; Hammer, B.; Molenbroek, A. M.; Nørskov, J. K.; Stensgaard, I. Design of a Surface Alloy Catalyst for Steam Reforming. *Science* **1998**, *279*, 1913−1915.
(12) Choudhary, T. V.; Choudhary, V. R. Energy-Efficient Syngas Production through Catalytic Oxy-Methane Reforming Reactions. *Angew. Chem., Int. Ed.* **2008**, *47*, 1828−1847.

DOI: 10.1021/jacs.8b13552
J. Am. Chem. Soc. 2019, 141, 5303−5313

(13) Tomishige, K.; Chen, Y.; Fujimoto, K. Studies on Carbon Deposition in CO_2 Reforming of CH_4 over Nickel−Magnesia Solid Solution Catalysts. *J. Catal.* **1999**, *181*, 91−103.
(14) Bradford, M. C. J.; Vannice, M. A. CO_2 Reforming of CH_4. *Catal. Rev.: Sci. Eng.* **1999**, *41*, 1−42.
(15) Froment, G. F. Production of Synthesis Gas by Steam- and CO_2-Reforming of Natural Gas. *J. Mol. Catal. A: Chem.* **2000**, *163*, 147−156.
(16) Van Hook, J. P. Methane-Steam Reforming. *Catal. Rev.: Sci. Eng.* **1980**, *21*, 1−51.
(17) Dissanayake, D.; Rosynek, M. P.; Kharas, K. C. C.; Lunsford, J. H. Partial Oxidation of Methane to Carbon Monoxide and Hydrogen over a Ni/Al_2O_3 Catalyst. *J. Catal.* **1991**, *132*, 117−127.
(18) Hickman, D. A.; Schmidt, L. D. Production of Syngas by Direct Catalytic Oxidation of Methane. *Science* **1993**, *259*, 343−346.
(19) Choudhary, V. R.; Rajput, A. M.; Prabhakar, B. Nonequilibrium Oxidative Conversion of Methane to CO and H_2 with High Selectivity and Productivity over Ni/Al_2O_3 at Low Temperatures. *J. Catal.* **1993**, *139*, 326−328.
(20) Wei, J.; Iglesia, E. Isotopic and Kinetic Assessment of the Mechanism of Reactions of CH_4 with CO_2 or H_2O to Form Synthesis Gas and Carbon on Nickel Catalysts. *J. Catal.* **2004**, *224*, 370−383.
(21) Latimer, A. A.; Kulkarni, A. R.; Aljama, H.; Montoya, J. H.; Yoo, J. S.; Tsai, C.; Abild-Pedersen, F.; Studt, F.; Nørskov, J. K. Understanding Trends in C-H Bond Activation in Heterogeneous Catalysis. *Nat. Mater.* **2017**, *16*, 225−229.
(22) Fung, V.; Tao, F.; Jiang, D. Low-Temperature Activation of Methane on Doped Single Atoms: Descriptor and Prediction. *Phys. Chem. Chem. Phys.* **2018**, *20*, 22909−22914.
(23) Tomkins, P.; Ranocchiari, M.; van Bokhoven, J. A. Direct Conversion of Methane to Methanol under Mild Conditions over Cu-Zeolites and Beyond. *Acc. Chem. Res.* **2017**, *50*, 418−425.
(24) Li, J.; Zhou, S.; Zhang, J.; Schlangen, M.; Weiske, T.; Usharani, D.; Shaik, S.; Schwarz, H. Electronic Origins of the Variable Efficiency of Room-Temperature Methane Activation by Homo- and Heteronuclear Cluster Oxide Cations $[XYO_2]^+$ (X, Y = Al, Si, Mg): Competition between Proton-Coupled Electron Transfer and Hydrogen-Atom Transfer. *J. Am. Chem. Soc.* **2016**, *138*, 7973−7981.
(25) Baek, J.; Rungtaweevoranit, B.; Pei, X.; Park, M.; Fakra, S. C.; Liu, Y. S.; Matheu, R.; Alshmimri, S. A.; Alshehri, S.; Trickett, C. A.; Somorjai, G. A.; Yaghi, O. M. Bioinspired Metal−Organic Framework Catalysts for Selective Methane Oxidation to Methanol. *J. Am. Chem. Soc.* **2018**, *140*, 18208−18216.
(26) Choudhary, T. V.; Aksoylu, E.; Goodman, D. W. Nonoxidative Activation of Methane. *Catal. Rev.: Sci. Eng.* **2003**, *45*, 151−203.
(27) Nave, S.; Jackson, B. Methane Dissociation on Ni(111) and Pt(111): Energetic and Dynamical Studies. *J. Chem. Phys.* **2009**, *130*, 054701.
(28) Bisson, R.; Sacchi, M.; Dang, T. T.; Yoder, B.; Maroni, P.; Beck, R. D. State-Resolved Reactivity of $CH_4(2\nu_3)$ on Pt(111) and Ni(111): Effects of Barrier Height and Transition State Location. *J. Phys. Chem. A* **2007**, *111*, 12679−12683.
(29) González, S.; Viñes, F.; García, J. F.; Erazo, Y.; Illas, F. A DF-vdW Study of the CH_4 Adsorption on Different Ni Surfaces. *Surf. Sci.* **2014**, *625*, 64−68.
(30) Kozlov, S. M.; Neyman, K. M. Insights from Methane Decomposition on Nanostructured Palladium. *J. Catal.* **2016**, *337*, 111−121.
(31) Liang, Z.; Li, T.; Kim, M.; Asthagiri, A.; Weaver, J. F. Low-Temperature Activation of Methane on the $IrO_2(110)$ Surface. *Science* **2017**, *356*, 299−303.
(32) Liu, K.; Yuan, C.; Zou, Q.; Xie, Z.; Yan, X. Self-Assembled Zinc/Cystine-Based Chloroplast Mimics Capable of Photoenzymatic Reactions for Sustainable Fuel Synthesis. *Angew. Chem., Int. Ed.* **2017**, *56*, 7876−7880.
(33) Park, J. B.; Graciani, J.; Evans, J.; Stacchiola, D.; Ma, S.; Liu, P.; Nambu, A.; Sanz, J. F.; Hrbek, J.; Rodriguez, J. A. High Catalytic Activity of $Au/CeO_x/TiO_2(110)$ Controlled by the Nature of the Mixed-Metal Oxide at the Nanometer Level. *Proc. Natl. Acad. Sci. U. S. A.* **2009**, *106*, 4975−4980.
(34) Rodriguez, J. A.; Liu, P.; Hrbek, J.; Pérez, M.; Evans, J. Water−Gas Shift Activity of Au and Cu Nanoparticles Supported on Molybdenum Oxides. *J. Mol. Catal. A: Chem.* **2008**, *281*, 59−65.
(35) Yang, Y.; Evans, J.; Rodriguez, J. A.; White, M. G.; Liu, P. Fundamental Studies of Methanol Synthesis from CO_2 Hydrogenation on Cu(111), Cu Clusters, and $Cu/ZnO(000\bar{1})$. *Phys. Chem. Chem. Phys.* **2010**, *12*, 9909−9917.
(36) Rodriguez, J. A.; Evans, J.; Feria, L.; Vidal, A. B.; Liu, P.; Nakamura, K.; Illas, F. CO_2 Hydrogenation on Au/TiC, Cu/TiC, and Ni/TiC Catalysts: Production of CO, Methanol, and Methane. *J. Catal.* **2013**, *307*, 162−169.
(37) Frantz, P. P.; Didziulis, S. V. Detailed Spectroscopic Studies of Oxygen on Metal Carbide. *Surf. Sci.* **1998**, *412-413*, 384−396.
(38) Rodriguez, J. A.; Kuhn, M. Electronic Properties of Gold on Mo(110): $d \rightarrow s,p$ Charge Redistribution and Valence Band Shifts. *Surf. Sci.* **1995**, *330*, L657−L664.
(39) Rodriguez, J. A.; Liu, P.; Takahashi, Y.; Nakamura, K.; Viñes, F.; Illas, F. Desulfurization of Thiophene on Au/TiC(001): Au-C Interactions and Charge Polarization. *J. Am. Chem. Soc.* **2009**, *131*, 8595−8602.
(40) Rodriguez, J. A.; Ramirez, J. P.; Asara, G. G.; Viñes, F.; Evans, J.; Liu, P.; Ricart, J. M.; Illas, F. Charge Polarization at a Au-TiC Interface and the Generation of Highly Active and Selective Catalysts for the Low-Temperature Water-Gas Shift Reaction. *Angew. Chem., Int. Ed.* **2014**, *53*, 11270−11274.
(41) Vidal, A. B.; Feria, L.; Evans, J.; Takahashi, Y.; Liu, P.; Nakamura, K.; Illas, F.; Rodriguez, J. A. CO_2 Activation and Methanol Synthesis on Novel Au/TiC and Cu/TiC Catalysts. *J. Phys. Chem. Lett.* **2012**, *3*, 2275−2280.
(42) Perdew, J. P.; Burke, K.; Ernzerhof, M. Generalized Gradient Approximation Made Simple. *Phys. Rev. Lett.* **1996**, *77*, 3865−3868.
(43) Grimme, S.; Antony, J.; Ehrlich, S.; Krieg, S. A Consistent and Accurate Ab Initio Parametrization of Density Functional Dispersion Correction (DFT-D) for the 94 Elements H-Pu. *J. Chem. Phys.* **2010**, *132*, 154104.
(44) Henkelman, G.; Uberuaga, B. P.; Jónsson, H. A Climbing Image Nudged Elastic Band Method for Finding Saddle Points and Minimum Energy Paths. *J. Chem. Phys.* **2000**, *113*, 9901−9904.
(45) Larsen, A. H.; Mortensen, J. J.; Blomqvist, J.; Castelli, I. E.; Christensen, R.; Dułak, M.; Friis, J.; Groves, M. N.; Hammer, B.; Hargus, C.; Hermes, E. D.; Jennings, P. C.; Jensen, P. B.; Kermode, J.; Kitchin, J. R.; Kolsbjerg, E. L.; Kubal, J.; Kaasbjerg, K.; Lysgaard, S.; Maronsson, J. B.; Maxson, T.; Olsen, T.; Pastewka, L.; Peterson, A.; Rostgaard, C.; Schiøtz, J.; Schütt, O.; Strange, M.; Thygesen, K. S.; Vegge, T.; Vilhelmsen, L.; Walter, M.; Zeng, Z.; Jacobsen, K. W. The Atomic Simulation Environment-a Python Library for Working with Atoms. *J. Phys.: Condens. Matter* **2017**, *29*, 273002.
(46) Smidstrup, S.; Pedersen, A.; Stokbro, K.; Jónsson, H. Improved Initial Guess for Minimum Energy Path Calculations. *J. Chem. Phys.* **2014**, *140*, 214106.
(47) Rogal, J.; Reuter, K. *Ab Initio Atomistic Thermodynamics for Surfaces: A Primer in Experiment, Modeling and Simulation of Gas-Surface Interactions for Reactive Flows in Hypersonic Flights*; Educational Notes: Neuilly-sur- Seine, France, 2007.
(48) Kresse, G.; Furthmüller, J. Efficient Iterative Schemes for Ab Initio Total-Energy Calculations Using a Plane-Wave Basis Set. *Phys. Rev. B: Condens. Matter Mater. Phys.* **1996**, *54*, 11169−11186.
(49) Kunkel, C.; Viñes, F.; Illas, F. Biogas Upgrading by Transition Metal Carbides. *ACS Appl. Energy Mater.* **2018**, *1*, 43−47.
(50) Li, K.; He, C.; Jiao, M.; Wang, Y.; Wu, Z. A First-Principles Study on the Role of Hydrogen in Early Stage of Graphene Growth during the CH_4 Dissociation on Cu(111) and Ni(111) Surfaces. *Carbon* **2014**, *74*, 255−265.
(51) Rodriguez, J. A.; Liu, P.; Viñes, F.; Illas, F.; Takahashi, Y.; Nakamura, K. Dissociation of SO_2 on Au/TiC(001): Effects of Au−C Interactions and Charge Polarization. *Angew. Chem., Int. Ed.* **2008**, *47*, 6685−6689.

DOI: 10.1021/jacs.8b13552
J. Am. Chem. Soc. 2019, 141, 5303−5313

(52) Rodriguez, J. A.; Illas, F. Activation of Noble Metals on Metal-Carbide Surfaces: Novel Catalysts for CO Oxidation, Desulfurization and Hydrogenation Reactions. *Phys. Chem. Chem. Phys.* **2012**, *14*, 427−438.
(53) Rodriguez, J. A.; Viñes, F.; Illas, F. Adsorption of Gold on TiC(001): Au−C Interactions and Charge Polarization. *J. Chem. Phys.* **2007**, *127*, 211102.
(54) Gómez, T.; Flórez, E.; Rodriguez, J. A.; Illas, F. Reactivity of Transition Metals (Pd, Pt, Cu, Ag, Au) toward Molecular Hydrogen Dissociation: Extended Surfaces versus Particles Supported on TiC(001) or Small Is Not Always Better and Large Is Not Always Bad. *J. Phys. Chem. C* **2011**, *115*, 11666−11672.
(55) Liu, H.; Yan, R.; Zhang, R.; Wang, B.; Xie, K. A DFT Theoretical Study of CH_4 Dissociation on Gold-Alloyed Ni(111) Surface. *J. Nat. Gas Chem.* **2011**, *20*, 611−617.
(56) Brønsted, J. N. Acid and Basic Catalysis. *Chem. Rev.* **1928**, *5*, 231−338.
(57) Evans, M. G.; Polanyi, M. Inertia and Driving Force of Chemical Reactions. *Trans. Faraday Soc.* **1938**, *34*, 11−24.
(58) Pallassana, V.; Neurock, M. Electronic Factors Governing Ethylene Hydrogenation and Dehydrogenation Activity of Pseudomorphic PdML/Re(0001), PdML/Ru(0001), Pd(111), and PdML/Au(111) Surfaces. *J. Catal.* **2000**, *191*, 301−317.
(59) Nørskov, J. K.; Studt, F.; Abild-Pedersen, F.; Bligaard, T. *Fundamental Concepts in Heterogeneous Catalysis*; John Wiley & Sons, Inc., 2014.
(60) Fajín, J. L. C.; Cordeiro, M. N. D. S.; Gomes, J. R. B.; Illas, F. On the need for spin polarization in heterogeneously catalyzed reactions on non-magnetic metallic surfaces. *J. Chem. Theory Comput.* **2012**, *8*, 1737−1743.
(61) Liu, J.; Ma, X.; Wang, Y.; Xiao, H.; Li, J. Heterogeneous Fe_3 Single-Cluster Catalyst for Ammonia Synthesis via an Associative Mechanism. *Nat. Commun.* **2018**, *9*, 1610.
(62) Liu, B.; Lusk, M. T.; Ely, J. F. Influence of Nickel Catalyst Geometry on the Dissociation Barriers of H_2 and CH_4: Ni_{13} versus Ni(111). *J. Phys. Chem. C* **2009**, *113*, 13715−13722.
(63) Lustemberg, P. G.; Ramirez, P. J.; Liu, Z.; Gutierrez, R. A.; Grinter, D. G.; Carrasco, J.; Senanayake, S. D.; Rodriguez, J. A.; Ganduglia-Pirovano, M. V. Room-Temperature Activation of Methane and Dry Re-Forming with CO_2 on Ni-CeO_2(111) Surfaces: Effect of Ce^{3+} Sites and Metal-Support Interactions on C-H Bond Cleavage. *ACS Catal.* **2016**, *6*, 8184−8191.
(64) Oyama, S. T. *The Chemistry of Transition Metal Carbides and Nitrides*; Chapman & Hall, 1996.
(65) Hwu, H. H.; Chen, J. G. Surface Chemistry of Transition Metal Carbides. *Chem. Rev.* **2005**, *105*, 185.

DOI: 10.1021/jacs.8b13552
J. Am. Chem. Soc. 2019, 141, 5303−5313

5.12. References

1. J. Feichter, U. Schurath, andR. Zellner. Luftchemie und Klima. *Chemie Unserer Zeit*., **2007**, 41, 3, 138–150.
2. R.W. Howarth, R. Santoro, and A. Ingraffea. Methane and the greenhouse-gas footprint of natural gas from shale formations. *Clim. Change*., **2011**; 106, *4*, 679–690.
3. D.Y.C. Leung, G. Caramanna, and M.M. Maroto-Valer. An overview of current status of carbon dioxide capture and storage technologies. *Renew. Sust. Energ. Rev.*, **2014**, 39, 426–443.
4. P. Markewitz, W. Kuckshinrichs, W. Leitner, J. Linssen, P. Zapp, R. Bongartz, A. Schreiber, and T.E Müller. Worldwide innovations in the development of carbon capture technologies and the utilization of CO_2. *Energy Environ. Sci.*, **2012**; 5, *6*, 7281–7305.
5. J.A. Rodriguez, P. Liu, F. Viñes, F. Illas, Y. Takahashi and K. Nakamura. Dissociation of SO_2 on Au/TiC (001): Effects of Au – C Interactions and Charge Polarization. *Angew. Chem. Int. Ed.*, **2008**; 129, *35*, 6685–6691.
6. G. Henkelman. A Climbing image nudged elastic band method for finding saddle points and minimum energy paths. *J Chem. Phys.*, **2000**, 113, 9901–9904.
7. A.H. Larsen, J.J. Mortensen, J. Blomqvist, I.E. Castelli, R. Christensen, M. Dułak, J. Friis, M.N. Groves, B. Hammer, C. Hargus, E.D. Hermes, P.C. Jennings, P.B. Jensen, J. Kermode, J.R. Kitchin, E.L. Kolsbjerg, J. Kubal, K. Kaasbjerg, S. Lysgaard, J.B. Maronsson, T. Maxson, T. Olsen, L.Pastewka, A. Peterson, C. Rostgaard, J. Schiøtz, O. Schütt, M. Strange, K.S. Thygesen, T. Vegge, L. Vilhelmsen, M. Walter, Z. Zeng, and K.W. Jacobsen, K. W. The Atomic Simulation Environment-a Python Library for Working with Atoms. *J. Phys.: Condens. Matter*., **2017**, 29, 273002
8. Smidstrup S, Pedersen A, Stokbro K, Jónsson H. Improved initial guess for minimum energy path calculations. *J. Chem. Phys*. **2014**;140, *21*, 214106
9. R. Sayós, A. Aguilar, J.M. Lucas, A. Solé, and J. Virgili. Therorical study of the reaction H + $ClCH_3$ → HCl + CH_3. *Chem. Phys. Lett*, **1985**, 93, 265-275.
10. F.M. Bickelhaupt, T. Ziegler, and P. Von Ragué Schleyer. $CH_3^•$ is planar due to H-H steric repulsion. Theoretical study of $MH_3^•$ and MH_3Cl (M = C, Si, Ge, Sn). *Organometallics*., **1996**, 15, *5*, 1477–1487.
11. R. Sayós, M. González, and A. Aguilar. Classical Dynamics study of the H + $BrCH_3$ → HBr_3 + CH_3 reaction. Chem. Phys. Lett, **1985**, 98, 409-419.
12. C. Kunkel, F. Viñes, and, F.Illas. Biogas Upgrading by Transition Metal Carbides. *ACS Appl. Energy Mater.* **2018**, 1, *1*, 43–47.
13. F. Viñes, Y. Lykhach, T. Staudt, M.P.A. Lorenz, C. Papp, H.P. Steinrück, J. Libuda, K.N. Neyman, and A. Görling. Methane activation by platinum: Critical role of edge and corner sites of metal nanoparticles. *Chemestry*, **2010**, 16, *22*, 6530–6539.
14. H. Nikoofard and A.H. Amin AH. DFT Study of the Structural and Electronic Properties of Conducting Oligo(p-Fluorophenylthiophene). *J. Struct. Chem.*, **2018**, 59, *6*, 1288–1298.
15. S. Goel S and A.E. Masunov. Density functional theory study of small nickel clusters. *J. Mol. Model.*, **2012**, 18, *2*, 783–790.
16. K. Li, C. He, M. Jiao, Y. Wang, and Z. Wu. A first-principles study on the role of hydrogen in early stage of graphene growth during the CH_4 dissociation on Cu(111) and Ni(111) surfaces. *Carbon*, **2014**, 74, 255–265.
17. H. Liu, R. Yan, R. Zhang, B. Wang, and K. Xie. A DFT theoretical study of CH_4 dissociation on gold-alloyed Ni(111) surface. *J. Nat. Gas. Chem*., **2011**, 20, *6*, 611–617.
18. H. Prats, G.A. Gutiérrez, J.J. Piñero, F. Viñes, S.T. Bromley, P.J. Ramírez, J.A. Rodriguez, and F. Illas. Room Temperature Methane Capture and Activation by Ni Clusters Supported on TiC(001): Effects of Metal-Carbide Interactions on the Cleavage of the C-H Bond. *J. Am. Chem. Soc.*, **2019**; 141, 5303–5313.

PART II: Nanoparticles

Chapter 6

Infrared vibrational spectra for TiC nanoparticles.

6. Infrared vibrational spectra for TiC nanoparticles

6.1. Introduction

Titanium carbide (TiC), due to its extreme hardness, is frequently incorporated into other materials (e.g. steels[1] and rubber[2]) as small particles, giving rise to composites with improved wear-resistance and strength. TiC nanoparticles (NPs) have further been proposed as high temperature nucleation seeds for dust growth around aging C-rich stars.[3] TiC surfaces and nanostructured TiC have be increasingly attracting attention for their potential to replace precious metals in catalysis,[4–6] and fuel cells.[7] In particular, TiC has been found to be highly active for catalysing important hydrogenation reactions,[8–10] which is likely linked to the range of intimate ways in which hydrogen and TiC can interact.[11,12]

Advances in all these areas are likely to be achieved through a better understanding the structure of TiC at the nanoscale. According to electronic structure calculations, even very small stoichiometric Ti_nC_n nanoclusters (*e.g.* for n = 6, 12) energetically prefer to exhibit the bulk rocksalt crystal structure.[13] Moving to C-rich Ti_xC_y compositions, nanoclusters start to exhibit C-C bonds and have non-rocksalt structures (*e.g.* the Ti_8C_{12} metcar).[14,15] For a similar small size and for a slightly C-poor composition, the infrared (IR) spectrum from cluster beam experiments for $Ti_{14}C_{13}$ is in good agreement with calculated IR spectrum for a structure based on a simple cubic cut from the rocksalt bulk crystal.[16] Cluster beam experiments have also provided IR spectra for a range of larger NPs with masses compatible with the set of C-poor compositions (Ti_nC_{n-4}, with n = 18, 24, 32, 40, 50, and one of Ti_nC_{n-5} for n = 63).[17] These experimental IR spectra are shown in Figure 6.1.

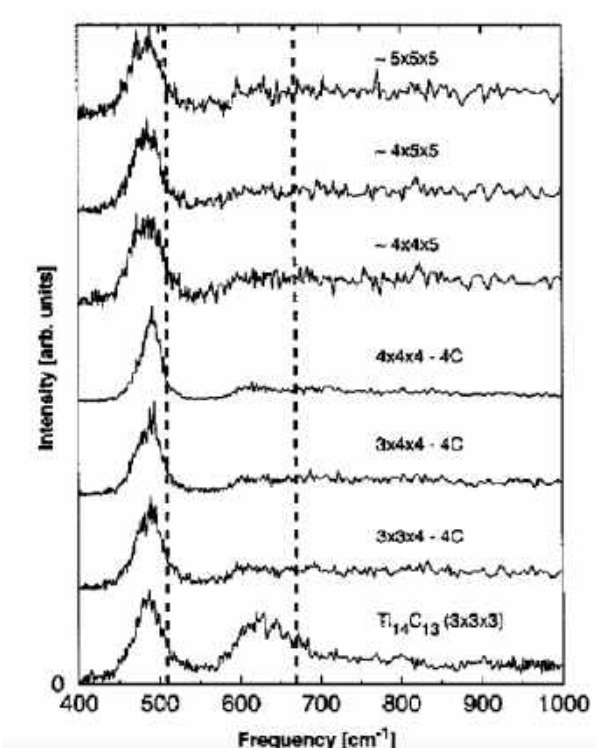

Figure 6.1. IR-Infrared-Resonance-Enhanced multiphoton ionization (IR-REMPI) spectra of different nanocrystalline titanium carbide clusters. Shown as dashed lines are the two optically active surface phonon modes of bulk TiC, measured by High resolution electron energy loss spectroscopy HREELS.[18]

These NPs are generally assumed be exhibit structures based on cubic cuts from the parent rocksalt crystal. In principle, as four carbon atoms have essentially the same mass as a single Ti atom (48 atomic mass units, or amu), the experimentally observed NP masses are also compatible with parent rocksalt cut structures with one Ti atom or 4C atoms missing. Herein, we investigate whether this lack of agreement between experiment and theory can be reconciled by accurately calculating the IR spectra of TiC-based NPs derived from parent cubic rocksalt cuts with either: *i)* four C atoms removed or *ii)* a single Ti atom removed.

Part of the work explained in this chapter has been submitted for publication **in Physical Chemistry Chemical Physics** under the title ***Can Calculated Harmonic Vibrational Spectra Rationalize the Structure of TiC-based Nanoparticles?*** under review 2021.

6.2. Methodology

In this Chapter, the calculations were performed using FHI-AIMS. The methodology used to study the stability and characterization on TiC NP has been, in a first step, the NP was optimized, in a second step the vibrational frequencies were obtained to calculate the IR spectra. The parameters used for these calculations, are explained in the Chapter 2, Section 2.12.

Two types of IR have been employed to obtain the IR spectrum of TiC NPs: i) harmonic IR spectra and ii) *ab initio* MD-based IR spectra. The harmonic spectra IR were obtained from 0K calculations while the AIMD-based IR spectra were obtained at different temperatures.

6.3. Factors affecting the IR spectra of TiC NPs

In this part of the thesis we examine factors which could affect the computed IR spectra of our TiC NPs.

6.3.1. Isomer effect

The smallest NP size for which experimental data is available (3×3×3) can exhibit two isomers: $Ti_{14}C_{13}$ and $Ti_{13}C_{14}$, as can be seen in Scheme 6.1.

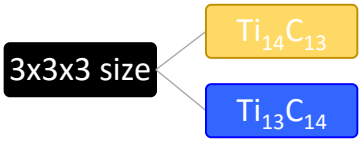

Scheme 6.1. Both possibilities for 3×3×3 size.

The $Ti_{14}C_{13}$ NP exhibits atoms of Ti at the corners while the $Ti_{13}C_{14}$ NP, at the corners are C atoms. Both structures are shown in Figure 6.2.

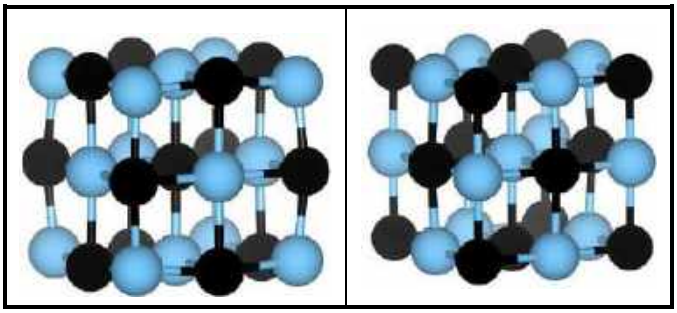

Figure 6.2. Left $Ti_{14}C_{13}$ NP. Right. $Ti_{13}C_{14}$ NP.

Both isomers have been optimized using the FHI-AIMS code. The harmonic IR spectra obtained for these NP structures can be seen in Figure 6.3.

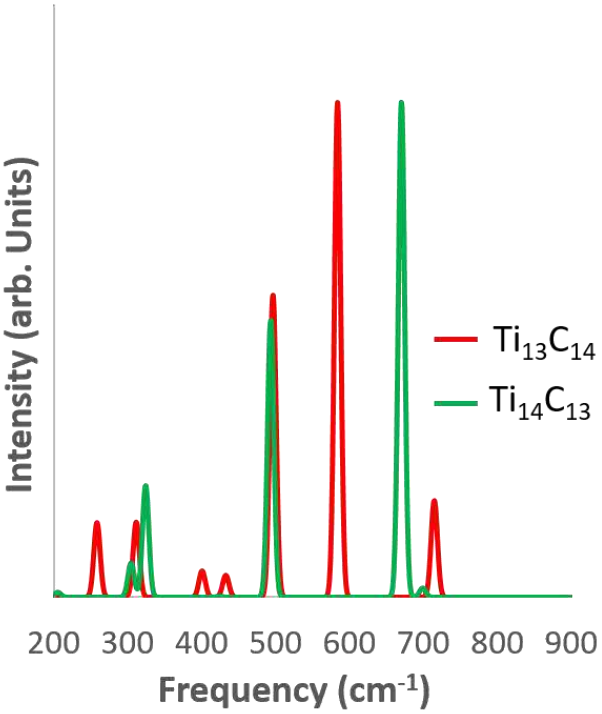

Figure 6.3. Harmonic IR spectra for $Ti_{14}C_{13}$ and $Ti_{14}C_{13}$ NPs.

The IR spectra for these structures are very different in the frequency range under study, $Ti_{14}C_{13}$ presents three peaks with the highest frequency peak at 671 cm^{-1} while the highest frequency peak for the $Ti_{13}C_{14}$ isomer appears at 584 cm^{-1} and has six more peaks. The frequency range for the experimentally measured IR data is between 400 cm^{-1} and 900 cm^{-1} (see Figure 6.1) The experimental spectrum presents two peaks in this range like the $Ti_{14}C_{13}$ isomer. The calculated harmonic IR spectrum for this isomer is compared with the experimental IR spectrum in Figure 6.4.

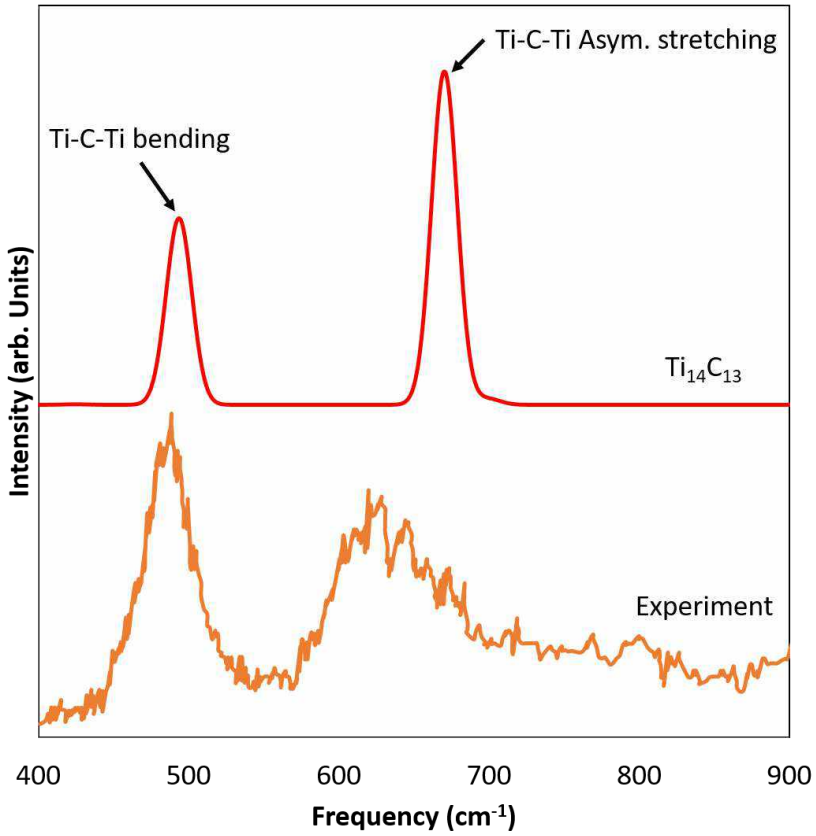

Figure 6.4. Harmonic IR spectrum simulated for $Ti_{14}C_{13}$ isomer compared with the experimental data.[18]

For larger TiC-based NPs the experimental IR vibrational spectra show only one significant peak with a maximum around 470-490 cm^{-1} (see Figure 6.1). The $Ti_{14}C_{13}$ spectrum also presents a peak at 490 cm^{-1} but in this case a higher frequency peak is also observed. This peak corresponds to a Ti-C-Ti bending mode, mainly exhibited at the NP edges. The simulated harmonic IR spectrum shows a higher frequency peak at 670 cm^{-1} approximately 50 cm^{-1} higher than corresponding high frequency peak obtained in the experimental IR. The peak at 670 cm^{-1} corresponds to an asymmetric Ti-C-Ti stretching mode exhibited mainly by edge atoms. Despite these differences, it can be considered that both spectra match quite well and therefore it we conclude that structure of the experimental 3×3×3 NP most likely corresponds to the $Ti_{14}C_{13}$ isomer.

6.3.2. Functional effect

In this Section, two different functionals have been used obtain harmonic IR spectra for the $Ti_{14}C_{13}$ NP isomer. Specifically, we compare PBE[19] —a pure GGA functional— and PBE0[20] —a hybrid with 25% of Hartree-Fock exchange.

After optimizing the NP structure, the effect of both functionals on the resulting harmonic IR spectrum is studied. The IR spectra obtained for each functional are shown in Figure 6.5.

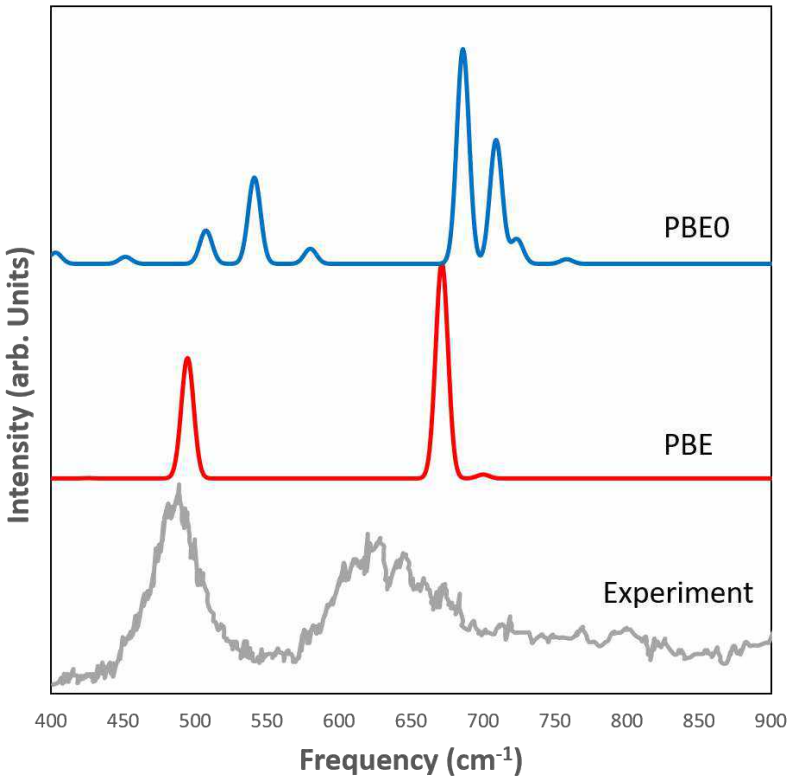

Figure 6.5. Harmonic IR spectra obtained for $Ti_{14}C_{13}$ using different functionals. In red the PBE functional, in blue the PBE0 functional, and grey the experimental spectrum.[18]

The results show significant differences with respect to the two functionals used. The peaks for the spectrum, calculated using the PBE functional are well defined and only three peaks are observed while when using PBE0 more peaks are obtained. In addition, the PBE0 peaks are relatively shifted to higher frequencies.

Comparing with the experimental data, the obtained spectrum with the PBE functional is in better quantitative and qualitative agreement with the experimental IR spectrum than with PBE0 functional (see Figure 6.5). In the remainder, all reported IR spectra are obtained using DFT calculations employing the PBE functional.

6.3.3. Charge effect

In this Section, three different charge states for the $Ti_{14}C_{13}$ NP have been studied: neutral (0), cationic (+1), and anionic (-1). The options under study in this case are shown in Scheme 6.2.

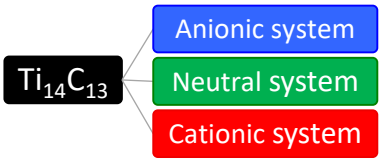

Scheme 6.2. Charge study.

The first electronic affinity (AE) and the ionization energy (IE) will be extracted for this system. The AE is defined as:

$$X_{(g)} + e^{-} \rightarrow X^{-}_{(g)} \qquad (6.1).$$

Therefore, the AE will be obtained by subtracting the energy of the anionic system from that of the neutral system. The IE is defined as:

$$X_{(g)} \rightarrow X^{+}_{(g)} + e^{-} \qquad (6.2).$$

In this case, the IE will be calculated by subtracting the energy of the cationic system from that of the neutral system.

For this structure, the electronic affinity is 0.97 eV and the ionization energy is 4.15 eV. The IR characterization of the neutral, cationic, and anionic $Ti_{14}C_{13}$ NP can be seen in Figure 6.6.

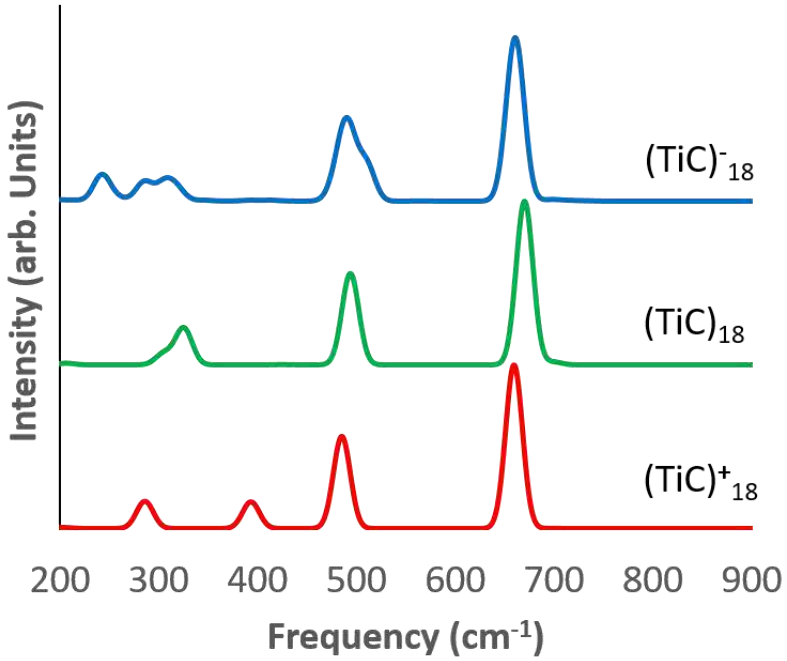

Figure 6.6. Harmonic IR spectra for neutral, positive, and negative charge for the $Ti_{14}C_{13}$ NP structure.

The spectra show significant differences at low frequencies, between 200 and 400 cm^{-1}. In this range the IR peaks of three structures do not coincide. The other two peaks that these species exhibit, around at 500 cm^{-1} and 650 cm^{-1} appear at similar frequencies in all cases. The neutral structure (green line) is slightly shifted to larger frequencies with respect to the anionic and cationic spectra. Specifically, the highest frequency peak for the neutral spectrum appears at 667 cm^{-1} which is 10 cm^{-1} higher than for the cationic and anionic structures. Finally, the peak around the 490 cm^{-1} is different for each of the three charge states. In order of increasing frequency, this peak appears first in the cationic structure (481 cm^{-1}), then in anionic structure (485 cm^{-1}), and finally the neutral structure at 490 cm^{-1}.

As the simulated spectra obtained do not exhibit significant differences in the experimental data range from 400 cm^{-1} to 900 cm^{-1} and us such they cannot be used to affirm the experimental system charge for this structure. In the remainder, all reported calculated IR spectra assume that the NPs are neutral species.

6.3.4. Temperature effect

In order to study the effect of temperature, molecular dynamics is used from which the IR spectrum was extracted (see details in the Chapter 2). The NP size chosen to do this test was the $Ti_{14}C_{13}$ NP at five different temperatures: at 0 (harmonic IR), 400, 900, 1500, and 2100 K. All temperatures considered are lower than the experimental melting point for TiC, which is about 3100K.[21]

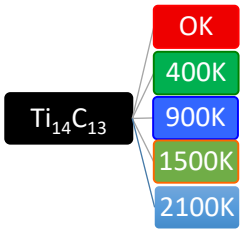

Scheme 6.3. Different temperatures under study on $Ti_{14}C_{13}$.

The results for this study are shown in Figure 6.7, where the IR spectra at different temperatures are plotted and compared with the experimental IR spectrum.

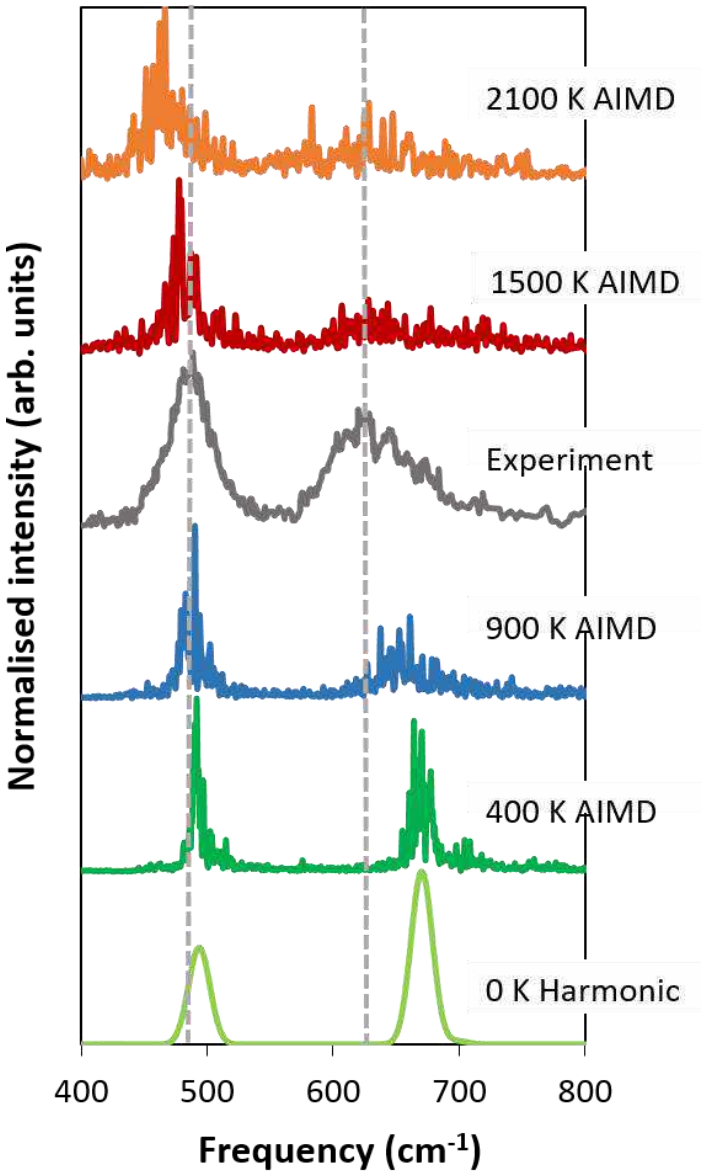

Figure 6.7. IR spectra simulated at different temperatures and experimental IR data for $Ti_{14}C_{13}$.

The calculated IR results all show two peaks between 400 cm^{-1} and 800 cm^{-1} in line with the experimental spectrum, and no peaks at higher frequencies. At 0 K, the more intense peak corresponds to the peak at higher frequency (675 cm^{-1}) with respect to the lower frequency peak (500 cm^{-1}). The higher peak is triply degenerate and it corresponds to Ti-C-Ti stretching mode from the C edge. The C atoms oscillate on edges between corner Ti atoms while the peak at 500 cm^{-1} is also triply degenerate and it is due to Ti-C-Ti bending mode. In this case, C edge atoms oscillate with respect to the cluster centre. However, as temperature increases the higher frequency peak broadens and flattens leading to the lower frequency peak having relatively more intensity. As the temperature increases, beyond 900 K, the higher frequency peak is increasingly difficult to differentiate due to the high level of thermally induced broadening. It is also observed that the lower

frequency peak gradually shifts to lower frequencies as the temperature increases. This shift in the low frequency peak amounts to around 30 cm^{-1} between 0 and 2100 K.

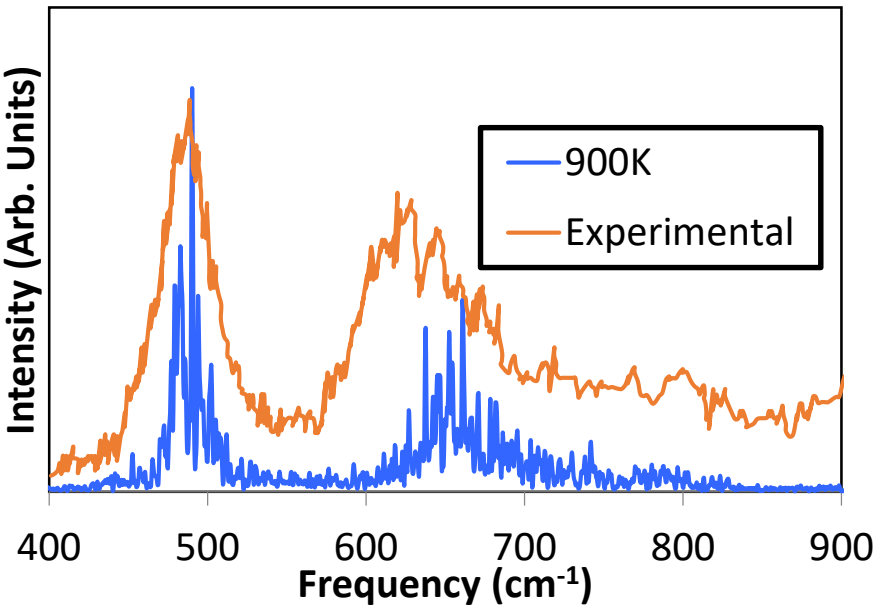

Figure 6.8. IR spectra derived from for molecular dynamics at 900K compared with the experimental IR spectrum for the $Ti_{14}C_{13}$ NP.

Comparing the MD-based spectra with the experimental spectrum we find that the simulated spectrum at 900K is the best match with the experimental spectrum. In this case (see Figure 6.8), the low frequency peak in both spectra coincides at 490cm^{-1}. The second higher frequency peak for the 900K simulated spectrum is somewhat shifted towards higher frequencies, around 30 cm^{-1} but has a similar intensity profile to the experimental peak. The 30 cm^{-1} shift could be due to the temperature of the $Ti_{14}C_{13}$ NP in the experiment being close to 900 K but slightly higher.

The results show that the temperature is an important effect to interpret IR spectra obtained from cluster beam experiments. In particular, this study strongly suggests that the temperature in the experiment for $Ti_{14}C_{13}$ NP is near to 900 K. This temperature effect on the IR spectra will be tested for other NP sizes in the remainder of this Chapter.

6.4. Stability of $(TiC)_{18}$ based NPs

In this section, the $(TiC)_{18}$ NP will be studied. This size is the second smallest NP size represented in Figure 6.1. For this NP size, two different cubic cut structures (isomers) are possible. One of these isomers is the 3×3×4 Np while the other isomer is 2×3×6. Both isomers are shown in Figure 6.9.

Isomer 4×3×3	Isomer 6×3×2
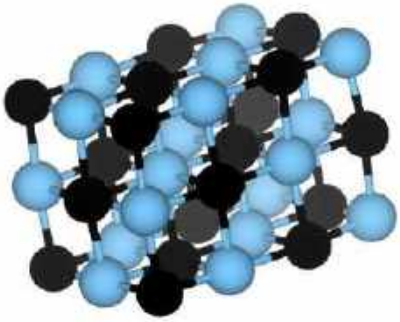	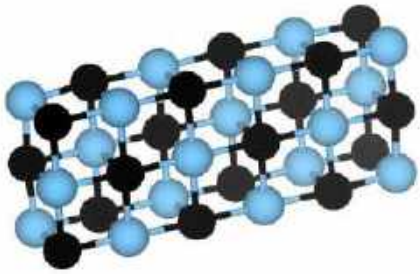

Figure 6.9. Different isomers for $(TiC)_{18}$.

The 4×3×3 is found to be 2.88 eV more stable than the isomer 2×3×6. For this reason, our calculations will be focused on the 3×3×4 isomer. In Figure 6.1, the experimental data indicate that the NPs for a size of $(TiC)_{18}$ and larger are "missing" four carbon atoms (labelled as "3×3×4 – 4C" in Figure 6.1). This is specifically noted for the $(TiC)_{18}$, $(TiC)_{24}$, and $(TiC)_{32}$ NPs. Four carbon atoms have a mass of 48 amu, which also corresponds to the mass of one Ti atom. For this reason, both possibilities will be studied. One possibility corresponds to a $Ti_{18}C_{14}$ composition and the other possibility corresponds to a $Ti_{17}C_{18}$ composition.

Considering the removal of four C atoms from a bulk cut 3×3×4 $(TiC)_{18}$ NP, these atoms can be lost from different positions. In this study, four possibilities will be studied. The possibilities we considered are summarised in in Scheme 6.4.

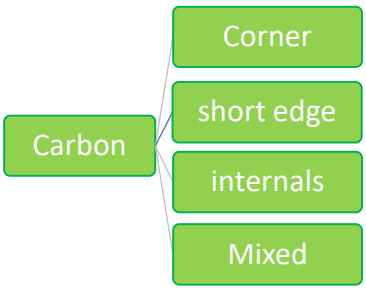

Scheme 6.4. Stuctures studied on $Ti_{18}C_{14}$.

The images for the NP with four C atoms removed, $Ti_{18}C_{14}$, for each case can be seen in Figure 6.10.

Corner	Short edges	Internal	Mixed
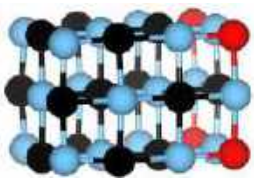	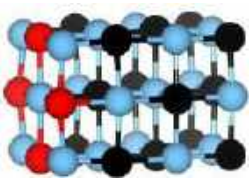	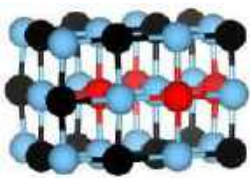	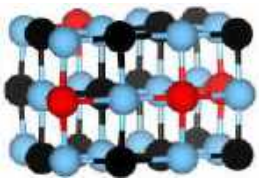

Figure 6.10. Examples of sets of four C atoms to remove (red) from the cubic parent $(TiC)_{18}$ NP to create initial.

The results show that the most stable isomer is when the 4C atoms are removed in the corners. The calculated relative energies for these NPs are reported in Table 6.1.

Table 6.1. Relative energies in eV for the different $Ti_{18}C_{14}$ structures when 4C atoms are removed from the bulk cut $(TiC)_{18}$ NP.

Corner	Short edges	Internal	Mixed
0.00	7.01	9.96	6.04

In order to search for alternative NP structures, classical molecular dynamics (MD) simulations were used. Specifically, a series of contiguous NVT MD simulations were run starting first from a high temperature (2500 - 3000K) and reducing the temperature in a step-wise manner by 500 K until a temperature of 1000K was reached. Low energy NP structures were then extracted and optimized using the above-described DFT approach. Using classical MD, another 10 $Ti_{18}C_{14}$ structures were thus obtained. None of the NP structures obtained by this procedure are more stable than $Ti_{18}C_{14}$ when the atoms are removed from the corners, see Figure 6.11.

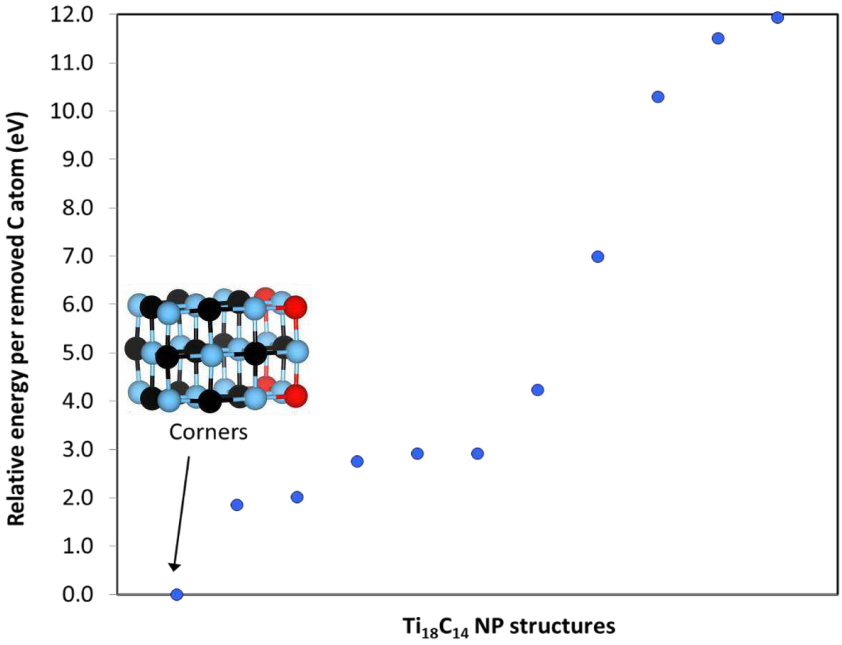

Figure 6.11. Energetic stabilities of $Ti_{18}C_{14}$ NPs structures relative to the lowest energy NP with C atoms removed from the corners.

The different considered positions of Ti when it is removed from $(TiC)_{18}$ are shown in Scheme 6.5.

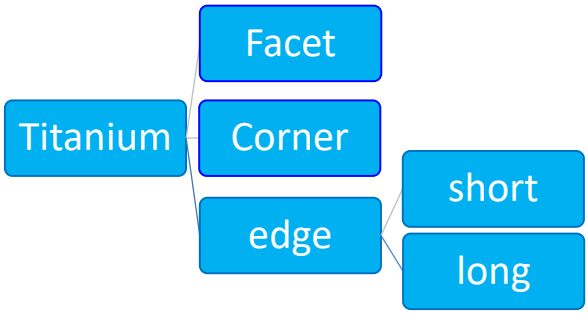

.

Scheme 6.5. Types of $Ti_{17}C_{18}$ NP studied strutuctures.

The structures of the$Ti_{17}C_{18}$ NPs with one Ti atom removed from the stoichiometric NP, are shown in Figure 6.12.

Facet	Corner	Long edge	Short edge
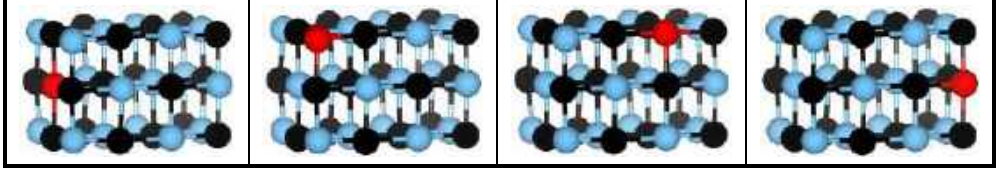			

Figure 6.12. Examples of one Ti atom to remove (red) from the cubic parent $(TiC)_{18}$ NP.

The relative energies obtained for these $Ti_{17}C_{18}$ NPs are shown in Table 6.2.

Table 6.2. Relative energies in eV for the four $Ti_{17}C_{18}$ structures considered.

Short edge	Facet	Corner	Long edge
0.00	8.56	6.14	0.23

The results indicate that the most stable $Ti_{17}C_{18}$ structure is when the Ti atom is removed from the short edge of the $Ti_{18}C_{18}$ NP. This structure is the most stable because a spontaneous C-C is formed. The same occurs when the Ti atom is removed on long edge. The formation of a C-C bond causes the structure to stabilize. In small stoichiometric $(TiC)_n$ nanoclusters, although the lowest energy structures tend to follow the Ti-C alternating order of the rocksalt crystal, low lying metastable isomers can exhibit C-C bonds.[13] With increasing C content, the formation of highly energetically stabilizing C_2 dimers becomes more facile,[15] and most C-rich Ti_xC_y NPs are likely to exhibit such moieties. In the other two cases under study, no C-C bonds are formed. The final structure for the four cases is shown in Figure 6.13.

Facet	Corner	Long edge	Short edge
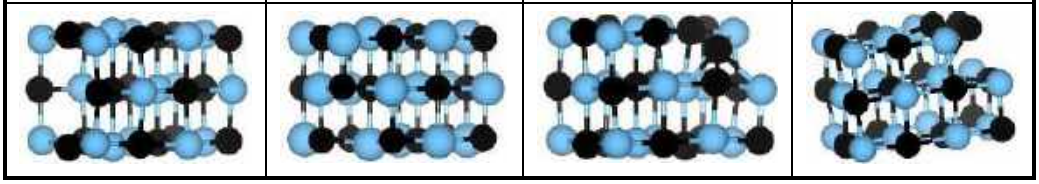			

Figure 6.13. Final structures for the four structures under study for $Ti_{17}C_{18}$.

A further 49 structures with the $Ti_{17}C_{18}$ stoichiometry were created. The 49 NPs resulting from either direct optimisation of the NPs after removal of a Ti atom and/or the classical MD annealing runs further support this tendency. In this case, after optimization many of these NP structures exhibit C-C bonds. The formation of C-C bonds is readily identified in the IR spectra of Ti_xC_y NPs due to a strong signature peak close to 1350-1400 cm^{-1} associated with C-C stretching.[13,14] We note that the experimental IR spectra for the NPs considered in this study are not reported to exhibit such a peak.[17] NP structures with C-C bonding are thus not considered as viable candidates to explain the experimental IR data. The lowest energy $Ti_{17}C_{18}$ NP without C-C bonding was found upon Ti removal from a corner of a $(TiC)_{18}$ rocksalt cut NP which we consider as the most likely C-rich NP candidate for potentially explaining the experimental IR results.

We thus take the reference to be NP where the Ti atom is removed from a corner, and the energy of rest of the NP structures have been energetically compared in Figure 6.14.

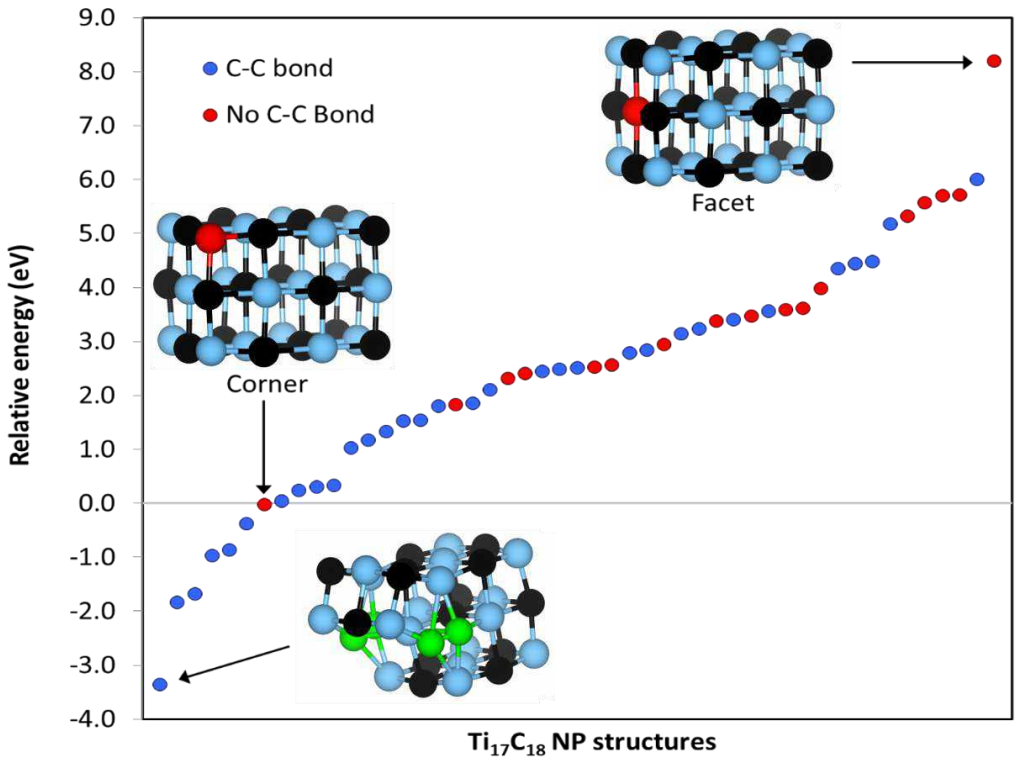

Figure 6.14. Relative energetic stabilities of $Ti_{17}C_{18}$ NPs structures with respect to the structure with a Ti atom removed from a corner of the 3×3×4 $(TiC)_{18}$ NP. The structures with C-C bonds are indicated in blue and the structures that do not possess C-C bonds are indicated in red.

We find that most $Ti_{17}C_{18}$ structures spontaneously form stabilising C-C bonds. In Figure 6.15 where the most stable $Ti_{17}C_{18}$ NP structure found using MD can be seen.

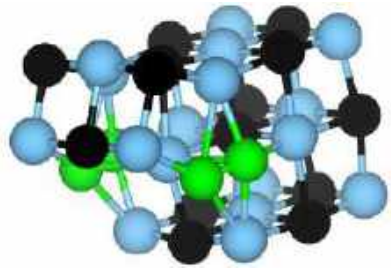

Figure 6.15. Most stable $Ti_{17}C_{18}$ structure found. The structure exhibits two C-C bonds.

6.5. IR spectra of TiC larger NPs

After investigating how various factors can affect the calculated IR spectrum of the $Ti_{14}C_{13}$ NP (section 6.3) we focus on the role of temperature in an attempt to explain the experimental IR spectra for the larger NPs.

6.5.1. Harmonic (0 K) IR Spectra

Within the harmonic IR approach different NP sizes have been studied. The sizes under study are: $(TiC)_{18}$, $(TiC)_{24}$, $(TiC)_{32}$, $(TiC)_{40}$, and $(TiC)_{50}$.

6.5.1.1. $(TiC)_{18}$ size

In Section 6.4, the energetic stability of both cubic cut isomers for the stoichiometric $(TiC)_{18}$ (*i.e.* the 4×3×3 and 2×3×6 isomers) was reported. The calculated harmonic IR spectra for both these isomers are shown in Figure 6.16.

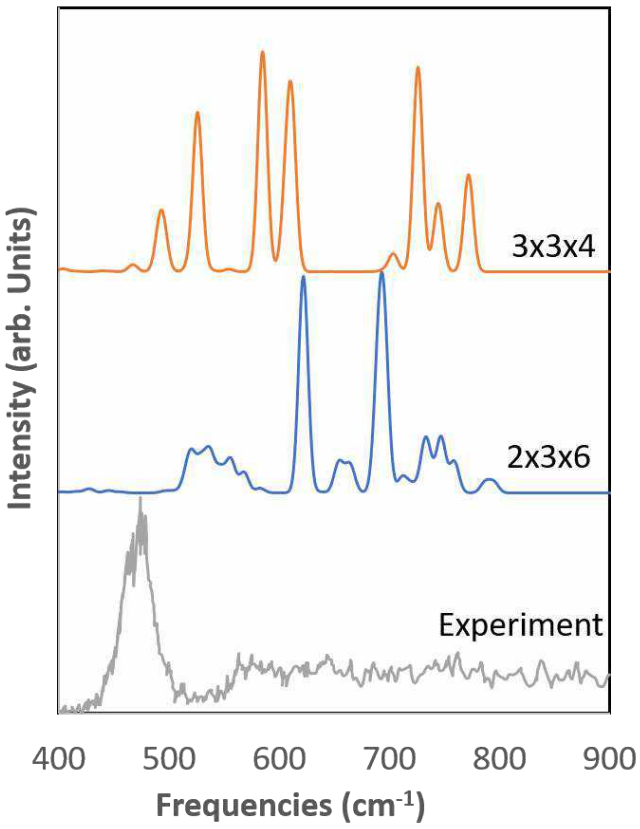

Figure 6.16. Simulated IR spectra obtained for two cubic cut stoichiometric $(TiC)_{18}$ isomers and the corresponding experimental IR spectrum.[18]

In Figure 6.16, the harmonic IR spectrum for the 2×3×6 isomer (blue line) shows two main peaks with high intensity, at 694 cm^{-1} and 624 cm^{-1}. In addition, this spectrum shows three groups of peaks with lower intensity. None of these three groups present intensities greater than 0.22 Arbitrary Units (A.U.). The IR spectrum for 3×3×4 (orange line) shows eight main peaks. The higger peak is at 584 cm^{-1}. The rest of the peaks obtained are at: 724, 609, 525, 770, 491, 742, and 698 cm^{-1} in decreasing order of intensity. Finally, the experimental spectrum only has one discernible peak at 475 cm^{-1}.

Clearly, neither of the two simulated spectra for the two $(TiC)_{18}$ isomers match with the experimental IR spectrum. With these results, both isomers can be ruled out as explaining the experimental data. Following the higher energetic stability of the 3×3×4 isomer and the discussion in Section 6.4, we now focus on the IR spectra of isomers obtained when this NP loses either: *i)* four carbon atoms ($Ti_{18}C_{14}$), or *ii)* one Ti atom ($Ti_{17}C_{18}$). The same four $Ti_{18}C_{14}$ isomers studied in section 6.4 were characterized by their harmonic IR spectra and compared with the experimental IR spectrum. All spectra can be seen in Figure 6.17.

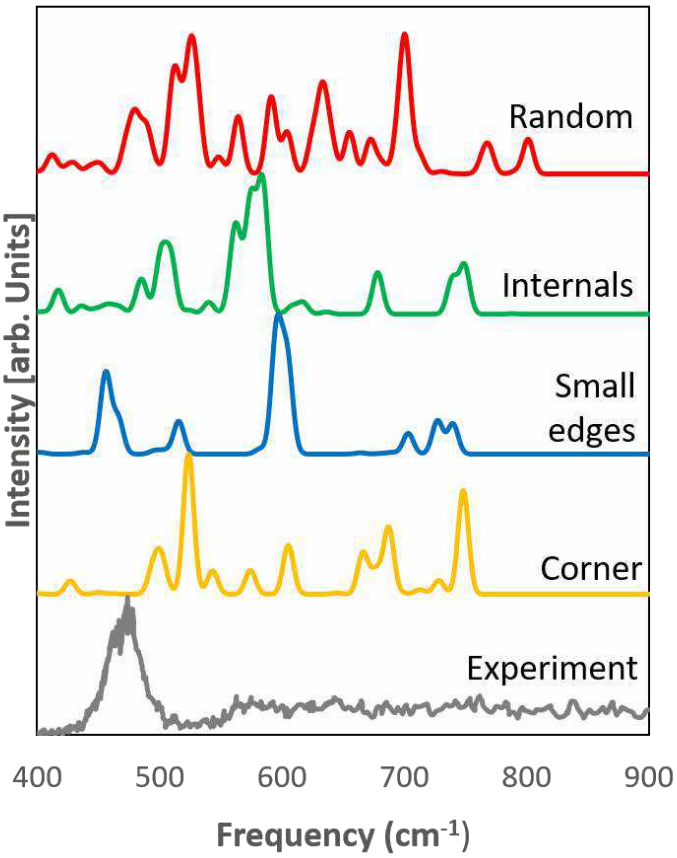

Figure 6.17. Simulated IR spectra for the four $Ti_{18}C_{14}$ isomers characterized and experimental IR.[18]

In Figure 6.17 it can be seen how none of the simulated harmonic spectra obtained matches with the experimental spectrum. Specifically, in all cases, the IR spectra for simulated isomers present more than one peak and have spectra extending to at least 750 cm^{-1}.

We do not see any improvement with respect to the experimental spectrum when considering the IR spectra of metastable $Ti_{18}C_{14}$ NPs, as compared to the most stable case where four C atoms are removed from 4×3×3 $(TiC)_{18}$ corners. Thus, for larger NP sizes, we only consider the most energetically stable case where carbon atoms are removed from corner sites.

$Ti_{17}C_{18}$ isomers

In the case of $Ti_{17}C_{18}$ isomers, the four NP structures studied are the same as in section 6.4 (see Figure 6.12). Note that two of the isomers studied (long edge and large edge) present C-C bond and have an extra high frequency peak outside of the experimental frequency range. The simulated harmonic spectra for all four $Ti_{17}C_{18}$ isomers and the corresponding experimental IR data are shown in Figure 6.18.

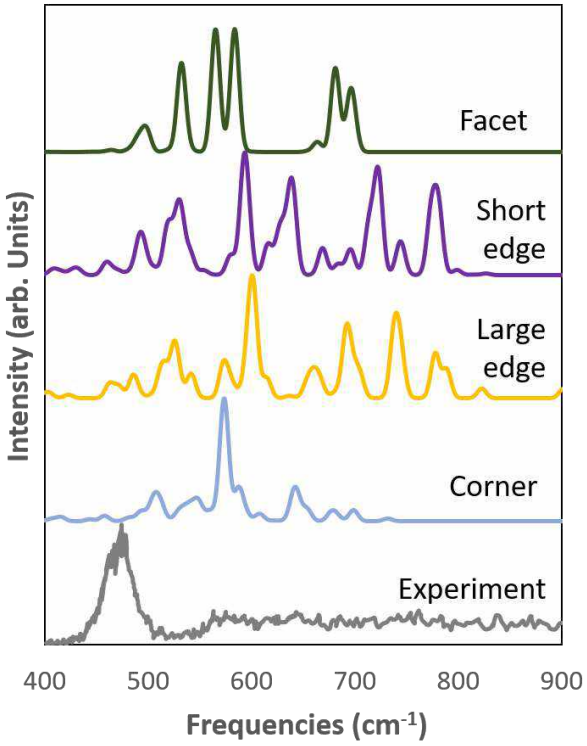

Figure 6.18. Simulated harmonic IR spectra for four $Ti_{17}C_{18}$ isomers (see Figure 6.13) and the experimental IR spectrum.[18]

In Figure 6.18 the harmonic IR spectra of the four considered $Ti_{17}C_{18}$ NPs are shown, despite the fact that two of them (Large edge and Short edge), as previously mentioned, are not good candidates due to the presence of C-C bonds. Of the other two candidates that, one of them (Facet) presents more peaks than the experimental IR spectrum. The other isomer (Corner) only presents one main peak like the experimental IR spectrum, but the peak is shifted 100 cm^{-1} to higher frequencies. Based on these results, this last case appears to be the best NP candidate to explain the experimental data. We will also study this type of isomer (*i.e.* with a single Ti atom removed from a corner) for larger NP sizes below.

6.5.1.2. $(TiC)_{24}$-based NPs

For this size the three NP structures that will be studied can be seen in Figure 6.19.

$(TiC)_{24}$	$Ti_{24}C_{20}$	$Ti_{23}C_{24}$
	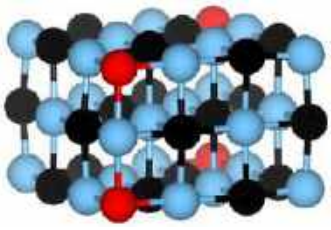	

Figure 6.19. Three structures under study for $(TiC)_{24}$ size.

The harmonic IR spectra obtained for each NP structures are compared with the IR experimental data for this size are shown in Figure 6.20.

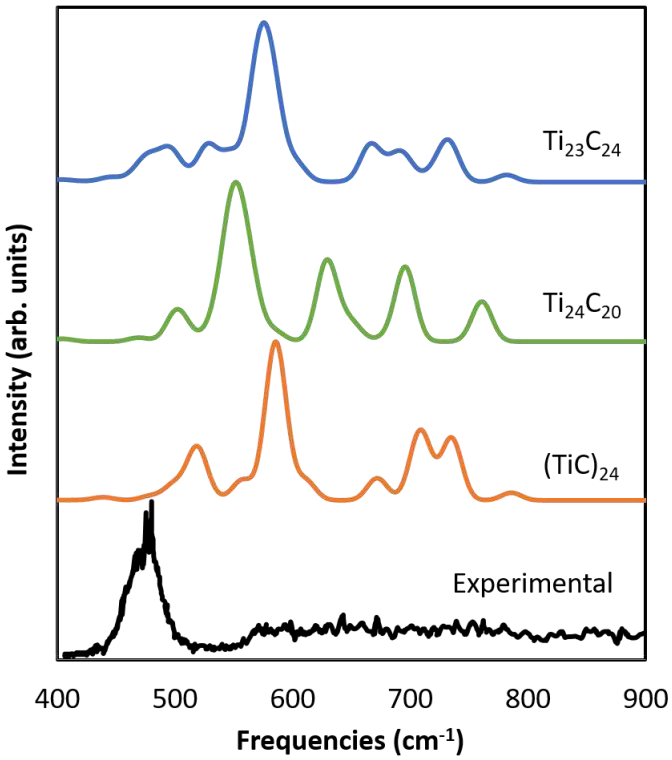

Figure 6.20. Simulated IR spectra for the $(TiC)_{24}$, $Ti_{24}C_{20}$, $Ti_{23}C_{24}$, and experimental IR.[18]

In the previous figure it is clearly observed that none of these simulated spectra of the three structures under study match well with the experimental data. As for the $(TiC)_{18}$ size, the simulated harmonic spectrum that better matches with the experimental IR is for the $Ti_{23}C_{24}$ NP.

6.5.1.3. $(TiC)_{32}$-based NPs

For this size the three NP structures studied can be seen in Figure 6.21.

$(TiC)_{32}$	$Ti_{32}C_{28}$	$Ti_{31}C_{32}$
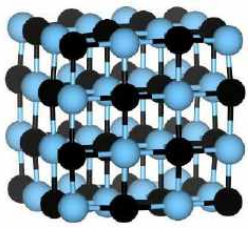	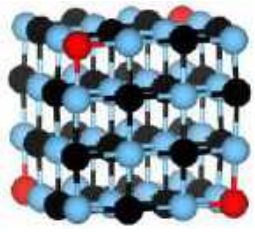	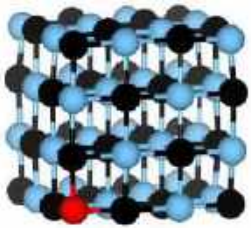

Figure 6.21. Three structures under study for $(TiC)_{32}$ size.

The harmonic IR spectra obtained for each NP structures are compared with the experimental IR data for this size are shown in Figure 6.22.

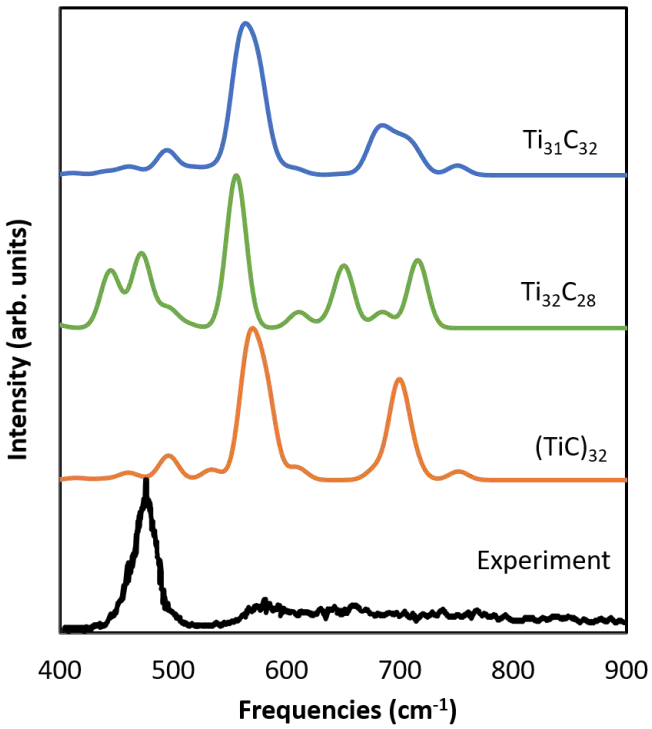

Figure 6.22. Simulated IR spectra for the $(TiC)_{32}$, $Ti_{32}C_{28}$, $Ti_{31}C_{32}$, and experimental IR.[18]

As for previously considered sizes, it is clearly observed that none of these simulated harmonic spectra match well with the experimental data. In this case, $Ti_{32}C_{28}$ presents a small peak at the same frequency that experimental data but except for this peak, the rest of the spectrum does not match. At this size, the $Ti_{31}C_{32}$ spectrum has two peaks, therefore this structure would not fit with the experimental data.

6.5.1.4. Larger TIC NPs

Finally, two larger NPs with 4×4×5 and 5×5×5 sizes are also studied corresponding with the experimental study. According with Figure 6.1, the masses of these NPs correspond approximately to the stoichiometric NPs. For this reason, in these sizes, only the stoichiometric cubic NP structures will be studied.

The $(TiC)_{40}$ size corresponds to the 4×4×5 NP case. The harmonic IR spectrum obtained is compared with the experimental data in Figure 6.23.

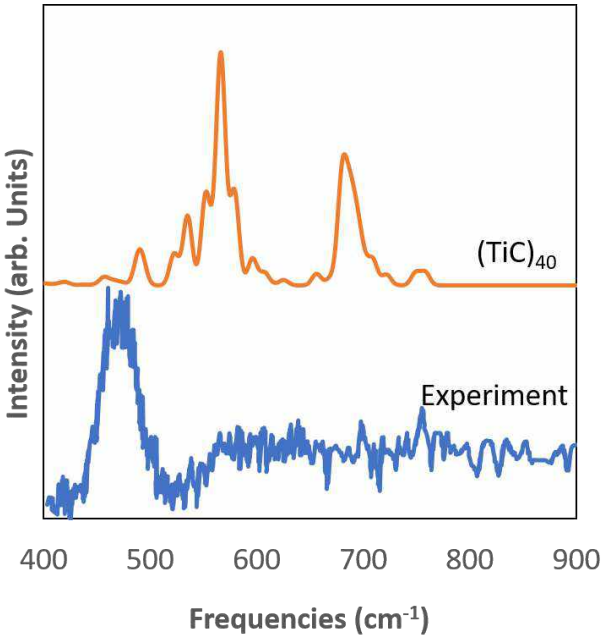

Figure 6.23. Simulated IR for the cubic $(TiC)_{40}$ NP and the experimental IR for the same size.[18]

The results in Figure 6.23 show that the harmonic IR simulated for $(TiC)_{40}$ does not match with the experimental IR. For this size, not other options are tested.

For the 3×3×3 size there are two isomers: $Ti_{63}C_{62}$ and $Ti_{63}C_{63}$. In this case, only first isomer has been characterized. This isomer has been chosen because it better corresponds with the stoichiometry of the identified $Ti_{14}C_{13}$ NP in experiment (*i.e.* the Ti-rich isomer) which has a lower tendency for C-C bond formation. The simulated harmonic IR spectrum for the $Ti_{63}C_{62}$ NP is compared with the experimental IR in Figure 6.24.

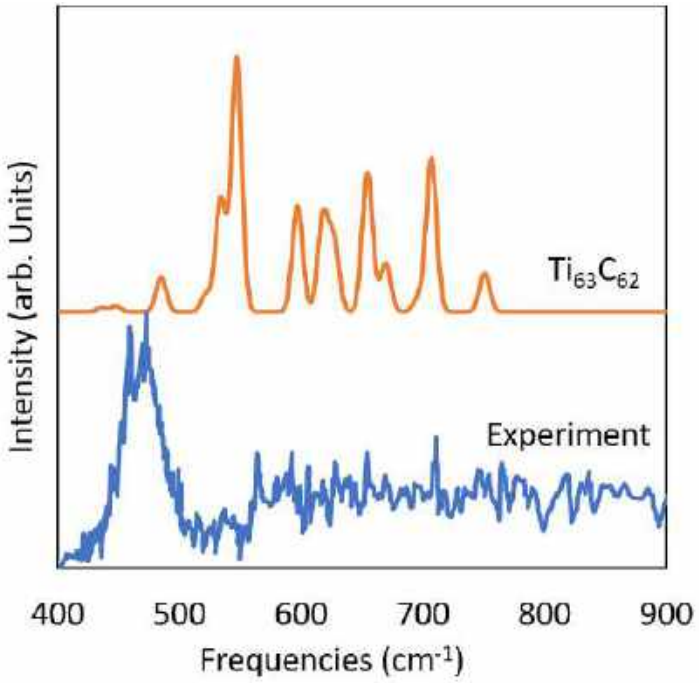

Figure 6.24. Simulated IR for the cubic$Ti_{63}C_{62}$ NP and the experimental IR data for the same NP size.[18]

As for the previous size, the IR simulated does not match with the experimental IR. The IR simulated presents more peaks than the simulated IR.

6.5.2. MD-based IR spectra

As seen in Section 6.3.5, temperature is an important effect which can improve the match between simulated IR spectra and experimental IR spectra. DFT-based MD runs at different temperatures were made in order to see if the derived IR spectra could improve the match with experiment with respect to the 0 K harmonic spectra. The temperatures tested were 900, 1500, and 2100 K in the $(TiC)_{18}$ size. In addition to the stoichiometric cubic structure, the $Ti_{18}C_{14}$ and $Ti_{17}C_{18}$ NPs were also studied. In the case of $Ti_{18}C_{14}$ and $Ti_{17}C_{18}$, the isomers studied are when the atoms are missing in the corners. In $Ti_{18}C_{14}$ because is the most energetically stable isomer that was found while the $Ti_{17}C_{18}$ in addition to being the most stable candidate that does not present C-C bonds, it is the isomer that best fits with the experimental one so far.

For the stoichiometric cubic $(TiC)_{18}$ size structure the spectra obtained at different temperatures have been compared with the experimental data. All spectra are shown in Figure 6.25.

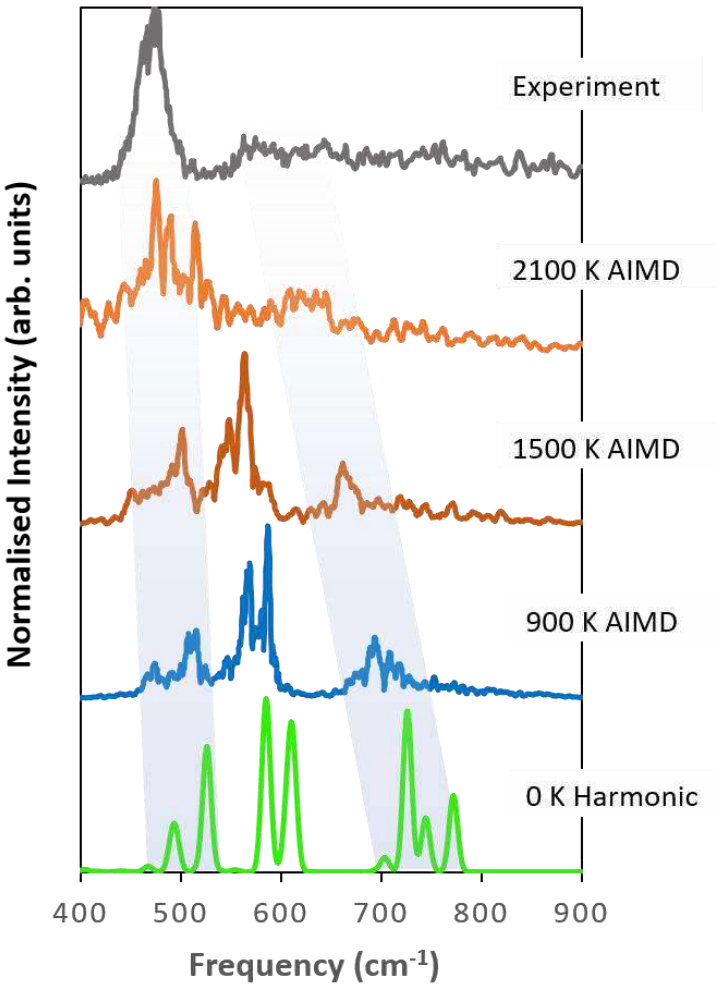

Figure 6.25. IR spectra at different temperatures for $(TiC)_{18}$ compared with the experimental IR.[18]

When one focuses on harmonic IR, three signals groups are shown. The first one is between 491 cm^{-1} and 537 cm^{-1}. In this interval there are two peaks, one at 491-494 cm^{-1} and other at 526-537 cm^{-1}. These peaks correspond to Ti-C-Ti bending modes (edges/corners) and some stretching modes. A second group of peaks are between 584-611 cm^{-1}. Here, another two peaks are shown, appearing at 586 cm^{-1} and 610 cm^{-1}. These vibrations modes involving large C corner motions. Finally, three peaks more have been found in the range of 725-772 cm^{-1}. These peaks are related with Ti-C-Ti stretching modes involving both edge and face C atoms.

The simulated IR spectra obtained by means of MD at 900, 1500, and 2100 K do not to match the experimental IR spectrum particularly well. While the experimental spectrum only presents one peak with a maximum close to 490 cm^{-1} the simulated IR at 2100 K present two peaks, one at similar frequency of the experimental and a second peak around the 600 cm^{-1}. This results indicate that the experimental IR spectrum does not correspond to the is the stoichiometric $(TiC)_{18}$ NP.

The same procedure of the stoichiometric compound was made for the $Ti_{17}C_{18}$ isomers. It should be remembered that for the harmonic spectrum, this compound is the one that best fits the experimental spectrum, since only one peak was obtained in its simulated IR. This peak drifted towards higher frequencies. In this case, the MD derived IR spectrum will better allow us to confirm or rule out this structure as the experimental IR structure. In Figure 6.26 all calculated IR spectra for $Ti_{17}C_{18}$ are compared with the corresponding experimental IR spectrum.

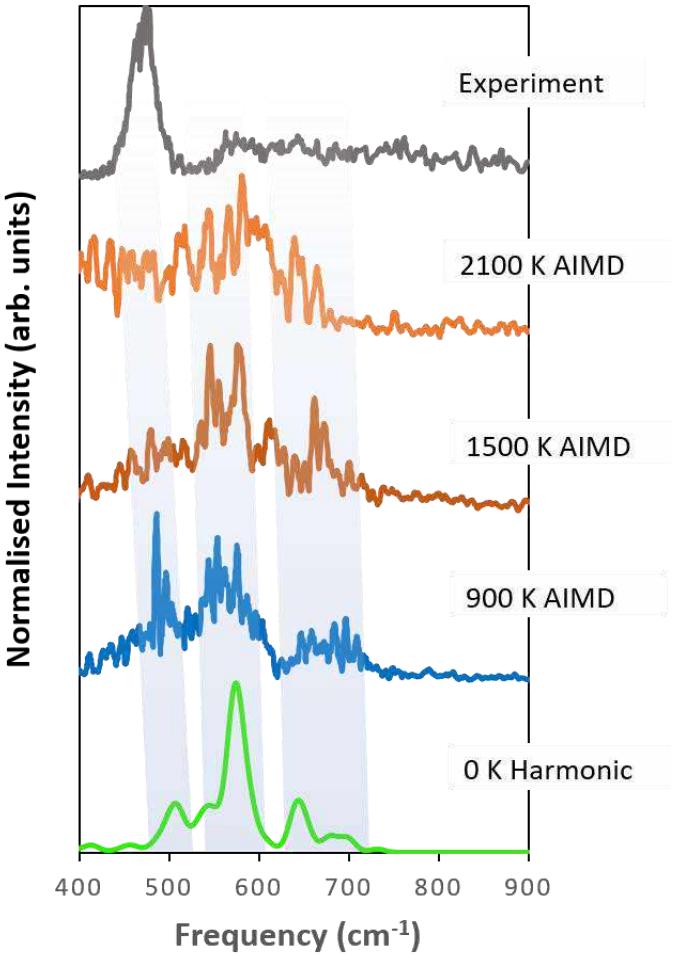

Figure 6.26. IR spectra at different temperatures for $Ti_{17}C_{18}$ compared with the experimental IR spectrum.[18]

As previously commented, in the harmonic IR spectrum, only one peak is observed, which corresponds to Ti-C-Ti bending modes. The temperature dependent MD-based spectra, are all found not match well with the experimental IR spectrum. With these results, this NP structure is also ruled out as a likely candidate to explain the experimental data.

For the $Ti_{18}C_{14}$ isomers Figure 6.27 shows the MD-derived IR spectra obtained at different temperatures compared with the corresponding experimental data.

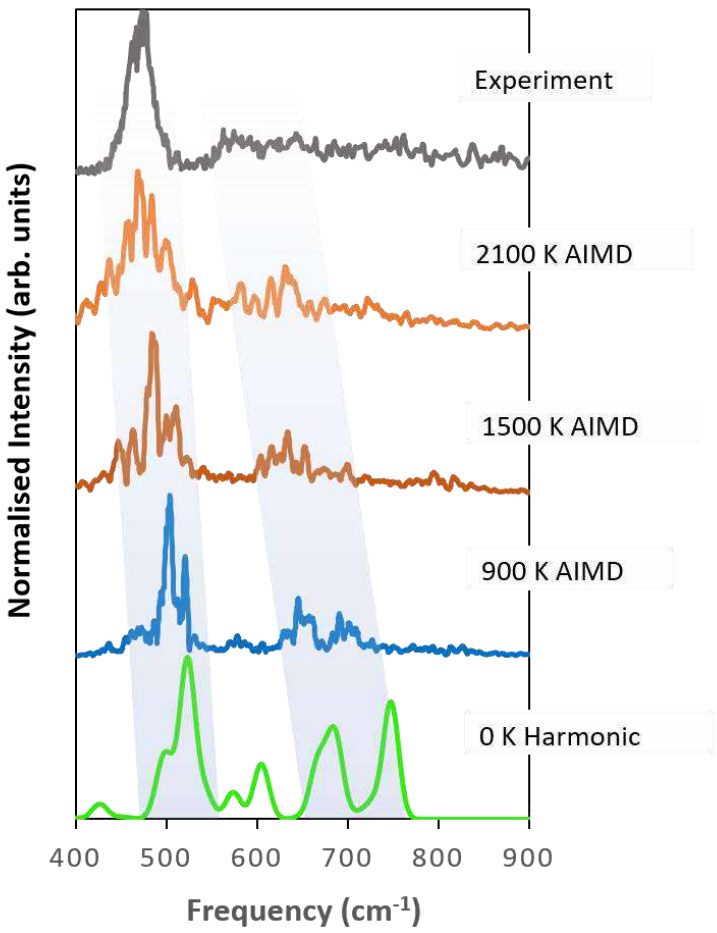

Figure 6.27. IR spectra at different temperatures for $Ti_{17}C_{18}$ compared with the experimental IR.[18]

In Figure 6.27 one can see that the MD-based IR spectra for $Ti_{18}C_{14}$ seems to match with the experimental IR for the higher temperatures considered. For the highest temperature considered (2100K) we compare the simulated IR spectra more detail in Figure 6.28.

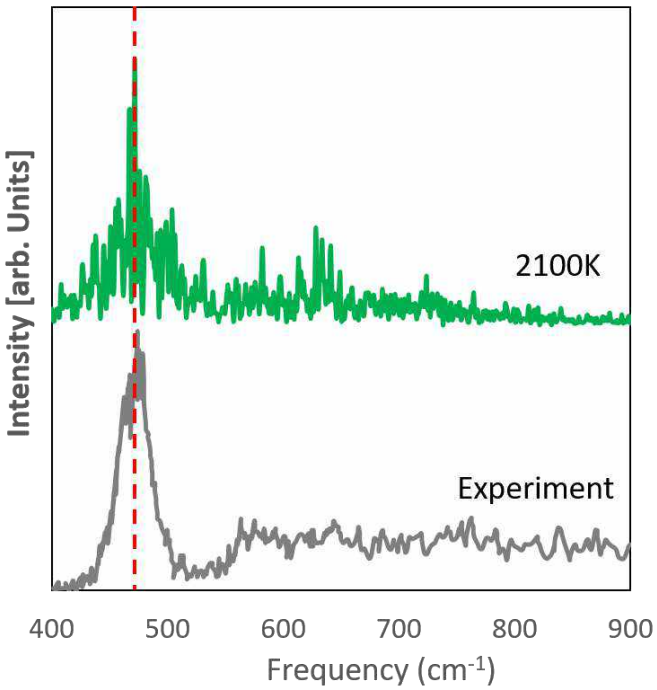

Figure 6.28. Experimental IR and Simulated IR spectrum for $Ti_{18}C_{14}$ compound at 2100 K.

In the last plot it can be seen clearly seen how the peak coincide. These results strongly suggest that the experimental IR spectrum corresponds to the $Ti_{18}C_{14}$ structure when the 4C atoms are missing from the stoichiometric NP in the corners.

6.6. Conclusions

The conclusion that can be drawn from this chapter are as follows. In the first place, different parameters of the simulation have been tested showing that some of them can modify the IR spectra (e.g. functional, charge state and temperature). The IR characterization of the simulated NPs has allowed us to compare with the experimental cluster beam derived IR spectra. The MD-derived IR spectra have allowed us to identify the likely NP structures in experiment for the two smaller NP sizes. In this case, it was found the that the experimental IR spectrum likely corresponds to the $Ti_{18}C_{14}$ structure when the 4C atoms are missing from the parent stoichiometric NP in the corners. Furthermore, this NP structure is the most stable found within all $Ti_{18}C_{14}$ isomer structures that have been studied. As it is the energetically most stable isomer, we tentatively suggest that this result could also be extrapolated to the larger NP sizes of $(TiC)_{24}$ and $(TiC)_{32}$ where it also happens that when the parent cubic structure loses the corners atoms it is the most stable isomer for Ti_xC_{x-4}.

6.7. Publication

Can Calculated Harmonic Vibrational Spectra Rationalize the Structure of TiC-based Nanoparticles?

Juan José Piñero,[1] Boutheina Kerkeni[2,3], Francesc Viñes,[1] and, Stefan T. Bromley,[1,4,*]

[1] *Departament de Ciència de Materials i Química Física & Institut de Química Teòrica i Computacional (IQTCUB), Universitat de Barcelona, c/ Martí i Franquès 1-11, 08028 Barcelona, Spain*

[2] *Département de Physique, Laboratoire de Physique de la Matière Condensée (LPMC) Faculté des Sciences de Tunis,Université de Tunis El Manar. Campus Universitaire 2092, Tunisia.*

[3] *ISAMM, Université de la Manouba, La Manouba 2010 Tunisia.*

[4] *Institució Catalana de Recerca i Estudis Avançats (ICREA), Passeig de Lluís Companys, 23, 08010 Barcelona (Spain)*

*** Corresponding author**: Stefan T. Bromley (s.bromley@ub.edu)

Nanoscale titanium carbide (TiC) is widely used in composites and energy applications. In order to design and optimize these systems and to gain a fundamental understanding of these nanomaterials, it important to understand the atomistic structure of nano-TiC. Cluster beam experiments have provided detailed infrared vibrational spectra of numerous Ti_xC_y nanoparticles with well defined masses. However, these spectra have yet to be convincingly assigned to Ti_xC_y nanoparticle structures. Herein, using accurate density functional theory based calculations, we perform a systematic survey of likely candidate nanoparticle structures with masses corresponding to those in experiment. Specifically, we calculate harmonic infrared vibrational spectra for a range of nanoparticles up to 100 atoms in size, all based on removing either four carbon atoms or a single titanium atom from parent rocksalt-structured stoichiometric TiC structures. Our calculations, clearly show that Ti-deficient nanoparticles are unlikely candidates to explain the experimental spectra as such structures are highly susceptible to C-C bonding, whose characteristic frequencies are not observed in experiment. However, our calculated infrared spectra for C-deficient

nanoparticles have some matching features with the experimental spectra but tend to have more complex infrared spectra with more peaks than those obtained from experiment. We suggest that the discrepancy between experiment and theory may be largely due to thermally induced anharmonicities and broadening in the former, which would not be accounted for in our harmonic vibrational calculations.

Introduction

Titanium carbide (TiC) is a refractory ceramic material which, due to its extreme hardness, is often incorporated as small particles into other materials (*e.g.* steels[1], rubber[2]), leading to composites with improved strength and wear-resistance. TiC nanoparticles (NPs) have further been proposed as high temperature nucleation seeds for dust growth around aging C-rich stars.[3] TiC surfaces and nanostructured TiC have be increasingly attracting attention for their potential to replace precious metals in catalysis,[4-6] and fuel cells.[7] In particular, TiC has been found to be highly active for catalysing important hydrogenation reactions,[8-10] which is likely linked to the range of intimate ways in which hydrogen and TiC can interact.[10-12]

Advances in all these areas are likely to be achieved through a better understanding the structure of TiC at the nanoscale. According to electronic structure calculations, even very small stoichiometric Ti_nC_n nanoclusters (*e.g.* for n = 6, 12) energetically prefer to exhibit the bulk rocksalt crystal structure.[13] Moving to C-rich Ti_xC_y compositions, nanoclusters start to exhibit C-C bonds and have non-rocksalt structures (*e.g.* the Ti_8C_{12} metcar).[14,15] For a similar small size and for a slightly C-poor composition, the infrared (IR) spectrum from cluster beam experiments for $Ti_{14}C_{13}$ is in good agreement with calculated IR spectra for a structure based on a simple cubic cut from the rocksalt bulk crystal.[14,16] Cluster beam experiments have also provided IR spectra for a range of larger NPs with masses compatible with the set of C-poor compositions (Ti_nC_{n-4}, with n = 18, 24, 32, 40, 50, and one of Ti_nC_{n-5} for n = 63).[17] These NPs are generally assumed be exhibit structures based on cubic cuts from the parent rocksalt crystal. In principle, as four carbon atoms have essentially the same mass as a single Ti atom (48 amu), the experimentally observed NP masses are also compatible with parent rocksalt cut structures with one missing Ti atom. As far as we are aware, theoretically calculated IR spectra have only been reported for some of the smaller parent rocksalt Ti_nC_n NP structures.[16] Unlike for the small cubic $Ti_{14}C_{13}$ and Ti_8C_{12} metcar nanoclusters, the calculated IR spectra of these parent rocksalt cut cubic NPs do not match well with the experimentally

observed spectra.[16] Herein, we investigate whether this lack of agreement between experiment and theory can be reconciled by accurately calculating the IR spectra of TiC-based NPs derived from parent cubic rocksalt cuts with either: *i)* four C atoms removed, or *ii)* a single Ti atom removed.

Computational methodology

All calculations of the TiC-based NPs were carried out using Density Functional Theory (DFT) based calculations as implemented in the Fritz-Haber Institute *Ab Initio* Molecular Simulations package (FHI-AIMS)[18]. The Generalized Gradient Approximation (GGA) Perdew-Burke-Ernzerhof (PBE) functional[19] was used in all calculations. GGA functionals have been found to provide calculated harmonic IR spectra for cubic $Ti_{14}C_{13}$ and Ti_8C_{12} metcar nanoclusters in good agreement with experimental spectra.[16,20] Considering the even number of electrons possessed by both atom types and the uncharged nature of the considered NPIs, all calculations were treated as non-spin polarized. The electronic density was expanded using a Light-Tier-1 basis of Numerical Atom-centered Orbitals (NAOs), providing results of a similar or higher quality to those obtained with valence triple-zeta plus polarization Gaussian type orbitals.[21–23]

All relative energies pertain to NP structures which have been optimized using the above DFT method and the Broyden-Fletcher-Goldfarb-Shanno (BFGS)[24] algorithm until the residual force component per atom was less than 10^{-2} eV/Å . Harmonic frequencies were then calculated using these optimized NP structures by calculating the second derivatives of the energy from the numerical changes in the forces arising from small finite atomic displacements (0.0025 Å). A 10 cm^{-1} full width at half maximum Gaussian broadening has been applied to all reported harmonic IR peaks for better approximating the finite width of the experimental peaks.

In order to search for alternative NP structures, a classical molecular dynamics (MD) simulated annealing approach was used employing modified embedded-atom method interatomic potentials[25] as implemented in the LAMMPS code.[26] Specifically, a series of contiguous NVT MD simulations were run

starting first from a high temperature (2500 - 3000K) and reducing the temperature in a step-wise manner by 500 K until a temperature of 1000K was reached. Low energy NP structures were then extracted and optimized using the above-described DFT approach.

Results and Discussion

We first confirm that our computational approach is adequate for the capturing the essential features of cubic TiC-based NP by calculating the harmonic IR spectrum for $Ti_{14}C_{13}$ (see Fig. 1). In agreement with other similar calculations,[16,27] we find two distinct peaks with frequencies closely in line with those observed experimentally. The first experimental peak with a maximum close to 490 cm^{-1} is very well reproduced by the DFT-based calculation, which gives a peak maximum at 496 cm^{-1}. This peak corresponds to a Ti-C-Ti bending mode mainly exhibited on the NP edges. We note that the peak width in the theoretical spectrum is fairly arbitrary and is added equally to all peaks *a posteriori* in order to mimic experimental broadening. The second experimental peak has a maximum around 630 cm^{-1} and is more broadened and lower in intensity compared to the first peak. With standard broadening, the corresponding theoretical peak in centred close to 670 cm^{-1} and has higher relative intensity compared the first peak. This peak corresponds to an asymmetric Ti-C-Ti stretching mode exhibited mainly by edge atoms. Generally, the two spectra are in good agreement if we take into account that the second peak appears to be more susceptible to broadening (*e.g.* due to anharmonic effects), which are intrinsically not captured by the harmonic approach.

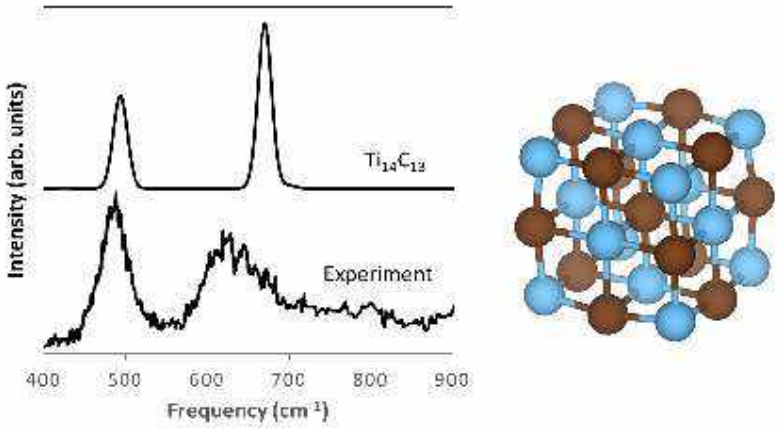

Figure 1. Left: Comparison of the experimental IR spectrum (lower) for the $Ti_{14}C_{13}$ NP (extracted with permission from ref. 14.) with the corresponding calculated harmonic DFT spectrum (upper). The intensity in each spectrum is normalized to the height of the highest peak. Right: Structure of the $Ti_{14}C_{13}$ NP. Atom key: Ti – blue, C – brown.

For larger TiC-based NPs the experimental IR vibrational spectra show only one significant peak with a maximum around 470-490 cm^{-1}. However, the calculated harmonic IR spectra for the corresponding parent TiC-based NPs show much more varied multi-peaked spectra for all the experimentally studied sizes. In Figure 2 we compare the DFT-calculated IR spectra for $(TiC)_n$ for n = 18, 24, 32, 40, 50 with a representative experimental spectrum for $(TiC)_{12}$. In addition to the theoretical spectra being significantly more complex than the experimental spectra, none of the calculated spectra have a peak with a frequency that convincingly corresponds to the single experimental 470-480 cm^{-1} peak. Considering the excellent match between theory and experiment for this peak for the $Ti_{14}C_{13}$ NP, it seems unlikely that any of these

parent stoichiometric cubic $(TiC)_n$ NPs contribute significantly to the experimental peaks. As mentioned above, this lack of theoretical-experimental correspondence is perhaps not surprising as the cluster beam experiments indicate that the NPs have masses which are 48 amu lower than the parent stoichiometric $(TiC)_n$ NPs. In the following we investigate two ways in which this mass lowering could be achieved with respect to the parent stoichiometric NPs: *i)* by removal of a single Ti atom, and *ii)* by removal of four C atoms for parent $(TiC)_n$ NPs with sizes n = 18, 24, 32.

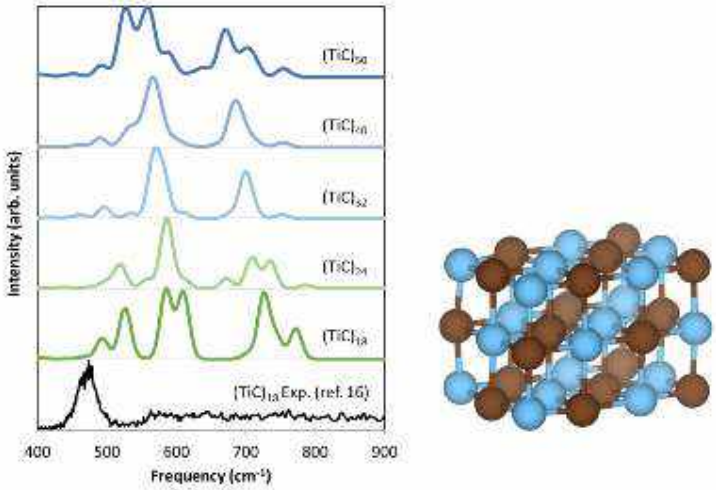

Figure 2. Left: Comparison of calculated IR spectra for $(TiC)_n$ NPs for n = 18, 24, 32, 40, 50 with a representative single-peaked experimental spectrum for $(TiC)_{18}$ (extracted with permission from ref. 17.). The intensity in each spectrum is normalized to the height of the highest peak. Right: The structure of the cubic rocksalt parent $(TiC)_{18}$ NP. Atom key: Ti – blue, C – brown.

$(TiC)_{18}$ based NPs

We first consider removal of a single Ti atom from the cubic parent $(TiC)_{18}$ NP. In Figure 3 we show four

different choices of Ti atoms to remove from the parent NP: *a)* the center of a square 3×3 facet, *b)* a corner, *c)* a long edge, and *d)* a short edge site. The resulting four $Ti_{17}C_{18}$ NPs were then directly optimized using DFT and used as initial structures for MD runs at a range of elevated temperatures (see above). The MD runs led to perturbation and thermal annealing of the initial NP structures leading to a total of 54 structurally distinct $Ti_{17}C_{18}$ NPs. From the direct DFT optimization of the four initial $Ti_{17}C_{18}$ NPs it is found that that removal of a Ti atom from either a short or long edge yields a much more stable optimized NP than taking a Ti atom from a corner (>3 eV) or a facet (>8 eV).

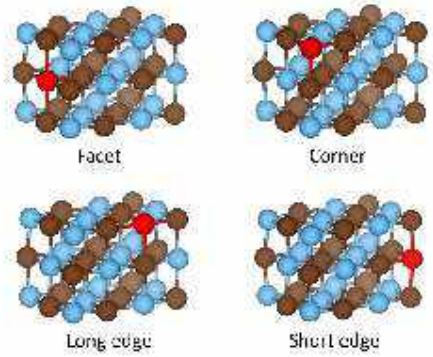

Figure 3. Selected Ti atoms to remove (red) from the cubic parent $(TiC)_{18}$ NP to create initial $Ti_{17}C_{18}$ NPs. Atom key: Ti – blue, C – brown.

The reason for these large energetic stability differences is due to the spontaneous formation of C-C bonds after structural optimization when a Ti is removed from an edge. In small stoichiometric $(TiC)_n$ nanoclusters, although the lowest energy structures tend to follow the Ti-C alternating order of the rocksalt crystal, low lying metastable isomers can exhibit C-C bonds. With increasing C content, the formation of highly energetically stabilizing C_2 dimers becomes more facile,[15] and most C-rich Ti_xC_y NPs are likely to exhibit such moieties. Our results comparing the DFT optimized energies of the 49 NPs resulting

from either direct optimisation of the NPs after removal of a Ti atom and/or the classical MD annealing runs further support this tendency, whereby the six lowest energy $Ti_{17}C_{18}$ NPs exhibit at least one C-C bond (see Fig. 4). The lowest energy $Ti_{17}C_{18}$ NPs of this set were found after direct optimization of the NPs with an edge Ti atom removed (see Fig. 3) where C-C bonds spontaneously formed between three C atoms upon relaxation of the initial NP structure (see Fig. 4).

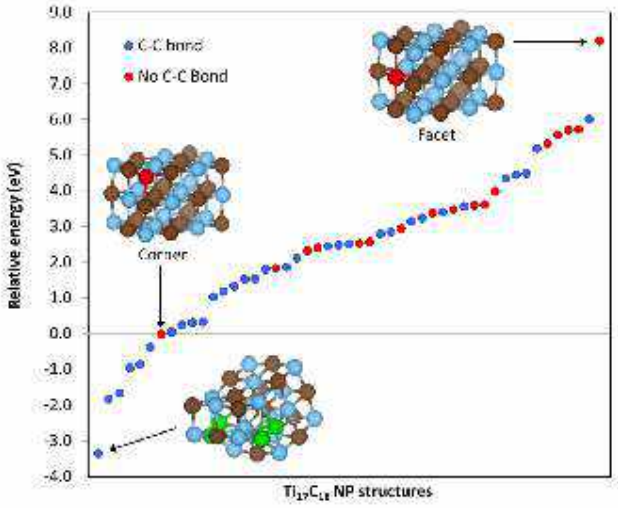

Figure 4. Energetic stabilities of $Ti_{17}C_{18}$ NPs structures containing at least one C-C bond (blue) and no C-C bonds (red) relative to the lowest energy NP with no C-C bond. The NP structures indicate the energies of the two $Ti_{17}C_{18}$ NPs which do not show C-C bonding (after removal of red Ti atoms) and the lowest energy $Ti_{17}C_{18}$ NP with two C-C dimers (highlighted by green C atoms). Atom key: Ti – blue, C – brown.

The formation of C-C bonds is readily identified in the IR spectra of Ti_xC_y NPs due to a strong signature peak close to 1350-1400 cm^{-1} associated with C-C stretching.[13,14] We note that the experimental IR spectra for the NPs considered in this study are not reported to exhibit such a peak[17] and NP structures

with C-C bonding are thus not considered as viable candidates. The lowest energy $Ti_{17}C_{18}$ NP without C-C bonding was found upon Ti removal from a corner of a $(TiC)_{18}$ rocksalt cut NP which we consider as the most likely C-rich NP candidate for potentially explaining the experimental IR results. We note that, although this candidate NP structure is a valid energy minimum (*i.e.* exhibits no imaginary frequencies), it is significantly metastable with respect to $Ti_{17}C_{18}$ NPs that exhibit C-C bonding and is unlikely to be stable at elevated temperatures. Indeed, our classical MD runs indicated that the structure of this NP could convert into one that shows C-C bonding.

As mentioned above, the mass of the experimental $(TiC)_{18}$ based NP is also compatible with a $Ti_{18}C_{14}$ stoichiometry. Based on comparison with experiments on vanadium carbide nanoparticles[28] and from theoretical studies on C bonding in TiC nanocrystals,[29] it is thought to be most likely that the C atoms are missing from the corners of such C-deficient NPs. As in the case of the $Ti_{17}C_{18}$ NPs, we first create a set of initial C-deficient $Ti_{18}C_{14}$ NPs by removing four C atoms from the parent $(TiC)_{18}$ cubic rocksalt NP. Compared to the removal of a single Ti atom there is greater number of possible initial choices for removing four carbon atoms. Thus, in addition to simple symmetric choices such as four corner atoms or four short edge atoms we also considered removal of from a variety of 'mixed' sites from the parent $(TiC)_{18}$ (see Fig. 5). These initial $Ti_{18}C_{14}$ NP structures were directly optimized using DFT and a selection of structures were also annealed using classical MD runs.

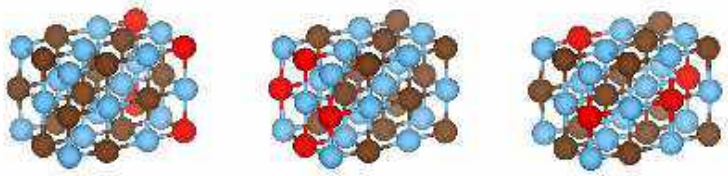

Figure 5. Examples of sets of four C atoms to remove (red) from the cubic parent $(TiC)_{18}$ NP to create initial

$Ti_{18}C_{14}$ NPs. Atom key: Ti – blue, C – brown.

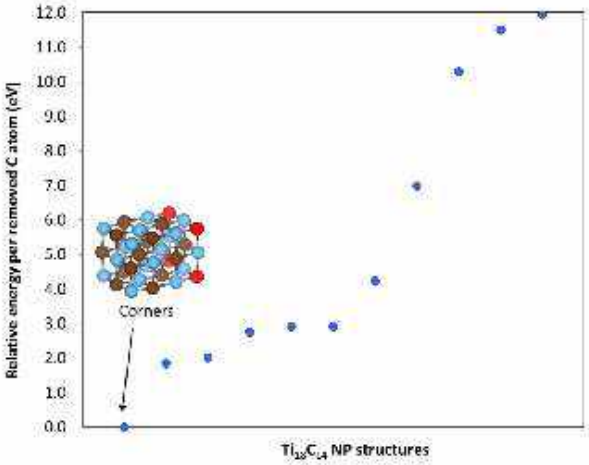

Figure 6. Energetic stabilities of $Ti_{18}C_{14}$ NPs structures relative to the lowest energy NP with C atoms removed from the corners as indicted by the NP structure (after removal of red Ti atoms). Atom key: Ti – blue, C – brown.

Of the $Ti_{18}C_{14}$ NPs resulting from this procedure, the NP with four C atoms from the corners was found to be the most energetically stable. Compared to the $Ti_{17}C_{18}$ case only relatively few structurally distinct $Ti_{18}C_{14}$ NPs were found within the same energy range (~12 eV per removed atom) – see Fig. 6. This relative lack of low energy $Ti_{18}C_{14}$ isomers seems to be due to the fact that removal of four C atoms is usually very structurally disruptive leading to high energy distorted NP structures. To achieve higher stability, it is energetically more favourable to remove low coordinated C atoms in a symmetric manner. In particular, the lowest energy $Ti_{18}C_{14}$ NP with corner C atoms missing was found to be 1.85 eV lower in energy than the next most stable $Ti_{18}C_{14}$ NP. These results clearly confirm arguments from both experiment[28] and theory[29] for parent TiC NPs with missing corner C atoms to be a very likely way to explain

the observed NP masses.

The calculated IR spectra for the lowest energy $Ti_{18}C_{14}$ NP, the lowest energy $Ti_{17}C_{18}$ NP without C-C bonding and the parent $(TiC)_{18}$ NP are compared with the corresponding experimental IR spectrum from ref. 17 in Figure 7. As can be clearly seen, none of the three simulated spectra is a good match for the experimental spectrum. While experimental IR spectrum only shows one dominant peak around 480 cm^{-1}, the calculated IR spectra display numerous peaks which all appear at higher frequencies. Of the three calculated IR spectra, only that for $Ti_{17}C_{18}$ has one dominant peak at 575 cm^{-1}. It is conceivable that effect of anharmonicity in the experimental spectrum would lead this peak to broaden and a shift towards lower frequencies, as in the case of the higher frequency peak in the $Ti_{14}C_{13}$ spectrum (see Fig. 1). However, this C-rich NP isomer is metastable to numerous other $Ti_{14}C_{13}$ NP isomers that contain C-C bonding and thus this assignment would also have to explain why this particular metastable isomer was favoured in the experimental set-up. For the lowest energy $Ti_{18}C_{14}$ we would have no such problem, and the spectrum shows a significant peak at 525 cm^{-1} which is closer to the main experimental peak than the main peak in the $Ti_{14}C_{13}$ spectrum and would require less anharmonic shifting/broadening. Clearly here, however, we also see numerous other significant peaks up to 750 cm^{-1} which would also have to simultaneously disappear in the experimental spectrum. Although, neither the $Ti_{14}C_{13}$ spectrum, nor the $Ti_{18}C_{14}$ are a convincing match for the experimental spectrum, both have fewer highly intense peaks compared to the calculated spectrum of the parent $(TiC)_{18}$ NP.

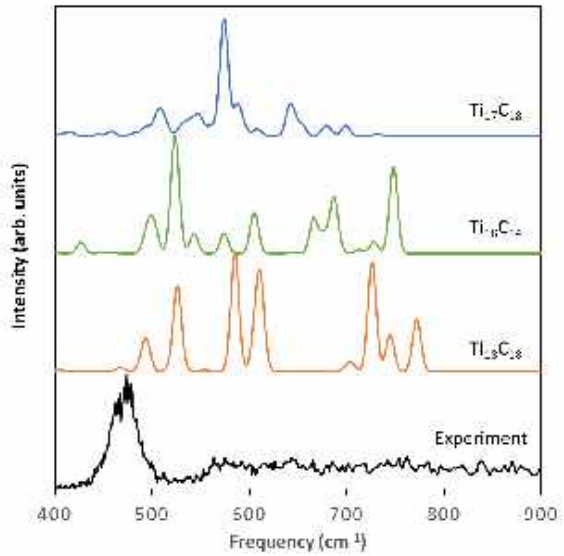

Figure 7. Comparison of calculated IR spectra for the lowest energy $Ti_{18}C_{14}$ NP, the lowest energy $Ti_{17}C_{18}$ NP without C-C bonding and the parent $(TiC)_{18}$ NP with the single-peaked experimental spectrum for $(TiC)_{18}$ (extracted with permission from ref. 17.). The intensity in each spectrum is normalized to the height of the highest peak.

$(TiC)_{24}$ and $(TiC)_{32}$ based NPs

We also consider a set of larger NPs based on removing a corner Ti atom and four corner C atoms from parent $(TiC)_{24}$ and $(TiC)_{32}$ NPs (see Fig. 8). In addition to be larger the structures of the parent NPs entail that the C atoms are present in symmetrically distinct arrangements as compared to the $(TiC)_{18}$, for which all corner C atoms are on one small facet. In $(TiC)_{24}$ the corner C atoms are arranged in pairs – with two C atoms on one edge and the other two on an opposite edge reflected through a mirror plane of the NP. For $(TiC)_{32}$ the four C atoms are present at alternating corner sites over the cubic NP. In Fig. 9 we show the

calculated IR spectra for the corresponding $Ti_{24}C_{20}$ and $Ti_{32}C_{28}$ NPs resulting from removing these C atoms. We also show the calculated IR spectra for the mass-equivalent Ti-deficient $Ti_{23}C_{24}$ and $Ti_{31}C_{32}$ NPs, respectively.

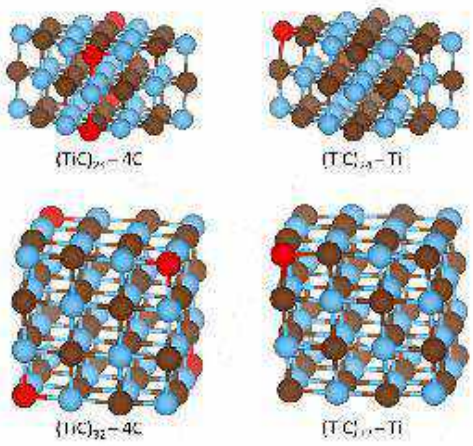

Figure 8. Parent $(TiC)_{24}$ (upper) and $(TiC)_{32}$ (lower) NPs with corner C atoms and corner Ti atoms (red) to be removed to create $Ti_{23}C_{24}$, $Ti_{24}C_{20}$, $Ti_{31}C_{32}$, and $Ti_{32}C_{28}$ NPs.

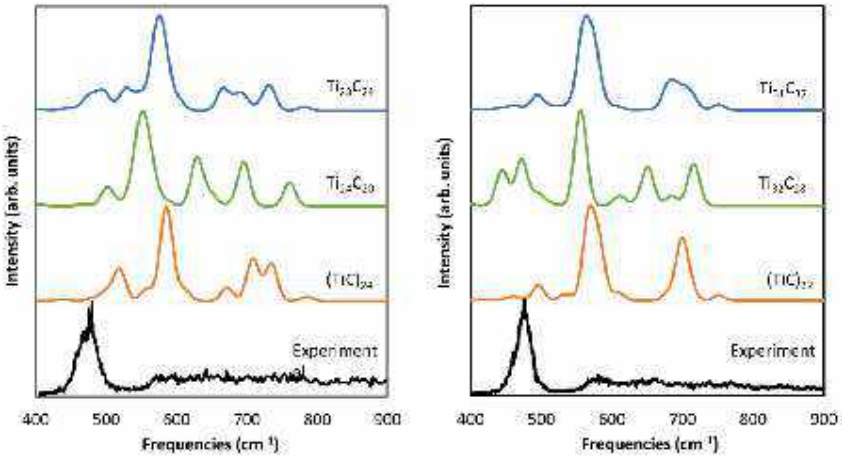

Figure 9. Left: Comparison of calculated IR spectra for the parent $(TiC)_{24}$ NP and for NPs resulting from the removal of four corner C atoms – $Ti_{24}C_{20}$, or the removal of a single corner Ti atom - $Ti_{23}C_{24}$, together with the corresponding experimental spectrum (extracted with permission from ref. 17.). Right: Comparison of calculated IR spectra for the parent $(TiC)_{32}$ NP and for NPs resulting from the removal of four corner C atoms – $Ti_{32}C_{28}$, or the removal of a single corner Ti atom – $Ti_{31}C_{32}$, together with the corresponding experimental spectrum (extracted with permission from ref. 17.). The intensity in each spectrum is normalized to the height of the highest peak.

Generally, the IR spectra for the C-rich $Ti_{23}C_{24}$ and $Ti_{31}C_{32}$ NPs and the C-poor $Ti_{24}C_{20}$ and $Ti_{32}C_{28}$ NPs appear to be somewhat simpler that the corresponding spectra for the $(TiC)_{18}$-based NPs (see Fig. 7) which is likely due to the higher structural symmetry of the larger NPs. The calculated IR spectrum for the C-rich NPs in Fig. 9 both show one main peak around 570-580 cm^{-1}, which is in line with the main peak of the spectrum for the $Ti_{17}C_{18}$ NP. Although this peak would likely be broadened and shifted in experimental, as

shown for the $Ti_{17}C_{18}$, we would expect that other more stable NP isomers exhibiting C-C bonding would also compete with the with these larger C-rich NPs. As such it is hard to rationalise the necessary abundance of such metastable NPs that would be needed to produce the observed single peak at 470-480 cm^{-1} in the experimental IR spectra. We also note that the spectra for these C-rich NPs are quite similar to the corresponding spectra of the parent stoichiometric NPs indicating that removal of a single Ti atom does not significantly perturb the overall vibrational response of these larger NPs.

The C-poor $Ti_{24}C_{20}$, $Ti_{32}C_{28}$ NPs also show one main peak at a slightly lower frequency (550-560 cm^{-1}) than the corresponding C-rich NPs. Here, the difference with the IR spectra of the corresponding parent NPs is larger, which is understandable due to the relatively larger structural perturbation caused by removal of four atoms. As in the case of the $Ti_{18}C_{14}$ NP the spectra for both $Ti_{24}C_{20}$, $Ti_{32}C_{28}$ NPs exhibit distinct peaks at significantly higher frequencies than the main peak (700 – 720 cm^{-1}), albeit with a lower relative intensity than in the spectrum of the smaller NP. Interestingly, the spectrum of the $Ti_{32}C_{28}$ NP is the first case we have found to show features around 450-475 cm^{-1}, which are close to the main peak in the corresponding experimental spectrum. These features are, however, quite low in intensity compared to the main peak of the $Ti_{32}C_{28}$ NP spectrum and thus are unlikely to fully explain the isolated low frequency peak in the experimental spectra. Overall, the C-poor spectra for these larger NPs have a clear main peak which is ~75 cm^{-1} higher than the corresponding experimental spectra, which potentially could be downshifted by anharmonicities. These C-poor NPs are likely structurally stable energetically low-lying candidates for the NPs produced in experiment. However, in addition to the main peak observed in the calculated spectra for all C-poor NPs, these spectra also contain numerous other significant peaks, which would have to be highly susceptible to severe broadening in experiment to explain their absence.

Conclusions

We have explored various TiC-based NP structures with masses compatible with those observed in the

cluster beam experiments reported in ref. 17. Matching with the experimental NP masses was achieved by taking the parent stoichiometric $(TiC)_n$ NP and either: *i)* removing one Ti atom, or *ii)* removing four C atoms. Removal of one Ti atom, leading to a slightly C-rich stoichiometry, tends to energetically favour NP structures that exhibit C-C bonding which is incompatible with the experimental IR spectra. Removal of one Ti atom from a NP corner leads to the lowest energy C-rich NP that does not display C-C bonding – albeit being metastable to NP structures with C-C bonds. Removal of four C atoms was found to be most energetically favourable from NP corners leading to structurally stable very low energy structures. The harmonic IR spectra of a series of NPs based on corner Ti-removal and corner C-removal were calculated and compared with the corresponding experimental spectra. Generally, the calculated spectra show more peaks over a wider frequency range and mainly at higher frequencies than the single main peak at ~480 cm^{-1} in the experimental spectra. Due to metastability of the C-rich NPs based on corner Ti-removal, it appears more probable that the experimental NPs are C-poor. Our calculated spectra for the C-poor NPs all have a main peak, which is 45-75 cm^{-1} higher than the single experimental peak, but also exhibit numerous other significant peaks that are not seen in experiment. Only if the calculated main peak in our C-corner deficient NPs in were downshifted due to anharmonic effects and all other peaks were severely broadened as to become almost noise, could we potentially assign the peaks in experiment to our NPs. As the experimental calculated spectra are not well reproduced by our harmonic spectra, in future studies we will pursue calculations, which explicitly permit us to assess the effects of anharmonicity and temperature.

Conflicts of interest

There are no conflicts to declare

Acknowledgements

This work has been supported by the Spanish MICIUN/FEDER RTI2018-095460-B-I00 and *María de Maeztu* MDM-2017-0767 grants and, in part, by *Generalitat de Catalunya* 2017SGR13 grant. F. V. is thankful to *Ministerio de Economía y Competitividad* (MEC) for his *Ramón y Cajal* (RYC-2012-10129) research contract. J.J.P. thanks the Spanish MINECO for *ayuda para la formación de doctores* contract (BES-2016-78816). The Red Española de Supercomputación (RES) is also acknowledged for the provision of supercomputing time.

References

(1) K. I. Parashivamurthy, R. K. Kumar, S. Seetharamu and M. N. Chandrasekharaiah, Review on TiC reinforced steel composites, *J. Mater. Sci.*, 2001, **36**, 4519-4530

(2) J. M. A. R. B. Jayasinghe, R. T. de Silva, K. M. N. de Silva, R. M. de Silva and V. A. Silva, Titanium carbide ceramic nanocrystals to enhance the physicochemical properties of natural rubber composites, *RSC Adv.*, 2020, **10**, 19290

(3) G. von Helden, A. G. G. M. Tielens, D. van Heijnsbergen, M. A. Duncan, S. Hony, L. B. F. M. Waters and G. Meijer, Titanium Carbide Nanocrystals in Circumstellar Environments, *Science*, 2000, **288**, 313-316

(4) S. T. Oyama, Preparation and catalytic properties of transition metal carbides and nitrides, *Catalysis Today*, 1992, **15**, 179-200

(5) F. Viñes, C. Sousa, P. Liu, J. A. Rodriguez and F. Illas, A systematic density functional theory study of the electronic structure of bulk and (001) surface of transition-metals carbides, *J. Chem. Phys*, 2005, **122**, 174709

(6) M. G. Quesne, A. Roldán, N. H. de Leeuw and C.R.A. Catlow, Bulk and surface properties of metal carbides: implications for catalysis, *J. Phys. Chem. C*, 2018, **20**, 6905

(7) S. Sahaa, B. M. Rajbongshi, V. Ramania and A. Verma, Titanium carbide: An emerging electrocatalyst for fuel cell and electrolyser, *Int. J. Hydrogen Energy*, 2021, **46**, 12801

(8) I. Kojima, E. Miyazaki, Y. Inoue and I. Yasumori, Catalytic activities of TiC, WC, and TaC for hydrogenation of ethylene, *J. Catal.*, 1979, **59**, 472-474

(9) J. A. Rodríguez, P. Liu, D. J. Stacchiola, S. D. Senanayake, M. G. White and J. G. Chen, Hydrogenation of CO_2 to Methanol: Importance of Metal–Oxide and Metal–Carbide Interfaces in the Activation of CO_2, *ACS Catal.*, 2015, **5**, 6696-6706

(10) H. Prats, J. J. Piñero, F. Viñes, S. T. Bromley, R. Sayós and F. Illas, Assessing the usefulness of transition metal carbides for hydrogenation reactions, *Chem. Commun*, 2019, **55**, 12797

(11) J. J. Piñero, P. J. Ramírez, S. T. Bromley, F. Illas, F. Viñes and J. A. Rodríguez, Diversity of adsorbed hydrogen on the TiC (001) surface at high coverages, *J. Phys. Chem. C*, 2018, **49**, 28013

(12)H. Ding, X. Fan, C. Li, X. Liu, X. D. Jiang and C. Wang, First-principles study of hydrogen storage in non-

stoichiometic TiC_x. *J. Alloys and Compounds*, 2013, **551**, 67
(13) O. Lamiel-Garcia, S. T. Bromley and F. Illas, Low-energy nanoscale clusters of $(TiC)_n$ n = 6, 12: A structural and energetic comparison with MgO, *Theor. Chem. Acc.*, 2013, **132**, 1312
(14) D. van Heijnsbergen, G. von Helden, M. A. Duncan, A. J. A. van Roij and G. Meije, Vibrational Spectroscopy of Gas-Phase Metal-Carbide Clusters and Nanocrystals, *Phys. Rev. Lett*, 1999, **83**, 4983
(15) J-O. Joswig and M. Springborg, The influence of C2 dimers on the stability of Ti_mC_n metcar clusters, *J. Chem. Phys.*, 2008, **129**, 134311
(16) M. Patzschke and D. Sundholm, Density-Functional-Theory Studies of the Infrared Spectra of Titanium Carbide Nanocrystals, *J. Phys. Chem. B*, 2005, **109**, 12503.
(17) G. von Helden, D. van Heijnsbergen and G. Meijer, Resonant Ionitzation Using IR light: A new tool to study the spectroscopy and dynamics of gas-Phase Molecules and Clursters, *J. Phys. Chem. A*, 2003, **107**, 1671-1688
(18) V. Blum, R. Gehrke, F. Hanke, P. Havu, V. Havu, X. Ren, K. Reuter and M. Scheffler, Ab initio molecular simulations with numeric atom-centered orbitals, *Comput. Phys. Commun.*, 2009, **180**, 2175-2196
(19) P. Perdew, K. Burke and M. Ernzerhof, Generalized Gradient Approximation Made Simple, *Phys. Rev. Lett.*, 1996, **77**, 3865-3868
(20) F. Viñes, J. A. Rodriguez, P. Liu and F. Illas, Catalyst size matters: Tuning the molecular mechanism of the water–gas shift reaction on titanium carbide based compounds, *J. Catal.*, 2008, **260**, 103-112
(21) O. Lamiel-Garcia, K. C. Ko, J. Y. Lee, S. T. Bromley, F. Illas, When Anatase Nanoparticles Become Bulklike: Properties of Realistic TiO2 Nanoparticles in the 1–6 nm Size Range from All Electron Relativistic Density Functional Theory Based Calculations, *J. Chem. Theory Comput.*, 2017, **13**, 1785-1793
(22) F. Viñes and F.; Illas, Electronic structure of stoichiometric and reduced ZnO from periodic relativistic all electron hybrid density functional calculations using numeric atom-centered orbitals, *J. Comput. Chem.*, 2017, **38**, 523-529
(23) S. R.Jensen, S. Saha, J. A. Flores-Livas, W. Huhn, V. Blum, S. Goedecker and L.Frediani, The Elephant in the Room of Density Functional Theory Calculations, *J. Phys. Chem. Lett.*,2017, **8**, 1449−1457
(24) J. Nocedal and S. J. Wright, Numerical optimization, *Springer*, 2006, 2. edition
(25) Y. M. Kim and B. J. Lee, Modified Embedded-Atom Method Interatomic Potentials for the Ti-C and Ti-N Binary Systems, *Acta Mater.*, 2008, **56**, 3481
(26) S. Plimpton, Fast Parallel Algorithms for Short-Range Molecular Dynamics, *J. Comp. Phys.*, 1995, **117**, 1-19
(27) F. Viñes, J. A. Rodriguez, P. Liu and F. Illas, Catalyst size matters: Tuning the molecular mechanism of the water–gas shift reaction on titanium carbide based compounds, *J. Catal.*,2008, **260**,103-112
(28) G. von Helden, D. van Heijnsbergen, M. A. Duncan and G. Meijer, IR-REMPI of vanadium-carbide nanocrystals: Ideal versus truncated lattices, *Chem. Phys. Lett.*, 2001, **333**, 350
(29) Q. Zhang and S. P. Lewis, Weak bonding of carbon atoms at corner sites in titanium-carbide nanocrystals, *Chem. Phys. Lett.*,2003, **372**, 836

19

6.8. References

1. K.I. Parashivamurthy, R.K. Kumar, S. Seetharamu, and M.N. Chandrasekharaiah. Review on TiC reinforced steel composites. *J. Mater. Sci.*, **2001**, 36, 4519–4530.
2. J.M.A.R.B. Jayasinghe, R.T. De Silva, K.M.N. De Silva, R.M. De Silva RM, and V. Asantha. Titanium carbide ceramic nanocrystals to enhance the physicochemical properties of natural rubber composites. *RSC Adv.*, **2020**,10, 19290–19299.

3. G. Von Helden, A.G.G.M Tielens, D. Van Heijnsbergen, M.A. Duncan, S. Hony, L.B.F.M. Waters, and G. Meijer. Titanium carbide nanocrystals in circumstellar environments. *Science*, **2000**, 288, *5464*, 313–316.
4. S.T. Oyama. Preparation and catalytic properties of transition metal carbides and nitrides. *Catal. Today.*, **1992**; 15, 179–200.
5. F. Viñes and C. Sousa. A systematic density functional theory study of the electronic structure of bulk and (001) surface of transition-metals carbides. *J. Chem. Phys.*, **2005**, 122, *17*, 4709.
6. M.G. Quesne, A. Roldan, N.H. De Leeuw, and C.R.A. Catlow. Bulk and surface properties of metal carbides: Implications for catalysis. *Phys. Chem. Chem. Phys*., **2018**, 20, *10*, 6905–6916.
7. S. Saha, B.M. Rajbongshi, V. Ramani V, and A. Verma. Titanium carbide: An emerging electrocatalyst for fuel cell and electrolyser. *Int J Hydrog. Energy*, **2021**,46, 24, 12801–12821.
8. I. Kojima, E. Miyazaki, Y. Inoue, and I. Yasumori. Catalytic activities of TiC, WC, and TaC for hydrogenation of ethylene. *J. Catal.*, **1979**, 59, *3*, 472–474.
9. J.A. Rodriguez, P. Liu, D.J. Stacchiola, S.D. Senanayake, M.G. White, and J.G.Chen. Hydrogenation of CO_2 to Methanol: Importance of Metal-Oxide and Metal-Carbide Interfaces in the Activation of CO_2. *ACS Catal.*, **2015**, 5, *11*, 6696–6706.
10. H. Prats, J.J. Piñero, F. Viñes, S.T. Bromley, R. Sayós, and F. Illas. Assessing the usefulness of transition metal carbides for hydrogenation reactions. *Chem Commun.*, **2019**, 55, *85*, 12797–800.
11. J.J. Piñero, P.J. Ramírez, S.T. Bromley,F. Illas, F. Viñes, and J.A. Rodriguez. Diversity of Adsorbed Hydrogen on the TiC(001) Surface at High Coverages. *J. Phys. Chem.* C., **2018**, 122, *49*, 28013–28020.
12. H. Ding, X. Fan, C. Li, X. Liu, D. Jiang, and C. Wang. First-principles study of hydrogen storage in non-stoichiometric TiC_x. *J. Alloys Compd.*, **2013**, 551, 67–71.
13. O. Lamiel-Garcia, S.T. Bromley, and F. Illas. Low-energy nanoscale clusters of $(TiC)_n$ n = 6, 12: A structural and energetic comparison with MgO. *Theor Chem Acc.*, **2013**; 132, *3*, 1–6.
14. D. Van Heijnsbergen, G. Von Helden, M.A. Duncan, A.J.A. Van Roij, and G. Meijer. Vibrational spectroscopy of gas-phase metal-carbide clusters and nanocrystals. *Phys Rev Lett*., **1999**, 83, *24*, 4983–4986.
15. J.O. Joswig and M. Springborg. The influence of C2 dimers on the stability of Ti(m)C(n) metcar clusters. *J. Chem. Phys.*, **2008**, 129,13, 4311.
16. M. Patzschke and D. Sundholm. Density-functional-theory studies of the infrared spectra of titanium carbide nanocrystals. *J. Phys. Chem. B.*, **2005**, 109, *25*, 12503–12508.
17. G. Von Helden, D. Van Heijnsbergen, and G. Meijer. Resonant ionization using IR light: A new tool to study the spectroscopy and dynamics of gas-phase molecules and clusters. *J. Phys. Chem. A.*, **2003**, 107, *11*, 1671–1688.
18. C. Oshima, T. Aizawa, M. Wuttig, R. Souda, S. Otani, Y. Ishizawa, H. Ishida, and K.Tekura. Surface-phonon dispersion curves of TiC(100). *Phys Rev B.*, **1987**, 36, *14*, 7510–7517.
19. J.P. Perdew, K. Burke, and M. Ernzerhof. Generalized gradient approximation made simple. *Phys Rev Lett.*, 1996, 77, 18, 3865–3868.
20. J.P. Perdew and M. Ernzerhof. Rationale for mixing exact exchange with density functional approximations. *J. Chem. Phys*., **1996**, 105, *22*, 9982–9985.
21. R.E. Báez, J.H. Díaz F., M.J. Espitia R. Estabilidad relativa del compuesto carburo de titanio TiC: Un estudio mediante DFT. *Rev Colomb Fis*., **2014**, 46, *2*, 39–42.

Chapter 7

H_2 adsorption and dissociation on TiC NPs

7. H_2 adsorption and dissociation on TiC NPs

7.1. Introduction

As discussed in the previous Chapter, nanoparticles are attracting increasing attention for their potential to replace precious metals in catalysis.[1,2] In many cases, NPs are already used as catalysts, as they have certain advantages over conventional catalysts due to less material use and a larger contact surface. This makes NPs very attractive catalysts. Currently NPs have a wide variety of potential applications in fields such as biomedical, optical, electronic, nanochemistry or agriculture.[3–6] In addition, they are also used for environmental purposes, such as the three-way catalysts used in cars to reduce the emission of gases that are harmful to the environment. TMC NPs have been synthetized and used as alkylation catalysts.[7]

In this Chapter we focus on the study of adsorption of hydrogen on TiC NPs, as was done on the TiC surface in Chapter 3. In this study the effect of the size of the NPs and their reactivity will be evaluated. Stoichiometric TiC NPs and C-deficient NPs reported in Chapter 6 will be studied.

7.2. Methodology

The approach to model hydrogen adsorption/dissociation on the TiC-based NPs closely follows the methodology employed for extended surfaces (see chapters 3 and 4). The adsorption of H_2 molecules has been studied by first adsorbing atomic H atom and then a H_2 molecule. Two separated H atoms are adsorbed to simulate the molecular dissociation. These adsorption calculations have been studied for a range of different locations on in the considered NPs and for different NP sizes and stoichiometries. The TiC NPs considered in this chapter were selected from those considered in Chapter 6. Specifically, we consider a range of NPs derived from cubic cuts from the parent TiC rocksalt crystal, and also such NPs with corner carbon atoms removed.

After studding H and H_2 adsorption, the H_2 dissociation reaction has been studied on these TiC NPs. In order to study the H_2 dissociation, the NEB method with FHI-aims has been employed. In this case, 8 intermediate images were made to find the TS. When the TS is found, the higher energy image corresponding to the candidate TS, is analysed using a vibrational frequency study to check if this point is a real TS.

The equation employed to obtained the adsorption energy is:

$$E_{ads}^{X} = E_{X/NP} - (E_X + E_{NP}) \qquad (7.1),$$

where $E_{X/N}$ is the total energy obtained for every position/coverage under study, E_x is the energy of one isolated H atom or isolated H_2 molecule under study, and E_{NP} is the energy of the NP.

7.3. H adsorption

In this part of the thesis, atomic H was adsorbed on TiC NPs. The NPs chosen to perform this study were $(TiC)_{18}$ and $Ti_{18}C_{14}$, when $(TiC)_{18}$ has lost four carbon atoms from the corners. The structures of these NPs are shown in Figure 7.1.

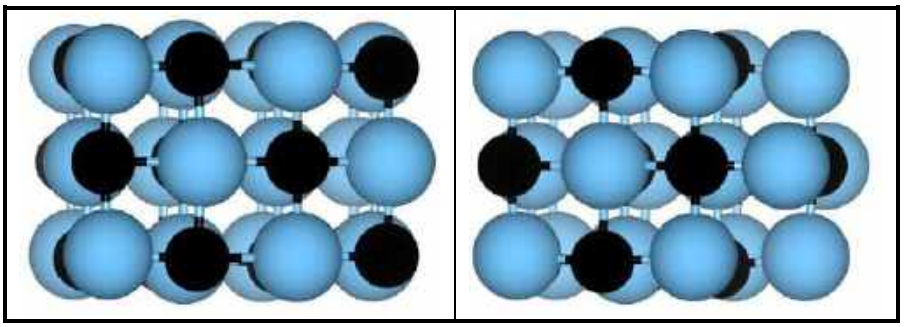

Figure 7.1. Left: $(TiC)_{18}$ NP. Right: $Ti_{18}C_{14}$ NP where four C atoms are removed from the corners. Blue Ti atoms and black C atoms. The same colour key will be used in all subsequent figures of TiC NPs.

The $(TiC)_{18}$ NP has been chosen because is the smallest size that exhibits many symmetrically distinct locations for H adsorption. In this case, the NP is a slightly elongated 4×3×3 cubic structure containing 36 atoms in total with two type of faces: Large rectangular faces and small square faces. The large face corresponds to the face that has four atoms and small face only has three atoms. The $Ti_{18}C_{14}$ NP is a low energy structure for this stoichiometry (see Chapter 6) and is a likely parent candidate for the carbon deficient $Ti_{18}C_{14}$ NP in IR-REMPI experiments.[8]

In this study four different adsorption locations were studied: Corner, edge, small face, and large face. In all cases, the adsorption has been studied on top of both Ti atoms and C atoms. The calculated adsorption energies of a single H atom at all considered locations on the $(TiC)_{18}$ and $Ti_{18}C_{14}$ NPs are reported in Table 7.1.

Table 7.1. Adsorption energy for one H atom on $(TiC)_{18}$ and $Ti_{18}C_{14}$ in eV.

E_{ads} H atom (eV)		$(TiC)_{18}$	$Ti_{18}C_{14}$
Corner	Ti	-2.95	-3.44
	C	-4.46	-
Edge	Ti	-2.46	-4.06
	C	-3.92	-3.79
Small face	Ti	-1.91	-2.17
	C	-3.08	-4.26
Large face	Ti	-2.04	-2.37
	C	-3.16	-2.93

The results shown that H adsorption in most cases is stronger on $Ti_{18}C_{14}$ than on $(TiC)_{18}$ with an exception for the large face when the H is adsorbed on C-Top, where adsorption is a little

more favourable (0.23 eV) on the $(TiC)_{18}$ NP. Generally, for both systems we note that adsorption on Top-C is more favourable than on Top-Ti.

Two cases attract attention in the case of H adsorption on the $Ti_{18}C_{14}$ NP. The first one is when H atom is adsorbed on Top-Ti on an edge. Here, the adsorption energy obtained is strong because the H migrates to a C-deficient corner forming a hydrogen bridge between two Ti atoms. This case is shown in Figure 7.2.

Figure 7.2. H adsorption on an edge for the $Ti_{18}C_{14}$ NP. The H atom migrates from its initial Ti_{edg} location to a C-deficient corner forming a bridge with two Ti atoms.

The second case corresponds when the H is adsorbed on Top-C on the small face. In this case, the obtained high adsorption energy is again due to the fact that H moves towards a C-deficient corner forming three bonds with three Ti atoms. See Figure 7.3.

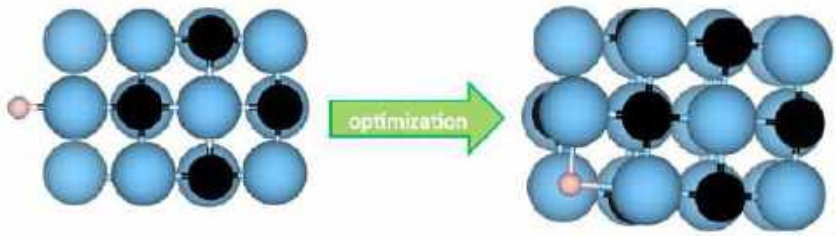

Figure 7.3. H adsorption on a small face for the $Ti_{18}C_{14}$ NP. The H atom migrates from its initial Ti_{fac} position to a C-deficient corner forming three bonds with Ti atoms.

Both phenomena significantly stabilize the structure of the NP + H system. For this reason, we consider these positions as likely H adsorption positions after H_2 molecule dissociation in the reported calculations below (Section 7.6).

7.4. H_2 adsorption

Following this scan of H atom adsorption on two example NPs, we move onto H_2 adsorption. In this section, we vary the NP size and test different locations for H_2 molecule adsorption.

7.4.1. Size effect in the H_2 adsorption

7.4.1.1 Cubic Nanoparticles.

In this part, cubic NPs have been studied. A cubic rocksalt cut NP possesses the same number of atoms in all three lattice directions. We separate cubic NPs into two blocks: Symmetric and Asymmetric NPs, See Scheme 7.1.

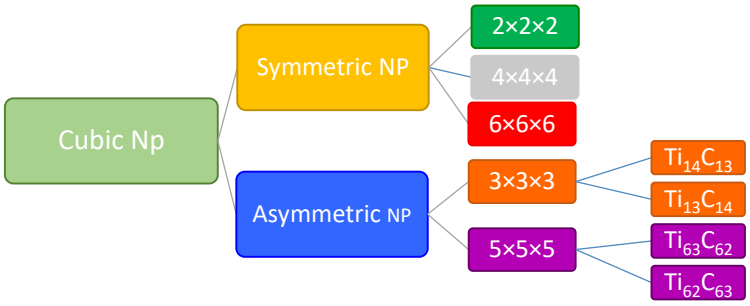

Scheme 7.1. Different Sizes of TiC NP under study. Three sizes will be studied for symmetrical NPs and two sizes more for asymmetrical NP. In addition, in asymmetrical NPs both isomers for each size will be studied.

Symmetric NPs

Symmetric cubic NPs are those which possess an equal number of Ti and C atoms, *i.e.* they follow the bulk TiC rocksalt stoichiometry, and are invariant with respect to interchange of Ti and C atoms. Three different sizes of symmetric cubic NPs are studied: 2×2×2, 4×4×4, and 6×6×6. The smaller size exhibits only eight atoms, four C and four Ti atoms. The medium size has a total of 64 atoms, 32 atoms of each element. Finally, the largest size possesses 108 C atoms and 108 Ti atoms making a total of 216 atoms. These NPs are shown in Figure 7.4.

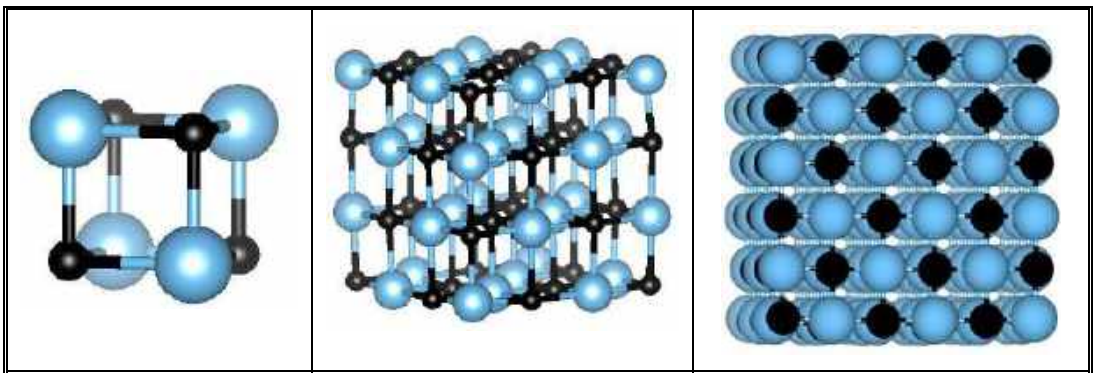

2×2×2 (TiC_4)	4×4×4 (TiC_{32})	6×6×6 (TiC_{108})

Figure 7.4. Structures of the two different symmetric NPs studied.

For each size, hydrogen molecule adsorption is studied in three positions: Corner, face, and edge. As these NPs are symmetrical, in any one NP all faces and edges are equivalent. The results obtained for H_2 adsorption are shown in Table 7.2.

Table 7.2. Adsorption energy in eV for symmetric TiC NPs using the FHI-AIMS code. * - No stable adsorption could be found. NA – not applicable due to unavailability of the site.

E_{ads}	Corner		Face		Edge	
	Carbon	Titanium	Carbon	Titanium	Carbon	Titanium
NP $TiC_4 + H_2$	-*	-0.22	NA	NA	NA	NA
NP $TiC_{32} + H_2$	-2.10	-0.24	-*	-0.07	-1.14	-0.26
NP $TiC_{108} + H_2$	-2.66	-0.26	-0.63	-0.10	-1.96	-0.25

In Table 7.2. one can see that as the NP size increases, the H_2 adsorption energy also increases. An exception is for Ti_{edg}, where we find almost exactly the same adsorption energy for TiC_{32} and TiC_{108}. The most favourable position for the H_2 adsorption is on C atoms at the corners. The adsorption of H_2 on C edge (C_{edg}) positions is the second place that H_2 prefers to be adsorbed. It is also important to note that the hydrogen molecule cannot be adsorbed on the faces and edges of $(TiC)_4$ because the NP is so small that it does not exhibit these positions. In addition, no stable adsorption for H_2 molecule could be found on C corners (C_{cor}) on $(TiC)_4$ and on C atom on the faces for $(TiC)_{32}$ NP.

Asymmetric NPs

Asymmetric cubic NPs possess an unequal number of Ti and C atoms with stoichiometry being either Ti_nC_{n-1} or $Ti_{n-1}C_n$. Here, two different NP sizes have been studied: 3×3×3 and 5×5×5. Asymmetric NPs are not invariant to atom interchange and two different NP have been investigated for each size: one with all C atoms at the corners and the other with all Ti atoms at the corners. In summary, four TiC asymmetric NP have been tested.

The NPs for sizes 3×3×3 (27 atoms) and 5×5×5 (125 atoms) the predominant atoms are the ones in the corners, and therefore there is always an atom more of this element than of the other. These NPs are shown in Figure 7.5.

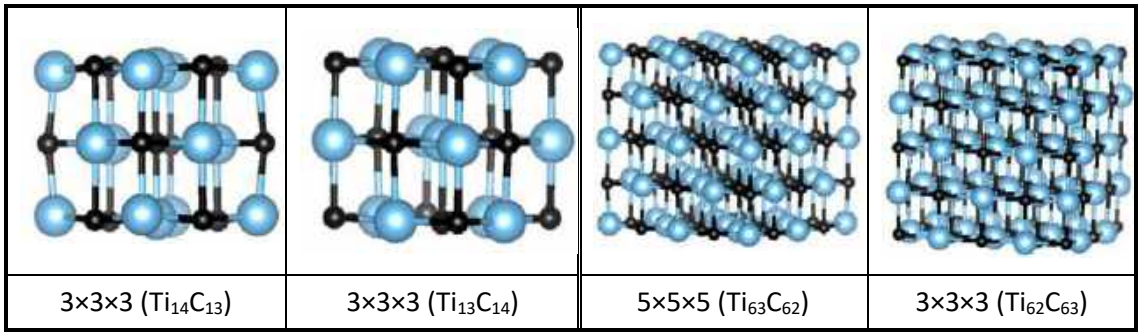

3×3×3 ($Ti_{14}C_{13}$)	3×3×3 ($Ti_{13}C_{14}$)	5×5×5 ($Ti_{63}C_{62}$)	3×3×3 ($Ti_{62}C_{63}$)

Figure 7.5. Structure of two different asymmetric NPs studied. In each case the NP can be realised in two ways: one with carbon atoms in the corners and the other with Ti atoms in the corners.

As for the symmetric NPs, for asymmetric NPs, three molecular hydrogen adsorption positions are studied: Corner, Face and Edge. The results obtained are classified by NP size below.

- **3×3×3 NP**

The calculated H_2 adsorption energies for both NP for 3×3×3 size are shown in Table 7.3. We note that certain H_2 adsorption locations were not possible depending of the structure of the NP being studied. For example, the $Ti_{13}C_{14}$ NP has no Ti corner sites for adsorption.

Table 7.3. H_2 adsorption energies in eV for various locations on the two 3×3×3 TiC NPs. NA – not applicable due to unavailability of the site.

E_{ads} (eV)	Corner		Face		Edge	
	Carbon	Titanium	Carbon	Titanium	Carbon	Titanium
NP $Ti_{14}C_{13} + H_2$	NA	-0.36	NA	-0.10	-0.75	NA
NP $Ti_{13}C_{14} + H_2$	-2.46	NA	0.96	NA	NA	-0.39

The results shown that the most energetically favourable locations for H_2 adsorption is on low coordinated C atoms. $Ti_{13}C_{14}$ NP has C atoms at the corners which thus provide the most energetically favourable locations for H_2 adsorption. The $Ti_{14}C_{13}$ NP lacks C atoms at the corners, and thus the most favourable adsorption occurs on the edge C atoms.

The results for both NPs for the 5×5×5 size are shown in Table 7.4.

Table 7.4. H_2 adsorption energies in eV for various locations on the two 5×5×5 TiC NPs. NA – not applicable due to unavailability of the site.

E_{ads} (eV)	Corner		Face		Edge	
	Carbon	Titanium	Carbon	Titanium	Carbon	Titanium
NP $Ti_{63}C_{62} + H_2$	NA	-0.26	-0.03	-0.12	-1.82	-0.25
NP $Ti_{62}C_{63} + H_2$	-2.53	NA	-0.36	-0.10	-1.73	-0.32

The results obtained for size 5×5×5 show that the H_2 adsorption is most favourable at the low coordinated Corners and edges, as for the 3×3×3 NPs. The $Ti_{63}C_{62}$ NP does not have C atoms at the corners leading to C_{edg} being the most favourable position for adsorption in this case.

In summary, the results show that the adsorption on carbon atoms increases with increasing size, this tendency can see in Figure 7.6 where the adsorption on C-edge in different NP sizes are represented. Regarding the titanium atoms, it can be said that this adsorption is independent of size since the adsorption energy does not show great variations.

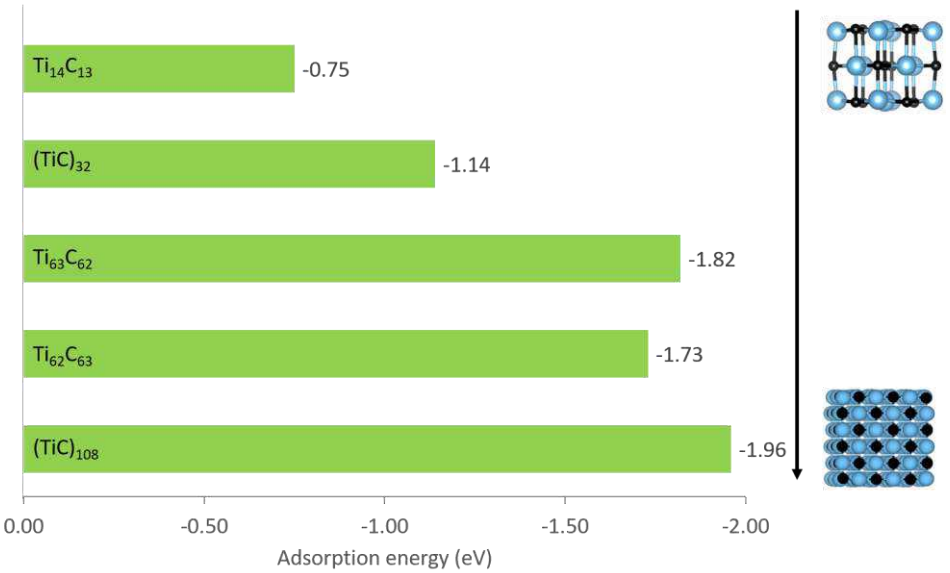

Figure 7.6. Trend in adsorption energy in eV for the H_2 molecule adsorption on C-edge positions for different NP sizes.

7.4.1.2 Non-cubic Nanoparticles

Non-cubic NPs have also been studied. For this type of NP, two different sizes are studied: 3×3×4 and 3×4×4.

The 3x3x4 NP size possesses a total of 36 atoms where 18 correspond to Ti and the other 18 are C. The 3x3x4 NP is a little bigger where there are 24 Ti and 24 C atoms forming a TiC NP of 48 atoms. Both NP structures are shown in Figure 7.7.

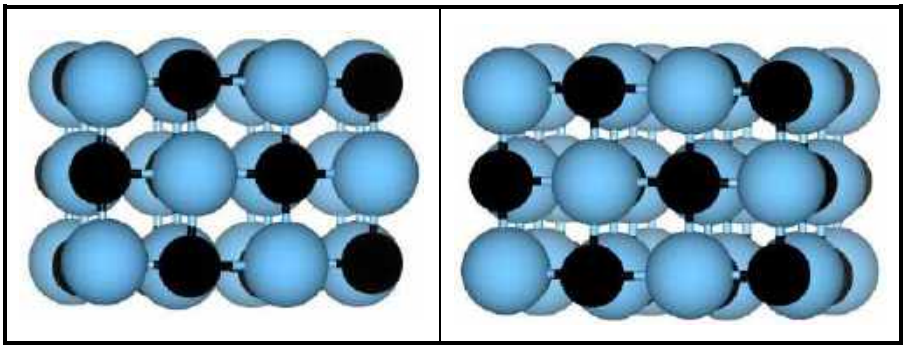

Figure 7.7. Left: 3×3×4 TiC NP $(TiC)_{18}$. Right: 3×4×4 TiC NP $(TiC)_{24}$.

The H_2 adsorption on these NPs are studied at the same locations as described above. The results obtained for both NPs are shown in Table 7.5.

Table 7.5. H_2 Adsorption energy for different locations on for $(TiC)_{18}$ and $(TiC)_{24}$ NPs. NFA – Not favorable adsorption.

E_{ads} (eV)	Corner		Face				Edge	
			small		large			
	Carbon	Titanium	Carbon	Titanium	Carbon	Titanium	Carbon	Titanium
NP $(TiC)_{18} + H_2$	-1.97	-0.27	NFA	-0.11	NFA	-0.05	-0.72	-0.35
NP $(TiC)_{24} + H_2$	-1.89	-0.26	NFA	-0.04	NFA	-0.09	-0.89	-0.29

The results show that the most energetically favourable adsorption place is on C corners as for the symmetric NPs. Like the symmetric NPs, the adsorption on the C atoms on the faces is not stable and during the simulation, the H_2 molecule migrates from C-Top site to a neighbouring Ti-Top site.

Finally, H_2 adsorption at different locations on both NPs with four corner carbon atoms removed has been considered.

$(TiC)_{18}$ (4×3×3)

Removal of 4C corner atoms from the stoichiometric 4×3×3 NP yields a $Ti_{18}C_{14}$ NP as shown in Figure 7.8.

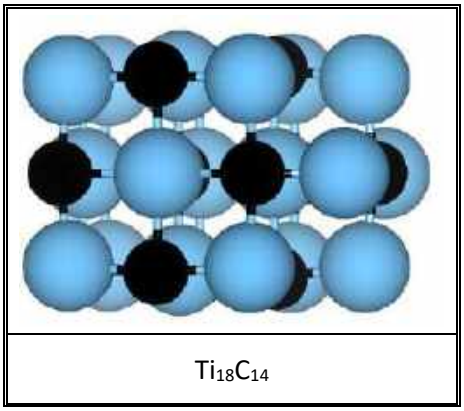

$Ti_{18}C_{14}$

Figure 7.8. $(TiC)_{18}$ NP for which four corner C atoms are removed.

This study has carried for four different positions: corner, edge, small face, and large face.

Table 7.6. Adsorption energy in eV for H_2 molecule on $(TiC)_{18}$ and $Ti_{18}C_{14}$ for different orientations and positions tested. NA – not applicable due to unavailability of the site.

H_2 adsorption		$Ti_{18}C_{14}$
Corner	Ti	-0.26
	C	NA
edge	Ti	-0.30
	C	-0.41
Small face	Ti	-0.02
	C	0.00
Large face	Ti	-0.03
	C	-2.01

The results show that for $(TiC)_{18}$ the adsorption is generally stronger than on $Ti_{18}C_{14}$ except in the case when the adsorption is on a large face on a C atom where the H_2 molecule dissociates. This happens because the H_2 molecule migrates to a nearby Ti, and then spontaneously dissociates. The final structure corresponds to two H atoms adsorbed on the C-deficient the corners. In Figure 7.9 we show the initial and final structures for this case.

Figure 7.9. Initial and final geometries of the H_2 disosiation allocated in Ti Face.

$(TiC)_{24}$ (4×4×3)

The same procedure that previous size has been carried out for this the $(TiC)_{24}$ NP with four removed C corners (i.e. a $Ti_{24}C_{20}$ NP). Note that for this size, the C atoms are not all in the same face, instead two C atoms are on one side of the NP and the other two C atoms are located on the opposite side (see Figure 7.10). The calculated H_2 adsorption values are shown in Table 7.7.

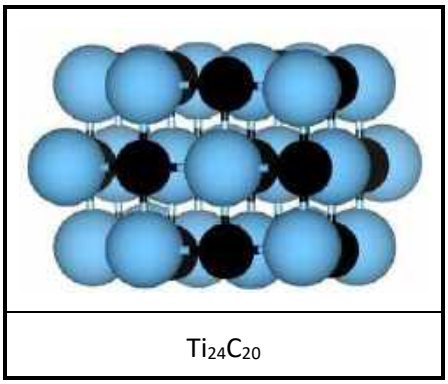

$Ti_{24}C_{20}$

Figure 7.10. $(TiC)_{24}$ NP with four C_{cor} atoms removed.

Table 7.7. H_2 adsorption energy in eV for $Ti_{24}C_{20}$ for different positions.

E_{ads} (eV)	Corner		Face				Edge	
			Small		Large			
	Carbon	Titanium	Carbon	Titanium	Carbon	Titanium	Carbon	Titanium
NP $Ti_{24}C_{20}$ + H_2	-	-0.28	-0.63	-0.06	-0.34	-0.05	-1.13	-0.33

The results obtained show that, in the same way as for the smaller NP size studied before, when the C-corners are removed, the reactivity increases. In this case, when the results of Table 7. are compared with the results for $(TiC)_{24}$ (Table 7.) the reactivity of the C-face increases, since the H_2 adsorption on $(TiC)_{24}$ is not favourable, while on $Ti_{24}C_{20}$ this adsorption is energetically favourable. The reactivity on Ti atoms is practically not affected when the four C-corners are removed.

7.4.2. Initial distance effect between NP and H_2 molecule in the H_2 adsorption

In this part, the initial distance between the $Ti_{18}C_{14}$ NP and the H_2 molecule and its direction of approach is examined. In this study, two adsorption locations which we name: i) lone Ti and ii) barycentre. These points have been chosen due the previous results where it has been observed that in these places, H_2 molecule dissociates spontaneously. Both sites can be seen in Figure 7.11.

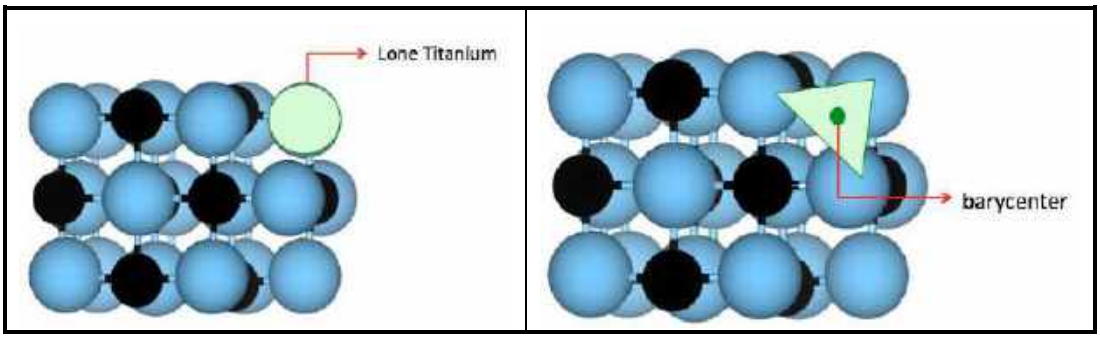

Figure 7.11. Two adsorption locations under study. Left: Lone titanium. Right: Barycentre.

In addition, in these two places, three different initial H_2 orientations with respect to the site are tested which we name: up, frontal, and, diagonal. These orientations are shown in Figure 7.12.

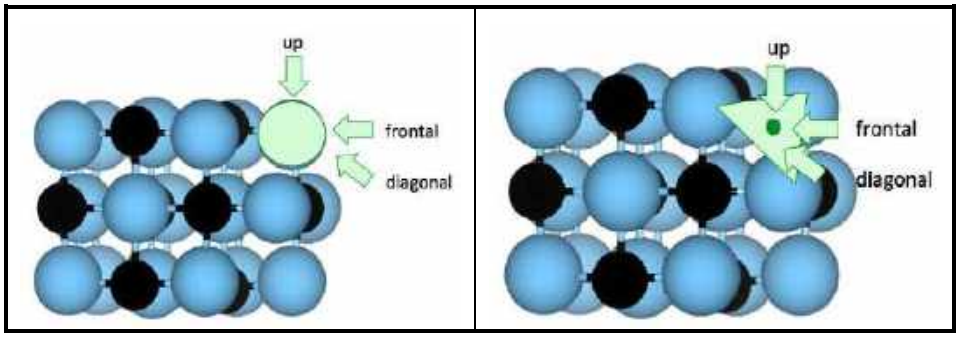

Figure 7.12. Different orientations for H_2 approach studied with respect to the two adsorptions locations studied.

The study has been carried out for H_2-NP distances between 1.5 Å and 7.0 Å. The results obtained for the lone Ti site can be seen in Table 7.8.

Table 7.8. E_{ads} for different orientations of H_2 and initial H_2 – NP distances with respect to the lone Ti in the NP, in eV.

Distance (Å)	E_{ads} up	E_{ads} Frontal	E_{ads} diagonal
1.50	-2.00	-2.00	-2.00
1.75	-2.00	-0.19	-2.00
2.00	-0.18	-0.19	-2.00
2.50	-0.18	-0.19	-2.00
3.00	-2.00	-2.00	-2.01
3.50	-1.34	-1.91	-0.08
4.00	-2.00	-2.00	-0.08
4.50	-2.00	-2.00	-0.08
5.00	-2.00	-2.00	-0.08
5.50	-1.34	-2.00	-0.08
6.00	-2.00	-2.00	-0.08
6.50	0.00	-2.00	-0.08
7.00	0.00	0.00	0.00

The results reveal three different groups of adsorption energy values. First of this group corresponds to energy values of -2.00 eV and -1.91 eV. In the first cases, the H_2 molecule dissociates and the H atoms are adsorbed on two C-deficient corners, each interacting with three different Ti atoms. This situation arises for all three initial orientations studied. Secondly, when the energy is -1.91 eV, this adsorption of the second H atom is not on the corner, in this

case, the H atom only interacts with two Ti atoms and only occurs when the H_2 molecule approaches frontally. Both cases can be seen in Figure 7.13.

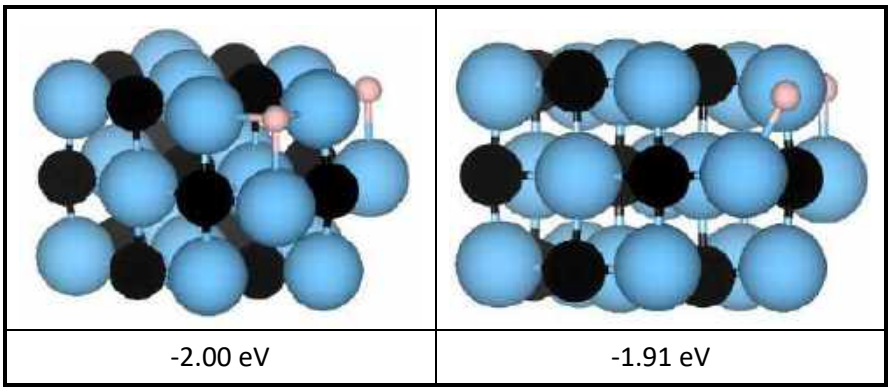

Figure 7.13. Final positions for the two most favourable H_2 molecule dissociations on the $Ti_{18}C_{14}$ NP.

The second group corresponds to an adsorption value of -1.34 eV. This case, only occurs when the H_2 molecule approaches from the "up" direction. In this case, the H_2 molecule dissociates and one H atom migrates to a C-deficient corner and the other H atom forms a bridge between two Ti atoms. The final geometry for this energy can be seen in Figure 7.14.

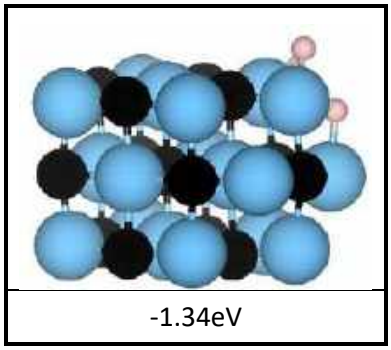

Figure 7.14. Final structure of dissociated H_2 when the adsortion energy corresponds to -1.34 eV on the $Ti_{18}C_{14}$ NP.

The last group of adsorption energies are below -0.20 eV. In this case, the interaction between the NP and the molecule is presumed to be a weak physisorption.

Finally, the adsorption energy versus distance is plotted to see better the effect of the initial distance and orientation on the H_2 molecule dissociation.

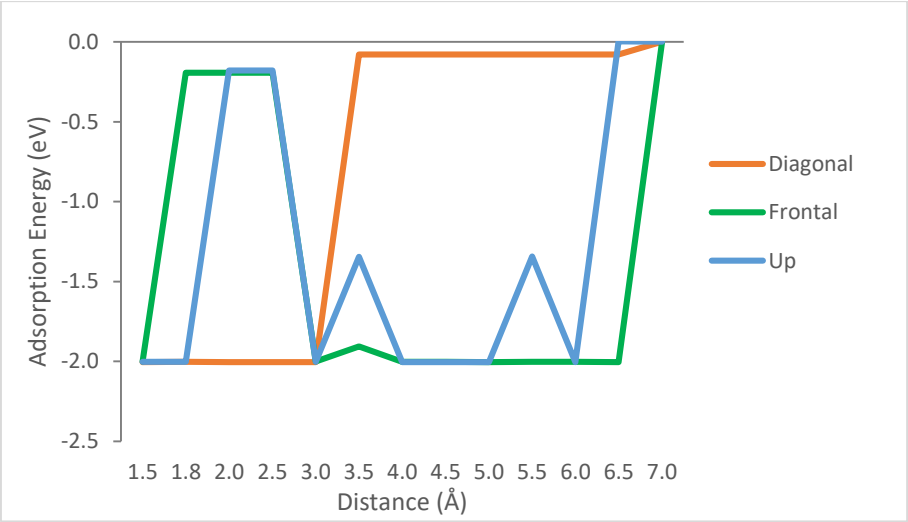

Figure 7.15. H_2 adsorption energy values with the three different orientations and different H_2 – NP initial distances with respect to the lone Ti site on the $Ti_{18}C_{14}$ NP.

In the diagonal orientation with respect to the lone Ti atom, when the initial H_2 – NP distance is lower than 3 Å, H_2 dissociates spontaneously giving place to both H atoms adsorbed on the corners as it is shown in Figure 7.15. For the other two orientations spontaneous dissociation occurs at distances greater than 3 Å and less than 6 Å. At the smallest initial distance of 1.5 Å, we find that spontaneous dissociation occurs for all orientations.

The above study was also done with respect to the barycenter site (see Figure 7.11 and Figure 7.12 and the results obtained are reported in Table 7.9.

Table 7.9. E_{ads} for different orientations of H_2 and initial H_2 – NP distances with respect to the barycenter site on the NP, in eV.

Distance (Å)	E_{ads} up	E_{ads} Frontal	E_{ads} diagonal
0.00	-1.34	-1.34	-1.34
1.50	-1.34	-1.10	-2.00
1.75	-1.34	-1.34	-2.00
2.00	-1.34	-1.34	-1.34
2.25	-0.08	-1.10	-1.34
2.50	-0.08	-0.08	-0.08
2.75	-0.08	-0.08	-0.08
3.00	-0.08	-0.08	-0.08
3.50	-0.08	-0.08	-0.08
4.00	-0.08	-0.08	-0.08
4.50	-0.08	-0.08	-0.08
5.00	-0.08	-0.08	-0.08
5.50	-0.08	-0.08	-0.08
6.00	-0.08	-0.08	-0.08
6.50	0.01	-0.08	-0.08
7.00	0.00	0.00	0.00

In this study the results obtained show four different adsorption energies. Three of them are greater than 1eV. The structure associated with these energies can be seen in Figure 7.16.

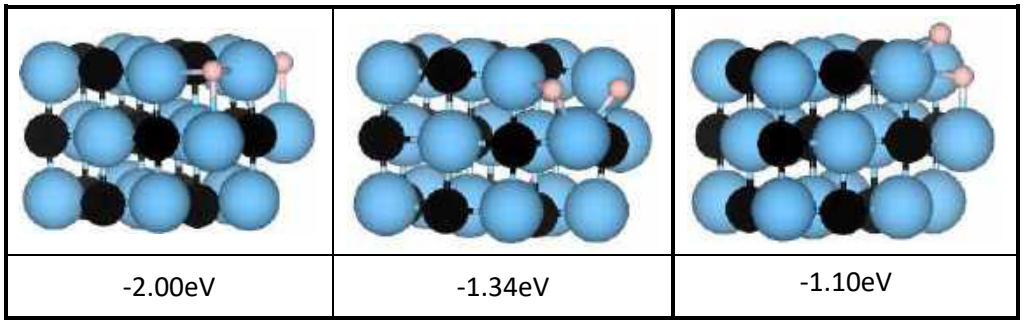

Figure 7.16. Different structures for H_2 adsorption on the $Ti_{18}C_{14}$ NP. Left: the two H atoms are completely dissociated and adsorbed on two separate corners. Center: both H atoms form a bridge between two Ti atoms. Right: one H atom is adsorbed on a corner and another H on a Ti edge.

The largest magnitude adsorption energy obtained is -2.00 eV for barycenter adsorption. This energy and structure is the same obtained in the previous study for the lone Ti site. In the case where the adsorption energy is -1.34 eV, the energy obtained is the same as that previously found, but the structure is different. In this case, both H molecules are dissociated and adsorbed on the same Ti atom located on the face, and each of them formed two bonds: one with Ti

located on a face and other on a Ti edge atom. Finally, the -1.10 eV adsorption corresponds to a structure where one H atom is on a C-deficient corner place interacting with three Ti atoms, and the other H atom is adsorbed on a Ti edge site near the corner where is the other H atom is located. Spontaneous dissociation on the barycentre only occurs for the diagonal orientation approach at initial distances of 1.50 Å and 1.75 Å. For distances greater than 2.50 Å, it is observed that there is only very weak H_2 molecule adsorption and no dissociation.

7.5. Adsorption Two H atoms

After studying the most favourable adsorption position for single H atoms and single H_2 molecules, the next step is to know what happens with two H atom adsorbed on nearby atoms. In this case, two different stoichiometric NP sizes have been studied: $(TiC)_{18}$ and $(TiC)_{32}$. In addition, we also studied $Ti_{18}C_{14}$ when four carbon atoms are removed from the corners of $(TiC)_{18}$.

7.5.1. $(TiC)_{32}$

For this NP, depending on the initial position of two H atoms (2H), different final positions can be obtained. Two initial positions will be studied: C corners (C_{cor}) and C_{edg}. These positions are chosen because they are the most stable positions to adsorb an H atom (see above). In total, seven different combinations of 2H atoms have been studied. These combinations are divided into two groups: i) those with an H atom adsorbed on a C-corner, and ii) those with an H atom adsorbed on a C-edge. Being a cubic NP (4×4×4), it is highly symmetric thus reducing the number of distinct adsorption sites.

- **C-corner**

If the initial position of the H_2 molecules is on a carbon corner, two final positions can take place for H_2 dissociation: One corresponds to the two atoms adsorbed on two C atoms, one atom adsorbed on C corner (C_{cor}) and other on C face (C_{fac}) and another possibility is one H atom adsorbed on a Ti edge atom and the other H atom on a C atom (C_{cor} - Ti_{edg}). The positions studied for the C-corner can be seen in Figure 7.17.

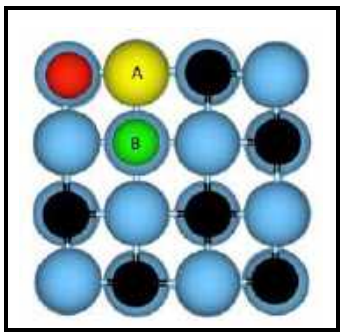

Figure 7.17. Different possibilities for the final positions (A – Ti_{edg} and B - C_{fac}) for a H atom after dissociative H_2 adsorption on a C_{cor} site (red), which is assumed to retain one H atom.

In the Figure 7.17, you can see the $(TiC)_{32}$ NP where the two options studied have been marked in different colours. The option A corresponds to C_{cor} – Ti_{edg} and B is C_{cor} – C_{fac}. The calculated adsorption energy for both cases are shown in Table 7.10.

Table 7.10. Adsorption energy for two Hydrogen atoms adsorbed on C_{cor}-C_{fac} or C_{cor}-Ti_{edg}.

	C_{cor} – Ti_{edg}	C_{cor} – C_{fac}
E_{ads} (eV)	-0.45	-1.12

The most favorable final position of the two dissociated H atoms when the initial position of the H_2 molecules is on a C corner corresponds to C_{cor} – C_{fac}. The final position for this situation can be seen in Figure 7.18.

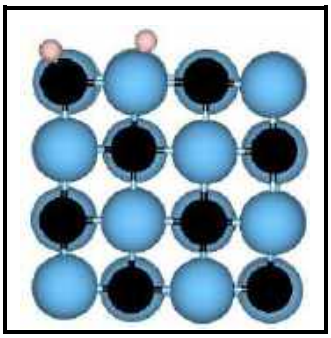

Figure 7.18. Final position for H atoms adsorbed on C_{cor} and C_{fac}.

- **C-edge**

For dissociative H_2 adsorption on a C_{edg} site as initial position, more possibilities can be studied. For the final configuration with the hydrogen atoms adsorbed on two carbon atoms there exist two possibilities: C_{edg} - C_{edg} and C_{edg} - $C_{fac.}$ While if for the final configuration it is considered that one hydrogen atom is adsorbed on a Ti atom and another on a C atom, it is possible to explore three more possibilities: C_{edg} - Ti_{edg}, C_{edg} - Ti_{fac} and C_{edg} - Ti_{cor}. We have studied a total of five different configurations, as shown in Figure 7.19.

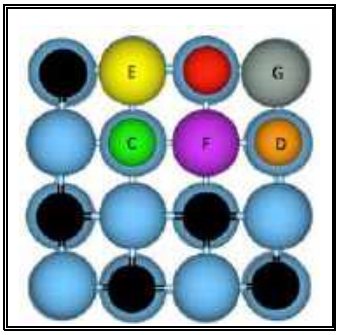

Figure 7.19. Different possibilities for final configurations (C to G) for a H atom after dissociative H_2 adsorption on a C-edge (red). which is assumed to retain one H atom.

In this image, C corresponds to C_{edg} – C_{fac}, D is a C_{edg} – C_{edg}, E represents C_{edg} – Ti_{edg}, and F shows C_{edg} –$Ti_{fac,}$ and finally G exhibits C_{edg} – Ti_{cor}. The calculated adsorption energies for all configurations are shown in Table 7.11.

Table 7.11. Adsorption energy in eV for the seven cases under study for two H atoms adsorbed on $(TiC)_{32}$.

	C_{edg} – C_{fac}	C_{edg} – C_{edg}	C_{edg} – Ti_{edg}	C_{edg} –Ti_{fac}	C_{edg} – Ti_{cor}
E_{ads} (eV)	-0.84	-1.37	-0.11	-1.14	-0.64

In this case, the the strongest adsorption energy occurs for the initial C_{edg} - C_{edg} configuration.

Note that the C_{edg} - Ti_{fac} final configuration has stronger energy adsorption than for two H atoms than the C_{edg} - C_{fac} configuration. However, in the former case, the H adsorbed initially on Ti_{fac} migrates to vicinal C_{edg} and in the final configuration, both H atoms are adsorbed at the same C-edge. For this reason, the energy value obtained for this initial configuration is the same that obtained for the H_2 adsorption on C-edge (Table 7.2). In the Figure 7.20 are shown this process.

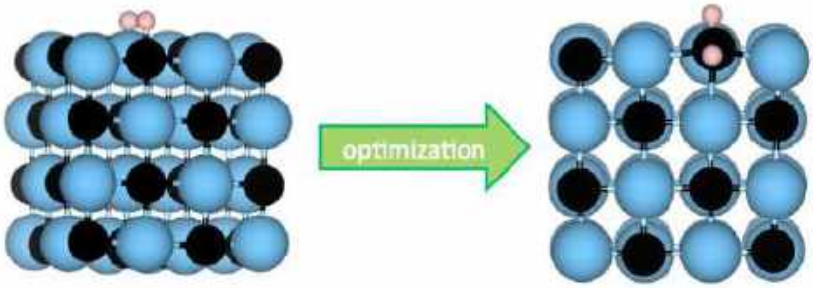

Figure 7.20. Initial and final positions for C_{edg} –Ti_{fac} optimization.

7.5.2. $Ti_{18}C_{14}$

For the $Ti_{18}C_{14}$ NP, six different combinations of dissociated 2H atoms have been studied. These combinations are shown in Scheme 7.2.

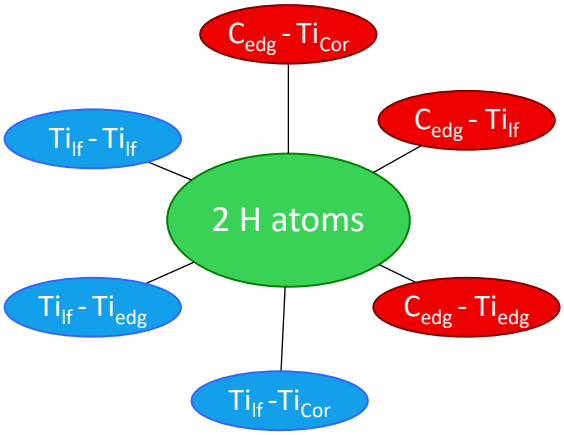

Scheme 7.2. Adsorption site configurations studied on $Ti_{18}C_{14}$ for two vicinal H atoms.

The calculated adsorption energies for all positions. are shown in Table 7.12.

Table 7.12. Adsorption energies for two vicinal H atoms on $Ti_{18}C_{14}$ in eV. NFA – Not favorable adsorption.

Initial Position	Energy (eV)
C_{edg} – Ti_{Cor}	-0.76
C_{edg} – Ti_{If}	NFA
C_{edg} – Ti_{edg}	-1.39
Ti_{If} – Ti_{Cor}	NFA
Ti_{If} – Ti_{edg}	NFA
Ti_{If} – Ti_{If}	NFA

The results obtained shown that only in one case the adsorption energy of two vicinal H atoms is particularly energetically favourable. This case is when the H atoms are initially adsorbed on C_{edg} and Ti_{edg}. The initial and final H positions for this case are shown in Figure 7.21.

Figure 7.21. Initial and final position for the most stable adsorption for two vicinal H atoms on $Ti_{18}C_{14}$.

In the Figure 7.21 you can see one H atom adsorbed on a Ti atom, which migrates to a corner forming a three bond with a Ti atom while the other H atom stays adsorbed on a C_{edg} atom. This final configuration is the most stable found.

The second most energetically stable 2H configuration corresponds to H atoms that are adsorbed on C_{edg} and $Ti_{Cor.}$ For this configuration the adsorption energy is 0.63 eV less than the most stable configuration. The final position for this case corresponds to one H atom adsorbed on a Ti_{cor} and the other H atom adsorbed to C_{edg}, Figure 7.22.

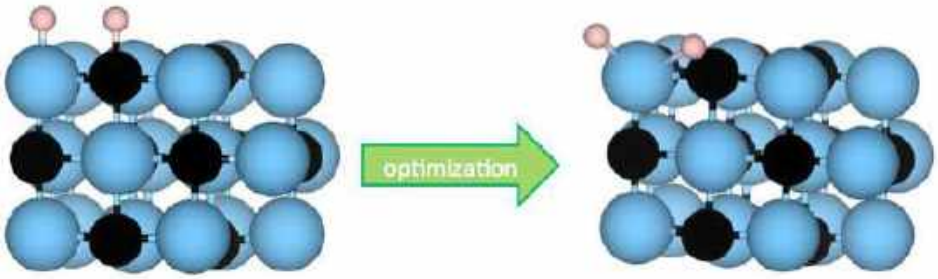

Figure 7.22. Initial configuration corresponds to the 2H atoms adsorbed one on Ti_{cor} and another on the C_{edg} and the final configuration the H atoms are adsorbed on the same vicinal atoms.

7.5.3. $(TiC)_{18}$ and $(TiC)_{24}$

For the $(TiC)_{18}$ and $(TiC)_{24}$ NPs, we studied the 2H configurations when two H atoms are adsorbed on two C_{edg} sites. This configuration is the most stable one studied for both the NP sizes studied in the previous sections. In Table 7.13 the adsorption energy values obtained for each NP size are reported.

Table 7.13. Adsorption energy in eV for H atom adsorbed on two C_{edg} atoms for $(TiC)_{18}$ and $(TiC)_{24}$.

E_{ads} (eV)	$TiC_{(18)}$	$TiC_{(24)}$
$C_{edg} - C_{edg}$	-0.94	-1.02

In both cases, the adsorption is energetically quite favourable. For this reason, the H_2 dissociation barriers will be studied for both NP sizes in the next section.

7.6. H_2 adsorption and dissociation on TiC Nanoparticles

In this section, we studied the barriers for H_2 dissociation on TiC NPs. To carry out this study, the NEB method together with the FHI-AIMS code was employed. The H_2 dissociation barriers were calculated for different NP sizes and NP models. We note that for the case of the $(TiC)_{18}$ NP, we had technical problems to establish the TS for H_2 dissociation.

7.6.1. $(TiC)_{32}$

For the $(TiC)_{32}$ NP, transition states for three H_2 dissociation pathways were tested. One corresponds to a H_2 molecule adsorbed on a C_{cor} as an initial position, and the other two are simulated using C-edge initial positions. For these studies, the NEB calculations have been performed using 8 images. The Scheme 7. shows all studies carried out for this NP size with the initial and final positions.

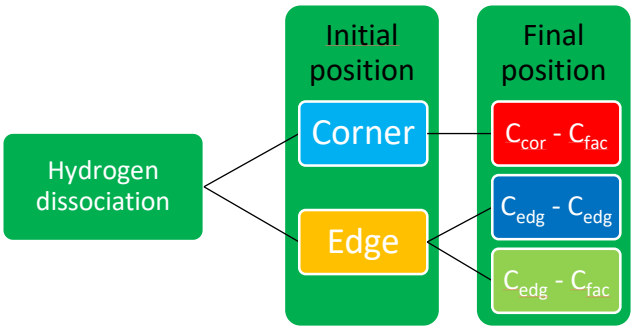

Scheme 7.3. Transitions states studied for H_2 dissociation on the $(TiC)_{32}$ NP.

7.6.1.1. Carbon corner as an initial position

Our results for H_2 adsorption have revealed that the adsorption on C_{cor} is the position most energetically favourable one for the NP size under study (Table 7.2). Knowing that this is the energetically preferred position, we proceed to study H_2 dissociation study for this position using the NEB method.

The image that represents the procedure under study can be seen in Figure 7.23 where the initial position corresponds to the H_2 molecule adsorbed on a C_{cor}. In the final position, the H_2 molecule dissociates and one H atom is adsorbed on the same C corner atom and the other H atom migrates to a C_{fac}.

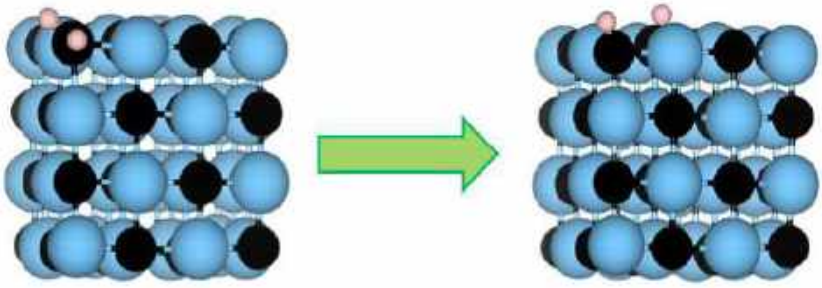

Figure 7.23. H_2 dissociation where initially the H_2 molecule is adsorbed on a C corner and finally H_2 is dissociated with one H atom adsorbed on a carbon corner and another H atom on a carbon face.

The TS for the H_2 dissociation at this location has been found and the dissociation energy (difference between initial and TS) for this process is 1.65 eV. In Figure 7.24 you can see the reaction profile for this process.

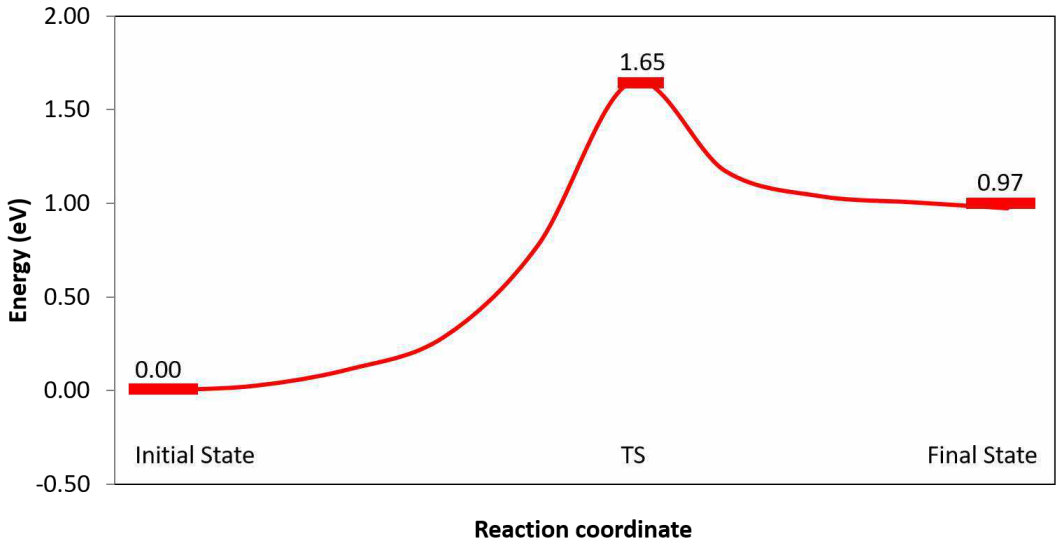

Figure 7.24. Reaction profile for H_2 dissociation where initial position is C-corner and final positions of the hydrogen atoms is adsorbed on C-corner and the other is adsorbed on C-face on the $(TiC)_{32}$ NP.

In addition to the relatively high barrier, the results show that the initial position is energetically more stable than the final position by 0.97 eV. This indicates that the molecular hydrogen dissociation reaction would not easily occur via this pathway. The structure of the transition state is shown in Figure 7.25.

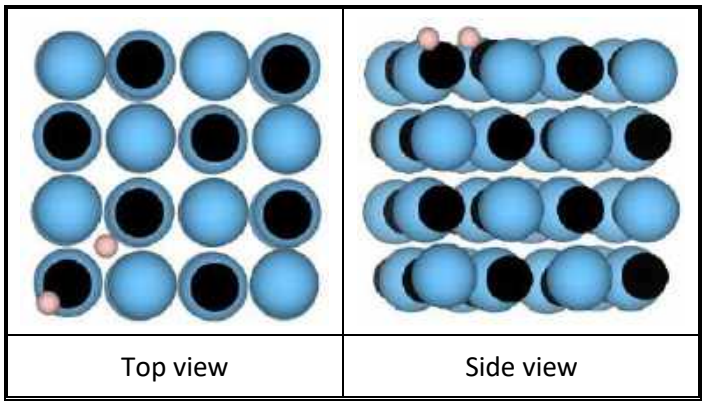

Figure 7.25. Transition State of molecular hydrogen dissociation where the initial position is C-corner and the final configuration has one hydrogen atom adsorbed on a C-edge and the other is on a C-face.

7.6.1.2. Carbon edge as initial position

As can see in the Scheme 7.3, when C_{edg} is an initial position, two final 2H configurations have been tested. In the first case, the dissociation leads to two H atoms adsorbed on two C-edge sites. The second case studied corresponds to one H atom adsorbed on a C_{edg} and another H atom adsorbed on a C-face.

- C_{edg} to two C_{edg} sites.

The initial and final structures associated with dissociation for this case can be seen in Figure 7.26 where the initial position with an H_2 molecule adsorbed on a C_{edg} and the final configuration where both H atoms are adsorbed on two different C-edge sites.

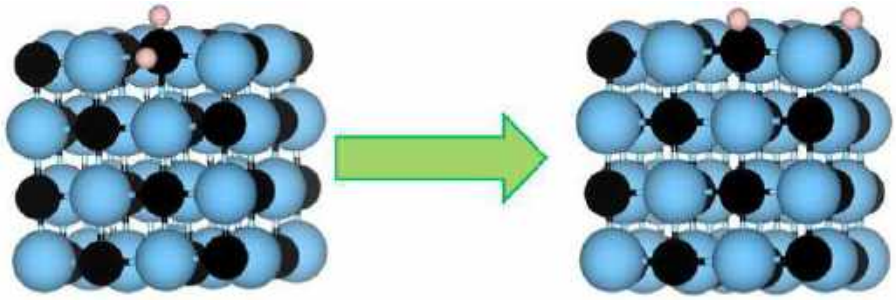

Figure 7.26. H_2 dissociation where the initial position H_2 is adsorbed on a C-edge and in the final in configuration the H_2 is dissociated with both H atoms adsorbed on two different Cedg-edge sites on $(TiC)_{32}$.

In Figure 7.27 we show the reaction profile for this calculation.

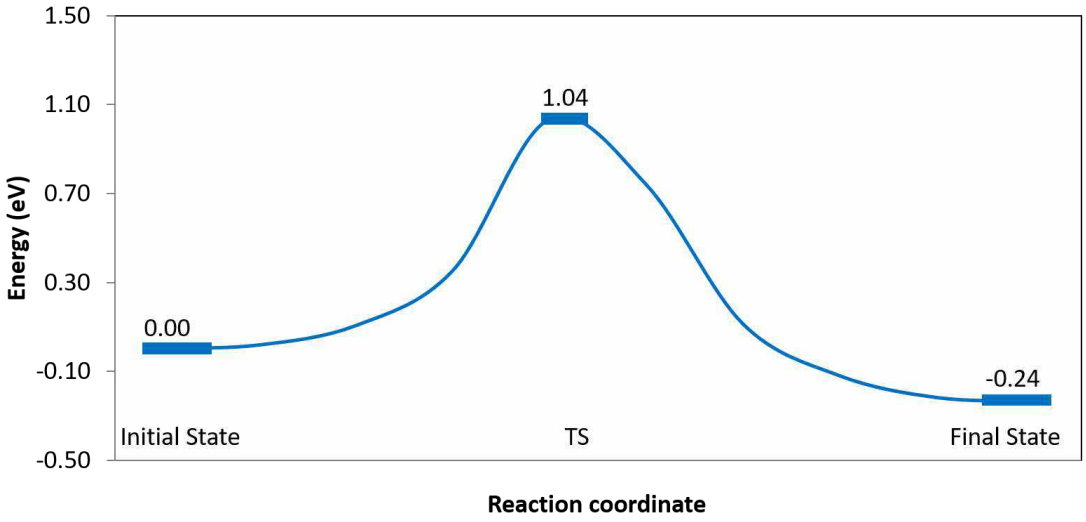

Figure 7.27. Reaction profile for H_2 dissociation where the initial position is a C-edge and finally both hydrogen atoms are adsorbed on two vicinal C-edge sites on the $(TiC)_{32}$ NP.

Figure 7.27 shows that TS barrier to this reaction profile is 1.04 eV and the difference between initial and final position is -0.24 eV. (i.e. the ore dissociated adsorbed hydrogen atoms are more energetically favourable than the initial state). The transition state is shown in Figure 7.28.

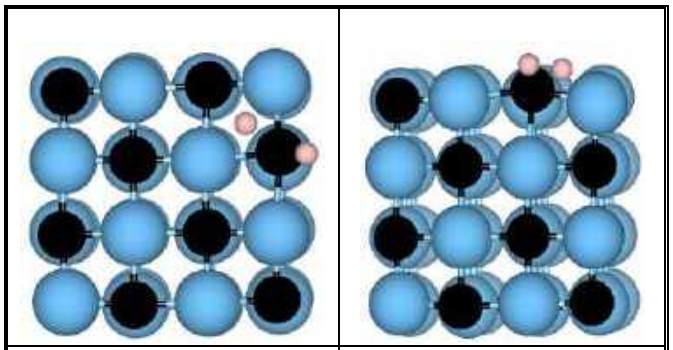

Figure 7.28. TS for molecular hydrogen dissociation where initial position is a C-edge and finally both hydrogen atoms are adsorbed on a C-edge.

- C- edge to C-edge and C-face.

In this case, the initial position corresponds to H_2 molecule adsorbed on C_{edg} and in the final position, on H atom is adsorbed on C_{fac} and the other has remained adsorbed on C_{edg}. The geometries of initial position and final position are shown in Figure 7.29.

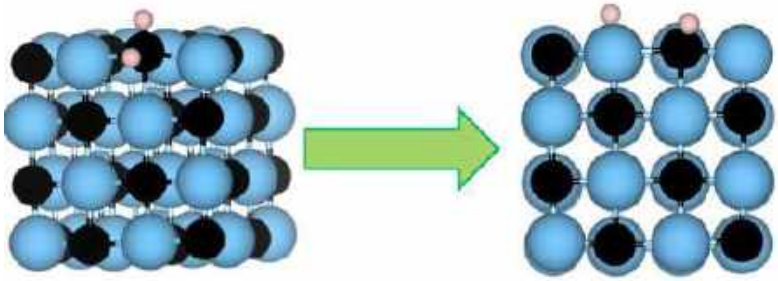

Figure 7.29. H_2 dissociation where initial position H_2 is adsorbed on C_{edg} and final in positions H_2 is dissociated being one H adsorbed in Carbon edge and other H in C_{fac}.

The reaction profile for this dissociation reaction is show in Figure 7.30.

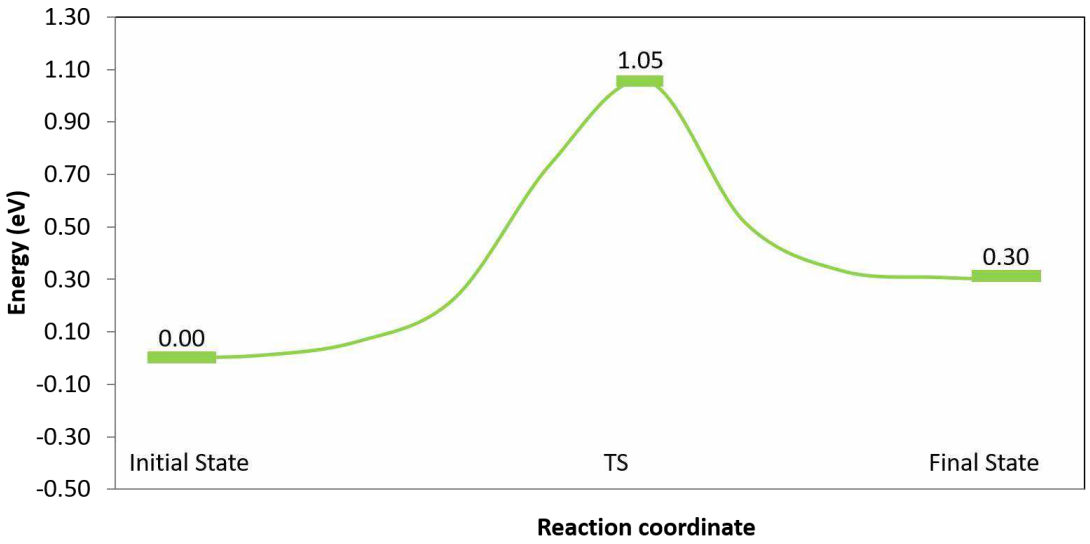

Figure 7.30. Reaction profile for H_2 dissociation on $(TiC)_{32}$ where the initial position is a C-edge and finally of the hydrogen atoms are adsorbed on a C-edge and on a C-face site.

The TS energy is 1.05 eV and the difference between initial and final position is 0.30 eV. In this case, the initial position is more stable than the final, as for the first case studied ($C_{cor} \rightarrow C_{cor} - C_{fac}$). As such this reaction is not thermodynamically favourable. The TS is shown in Figure 7.31.

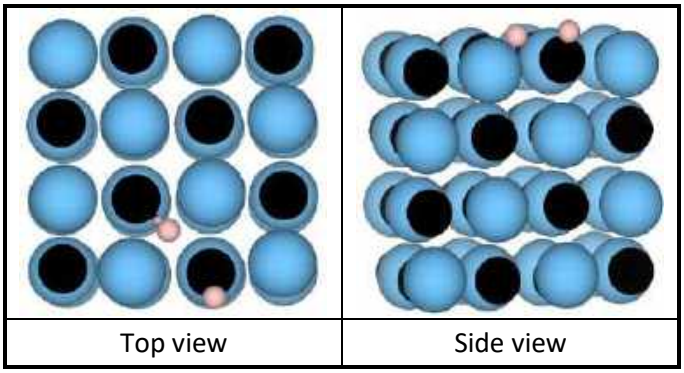

Figure 7.31. TS structure for molecular hydrogen dissociation on $(TiC)_{32}$ where initial position is C-edge and final configuration of the hydrogen atoms is adsorbed on a C-edge and the other on a C-face.

In both cases studied when the H_2 molecule is adsorbed on Carbon edge as an initial position, the TS is the same and it displays the same energy and the same geometry.

In this case, a new method to corroborate the TS has been tested. As the CI-NEB method is not implemented in the FHI-AIMS code, the method tested has consisted of a new NEB between previous and later TS images. The new NEB has carried out using 5 intermediate images. The new method tested cannot found the TS, because the NEB is not optimized. The NEB found structures energetically more stable than the initial and final positions, and this prevents the NEB from being optimized. It is normal that NEB find those more stable positions, since in this

case both of the initial and the final images are not stable positions. For this reason, the TS cannot be corroborated by this method and the method and test are abandoned.

In summary, the TS energies found for the three cases studied in $(TiC)_{32}$ size are shown in Table 7.13.

Table 7.13. Energy in eV for initial, Transition state, and the difference between initial and final positions in the three NEB cases studied for $(TiC)_{32}$ NP.

Energy (eV)	Transition state	ΔE initial and final position
Corner to C_{cor} - C_{fac}	1.65	0.97
Edge to C_{edg} - C_{edg}	1.04	-0.24
Edge to C_{edg} - C_{fac}	1.05	0.30

According with the results, the only possibility for thermodynamically favourable H_2 dissociation to occur on the $(TiC)_{32}$ NP is when the initial position of H_2 molecule is adsorbed on C_{edg} and in the final position both H atoms are adsorbed on two vicinal C_{edg} atoms. This case also gives an energy barrier lower than the other two cases studied.

7.6.2. $(TiC)_{18}$

As above size studied, only one option was thermodynamically favourable ($C_{edg} \rightarrow C_{edg} - C_{edg}$), in this size only this option has been studied for the $(TiC)_{18}$ NP. In addition, for this size, two options were tested: when the NP has all atoms (i.e. the stoichiometric NP) and when four C atoms are removed from the corners.

7.6.2.1. Stoichiometric NP

For this size, only one option has been tested to know the barrier energy. The option under study is shown in Figure 7.32.

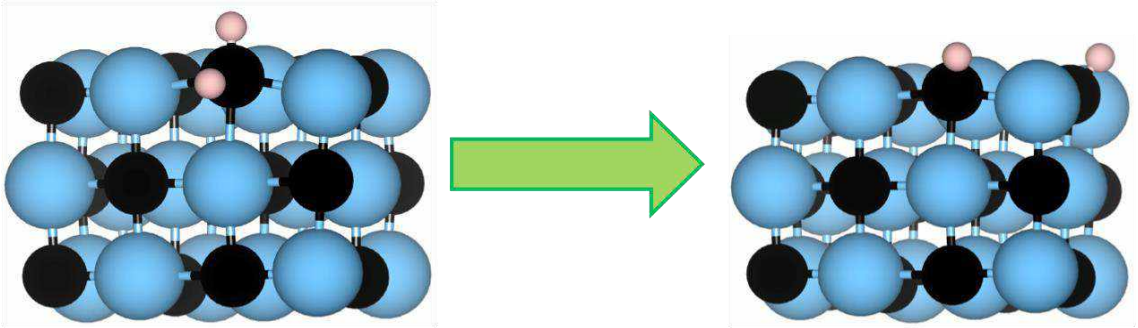

Figure 7.32. H_2 dissociation on $(TiC)_{18}$ where the initial position of H_2 is adsorbed on a C-edge site and finally H_2 is dissociated with both H atoms adsorbed on two different Carbon edge.

You can see the reaction profile which has been obtained for this size in Figure 7.33.

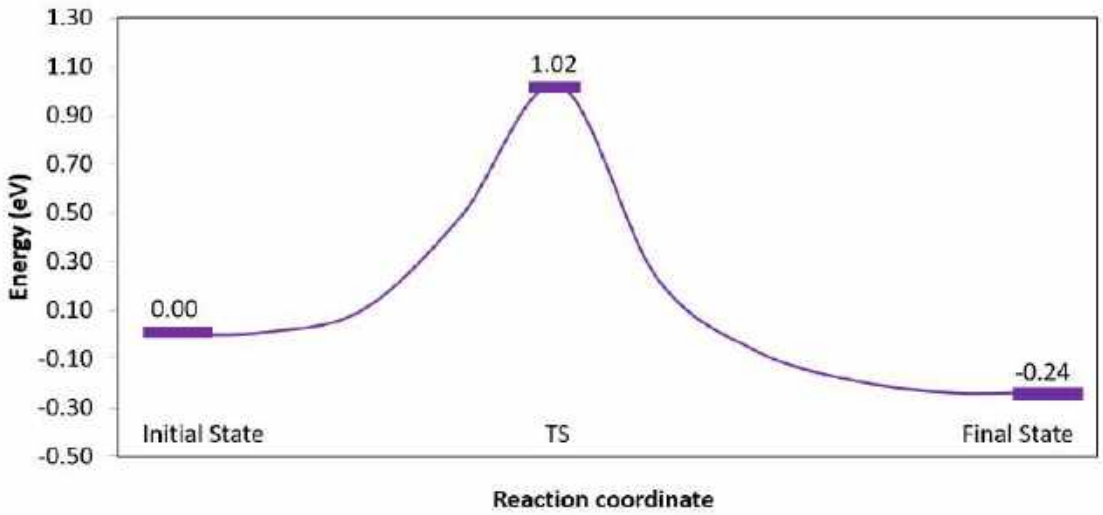

Figure 7.33. Reaction profile of H_2 dissociation on $(TiC)_{18}$ where the initial position is a C-edge and finally both hydrogen atoms are adsorbed on two vicinal C-edge

The TS barrier in this reaction profile is 1.02 eV and the difference between initial and final position is -0.24 eV (i.e. the dissociated hydrogen atoms are more stable than the initial state). Figure 7.34 shows the TS geometry.

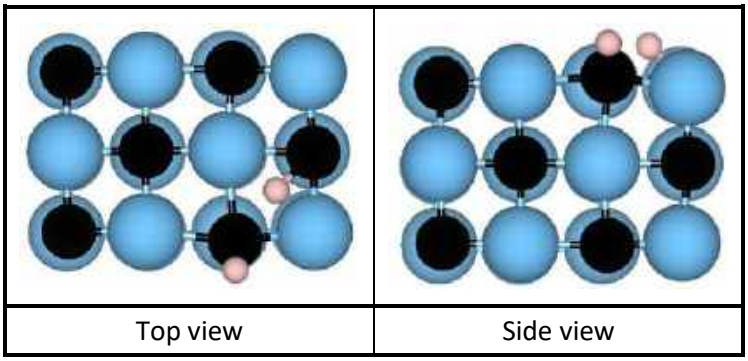

Figure 7.34. Geometry of Transition State found in $(TiC)_{18}$ size.

7.6.3. $(TiC)_{24}$

The H_2 dissociation path has been studied from H_2 adsorbed on a C-edge to two H atoms adsorbed on two C-edge sites on the $(TiC)_{24}$. The initial and final structures can be seen in Figure 7.35.

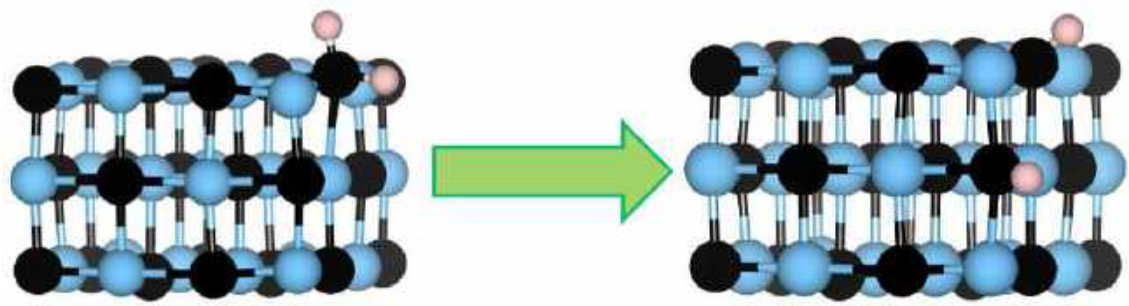

Figure 7.35. H_2 dissociation on $(TiC)_{24}$ where initial the position of H_2 is adsorbed on a C-edge and finally is dissociated with both H atoms adsorbed in two different C- edge sites.

The reaction profile is shown in Figure 7.36.

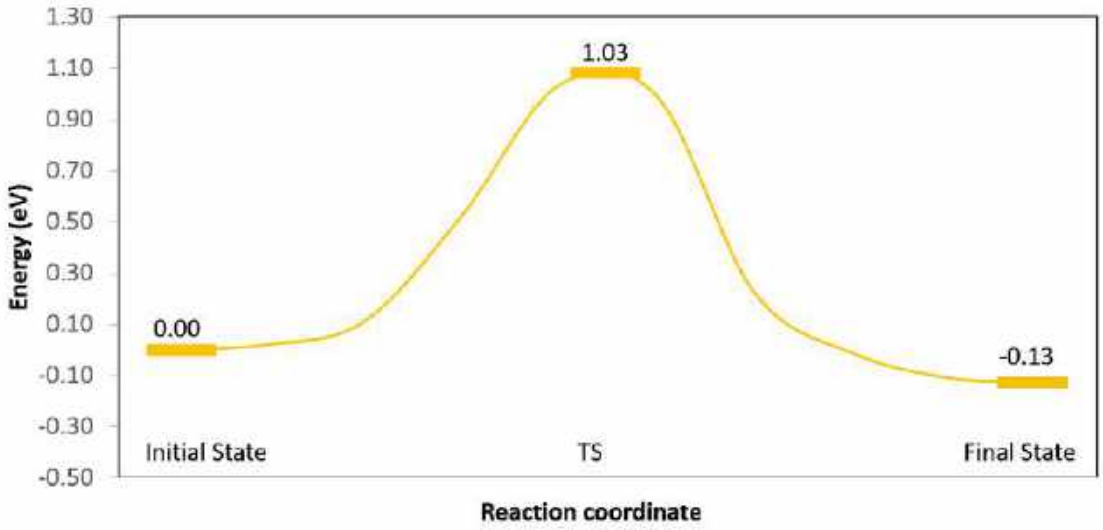

Figure 7.36. Reaction profile of H_2 dissociation on the $(TiC)_{24}$ NP where initial the position is a C-edge and finally both hydrogen atoms are adsorbed on two vicinal C-edge sites.

The geometry of the TS is shown in Figure 7.37.

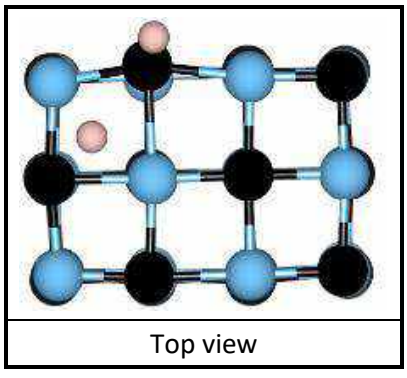

Figure 7.37. Geometry of Transition State for H_2 dissociation on $(TiC)_{24}$ where the initial position of H_2 is adsorbed on a C-edge.

7.7. Conclusions.

According to the above results, TiC NP is good material to adsorb H_2. As for the bulk TiC surface studied previously, the H_2 molecule energetically prefers to adsorb on C atoms. The most energetically favouable adsorption positions is the C-Corner. When the NP size increases, the magnitude of the adsorption energy also increases when the H_2 molecule is adsorbed on C atoms. When the adsorption occurs on the Ti atom, practically no variation of adsorption energy is observed with increasing the size. When NPs are poor in C atoms, their reactivity increases and in for some H_2 adsorption sites H_2 spontaneously dissociates. Finally, the TiC NP exhibits lower barrier energies for H_2 dissociation reaction than TiC surfaces. The energy barrier for H_2 dissociation does not vary significantly with respect to the NP sizes studied.

7.8. References

1. B.R. Cuenya. Synthesis and catalytic properties of metal nanoparticles: Size, shape, support, composition, and oxidation state effects. *Thin Solid Films*., **2010**, 518, *12*, 3127–3150.
2. J. Wu, P. Li, Y.T. Pan, S. Warren, X. Yin, and H. Yang. Surface lattice-engineered bimetallic nanoparticles and their catalytic properties. *Chem. Soc. Rev*., **2012**, 41, *24*, 8066–8074.
3. C. Lárez, S. Koteich, and L. Floralba (Eds). *Nanopartículas: fundamentos y aplicaciones*. Nanotecnología Fundam y Apl. **2015**, 203–222. ISBN: 978-980-12-8382-9.
4. R. Taylor, S. Coulombe, T. Otanicar, P. Phelan, A. Gunawan, W. Lv, G. Rosengarten, R. Prasher, and H. Tyagi. Small particles, big impacts: A review of the diverse applications of nanofluids. *J Appl Phys*. **2013**, 113, 1, 1301.
5. R.A. Taylor, T. Otanicar, and G. Rosengarten. Nanofluid-based optical filter optimization for PV/T systems. *Light Sci Appl*. **2012**, 1, 1–7.
6. D.G. Panpatte, Y.K. Jhala, H.N. Shelat (eds). *Nanoparticles: The Next Generation Technology for Sustainable Agriculture. In: Microbial Inoculants in Sustainable Agricultural Productivity*. New Delhi: Springer; 2016. p. 1–308.
7. W. Yao, P. Makowski, C. Giordano, and F. Goettmann. *Synthesis of Early-Transition-Metal Carbide and Nitride Nanoparticles through the Urea Route and Their Use as Alkylation Catalysts*. *Chem. Eur. J*., **2009**, 15, 11999–12004.
8. C. Oshima, T. Aizawa, M. Wuttig, R. Souda, S. Otani, Y. Ishizawa, H. Ishida, and K.Tekura. Surface-phonon dispersion curves of TiC(100). *Phys Rev B.*, **1987**, 36, *14*, 7510–7517.

Chapter 8

Global conclusions

8. Global conclusions

The present Thesis consists of different studies about TMCs and their role in H_2 interaction and dissociation, as well as on CH_4 dissociation being a support of Ni clusters, and their NP stability and IR recognition.

As far **surface results** are being concerned, the following conclusions can be withdrawn:

- H atoms prefer to occupy surface C-Top positions on TiC (001) surface, up to a full ML situation. The adsorption energy decreases with coverage, making it suitable to have H adatoms occupying Ti-Top sites, which can be occupied when surrounded by C-Top sites, forming sort of pyramidal H, particularly occupied when going over a 1 ML situation. These results made it possible to understand experimental studies, allowing the assignment of the peaks obtained in the experimental TPD. Aside from C-Top sites, H_2 can be adsorbed as an elongated H_2 moiety, called *Kubas* model. The dissociation of H_2 molecule into 2H adatoms is an exothermic process and presents a small energy barrier. The as generated H adatoms may diffuse over the TiC (001) surface, through moderate energy barriers. Such results point out the use of TiC as a possible hydrogenating catalyst.
- Results obtained for the rest six TMCs studied revealed that the H_2 molecule preferably physisorbs on C-Top for Group IV TMCs and δ-MoC, but on M-Top for group V TMCs (VC, NbC, and TaC). When the H_2 molecule adsorbs on C-Top, the H_2 molecule adopts a *Kubas* mode adsorption, where the H_2 bond is sensibly elongated. This mode adsorption has been found on all TMC even though it is not the most favourable adsorption mode. The only compound where the *Kubas* mode has not been found has been in TaC. Once adsorbed, the H_2 molecule is thermodynamically driven to dissociate on group IV TMCs (TiC, ZrC, and HfC), where H adatoms occupy vicinal C-Top sites, and, in all cases, the H_2 dissociation energy barriers are easily surmountable. This not occurs on Group V TMCs, where the physisorption and the generally endothermic dissociation step is translated in somewhat larger E_b values. Finally, δ-MoC features a strong H_2 adsorption, but a somewhat high E_b value, making it a viable hydrogenating catalyst, but at temperatures large enough so as to overcome this reaction step energy barrier. At this point, only the group IV TMCs are good candidates to performed the H_2 dissociation reaction.
- With respect to the CH_4 molecule, it presents a lower adsorption energy on TiC (001) surface, and the dissociation will hardly occur, since the molecule would likely desorb before breaking into CH_3 and H, this last step featuring a very large energy barrier. On the other hand, when the surface supports Ni clusters, the CH_4 adsorption energy increases 1.5-2.5 times with respect that on the clean TiC (001) surface, depending on the size of the Ni clusters. Furthermore, the activation energy decreases considerably in the best of cases studied (Ni_4/TiC). Thus, it seems plausible that a combination of lack of

coordination and particular electronic structure of Ni clusters provokes that this CH_4 activation can occur more easily.

As far **NP results** are being concerned, the following conclusions can be withdrawn:

- Concerning IR identification, different parameters of the simulation have been tested showing that some of them can modify the IR spectra (*e.g.* functional, charge state, and temperature). The IR characterization of the simulated NPs has allowed us to compare with the experimental cluster beam derived IR spectra. The MD-derived IR spectra allowed us identifying the likely NP structures in experiment for the two smaller NP sizes. In addition, it was found the that the experimental IR spectrum likely corresponds to the $Ti_{18}C_{14}$ structure when the 4C atoms are missing from the parent stoichiometric NP in the corners. Furthermore, this NP structure is the most stable found within all $Ti_{18}C_{14}$ isomer structures that have been studied. As it is the energetically most stable isomer, we tentatively suggest that this result could also be extrapolated to the larger NP sizes of $(TiC)_{24}$ and $(TiC)_{32}$ where it also happens that when the parent cubic structure loses the corners atoms it is the most stable isomer for Ti_xC_{x-4}.

With respect to H_2 adsorption and dissociation NP, the results show that H_2 molecule, in the same way that in the (001) surface, prefers to adsorb on C atoms. The most energetically favorable adsorption position is the C-Corner. When the NP size increases, the magnitude of the adsorption energy also increases when the H_2 molecule is adsorbed on C atoms. When the adsorption occurs on the Ti atom, practically no variation of adsorption energy is observed with increasing the size. When NPs are put in C atoms, their reactivity increases and in for some H_2 adsorption sites H_2 spontaneously dissociates. Finally, the TiC NP exhibits lower barrier energies for H_2 dissociation reaction than TiC surfaces. The energy barrier for H_2 dissociation does not vary significantly with respect to the NP sizes studied. In addition, the energy barrier obtained on TiC NP is higher that the found for TiC (001) surface in the same conditions that the NP has been studied

Chapter 9

List of publications

9. List of publications

In this thesis, the following publications have been published:

- J.J. Piñero, P.J. Ramírez, S.T. Bromley,F. Illas, F. Viñes, and J.A. Rodriguez. Diversity of Adsorbed Hydrogen on the TiC(001) Surface at High Coverages. *J. Phys. Chem.* C., **2018**, 122, *49*, 28013–28020.
- H. Prats, J.J. Piñero, F. Viñes, S.T. Bromley, R. Sayós, and F. Illas. Assessing the usefulness of transition metal carbides for hydrogenation reactions. *Chem Commun.*, **2019**, 55, *85*, 12797–800.
- H. Prats, G.A. Gutiérrez, J.J. Piñero, F. Viñes, S.T. Bromley, P.J. Ramírez, J.A. Rodriguez, and F. Illas. Room Temperature Methane Capture and Activation by Ni Clusters Supported on TiC(001): Effects of Metal-Carbide Interactions on the Cleavage of the C-H Bond. *J. Am. Chem. Soc.*, **2019**; 141, 5303–5313.
- J.J. Piñero, B. Kerkeni, F. Viñes, and S.T. Bromley. Can Calculated Harmonic Vibrational Spectra Rationalize the Structure of TiC-based Nanoparticles? *Phys. Chem. Chem. Phys.* under review 2021.

Chapter 10

Summary in Spanish

10. Summary in Spanish

En esta memoria se han plasmado los resultados correspondientes a la tesis titulada "**Modelización computacional de carburos de metales de transición con relevancia para la nanotecnología y catálisis**". En esta Tesis Doctoral se llevan a cabo diferentes estudios sobre Carburos de Metales de Transición (TMC por sus siglas en inglés). Estos estudios se han realizado sobre superficies y nanopartículas de estos materiales.

10.1. Introducción

En la mayoría de reacciones químicas de la industria se utilizan utilizados catalizadores. Un catalizador se define por la Unión internacional de Química Pura Aplicada (IUPAC) como una sustancia que aumenta la velocidad de una reacción sin modificar el cambio de energía libre estándar general de la reacción; el proceso se llama catálisis.[1] Un catalizador interactúa con los reactivos, productos e intermedios para disminuir a energía de activación de una reacción. En muchos casos, esta disminución viene dada por la modificación del mecanismo de reacción (Figura 10.1). Un catalizador sólo modifica la velocidad de reacción, manteniendo intactas las magnitudes termodinámicas. Además, no afecta a los reactivos ni productos y al final de la reacción se puede recuperar.

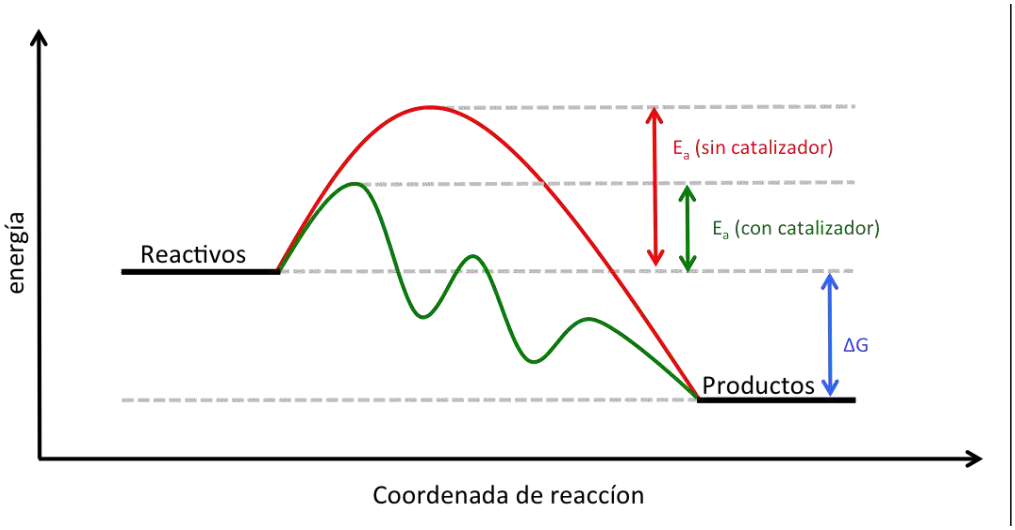

Figura 10.1. Representación de un perfil de reacción arbitrario para una reacción catalizada (línea verde) y una reacción no catalizada (línea roja).

La catálisis se puede clasificar según la naturaleza del catalizador y del estado en el que se encuentran las sustancias que participan en la reacción como catálisis enzimática, catálisis homogénea o catálisis heterogénea. La catálisis enzimática es aquella en la que el catalizador son moléculas biológicas que reciben el nombre de enzimas, un ejemplo de este tipo reacciones serían las que se producen en el cuerpo humano. En la catálisis homogénea, los reactivos y el catalizador se encuentran en el mismo estado físico. Un ejemplo de estas reacciones es el proceso Fenton[2] para la eliminación de contaminantes en agua. Finalmente, nos encontramos

con la catálisis heterogénea, donde los reactivos se encuentran en fase gas o bien en líquido y el catalizador es sólido. El 90% de la producción química se obtiene mediante un catalizador sólido.[3] Estos procesos son algunos de los ejemplos:

Tabla 10.1. Importancia de la catálisis heterogénea en la industria química.

Proceso	catalizador	reacción
Haber-Bosh	Hierro	$N_{2(g)} + 3H_{2(g)} \rightarrow 2NH_{3(g)}$
Reformado de gas natural	Níquel	$CH_{4(g)} + H_2O_{(g)} \rightarrow CO_{(g)} + 3H_{2(g)}$
Cracking del petróleo	Zeolitas	Productos: • En gas: etano, propano • En liquido: gasolina • como residuo: gasoil
Reformado de Nafta	Platino y Renio sobre alúmina	$CH_3CH_2CH_2CH_2CH_2CH_3(g) \rightarrow$ $(g) + H_2(g)$
Síntesis de Epoxi etano	Plata sobre alúmina	$C_2H_4(g) + \frac{1}{2}O_2(g) \rightarrow$ (g)
Síntesis de ácido sulfúrico	Oxido de Vanadio (V) sobre sílice	$2SO_{2(g)} + O_{2(g)} \rightarrow 2SO_{3(g)}$
Síntesis del ácido nítrico	Platino y Rodio	$4NH_{3(g)} + 5O_{2(g)} \rightarrow 4NO_{(g)} + 6H_2O_{(g)}$

La catálisis heterogénea implica sistemas extremadamente complejos donde el proceso catalítico se lleva a cabo en la superficie. La mayoría de los catalizadores industriales son metales preciosos, y esto es una gran desventaja debido al gran coste económico de estos metales y su baja abundancia en la tierra. Esto lleva a buscar nuevos catalizadores alternativos, donde los catalizadores de TMC han llamado la atención de los investigadores.

Estos nuevos materiales se sintetizan introduciendo átomos de Carbono en sitios intersticiales de sus metales originales, que normalmente incluyen todos los elementos 3*d* y elementos 4*d*/5*d* de los metales de transición tempranos de los grupos III-VI, aunque también la incorporación de átomos de C puede implicar un cambio es su estructura cristalina.[4] Los TMCs tienen propiedades físicas y químicas que combinan los rasgos característicos de tres clases diferentes de materiales: En primer lugar, los TMC muestran la extrema dureza y fragilidad de los sólidos covalentes. En segundo lugar, tienen una temperatura de fusión alta y estructuras cristalinas simples, típicas de los cristales iónicos. Y, por último, también tienen propiedades eléctricas y magnéticas, propias de los metales de transición.[4] Los TMC también presentan algunas ventajas con respecto a los metales preciosos (Ru, Rh, Pd, Os, Ir y Pt). El primero es su coste; los TMC son materiales rentables, mientras que los metales nobles son muy caros dada

su escasez. La segunda ventaja es que en los TMC la adsorción es menos fuerte que en los metales preciosos. Este hecho provoca que la disociación de algunos productos sea más sencilla. Finalmente, los catalizadores de TMC son resistentes al envenenamiento por carbono o azufre, aunque pueden envenenarse con oxígeno, la formación de oxicarburos reduce así su actividad catalítica. Sin embargo, incluso en el último caso, existen estudios recientes en los que el oxicarburos de superficie puede retener la actividad química, como se ve, por ejemplo, en la captura de CO_2 por los oxicarburos TMC del grupo IV.[5] Estos catalizadores se presentan como unos excelentes catalizadores para diferentes reacciones como: disociación de H_2,[6] oxidación de CO, [7,8] y activación de metano,[9] entre otras.

En esta Tesis Doctoral se va estudiar la adsorción y disociación de Hidrógeno, debido a su gran interés entre otros usos como energía limpia. El hidrógeno es el elemento más abundante del universo[10] pero debido a su gran volatilidad, en la tierra no se encuentra. Por esa razón es necesario producirlo. El 96% de hidrogeno que se produce, se obtiene del carbono y únicamente el 4% se obtiene mediante la electrolisis del agua. (Figura 10.2)

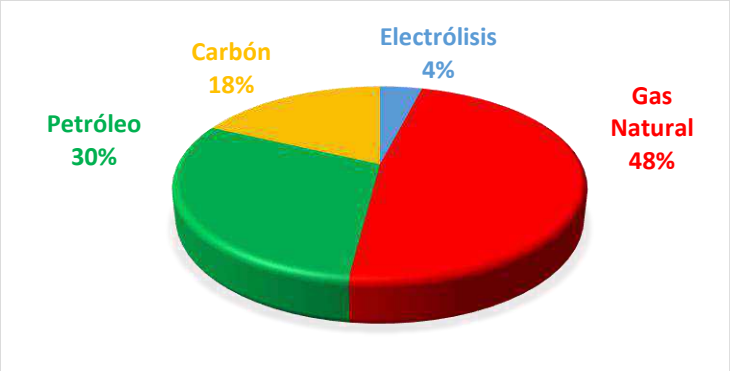

Figura 10.2. Producción de hidrogeno.

Dentro de los usos del Hidrógeno, la mayoría de se usa en la industria química y la industria petroquímica (cerca del 72%), dentro de estas industrias, el hidrogeno se emplea en la síntesis de amoníaco (Proceso Haber-Bosh), refinamiento de petróleo y síntesis de metanol (Figura 1.3).

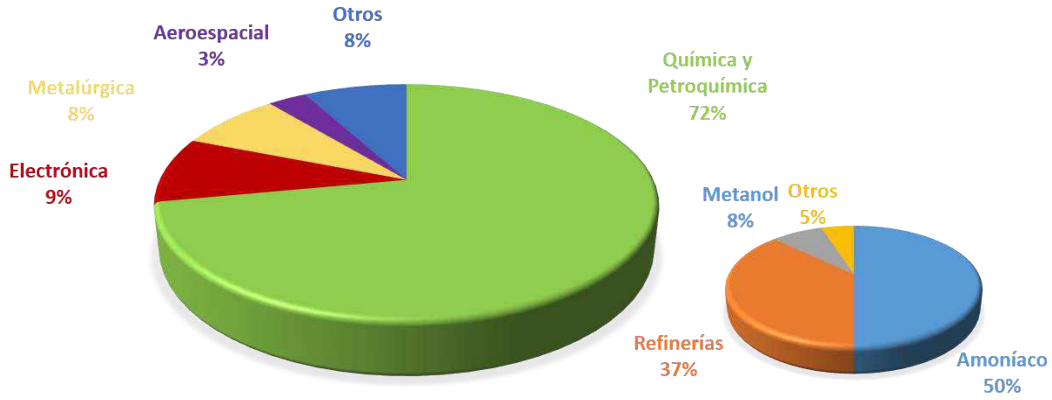

Figura 10.3. Usos del Hidrogeno.

10.2.1. Adsorción y disociación de H_2 en la superficie (001) de TiC

En un primer lugar, se ha estudiado la adsorción y disociación de hidrogeno en siete TMC. (Figura 10.4). Además, sobre la superficie del TiC, se ha estudiado la disociación de metano (CH_4).

grupo / series	IV	V	VI
3*d*	TiC	VC	
4*d*	ZrC	NbC	δ-MoC
5*d*	HfC	TaC	

Figura 10.4. TMC donde se van a estudiar la adsorción y disociación de hidrogeno.

10.2.1.1 Adsorción de H atómico y H_2 molecular en la superficie (001) de TiC.

En primer lugar, se define la celda unidad como 8 átomos de Carbono y 8 de Titanio, por lo tanto, una monocapa (ML) está constituida por 8 átomos. Una vez definida la celda unidad, se lleva a cabo la adsorción de H atómico a bajo recubrimiento, esto es decir 1 átomo de H (12,5% de recubrimiento). Para esta situación, se estudian 6 posiciones diferentes donde se ubica el átomo de H dentro de la celda. Estas seis posiciones son definidas como: (1) Top metal (M-Top), (2) Top Carbón (C-Top), (3) Puente entre un carbono un átomo metálico, (4) Hueco cuádruple, (5) Hueco triple formado por 2 átomos de metal y 1 de carbono (MMC), y (6) hueco triple formado por 2 átomos de carbono y 1 de metal (CCM). Estas posiciones se muestran en la Figura 10.5.

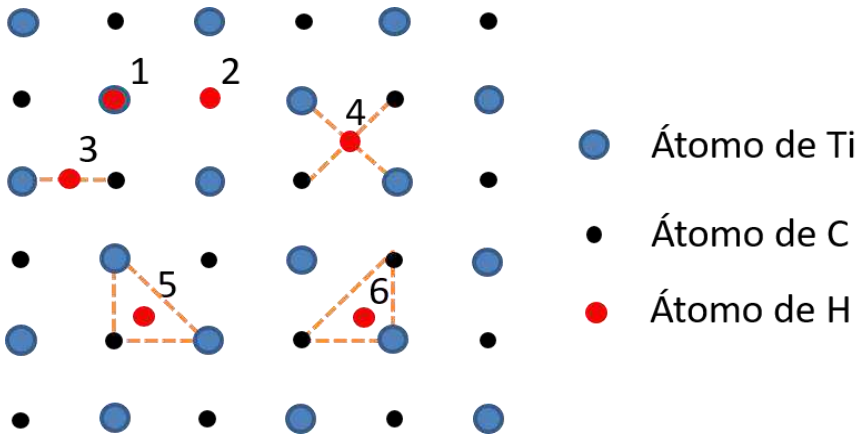

Figura 10.5. Vista en planta esquemática de un TiC (001). La imagen muestra átomos de C (negro), átomos metálicos (azul) y átomos de H (rojo) en las seis posiciones iniciales bajo estudio. Las líneas discontinuas de color naranja son guías para los ojos.

Una vez adsorbidos los átomos, se ha calculado la energía de adsorción para conocer en cuál de las posiciones estudiadas es energéticamente más favorable la adsorción del átomo de hidrogeno. Para calcular la adsorción, se emplea la siguiente fórmula:

$$E^{H}_{ads/abs} = E_{H/TMC} - (\mathrm{E_H} - \mathrm{E_{TMC}}) \quad (10.1),$$

donde $E_{H/TMC}$ es la energía total de la superficie de TiC con el átomo de H adsorbido en ella, E_H la energía total de un átomo de hidrógeno aislado en el vacío y E_{TMC} la energía total de la superficie de TiC (001). Observe que se usa la misma ecuación al calcular la adsorción de H consecutiva, pero considerando como E_{TMC} la superficie con una cobertura de H dada, en la que se adsorbe un H adicional. Observe que EH se obtiene colocando el átomo de H en una celda unitaria de simetría rota de dimensiones de 9×10×11 Å y llevando a cabo una optimización de Γ puntos. De manera similar, la adsorción de energía de H_2 se calcula con la misma ecuación, pero usando en lugar de E_H la energía de una molécula de H_2 aislada.

Para este caso, se ha encontrado que la posición de adsorción más favorable es en C-Top con una energía de adsorción de -2,73 eV para el funcional PBE[11] y -2,83 eV para PBE con corrección Grimme D3.[12] A continuación, se ha incrementado la cobertura de los átomos de H en la superficie, estudiando los casos de cobertura de 0,25 ML (2 átomos), 0,65 ML (5 átomos) y 1 ML (8 átomos).

Los resultados obtenidos han mostrado que, en todas las coberturas estudiadas, la adsorción se produce sobre C-Top. Cabe destacar que se ha descubierto, que los átomos de H adsorbidos sobre átomos de C, favorecen la adsorción sobre átomos de Ti. En el caso de 5 átomos de H adsorbidos, se aprecia claramente este efecto. Cuando los cuatro átomos de H se encuentran adsorbidos sobre cuatro átomos de C y se quiere añadir un quinto átomo de H se puede colocar en las posiciones que se muestran en la Figura 10.6.

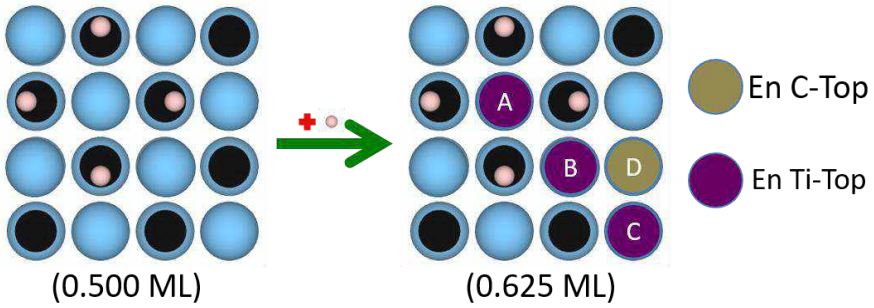

Figura 10.6. Esquema de vista superior de un quinto átomo con H añadido.

Los resultados para esta situación han mostrado que la posición más estable para el quinto átomo de H es sobre el C-Top (posición D) pero que al adsorberse en la posición A, la energía de adsorción incrementa debido a las interacciones entre los átomos de hidrogeno. En este caso, se forma una estructura piramidal entre los átomos de Hidrógenos adsorbidos como se muestra en la Figura 10.7.

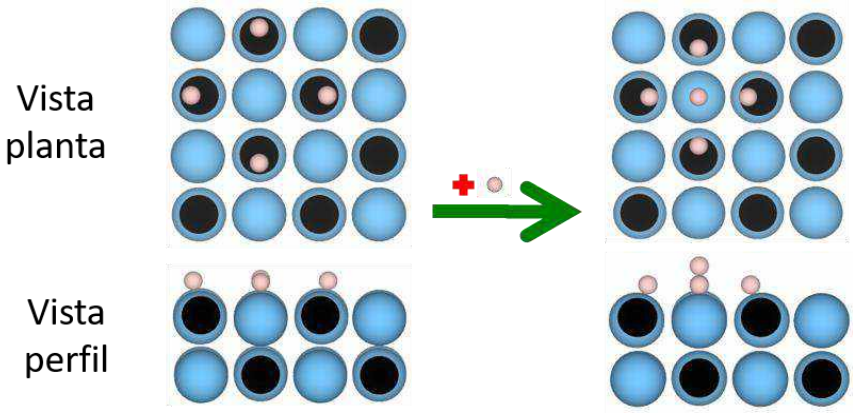

Figura 10.7. Quinto átomo de H agregado en Ti-Top en medio de cuatro átomos de hidrógeno adsorbidos en C-Top, formando una piramidal de átomos de H.

Cuando la adsorción se realiza en posiciones más separadas, la energía de adsorción disminuye como se puede ver en la Figura 10.8.

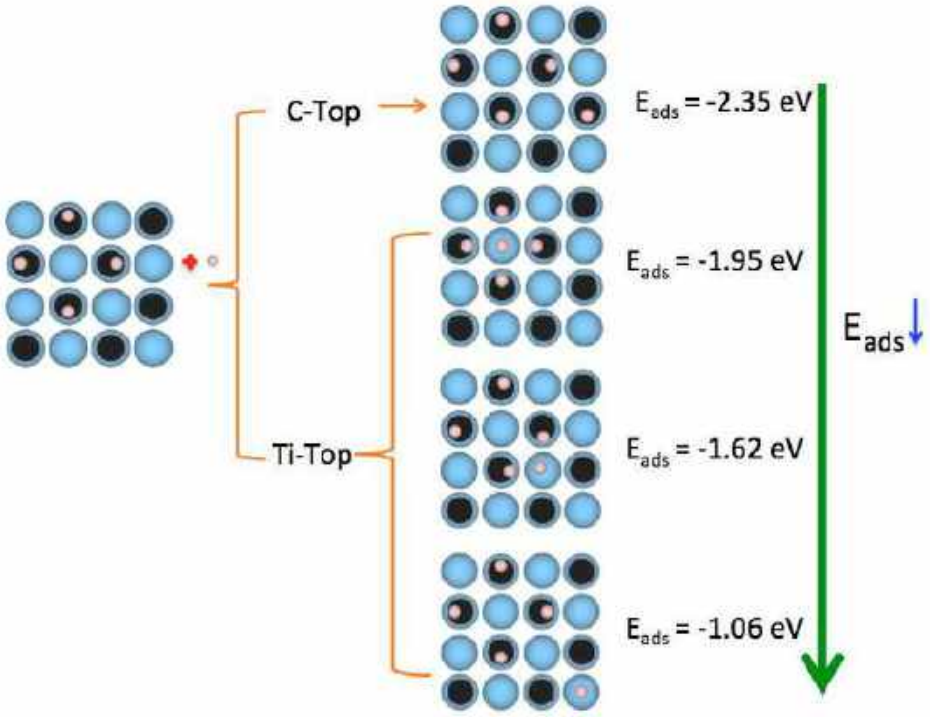

Figura 10.8. Vistas superiores de la variación de E_{ads} para el quinto en sitios C-Top y Ti-Top.

Para una cobertura de 1 ML (cobertura completa) se han estudiado 3 maneras posibles de realizar dichas coberturas. Obteniendo como resultados que la posición más estable para adsorber H es sobre C-Top. Finalmente, se ha estudiado la posibilidad de adsorber a sobre la cobertura máxima de la superficie. En este caso, se ha encontrado que los átomos de H, se adsorben en Ti-Top, favorecidos por la interacción con los átomos previamente adsorbidos. En ningún caso, la adsorción de H se produce entre capas, es decir la absorción es menos favorable que la adsorción.

Estos estudios nos han permitido explicar los datos de los investigadores experimentales del grupo del Dr. Rodríguez del laboratorio nacional de Brookhaven, en EE.UU.

A continuación, se ha estudiado la adsorción de la molécula de H_2, en este caso, se han examinado 19 posiciones diferentes sobre la superficie del TiC. Los resultados han mostrado que la adsorción de la molécula de H_2 es débil sobre estas posiciones excepto en la posición sobre el átomo de C cuando la molécula de hidrogeno esta paralela a la superficie. En este caso, la adsorción de H se produce formando el denominado modos *kubas*, donde el enlace H_2 se alarga sensiblemente. El modo *kubas* se muestra en la Figura 10.9.

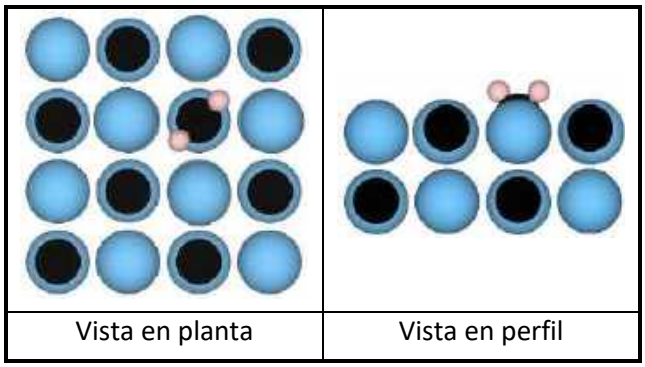

Figura 10.9. Vista en planta superior (izquierda) y perfil (derecha) de la adsorción de H_2 en un modo *Kubas* en TiC (001).

10.2.1.2 Disociación de H_2 en la superficie (001) de TiC.

Para llevar a cabo el estudio de la disociación de H_2 se han utilizado los métodos CI-NEB[13] y Dimmer.[14] En este caso, se ha utilizado como posición inicial la molécula de H_2 adsorbida en modo *kubas* y en la posición final, los átomos de hidrógeno se encuentran adsorbidos sobre 2 átomos de C vecinos. La coordenada de reacción obtenida se puede ver en la Figura 10.10.

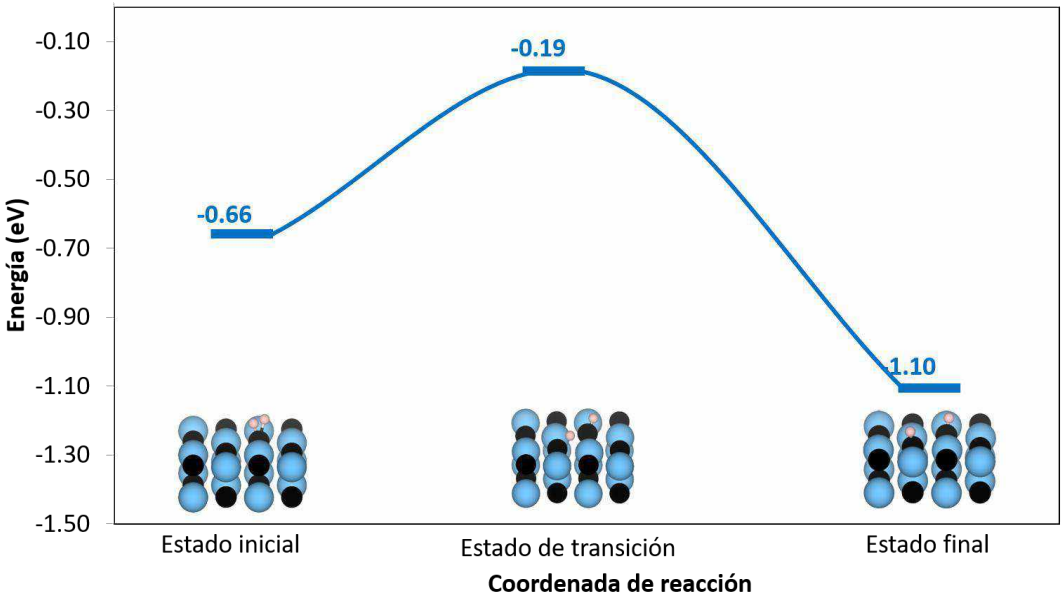

Figura 10.10. Perfil energético de la reacción de disociación H_2.

Los resultados obtenidos muestran una barrera de 0.47 eV cuando PBE-D3 es empleado. Esta barrera disminuye hasta los 0.34 eV cuando se añade la corrección ZPE.

10.2.2. Adopción y disociación de H_2 en la superficie (001) de diferentes TMCs.

El mismo procedimiento descrito para el TiC, se han llevado a cabo para el resto de los TMCs. En primer lugar, se ha estudiado la adsorción de un átomo de H sobre las superficies a una cobertura de 0.125 ML. los resultados han mostrados que, en todos los casos, la adsorción de H se produce sobre C-Top y los valores obtenidos se muestran en la Tabla 10.1.

Tabla 10.1. Valores de E_{ads}, en eV, obtenidos a nivel PBE-D3 en TMCs (001) superficies para un átomo de H.

	TiC	VC	ZrC	NbC	δ-MoC	HfC	TaC
E_{ads}	-2.83	-2.26	-2.91	-2.05	-2.94	-2.84	-2.35

A continuación, la adsorción de la molécula de H_2 se ha estudiado. En este caso, los resultados obtenidos han mostrado que la molécula de H_2 se fisisorbe preferiblemente en C-Top para las TMC del grupo IV y δ-MoC, pero en M-Top para las TMC del grupo V (VC, NbC y TaC). Cuando la molécula de H_2 se adsorbe en C-Top, la molécula de H_2 adopta una adsorción en modo *Kubas*. Este modo de adsorción se ha encontrado en todos los TMC, aunque no es el modo de adsorción más favorable excepto en el compuesto de TaC donde no se ha logrado encontrar.

Una vez conocido la posición de adsorción más estable para la molécula de H_2, se ha procedido a estudiar la disociación de esta. Para ello, se han empelado los métodos de CI-NEB y Dimer.

Como posición inicial la posición más estable en cada caso, para los metales del grupo IV y δ-MoC, la molécula de H_2 adsorbida en modo *kubas* sobre el átomo de Carbono, y para los metales de del grupo V, la molécula de H_2 se encuentra fisiadsorbida sobre el metal mientras que para la posición final, en todos los casos se utilizan los dos H adsorbidos se encuentran adsorbidos sobre dos átomos de C vecinos, excepto en el Ta, que se encuentran adsorbidos sobre 2 átomos de Ta (posición energéticamente más estable). Las barreras de activación encontrada para cada material se muestran en la Tabla 10.2.

Tabla 10.2. Barreras de energía de disociación H_2, E_b, PBE-D3 con ZPE, expresadas en eV.

	TiC	VC	ZrC	NbC	δ-MoC	HfC	TaC
E_b (eV)	0.35	1.08	0.59	0.86	0.90	0.46	1.11

Finalmente, los perfiles son graficados en la Figura 10.11.

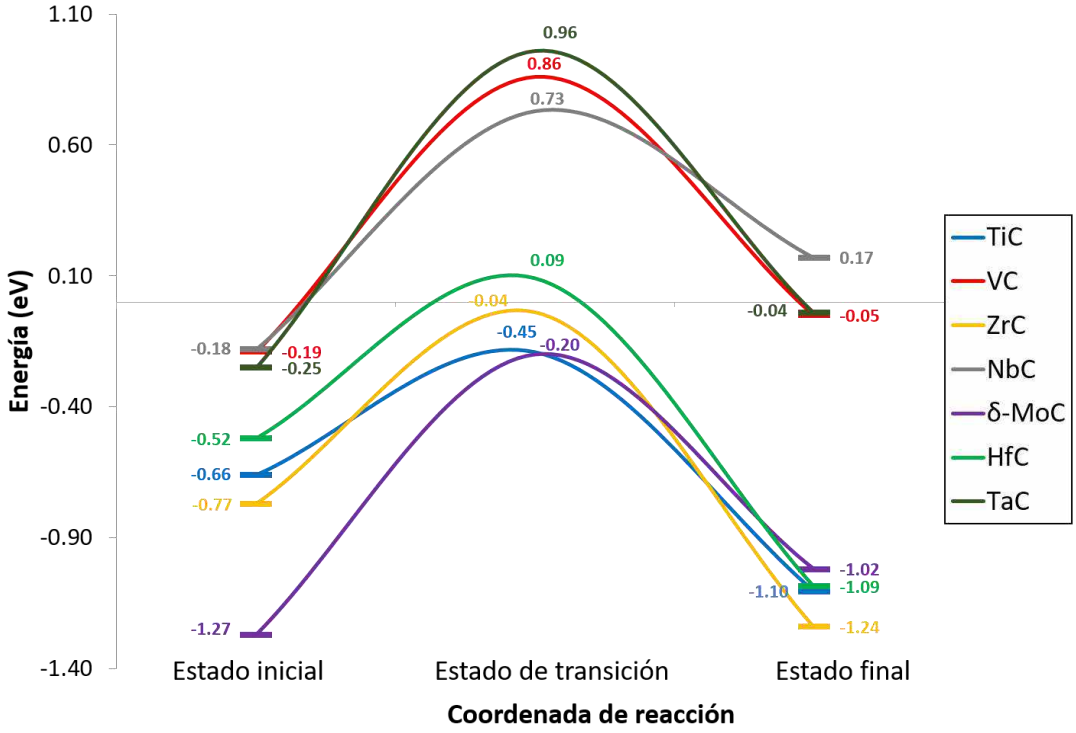

Figura 10.11. Perfiles de la reacción de disociación de hidrógeno con PBE-D3 en la superficie (001) de todos las TMC estudiados.

Con estos resultados, los únicos TMCs que sus resultados revelan que pueden ser buenos candidatos para albergar la reacción de disociación de H_2 son los metales del grupo IV (Ti, Zr y Hf).

10.2.3. Adsorción y disociación de CH_4 en la superficie (001) de TiC

En este caso, se han seguido el mismo procedimiento descrito para la disociación de H_2. El estudio de la disociación de metano ha sido estudiado para dos situaciones diferentes. La primera de ellas es cuando se dispone de la superficie de TiC (001) limpia como ocurría en el estudio de la disociación de H_2, y la segunda situación que se ha explorado es cuando la superficie TiC (001) se encuentra dopada con clústeres de Ni de diferente tamaño. Los clústeres de Ni estudiados han sido el clúster Ni_4, el Clúster Ni_9 plano, y el Clúster Ni_{13} piramidal. Estos clústeres soportados por la superficie de TiC (001) se muestran en la Figura 10.12.

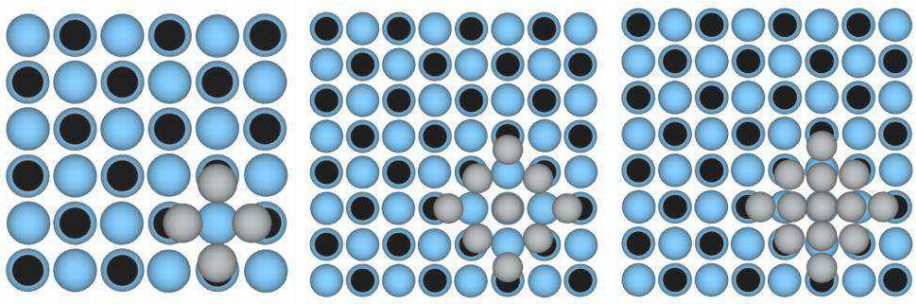

Figura 10.12. Clústeres de Ni_4, Ni_9 y Ni_{13} soportados sobre TiC donde se van a estudiar la adsorción y disociación de CH_4.

En este caso, se estudia la adsorción de CH_4 (posición inicial) y CH_3 + H (posición final) sobre los 3 sistemas de clústeres de Ni soportados en la superficie TiC y en la superficie limpia de TiC (001). Los resultados para ambos casos se muestran en la Tabla 10.3.

Tabla 10.3. Energía de adsorción para CH_4, CH_3, H, y CH_3 + H en los diferentes sistemas Ni_X/TiC estudiados y en la superficie limpia.

Catalizador	Ni_4/TiC	Ni_9/TiC	Ni_{13}/TiC	TiC(001)
CH_4 E_{ads}	-0.57	-0.64	-0.36	-0.23
CH_3 + H	-1.32	-1.69	-1.05	-0.43

Se puede observar como la energía de adsorción cuando la superficie se encuentra dopada con clúster de Ni es entre 2-2,5 veces superior que cuando la superficie no se encuentra dopada. Esto es debido a la estructura electrónica particular de los clústeres de Ni que provoca que esta activación de CH_4 pueda ocurrir más fácilmente. Las posiciones de adsorción para los valores de CH_4 se muestran en la Figura 10.13.

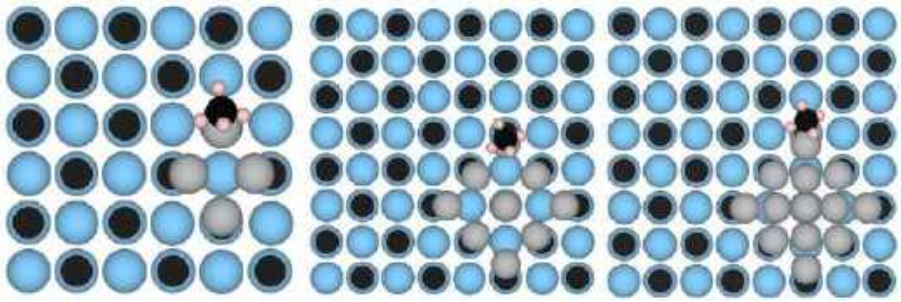

Figura 10.13. Posición más estable para la adsorción de CH_4 en los sistemas Ni_4/TiC, Ni_9/TiC y Ni_{13}/TiC.

En la Figura 10.13 se aprecia como la posición de adsorción más estable para el CH_4 en los clústeres Ni_4 y Ni_9 es sobre el átomo de Ni que se encuentra en el vértice, mientras que en el caso del clúster Ni_{13}, esta posición difiere un poco respecto a la anterior, siendo la posición más estable la adsorción sobre la arista del átomo de Ni.

Finalmente, se lleva a cabo el estudio de la disociación de CH_4. En este caso, el estudio se ha llevado a cabo utilizando en método NEB. Las barreras de energía obtenidas para los diferentes catalizadores se muestran en la Tabla 10.4.

Tabla 10.4. Barreras de energía obtenidas para los diferentes catalizadores.

Catalizador	Ni_4/TiC	Ni_9/TiC	Ni_{13}/TiC	TiC(001)
CH_4 E_b	0.18	0.25	0.38	1.22

Como se puede ver, las barreras de energía obtenidas son muy pequeñas. Esto demuestra que la superficie (001) de TiC dopada con clústeres de Ni es un buen catalizador para disociar metano. Los perfiles obtenidos para los 4 casos, también son mostrados en la Figura 10.14.

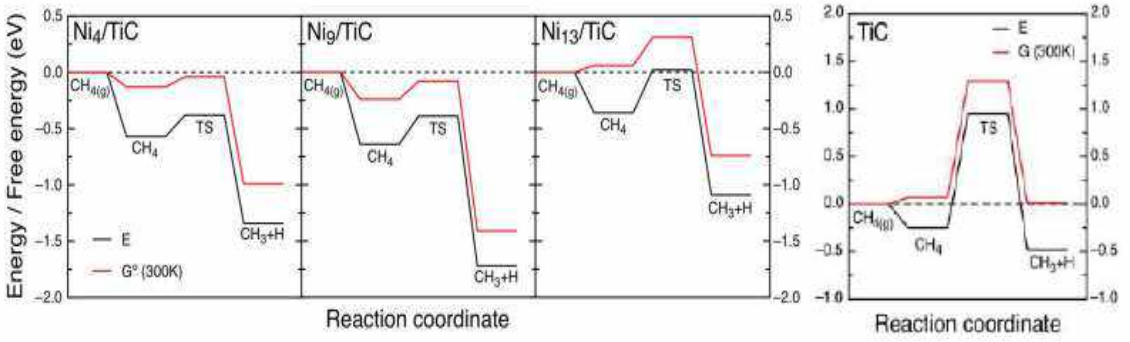

Figuras 10.14. Cordenada de reaccion para los 4 casos estudiados. Izquierda: 3 casos con la superficie dopada con clústeres de Ni. Derecha: cuando la superficie de TiC está limpia. "taken from Ref

10.3. Espectros infrarrojos vibraciones para Nanopartículas de TiC

En esta parte del trabajo, se han estudiado la estabilidad y su posterior caracterización de diferentes tamaños de Np con el objetivo de encontrar la estructura de unas partículas de TiC de las cuales únicamente se dispone de sus espectros de IR.

La información experimental de la cual se dispone es el conjunto de espectros que ya se encuentra publicado en la literatura.[15]

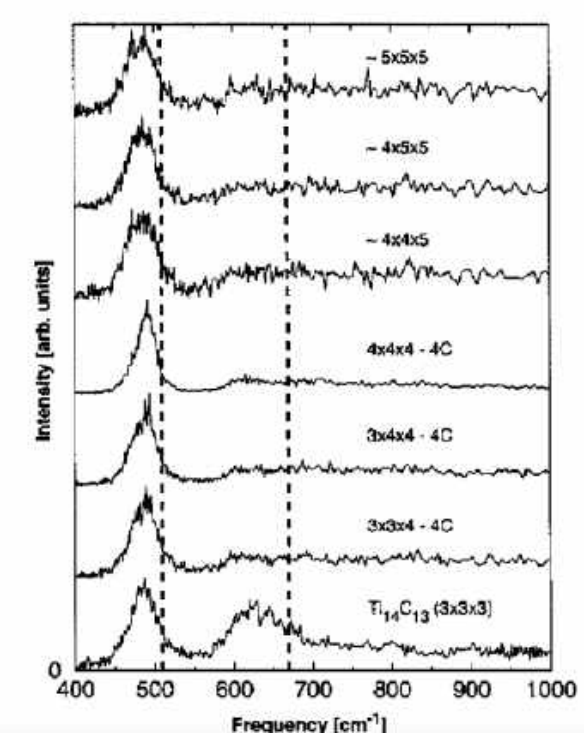

Figura 10.15. Espectros de ionización multifotónica mejorados por resonancia infrarroja IR (IR-REMPI) de diferentes grupos de carburo de titanio nanocristalino. Los dos modos de fonón de superficie ópticamente activos de TiC a granel, medidos por espectroscopía de pérdida de energía electrónica de alta resolución (HREELS), se muestran como líneas discontinuas. "Taken from Ref. 15"

10.3.1. Factores que afectan los espectros de IR de las NP de TiC

En primer lugar, se han estudiado diferentes factores que podrían afectar a los IR simulados de nuestras NP. En total se han examinado cuatro factores: el factor de los isómeros, el uso de distintos funcionales, el efecto de la carga global de las NP y por último el efecto de la temperatura.

- Efecto de los isómeros.

El efecto de los isómeros se ha estudiado sobre el tamaño más pequeño del cual se disponen datos experimentales, el 3×3×3. Para este tamaño, existen dos posibles isómeros el $Ti_{14}C_{13}$ y el $Ti_{13}C_{14}$. Ambos isómeros se muestran en la Figura 10.16.

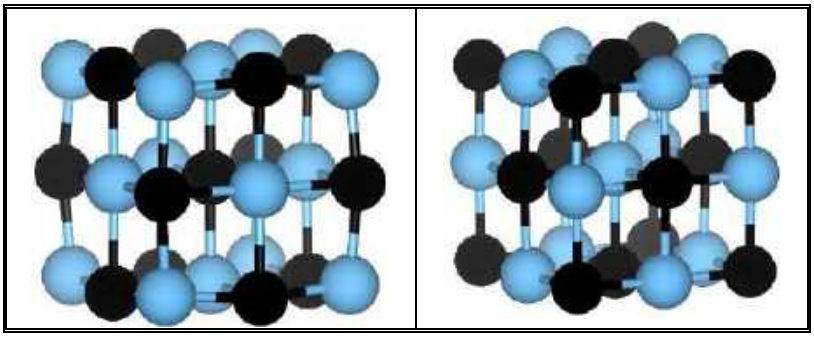

Figura 10.16. Izquierda: $Ti_{14}C_{13}$ NP. Derecha: $Ti_{13}C_{14}$ NP.

En primer lugar, se ha de optimizar la estructura, condición imprescindible para poder simular el IR de una estructura. Después de optimizar la estructura, los IR son calculados a través de las frecuencias de vibraciones y, por último, se comparan los IR obtenidos para ambos isómeros. Los dos espectros se pueden ver en la Figura 10.17.

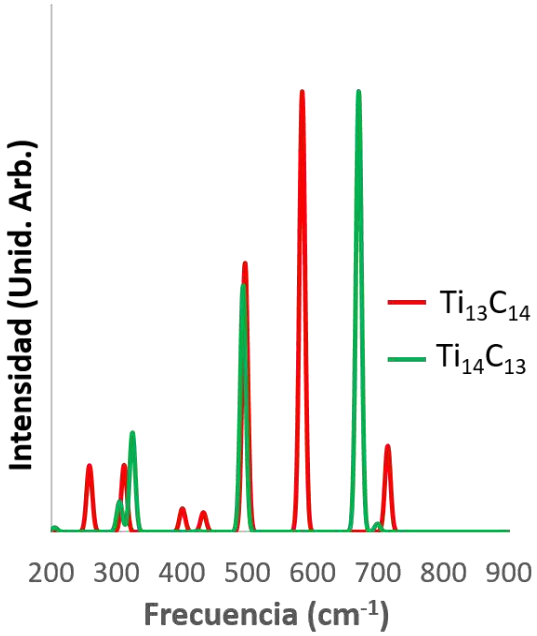

Figura 10.17. Espectros de IR armónicos para NP $Ti_{14}C_{13}$ y $Ti_{14}C_{13}$.

Como se puede apreciar en la figura anterior, los espectros de IR obtenidos son claramente diferentes, esto permite distinguir los isómeros mediante esta técnica. Los resultados muestran que el isómero $Ti_{14}C_{13}$, encaja mejor con el espectro experimental como se puede apreciar en la Figura 10.18.

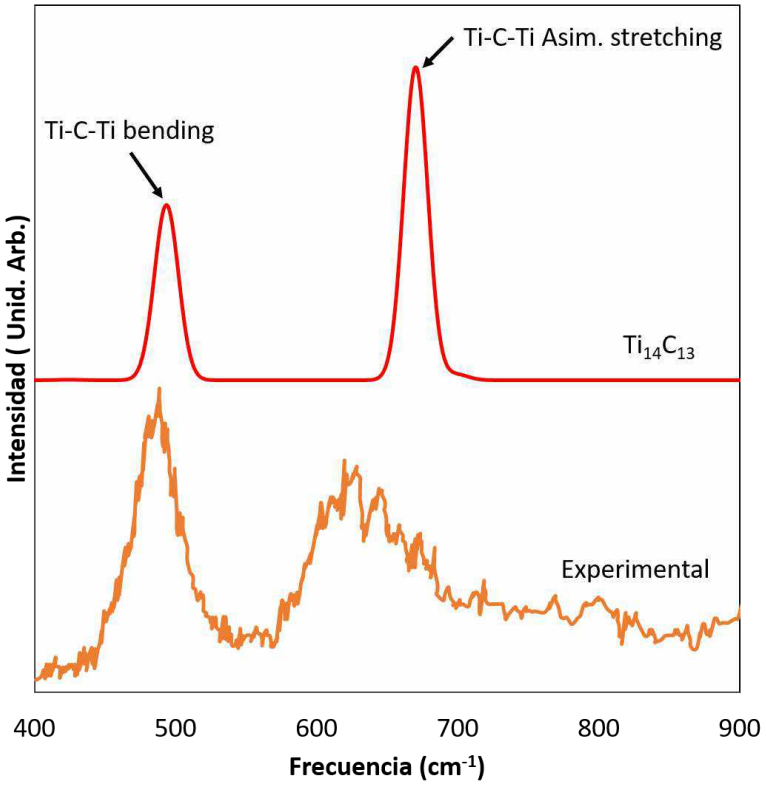

Figura 10.18. Espectro de IR armónico simulado para el isómero $Ti_{14}C_{13}$ comparado con los datos experimentales.[15]

- Efecto del funcional

En este caso, dos funcionales son comparados para comprobar cuál de los dos simula mejor el IR experimental. Los funcionales utilizados son PBE[11] y PBE0.[16] Los espectros obtenidos para la estructura $Ti_{14}C_{13}$ con cada uno de los funcionales, junto con el IR experimental son mostrados en la Figura 10.19.

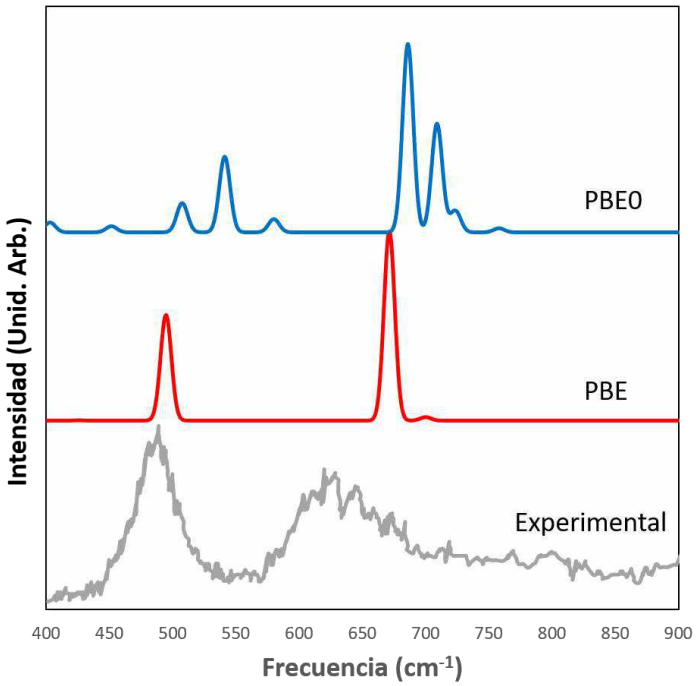

Figura 10.19. Espectros de IR armónicos obtenidos para $Ti_{14}C_{13}$ utilizando diferentes funcionales. En rojo el funcional PBE, en azul el funcional PBE0 y en gris el espectro experimental.[15]

Los resultados muestran como el funcional PBE se ajusta mejor a los datos experimentales ya que únicamente presenta 2 picos, mientras que el funcional PBE0 presenta 4 picos. Además, estos picos se encuentran a frecuencias mayores que las experimentales.

- Efecto de la carga

En esta sección, se han estudiado tres estados de carga diferentes para el $Ti_{14}C_{13}$ NP: neutro (0), catiónico (+1) y aniónico (-1). Aprovechando que se disponen de las tres estructuras, se han calculado la afinidad electrónica y la energía de ionización, siendo la primera de 0.97 eV y la segunda de 4.15 eV. Los tres espectros obtenidos se representan en la Figura 10.20.

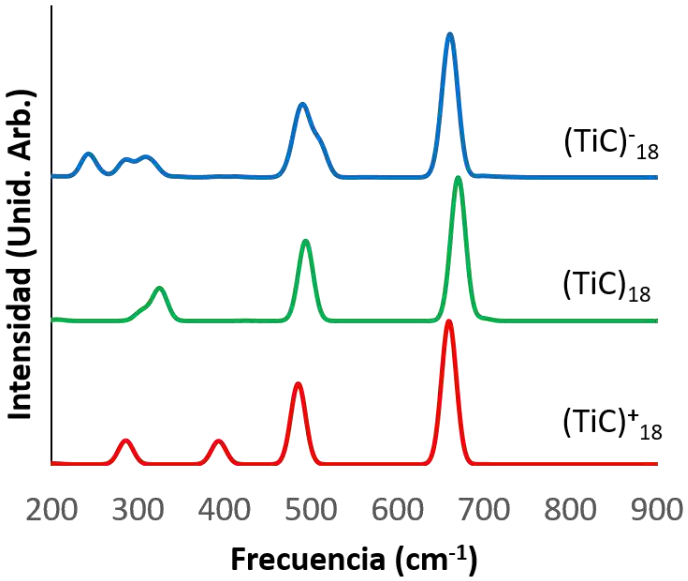

Figura 10.20. Espectros de IR armónicos para carga neutra, positiva y negativa para la estructura NP $Ti_{14}C_{13}$.

Los espectros muestran diferencias significativas a bajas frecuencias, entre 200 y 400 cm^{-1}. En este rango, los picos de IR de tres estructuras no coinciden. Los otros dos picos que exhiben estas especies, alrededor de 500 cm^{-1} y 650 cm^{-1} aparecen en frecuencias similares en todos los casos. La estructura neutra (línea verde) se desplaza ligeramente a frecuencias más grandes con respecto a los espectros aniónico y catiónico. Específicamente, el pico de frecuencia más alto para el espectro neutro aparece en 667 cm^{-1} que es 10 cm^{-1} más alto que para las estructuras catiónica y aniónica. Finalmente, el pico alrededor de los 490 cm^{-1} es diferente para cada uno de los tres estados de carga. En orden de frecuencia creciente, este pico aparece primero en la estructura catiónica (481 cm^{-1}), luego en la estructura aniónica (485 cm^{-1}) y finalmente la estructura neutra a 490 cm^{-1}.

Como los espectros simulados obtenidos no exhiben diferencias significativas en el rango de datos experimentales de 400 cm^{-1} a 900 cm^{-1}, no se pueden utilizar para afirmar la carga del sistema experimental para esta estructura. Por lo tanto, en el resto de espectros de IR simulados se realizarán de compuestos neutros.

- Efecto de la temperatura

Para estudiar el efecto de la temperatura, se utiliza la dinámica molecular para obtener el espectro IR. El tamaño de NP elegido para realizar esta prueba fue el NP de $Ti_{14}C_{13}$ a cinco temperaturas diferentes: a 0 (IR armónico), 400, 900, 1500 y 2100 K. Todas las temperaturas consideradas son inferiores al punto de fusión experimental del TiC, que es aproximadamente 3100K.[17] Los resultados obtenidos para este estudio son mostrados en la Figura 10.21, junto con el espectro experimental.

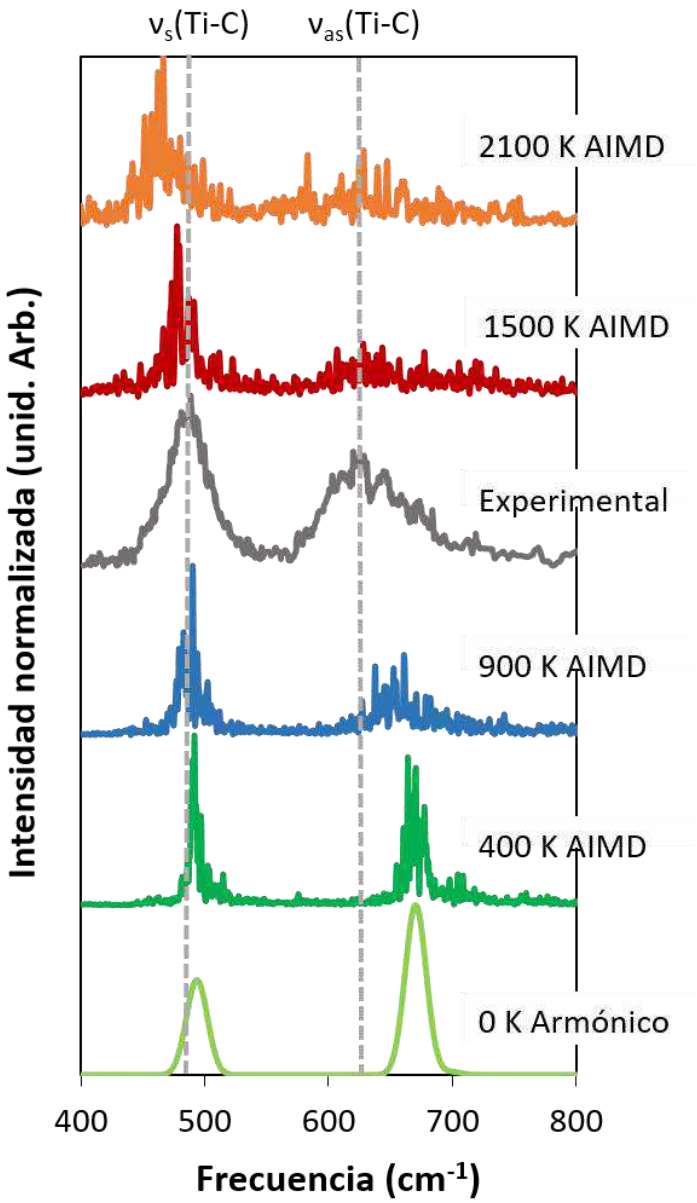

Figura 10.21. Espectros de infrarrojos simulados a diferentes temperaturas y datos de infrarrojos experimentales para $Ti_{14}C_{13}$.

Todos los resultados de IR simulados muestran dos picos entre 400 cm^{-1} y 800 cm^{-1} en línea con el espectro experimental, y ninguno de ellos presenta picos a frecuencias más altas. A 0 K, el pico más intenso corresponde al pico de mayor frecuencia (675 cm^{-1}) con respecto al pico de menor frecuencia (500 cm^{-1}). El pico más alto está triplemente degenerado y corresponde al modo de estiramiento Ti-C-Ti desde el borde C. Los átomos de C oscilan en los bordes entre los átomos de Ti de las esquinas, mientras que el pico a 500 cm^{-1} también está triplemente degenerado y se debe al modo de flexión Ti-C-Ti. En este caso, los átomos del borde C oscilan con respecto al centro del cúmulo. Sin embargo, a medida que aumenta la temperatura, el pico de frecuencia más alta se ensancha y aplana, lo que lleva a que el pico de frecuencia más baja tenga relativamente más intensidad. A medida que aumenta la temperatura, más allá de 900 K, el pico de frecuencia más alto es cada vez más difícil de diferenciar debido al alto nivel de

ensanchamiento inducido térmicamente. También se observa que el pico de frecuencia más baja se desplaza gradualmente a frecuencias más bajas a medida que aumenta la temperatura. Este cambio en el pico de baja frecuencia asciende a alrededor de 30 cm^{-1} entre 0 y 2100 K.

Para este estudio, el espectro simulado que más se asemeja al experimental es el obtenido a 900 K. En este caso, el pico de menor frecuencia en ambos espectros coincide con 490 cm^{-1}. El segundo pico de frecuencia más alto para el espectro simulado de 900 K está algo desplazado hacia frecuencias más altas, alrededor de 30 cm^{-1}, pero tiene un perfil de intensidad similar al pico experimental. El cambio de 30 cm^{-1} podría deberse a que la temperatura del NP $Ti_{14}C_{13}$ en el experimento está cerca de 900 K pero ligeramente más alta.

Los resultados muestran que la temperatura es un efecto importante para interpretar los espectros IR obtenidos de experimentos de haz de racimo. En particular, este estudio sugiere fuertemente que la temperatura en el experimento para $Ti_{14}C_{13}$ NP es cercana a 900 K. Este efecto de temperatura en los espectros de IR se probará para otros tamaños de NP en el resto de este Capítulo.

10.3.2. Estabilidad de NP basadas en $(TiC)_{18}$

En este apartado se estudiará el $(TiC)_{18}$ NP. Este tamaño es el segundo tamaño NP más pequeño representado en la Figura 10.15. Para este tamaño de NP, son posibles dos estructuras de corte cúbico diferentes (isómeros). Uno de estos isómeros es el 3×3×4 NP mientras que el otro isómero es 2×3×6. Ambos isómeros son estudiados y se obtiene que el isómero 3×3×4 es 2.88 eV más estable que el isómero 2×3×6.

En la Figura 10.15, los datos experimentales indican que a los NP para un tamaño de $(TiC)_{18}$ y mayores les "faltan" cuatro átomos de carbono (etiquetados como "3×3×4 - 4C". Esto se observa específicamente para los tamaños $(TiC)_{18}$, $(TiC)_{24}$ y $(TiC)_{32}$. Cuatro átomos de carbono tienen una masa de 48 amu, que también corresponde a la masa de un átomo de Ti. Por ello, se estudiarán ambas posibilidades. Una posibilidad corresponde a una composición de $Ti_{18}C_{14}$, donde los 4 átomos de carbono se han eliminado y la otra posibilidad corresponde a una composición de $Ti_{17}C_{18}$, donde el átomo eliminado es uno de Titanio.

- $Ti_{18}C_{14}$.

Para este compuesto, se estudiarán cuatro posibilidades (isómeros). Las posibilidades que consideramos que se eliminan los 4 átomos de carbono son: en las esquinas, en las aristas de la cara pequeña, internos y aleatorios. Los 4 isómeros se pueden ver en la Figura 10.22.

esquinas	Arista pequeña	internos	aleatorios
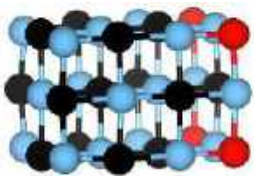	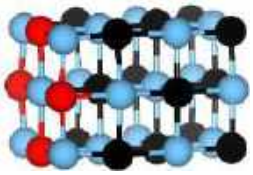	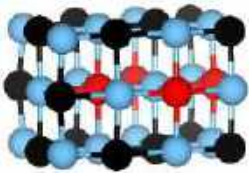	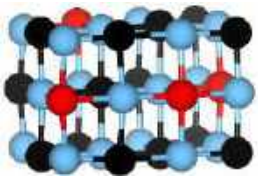

Figura 10.22. Isómeros de $Ti_{18}C_{14}$ estudiados a partir de $(TiC)_{18}$, donde los átomos eliminados se muestran en rojo.

Los resultados muestran que el isómero más estable es cuando se eliminan los átomos de 4C en las esquinas. Las energías relativas calculadas para estos NP se informan en la tabla 10.5.

Tabla 10.5. Energías relativas en eV para las diferentes estructuras de $Ti_{18}C_{14}$ cuando se eliminan átomos de 4C de $(TiC)_{18}$ NP.

esquinas	Arista pequeña	internos	aleatorios
0.00	7.01	9.96	6.04

Para buscar estructuras de NP alternativas, se utilizaron simulaciones de dinámica molecular clásica (MD). Específicamente, se ejecutaron una serie de simulaciones NVT MD contiguas comenzando primero desde una temperatura alta (2500 – 3000 K) y reduciendo la temperatura de manera escalonada en $_{14}$500 K hasta alcanzar una temperatura de 1000 K. A continuación, se extrajeron y optimizaron las estructuras de las NP. Con este método se obtuvieron así otras 10 estructuras de $Ti_{18}C_{14}$. Ninguna de las estructuras NP obtenidas por este procedimiento es más estable que $Ti_{18}C$ cuando los átomos se eliminan de las esquinas como se puede ver en la Figura 10.23. Estabilidades energéticas de las estructuras NP de $Ti_{18}C_{14}$ en relación con el NP de energía más baja con átomos de C eliminados de las esquinas, ver Figura 10.23.

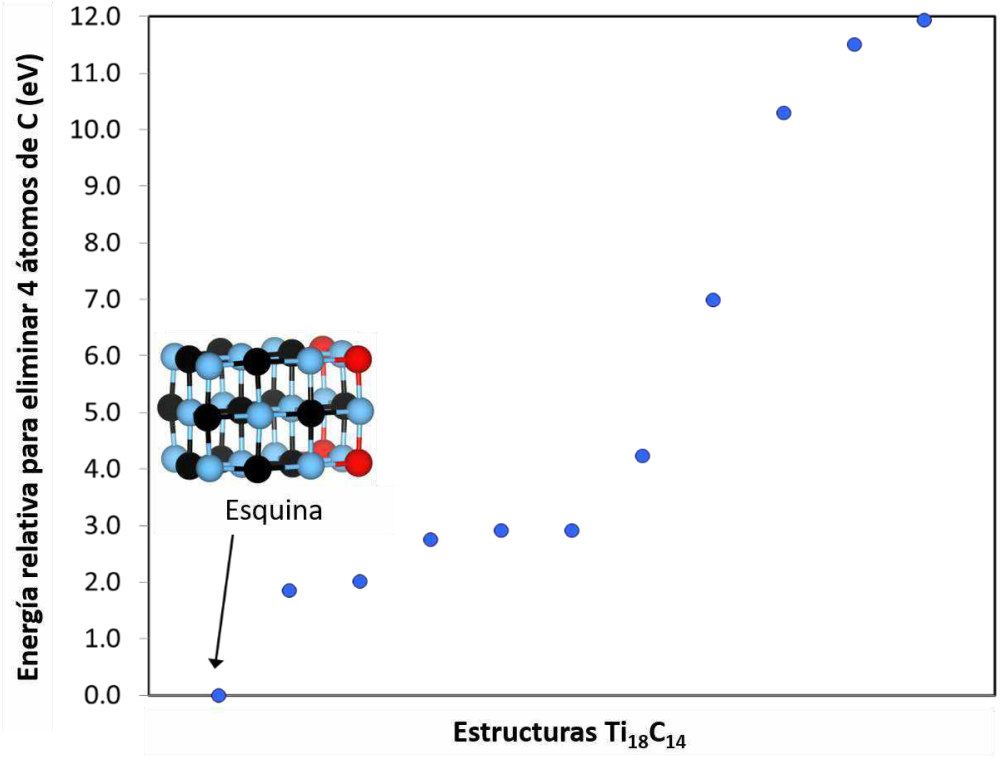

Figura 10.23. Estabilidades energéticas de las estructuras NP de $Ti_{18}C_{14}$ en relación con el NP de menor energía con átomos de C eliminados de las esquinas.

- $Ti_{17}C_{18}$.

Para este compuesto, igual que en el caso anterior, también se han estudiado 4 isómeros de $Ti_{17}C_{18}$, donde el átomo de Ti ha sido eliminado de diferentes posiciones. Las posiciones donde se ha eliminado el átomo de Ti son: centro de la cara, esquina, arista larga y arista corta. Los cuatro isómeros se muestran en la Figura 10.24.

Centro de la cara	esquina	Arista larga	Arista corta
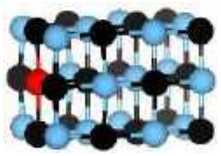	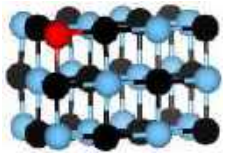	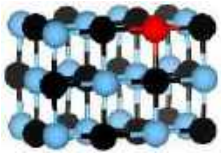	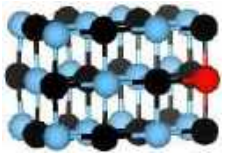

Figura 10.24. Isómeros de $Ti_{17}C_{18}$ estudiados a partir de $(TiC)_{18}$, donde los átomos eliminados se muestran en rojo.

Las energías relativas obtenidas para estos NP de $Ti_{17}C_{18}$ se muestran en la Tabla 10.6.

Tabla 10.6. Energías relativas en eV para las diferentes estructuras de $Ti_{17}C_{18}$ cuando se elimina un átomo de Ti de $(TiC)_{18}$ NP.

Arista corta	Centro de la cara	esquina	Arista larga
0.00	8.56	6.14	0.23

Los resultados indican que la estructura de $Ti_{17}C_{18}$ más estable es cuando el átomo de Ti se elimina del borde corto del NP de $Ti_{17}C_{18}$. Esta estructura es la más estable porque se forma un C-C espontáneo. Lo mismo ocurre cuando el átomo de Ti se elimina por el borde largo. La formación de un enlace C-C hace que la estructura se estabilice. En nanoclústeres estequiométricos pequeños $(TiC)_n$, aunque las estructuras de energía más baja tienden a seguir el orden alterno Ti-C del cristal de sal de roca, los isómeros metaestables bajos pueden exhibir enlaces C-C.[18] Con el aumento del contenido de C, la formación de dímeros C2 altamente estabilizadores energéticamente se vuelve más fácil,[19] y es probable que la mayoría de las NP de Ti_xC_y ricas en C presenten tales fracciones. En los otros dos casos en estudio, no se forman enlaces C-C. La estructura final para los cuatro casos se muestra en la Figura 10.25.

Centro de la cara	esquina	Arista larga	Arista corta
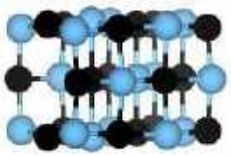	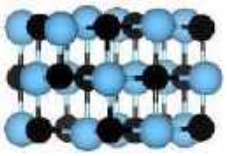	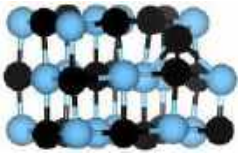	

Figura 10.25. Estructuras definitivas para las cuatro estructuras en estudio para $Ti_{17}C_{18}$.

Se crearon 49 estructuras más con la estequiometría $Ti_{17}C_{18}$. Los 49 NP resultantes de la optimización directa de los NP después de la eliminación de un átomo de Ti y/o las ejecuciones clásicas de recocido MD apoyan aún más esta tendencia. En este caso, después de la optimización, muchas de estas estructuras NP exhiben enlaces C-C. La formación de enlaces C-C se identifica fácilmente en los espectros de IR de las NP de Ti_xC_y debido a un pico de firma fuerte cercano a 1350-1400 cm^{-1} asociado con el estiramiento C-C.[18,20] Observamos que no se informa que los espectros IR experimentales para los NP considerados en este estudio exhiban tal pico.[21] Por tanto, las estructuras NP con enlace C-C no se consideran candidatos viables para explicar los datos experimentales de RI. La energía más baja de NP de $Ti_{17}C_{18}$ sin enlace C-C se encontró tras la eliminación de Ti de una esquina del compuesto $(TiC)_{18}$ que consideramos como el candidato NP rico en C más probable para explicar potencialmente los resultados experimentales de IR.

Por lo tanto, tomamos la referencia como NP donde el átomo de Ti se quita de una esquina, y la energía del resto de las estructuras NP se ha comparado energéticamente en la Figura 10.26.

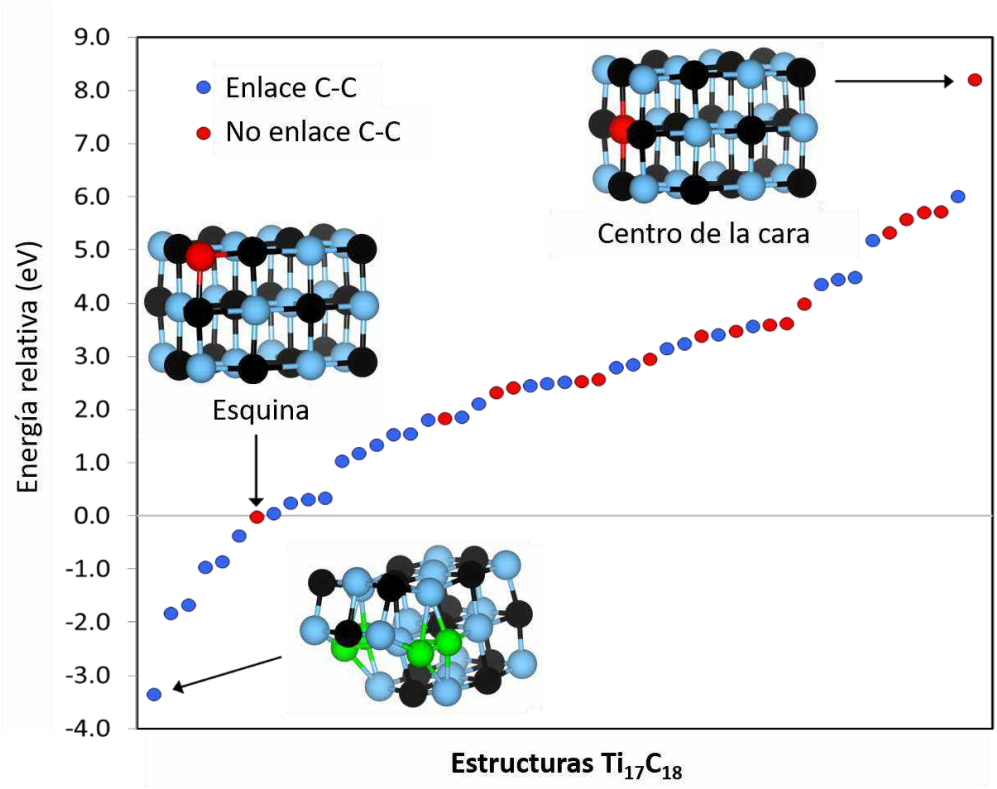

Figura 10.26. Estabilidades energéticas relativas de las estructuras de NP de $Ti_{17}C_{18}$ con respecto a la estructura con un átomo de Ti extraído de una esquina del NP de 3×3×4 $(TiC)_{18}$. Las estructuras con enlaces C-C se indican en azul y las estructuras que no poseen enlaces C-C se indican en rojo.

Como se puede observar en la Figura 10.26, la estructura más estable es la que forma enlace C-C y además presenta más simetría.

10.3.3. Espectros infrarrojos basados en MD.

Diferentes tamaños de NP han sido caracterizados utilizando el IR armónico, pero no se han conseguido encontrar ningún compuesto que encaje con el experimental. Por eso, se han empleado el espectro basados en MD, para así poder simular espectros a diferentes temperaturas (900K, 1500K y 2100K). En este caso, el tamaño de Np escogido es el 3×3×4 $(TiC)_{18}$ y se estudiaran el compuesto estequiométrico, el $Ti_{17}C_{18}$ cuando pierde el átomo en la esquina y el $Ti_{18}C_{14}$ cuando pierde los 4 átomos de C en las esquinas. Los resultados, han mostrado que el compuesto que más se acerca al IR experimental es el del compuesto $Ti_{18}C_{14}$. Los espectros para este compuesto a diferente temperatura se muestran en la Figura 10.27.

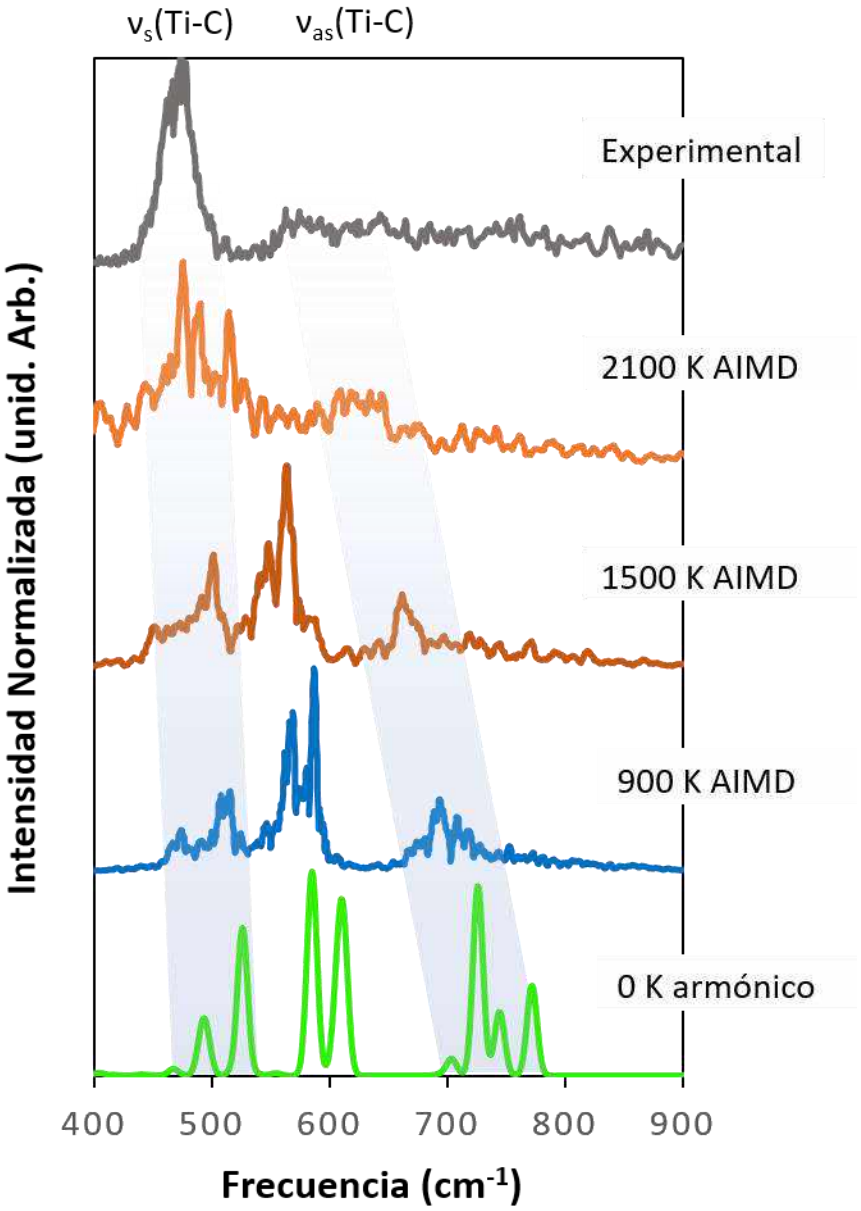

Figura 10.27. Espectros de IR a diferentes temperaturas para $Ti_{18}C_{14}$ en comparación con el IR experimental.

Como se puede observar en la Figura 10.27, el espectro simulado a 2100K encaja bastante bien con el experimental. Estos resultados sugieren que el espectro IR experimental corresponde a la estructura $Ti_{18}C_{14}$ cuando faltan los átomos 4C del NP estequiométrico en las esquinas.

10.4. Adsorción de H_2 en NP de TiC

Emulando los estudios realizados para las superficies, se han llevado a cabo la adsorción y disociación de H_2 en TiC NP. Diferentes tamaños de NP han sido estudiados desde el tamaño 2×2×2 hasta el tamaño 6×6×6.

10.4.1. Adsorción de H sobre TiC NP

Los resultados obtenidos revelan que la posición más estable para adsorber la molécula de H_2 es en el córner de un átomo C. Además, la adsorción del H_2 sobre el C es mayor cuanto mayor es el tamaño de la nanopartículas mientras que la energía de adsorción sobre un átomo de Ti no varía al incrementar el tamaño de la NP.

Para el tamaño $(TiC)_{18}$ y $(TiC)_{24}$ se ha estudiado las NPs donde 4 átomos de carbono en las esquinas son eliminados. En ambos casos, los resultados han demostrado que la reactividad aumenta. Además, cuando se han estudiado las posiciones del átomo de Ti solitario y el baricentro formado por tres átomos de Ti (Figura 10.28) los resultados han revelado que se produce una disociación espontanea de la molécula de H_2.

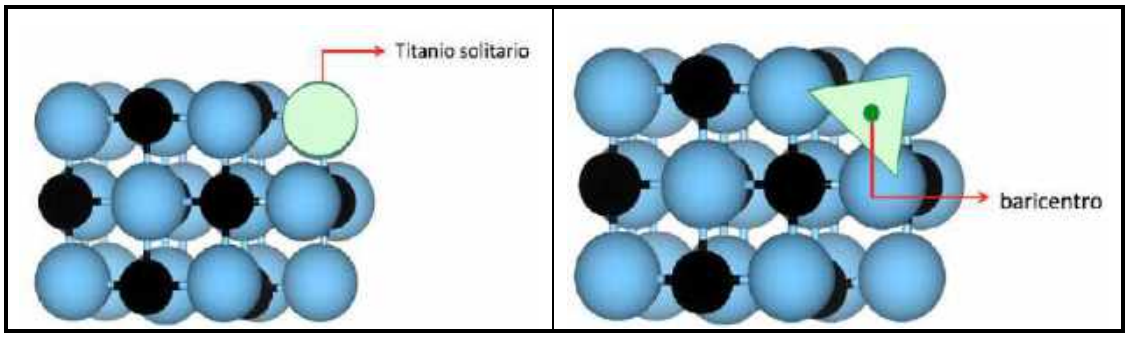

Figura 10.28. Dos casos peculiares estudiados. Izquierda: el Ti solitario. Derecha: baricentro.

10.4.2. Disociación de H_2 en TiC NP

La disociación de H_2 en el tamaño $(TiC)_{32}$ se va a estudiar en diferentes situaciones como se indica en la Figura 10.29.

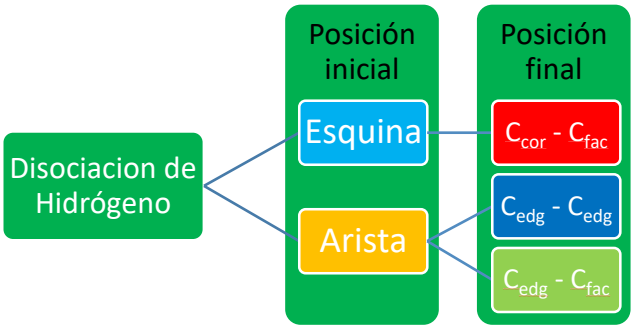

Figura 10.29. Estados de transición estudiados para la disociación de H_2 en el $(TiC)_{32}$ NP.

Los resultados han revelado que únicamente una de estas disociaciones es energéticamente favorable. El caso favorable es el en que la molécula de H_2 en posición inicial para se encuentra adsorbida sobre la arista y en la posición final los dos átomos de H se encuentran adsorbidos sobre 2 átomos de C en las aristas. Esta situación se muestra en la Figura 10.30.

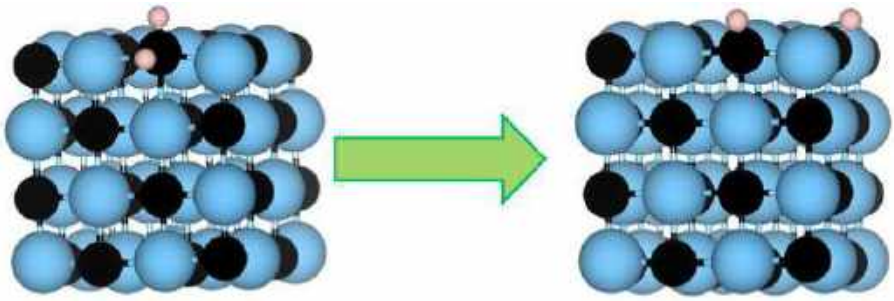

Figura 10.30. Disociación de H_2 donde la posición inicial H_2 se adsorbe en un átomo de C en la arista y en la configuración final el H_2 se disocia con ambos átomos de H adsorbidos en dos átomos de C ubicados en la arista para el tamaño $(TiC)_{32}$.

El perfil de reacción que se obtiene se muestra en la Figura 10.31.

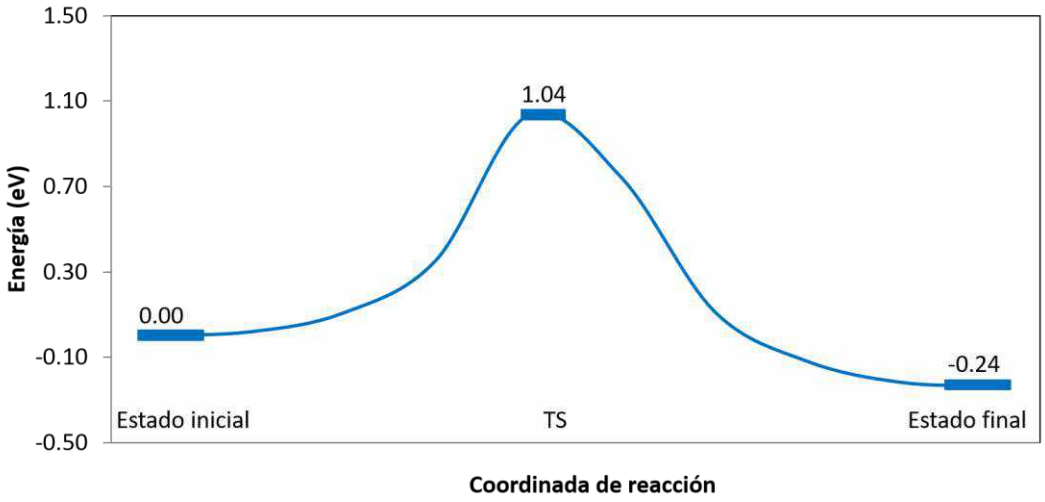

Figura 10.31. Perfil de reacción obtenido para la disociación de Hidrógeno en la NP $(TiC)_{32}$.

En la figura anterior se muestra que la barrera de TS a este perfil de reacción es 1.04 eV y la diferencia entre la posición inicial y final es -0.24 eV. (es decir, los átomos de hidrógeno adsorbidos disociados de mineral son más favorables energéticamente que el estado inicial).

Esta misma situación se ha estudiado para otros tamaños, dando valores de barreras semejantes.

10.5. Conclusiones

La presente tesis consta de diferentes estudios sobre TMC. Estos estudios se han realizado sobre superficies y nanopartículas de estos materiales. En la primera parte de la tesis se han realizado estudios de adsorción y disociación de hidrógeno en la superficie (001) de diversos materiales, además de la superficie de TiC (001) se ha estudiado la adsorción y disociación de metano. En una segunda parte, se ha estudiado la estabilidad de diferentes tamaños de NP cúbicas de TiC. Además, se ha estudiado el efecto de eliminar átomos de estos NP, tanto de 4 átomos de carbono como de un átomo de Ti. Posteriormente, estas nanopartículas han sido caracterizadas

por IR para su comparación con datos experimentales previamente publicados y así poder conocer las estructuras de estas nanopartículas. Finalmente, se ha estudiado la adsorción y disociación de hidrógeno en diferentes tamaños de nanopartículas.

Los resultados de estos estudios han permitido conocer la preferencia de que los átomos de H ocupen posiciones C-Top en la superficie de TiC (001). En el mismo material también se estudia la secuencia de llenado hasta la cobertura total donde los resultados demostraron que los átomos de H prefieren ser adsorbidos en la superficie en lugar de ser absorbidos entre las capas. La adsorción de átomos de H ocurre en C-Top, esta energía de adsorción es más débil a medida que la capa de átomos de H se llena, incluso los adatomos C-Top H estabilizan los H adatomos vecinos en los sitios Ti-Top. Sin embargo, los sitios Ti-Top pueden estar ocupados cuando están rodeados por sitios C-Top, formando una especie de H piramidal, particularmente ocupado cuando se pasa por una situación de 1 ML. Estos resultados han permitido comprender lo que ocurre en los estudios experimentales, permitiendo la asignación de los picos obtenidos en la TPD experimental. En TiC (superficie 001), la adsorción de H_2 también se prefiere sobre los sitios C-Top, pero en forma de un resto H_2 alargado, llamado modelo de *Kubas*. La disociación de la molécula de H_2 en adatomos 2H es un proceso exotérmico y presenta una pequeña barrera energética. Los H adatomos generados pueden difundirse sobre la superficie de TiC (001), pero con barreras de energía moderadas. Dichos resultados señalan el uso de TiC como posible catalizador de hidrogenación.

Los resultados obtenidos para el resto de las seis TMC estudiadas revelan que la molécula de H2 preferiblemente physisorbs en C-Top para las TMC del grupo IV y δ-MoC, pero en M-Top para las TMC del grupo V (VC, NbC y TaC). Cuando la molécula de H_2 se adsorbe en C-Top, la molécula de H_2 adopta una adsorción en modo *Kubas*, donde el enlace H_2 se alarga sensiblemente. Este modo de adsorción se ha encontrado en todos los TMC aunque no es el modo de adsorción más favorable. El único compuesto donde no se ha encontrado el modo *kubas* ha sido en TaC. Una vez adsorbida, la molécula de H_2 es impulsada termodinámicamente para disociarse en las TMC del grupo IV (TiC, ZrC y HfC), donde los H adatomos ocupan sitios C-Top vecinos y, en todos los casos, las barreras de energía de disociación de H_2 se pueden superar fácilmente. No ocurre lo mismo en las TMC del Grupo V, donde la fisisorción y el paso de disociación generalmente endotérmica se traducen en valores de E_b algo mayores. Finalmente, el δ-MoC presenta una fuerte adsorción de H_2, pero un valor E_b algo alto, lo que lo convierte en un catalizador de hidrogenación viable, pero a temperaturas lo suficientemente grandes como para superar esta barrera energética del paso de reacción. En este punto, solo los TMC del grupo IV son buenos candidatos para realizar la reacción de disociación de H_2.

Respecto a la molécula de CH_4, esta molécula presenta una menor energía de adsorción en la superficie de TiC (001). El estudio de disociación de esta molécula muestra que, en lo que respecta a la superficie de TiC (001), esta disociación difícilmente ocurrirá, ya que la adsorción de CH_4 es muy débil y la molécula probablemente se desorbería antes de romperse en CH_3 y H,

ya que esto cuenta con una barrera de energía muy grande. Por otro lado, cuando la superficie soporta racimos de Ni, la energía de adsorción de CH_4 aumenta 1,5-2,5 veces con respecto a la superficie limpia de TiC (001), dependiendo del tamaño de los racimos de Ni. Además, la energía de activación disminuye considerablemente en el mejor de los casos estudiados (Ni_4/TiC). Parece plausible que una combinación de falta de coordinación y una estructura electrónica particular de los grupos de Ni provoque que esta activación de CH_4 pueda ocurrir más fácilmente.

Las conclusiones que se pueden extraer de los resultados obtenidos en los estudios de NP son las siguientes. En primer lugar, se han probado diferentes parámetros de la simulación mostrando que algunos de ellos pueden modificar los espectros IR (por ejemplo, funcional, estado de carga y temperatura). La caracterización IR de las NP simuladas nos ha permitido comparar con los espectros IR derivados del haz de racimo experimental. Los espectros de IR derivados de MD nos han permitido identificar las estructuras NP probables en el experimento para los dos tamaños de NP más pequeños. Además, se encontró que el espectro IR experimental probablemente corresponde a la estructura $Ti_{18}C_{14}$ cuando faltan los átomos 4C del NP estequiométrico original en las esquinas. Además, esta estructura NP es la más estable que se encuentra dentro de todas las estructuras de isómeros $Ti_{18}C_{14}$ que se han estudiado. Como es el isómero energéticamente más estable, sugerimos tentativamente que este resultado también podría extrapolarse a los tamaños NP más grandes de $(TiC)_{24}$ y $(TiC)_{32}$ donde también sucede que cuando la estructura cúbica madre pierde los átomos de las esquinas es el isómero más estable para Ti_xC_{x-4}. Respecto al NP de adsorción y disociación de H_2, los resultados muestran que la molécula de H_2, de la misma forma que en la superficie (001) prefiere adsorberse en átomos de C. Las posiciones de adsorción más favorecidas energéticamente es el C-Corner. Cuando aumenta el tamaño de NP, la magnitud de la energía de adsorción también aumenta cuando la molécula de H_2 se adsorbe en átomos de C. Cuando se produce la adsorción en el átomo de Ti, prácticamente no se observa variación de la energía de adsorción al aumentar el tamaño. Cuando los NP son pobres en átomos de C, su reactividad aumenta y en algunos sitios de adsorción de H_2, el H_2 se disocia espontáneamente. Finalmente, el TiC NP exhibe energías de barrera más bajas para la reacción de disociación de H_2 que las superficies de TiC. La barrera energética para la disociación de H_2 no varía significativamente con respecto a los tamaños de NP estudiados. Además, la barrera energética obtenida sobre TiC Np es superior a la encontrada para la superficie de TiC (001) en las mismas condiciones que se ha estudiado el NP.

10.6. Referencias

1. A.D. McNaught and A. Wilkinson. IUPAC. Compendium of Chemical Terminology. 2nd ed (th. Vol. 2291, IUPAC Compendium of Chemical Terminology. Oxford: Blackwell Scientific Publications; **1997**. 2293 p.
2. A. Babuponnusami and K. Muthukumar. A review on Fenton and improvements to the Fenton process for wastewater treatment. *J. Environ. Chem. Eng.*, **2014**, 2, *1*, 557–572.
3. G. Rothenberg. *Catalysis: concepts and green applications*. Weinheim [Germany]: Wiley. **2008**. ISBN 9783527318247.

4. H.H. Hwu and J.G. Chen. Surface chemistry of transition metal carbides. *Chem. Rev.*, **2005**;105, *1*, 185–212.

5. C. Kunkel, F. Viñes, P.J. Ramirez, J.A. Rodriguez, and F. Illas. Combining Theory and Experiment for Multitechnique Characterization of Activated CO on Transition Metal Carbide (001) Surfaces. *J. Phys. Chem. C*, **2019**, 123, *13*, 7567–7576.

6. J.A. Rodriguez, P. Liu, F. Viñes, F. Illas, Y. Takahashi and K. Nakamura. Dissociation of SO_2 on Au / TiC (001): Effects of Au – C Interactions and Charge Polarization. *Angew. Chem. Int. Ed.*, **2008**; 129, *35*, 6685–6691.

7. J.A. Rodriguez, P. Liu, D.J. Stacchiola, S.D. Senanayake, M.G. White, and J.G.Chen. Hydrogenation of CO_2 to Methanol: Importance of Metal-Oxide and Metal-Carbide Interfaces in the Activation of CO_2. *ACS Catal.*, **2015**, 5, *11*, 6696–6706.

8. J.A. Rodriguez, J. Evans, L. Feria, A.B. Vidal AB, P. Liu, K. Nakamura, and F. Illas. CO_2 hydrogenation on Au/TiC , Cu/TiC , and Ni/TiC catalysts : Production of CO, methanol , and methane. *J. Catal.*, **2013**, 307, 162-169.

9. C. Kunkel, F. Viñes, and, F.Illas. Biogas Upgrading by Transition Metal Carbides. *ACS Appl. Energy Mater.* **2018**, 1, *1*, 43–47.

10. R.A. Alpher and R.C. Herman. Erratum: Theory of the origin and relative abundance distribution of the elements. *Rev Mod Phys.*, **1950**, 22, *4*, 153–212.

11. J.P. Perdew, K. Burke, and M. Ernzerhof. Generalized gradient approximation made simple. *Phys Rev Lett.*, **1996**, 77, *18*, 3865–3868.

12. S. Grimme, J. Antony, S. Ehrlich, and H. Krieg H. A consistent and accurate ab initio parametrization of density functional dispersion correction (DFT-D) for the 94 elements H-Pu. *J. Chem. Phys.*, **2010**, 132; 154104.

13. G. Henkelman and H. Jónsson. Improved tangent estimate in the nudged elastic band method for finding minimum energy paths and saddle points. *J Chem Phys.*, **2000**, 113, *22*, 9978–9985.

14. G. Henkelman and H. Jónsson H. A dimer method for finding saddle points on high dimensional potential surfaces using only first derivatives. *J Chem Phys*., **1999**; 111, *15*, 7010–7022.

15. C. Oshima, T. Aizawa, M. Wuttig, R. Souda, S. Otani, Y. Ishizawa, H. Ishida, and K.Tekura. Surface-phonon dispersion curves of TiC(100). *Phys Rev B.*, **1987**, 36, *14*, 7510–7517.

16. J.P. Perdew and M. Ernzerhof. Rationale for mixing exact exchange with density functional approximations. *J. Chem. Phys*., **1996**, 105, *22*, 9982–9985.

17. R.E. Báez, J.H. Díaz F., M.J. Espitia R. Estabilidad relativa del compuesto carburo de titanio TiC: Un estudio mediante DFT. *Rev Colomb Fis*., **2014**, 46, *2*, 39–42.

18. O. Lamiel-Garcia, S.T. Bromley, and F. Illas. Low-energy nanoscale clusters of $(TiC)_n$ n = 6, 12: A structural and energetic comparison with MgO. *Theor Chem Acc.*, **2013**; 132, *3*, 1–6.

19. J.O. Joswig and M. Springborg. The influence of C2 dimers on the stability of Ti(m)C(n) metcar clusters. *J. Chem. Phys.*, **2008**, 129,13, 4311.

20. D. Van Heijnsbergen, G. Von Helden, M.A. Duncan, A.J.A. Van Roij, and G. Meijer. Vibrational spectroscopy of gas-phase metal-carbide clusters and nanocrystals. *Phys Rev Lett*., **1999**, 83, *24*, 4983–4986.

21. G. Von Helden, D. Van Heijnsbergen, and G. Meijer. Resonant ionization using IR light: A new tool to study the spectroscopy and dynamics of gas-phase molecules and clusters. *J. Phys. Chem. A.*, **2003**, 107, *11*, 1671–1688.

Appendix A: Supporting information to “Diversity of Adsorbed Hydrogen on the TiC (001) Surface at High Coverages”

Supplementary Information

Diversity of Adsorbed Hydrogen on the TiC (001) Surface at High Coverages

Juan José Piñero,[†] Pedro J. Ramírez, [‡] Stefan T. Bromley,[†,§] Francesc Illas,[†] Francesc Viñes, [*,†] and José A. Rodriguez, [*,‖]

[†] Departament de Ciència de Materials i Química Física & Institut de Química Teòrica i Computacional (IQTCUB), Universitat de Barcelona, c/ Martí i Franquès 1-11, 08028 Barcelona, Spain

[‡] Facultad de Ciencias, Universidad Central de Venezuela, Apartado 20513, Caracas 1020-A, Venezuela

[§] Institució Catalana de Recerca i Estudis Avançats (ICREA),Passeig de Lluís Companys, 23, 08010 Barcelona (Spain)

[‖]Chemistry Department, Brookhaven National Laboratory, Upton, NY 11973, United States

* Corresponding authors: francesc.vines@ub.edu, rodrigez@bnl.gov

Figure S1 Top view of the TiC(001) surface. The image show C atoms (black), Ti atoms (blue), and H atom (pink) in the six initials positions under study. Top metal (M-top, 1), Top carbon (C-top, 2), Bridge between vicinal carbon and metal atoms (3), 4-fold hollow (4), 3-fold hollow formed by two metal and one carbon atoms (MMC, 5), and 3-fold hollow formed by two carbon and one metal atoms (CCM, 6).

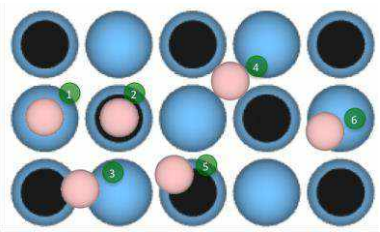

Supplementary Information

Table S1. Adsorption energies of an H atom on the TiC(001) surface. Values are given in eV.

TiC	M-top	C-top	CCM
PBE	-0.73	-2.73	-1.77
PBE-D3	-0.83	-2.83	-1.89

S2

Figure S2. Top view of the TiC(001) surface. The image shows C atoms (black), Ti atoms (blue), and H_2 molecule (pink) in the 19 initial positions under study. Positions 1 to 6 correspond to a vertical orientation of the H_2 molecule and positions 7 to 19 correspond to horizontal orientation of the of the H_2 molecule. Dashed orange lines are guides to the eyes.

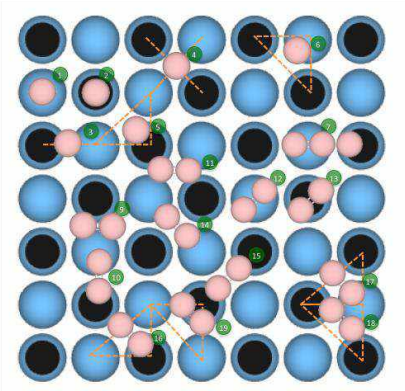

Supplementary Information

Tabla S2. H_2 adsorption energies on the TiC(001) surface. All values are given in eV.

Position	1	7	8	10	12	13
PBE	-0.07	-0.07	-0.23	-0.07	-0.07	-0.46
PBE-D3	-0.21	-0.21	-0.41	-0.21	-0.20	-0.66

S4

Figure S3. Top view of the H atom addition sequence on C-top sites on the TiC(001) surface.

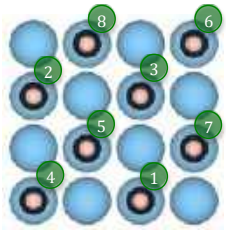

Table S3. Adsorption energies (E_{ads}, in eV) for different H atom coverages on the TiC (001) surface.

H atoms	1	2	3	4	5	6	7	8
PBE	-2.73	-2.71	-2.47	-2.36	-2.49	-2.30	-2.11	-1.94
PBE-D3	-2.83	-2.81	-2.64	-2.61	-2.61	-2.41	-2.21	-2.02

Table S4. Adsorption energies (E_{ads}, in eV) for different H atoms coverages on the TiC (001) surface using $^1/_2 \cdot H_2$ molecule as reference.

H atoms	1	2	3	4	5	6	7	8
PBE	-0.47	-0.44	-0.20	-0.10	-0.23	-0.03	0.15	0.33
PBE-D3	-0.56	-0.54	-0.29	-0.19	-0.35	-0.14	0.05	0.24

Appendix B: Supporting information to “Assessing the usefulness of transition metal carbides for hydrogenation reactions”

Electronic Supplementary Material (ESI) for ChemComm.
This journal is © The Royal Society of Chemistry 2019

Electronic Supplementary Information (ESI)

Assessing the Usefulness of Transition Metal Carbides for Hydrogenation Reactions

Hèctor Prats,[a] Juan José Piñero,[a] Francesc Viñes,[a*] Stefan T. Bromley,[ab] Ramón Sayós,[a] and Francesc Illas[a]

[a] *Departament de Ciència de Materials i Química Física & Institut de Química Teòrica i Computacional (IQTCUB), Universitat de Barcelona, c/ Martí i Franquès 1-11, 08028 Barcelona, Spain*

[b] *Institució Catalana de Recerca i Estudis Avançats (ICREA), Passeig de Lluís Companys, 23, 08010 Barcelona, Spain*

* Corresponding author: [redacted]

S1. Computational Details

Present details of the periodic Density Functional Theory (*DFT*) calculations follow the discussion in the main text. The valence electron density was expanded in a plane wave basis set with a kinetic energy cutoff of 415 eV. The effect of core electrons on the valence electron density was taken into account through the Projected Augmented Wave (PAW) method.[1,2] The employed **k**-point meshes have been selected by a Monkhorst-Pack scheme,[3] and a 9×9×1 mesh was used for all the slab calculations. A separating vacuum region of 10 Å between periodically repeated slabs was found to be sufficient to avoid spurious interactions between the interleaved slabs. The slabs were constructed using the lattice parameter taken from the optimized bulk TMC crystal.[4] Each slab contains four atomic layers; the two uppermost ones have been allowed to fully relax, whereas the two bottom layers were fixed at optimized bulk crystal positions to simulate the bulk rigidity. To represent the (001) surface of the different TMCs, $(2\sqrt{2} \times 2\sqrt{2})$R45° supercells containing 32 C and 32 M (metal) atoms were used. All surface geometries were optimized before placing any adsorbate. Initial guesses for adsorbate geometries were obtained by placing the adsorbate at different sites. For atomic structure optimizations, the conjugated-gradient algorithm has been employed with an energy convergence criterion for electronic updates of 10^{-5} eV, and an atomic force convergence criterion of 0.02 eV $Å^{-1}$. Final total energies were obtained by extrapolation to 0 K (no smearing). The optimized geometries have been characterized as minima in the potential energy surface by frequency analysis with elements of the Hessian matrix computed as finite differences (0.03 Å displacements) of analytical gradients.

The gas-phase energy for molecular hydrogen, $E_{H_2(g)}$, is calculated by placing the H_2 molecule in an

asymmetric box of 9×10×11 Å at the Γ-point. Then, the adsorption energy, $^{\Delta E_{i,ads}}$, of either the adsorbed H_2 or the H species is calculated as:

$$\Delta E_{H_2,ads} = E_{H_2,slab} - \left(E_{slab} + E_{H_2(g)}\right) \quad (1),$$

$$\Delta E_{H,ads} = E_{H,slab} - \left(E_{slab} + \frac{1}{2}E_{H_2(g)}\right) \quad (2),$$

where $^{E_{i,slab}}$ is the energy of the species i adsorbed on the corresponding slab model and $^{E_{slab}}$ is the energy of the relaxed clean slab. With this definition, the more negative the $^{\Delta E_{i,ads}}$ value is, the stronger the adsorption is. Note that the Zero Point Energy (*ZPE*) term is included in all reported energy values.

S2. Optimized Geometries of Adsorbate Species

Figure S1. Optimized geometries (top view) for H_2, H, and $H_{2,Kubas}$ on all TMCs studied. C and H atoms are shown as grey and white spheres, respectively, whereas M atoms (M = Ti, Zr, Hf, V, Nb, Ta, Mo) are represented by spheres with a different color.

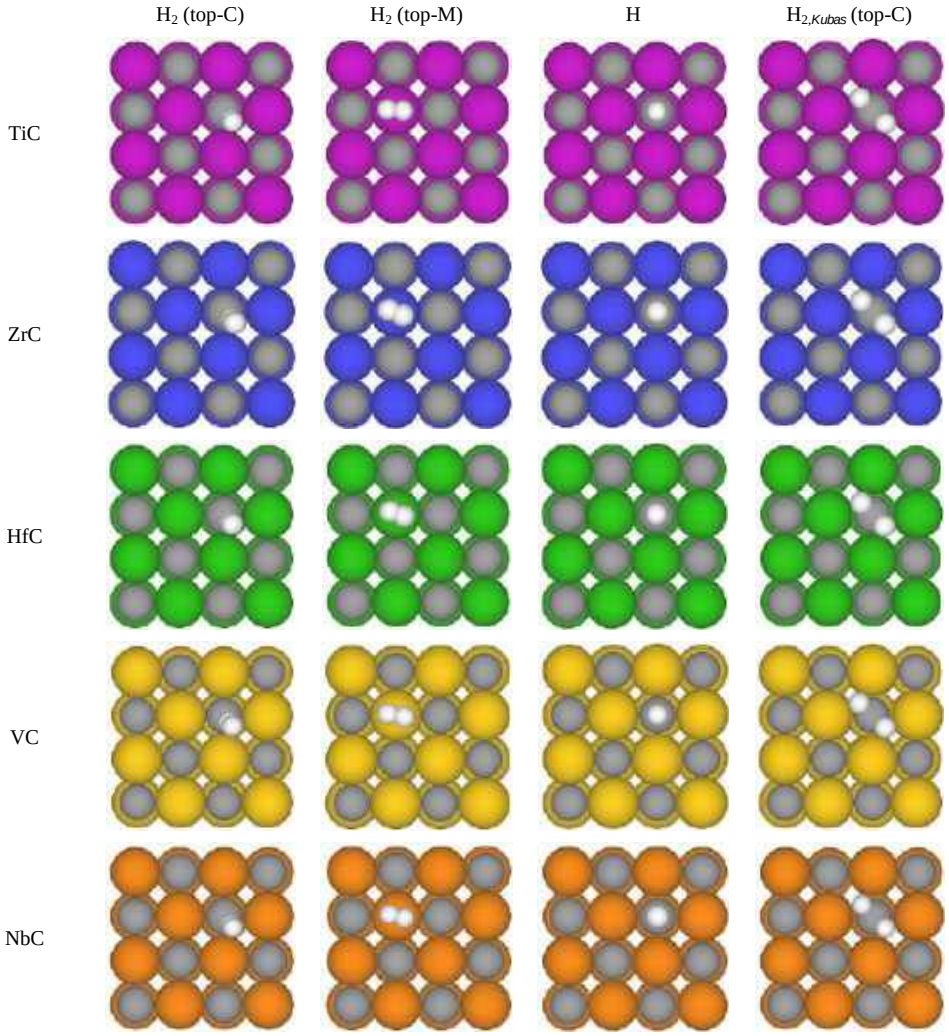

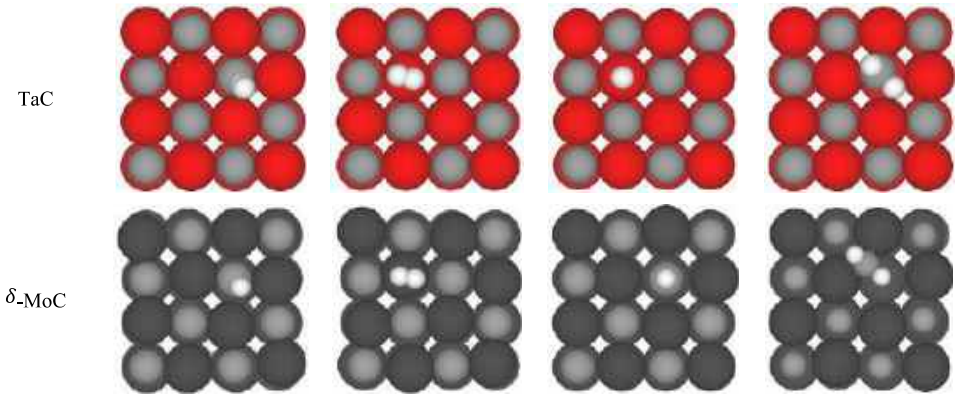
TaC
δ-MoC

S3. Optimized Geometries of Transition States

Figure S2a. Optimized geometries (top view) for the TSs I-III on all studied TMCs. Colour code is as in Figure S1.

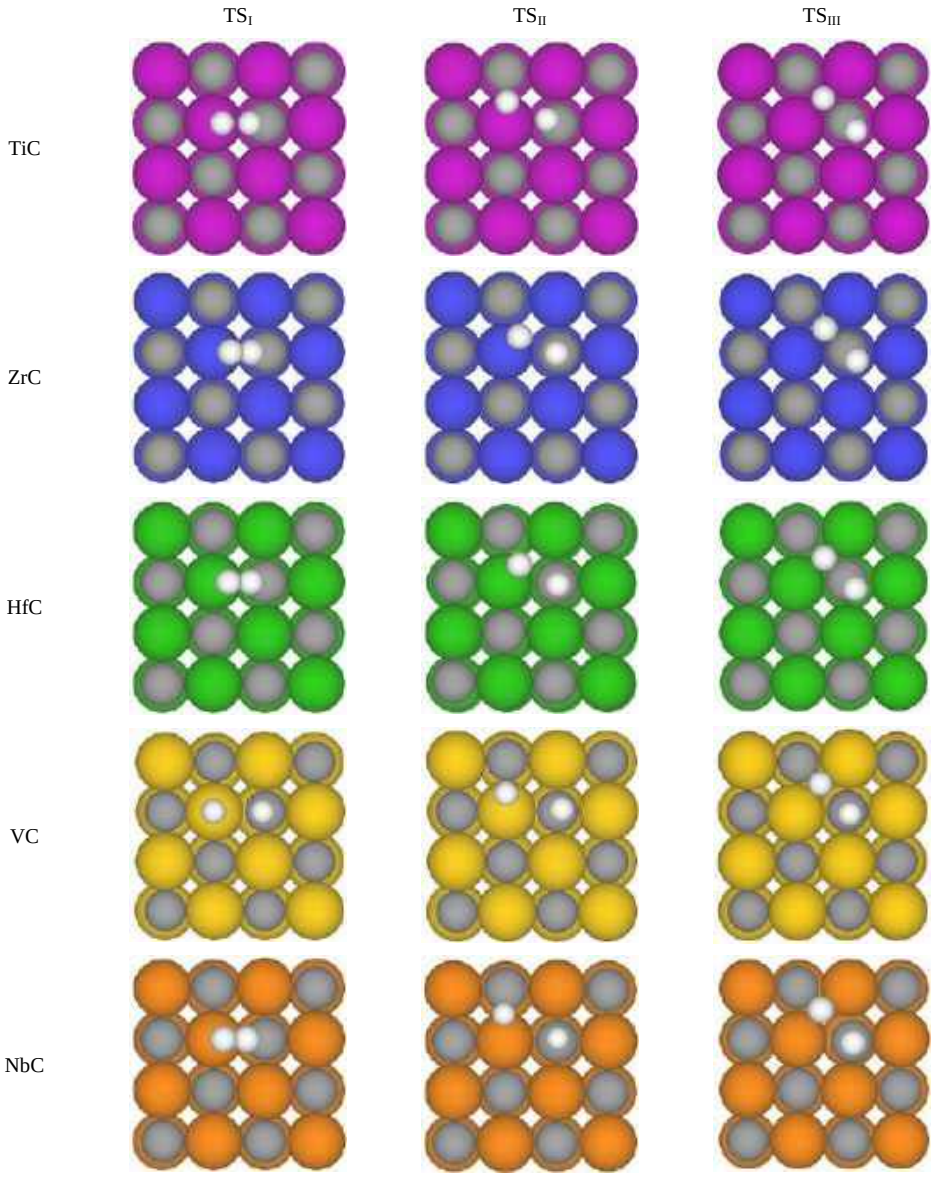

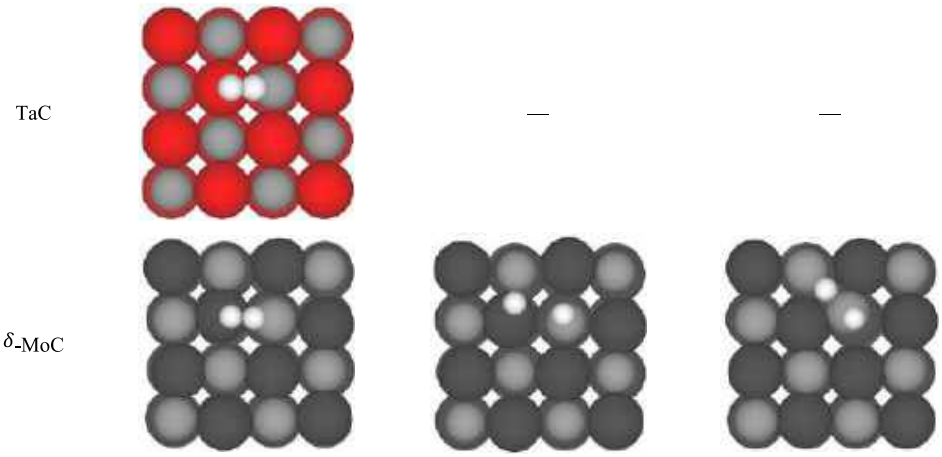
TaC
—
—
δ-MoC

Figure S2b. Optimized geometries (top view) for the TSs IV-VI on all studied TMCs. Colour code is as in Figure S1.

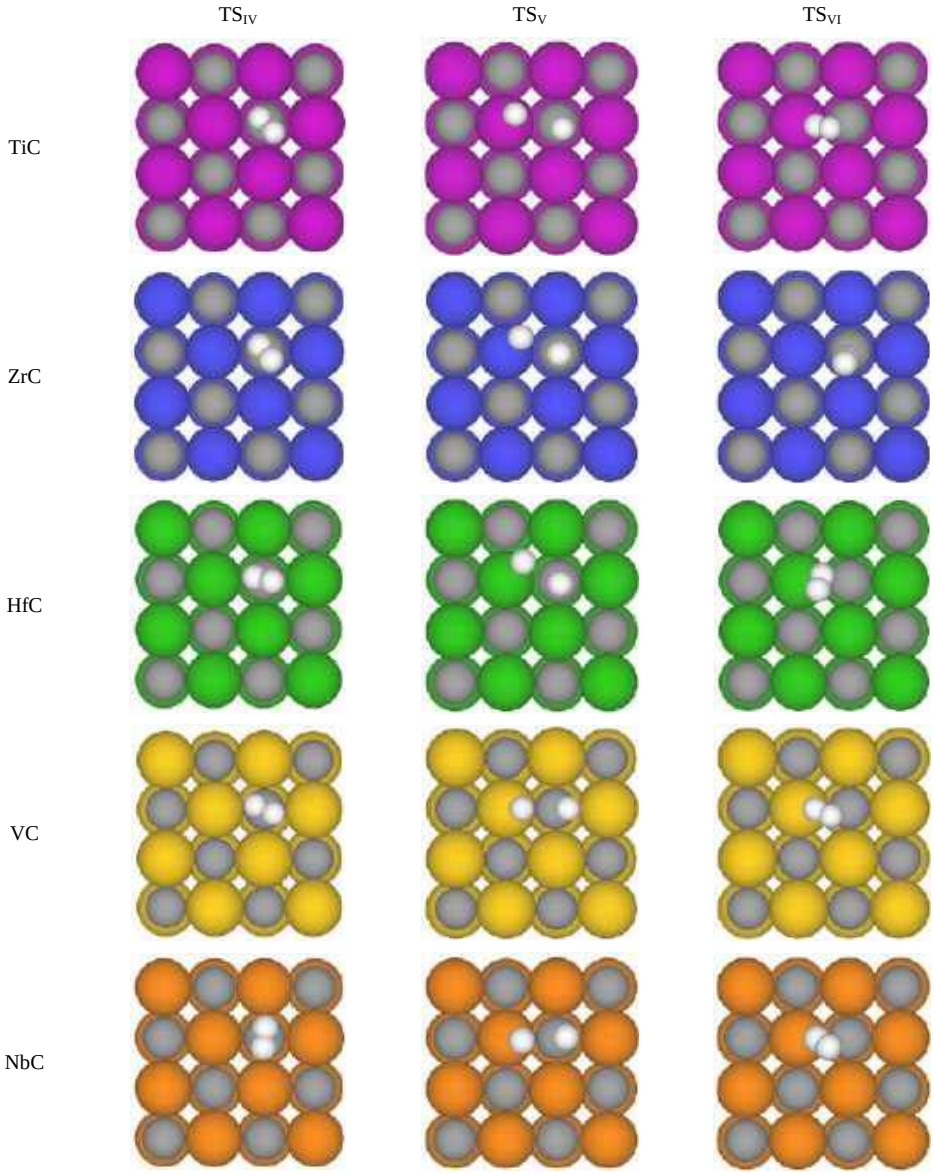

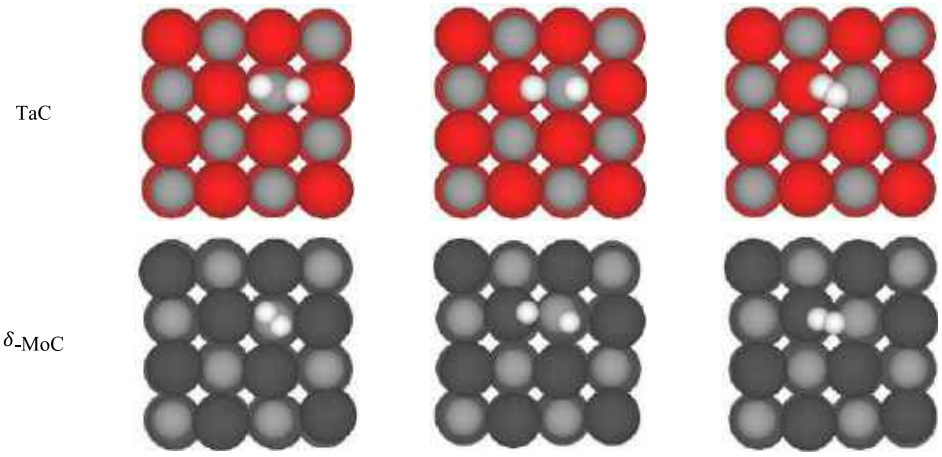
TaC
δ-MoC

Figure S2c. Optimized geometries (top view) for the TSs VII and VIII on TaC. Colour code is as in Figure S1.

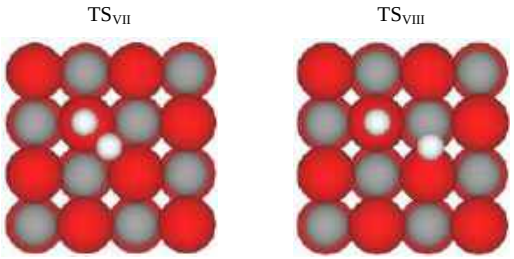

S4. Energy Profile for TaC

Figure S3. Energy profile (PBE-D3, including ZPE) for the H_2 adsorption, diffusion, desorption, and dissociation on TaC(001) including TSs IV, V, VII, and VIII.

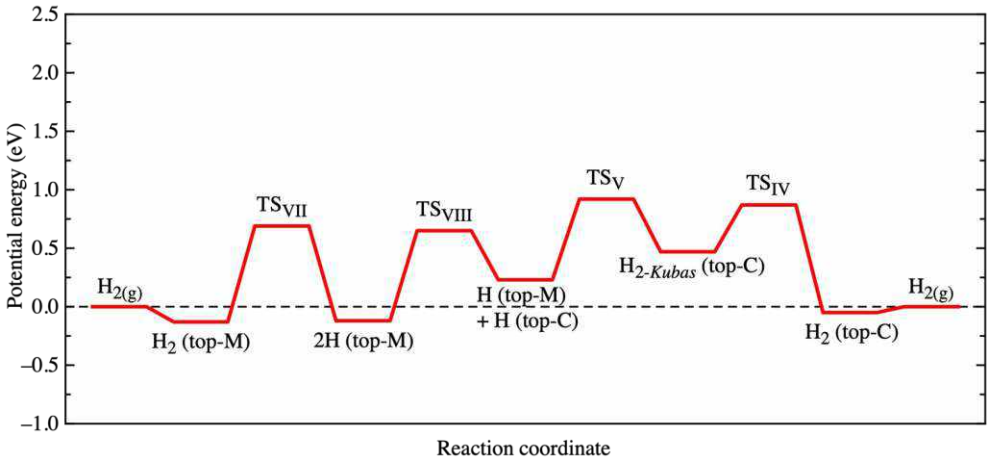

S5. Adsorption Energies without Dispersive Forces

Table S1. Calculated adsorption energy values ($^{\Delta E_{ads}}$) for H_2, H, and $H_{2,Kubas}$ on the (001) surface of the studied TMCs. All values have been obtained using the PBE exchange-correlation functional, and include the ZPE term.

	ΔE_{ads} (eV)						
Site	TiC	ZrC	HfC	VC	NbC	TaC	δ-MoC
$H^{*(top-M)}_{2}$	0.04	0.00	-0.01	0.10	0.03	0.00	-0.27
$H^{*(top-C)}_{2}$	0.03	0.03	0.03	0.06	0.05	0.04	-0.49
$H^{*(top-M)}$	1.77	1.57	1.20	0.88	0.58	0.26	0.46
$H^{*(top-C)}$	-0.15	-0.26	-0.19	0.46	0.48	0.57	-0.09
$H^{*(top-C)}_{2,Kubas}$	-0.20	-0.36	-0.11	0.41	0.34	0.58	-0.91

S6. Adsorption Energies without Dispersive Forces

Table S2. Calculated H-H bond length, $d(H_2)$, and interaction energy in between both H atoms, E_{int} — E_{int} = $E_{Kubas} - 2 \cdot H_{vac}$— for the obtained $H_{2,Kubas}$ situations on the (001) surface of the studied TMCs. Distances are given in Å and energies in eV, respectively.

TMC	$d(H_2)$	E_{int}
TiC	1.73	-0.79
ZrC	1.72	-0.82
HfC	1.72	-0.83
VC	1.69	-0.90
NbC	1.69	-0.92
TaC	1.71	-0.85
δ-MoC	1.80	-0.55

S7. Comparison with Other Materials on the Literature

Table S3. Calculated energy barriers for H_2 dissociation with respect to $H_{2(g)}$ ($^{H_{2(g)}\rightarrow 2H}$) on different TMCs and transition metal surfaces. All values except that for Ni(111) include the ZPE term.

Surface	Energy barrier (eV)	Ref.
TiC(001)	0.59	This work
ZrC(001)	0.41	This work
HfC(001)	0.37	This work
VC(001)	0.60	This work
NbC(001)	0.54	This work
TaC(001)	0.34	This work
δ-MoC(001)	~0.00	This work
WC(001)	~0.00	5
Cu(111)	0.47	6
Cu(100)	0.54	[illegible]
Cu(211)	0.56	[illegible]
Ag(111)	1.03	[illegible]
Ag(100)	1.06	[illegible]
Ag(211)	1.03	[illegible]
Au(111)	0.95	[illegible]
Au(100)	0.68	[illegible]
Au(211)	0.75	[illegible]
Ni(111)	0.13	7
Pt(111)	~0.00	8

REFERENCES

1 P. E. Blöch, Projector Augmented-Wave Method. *Phys. Rev. B: Condens. Matter Mater. Phys.* 1994, **50**, 17953

2 G. Kresse and D. Joubert, From Ultrasoft Pseudopotentials to the Projector Augmented-Wave Method. *Phys. Rev. B: Condens. Matter Mater. Phys.* 1999, **59**, 1758

3 H. J. Monkhorst and J. D. Pack, Special Points for Brillouin-Zone Integrations. *Phys. Rev. B: Solid State* 1976, **13**, 5188

4 C. Kunkel, F. Viñes and F. Illas, Transition Metal Carbides as Novel Materials for CO_2 Capture, Storage, and Activation. *Energy Environ. Sci.* 2016, **9**, 141-144

5 A. A. Koverga, E. Flórez, L. Dorkis and J. A. Rodriguez, CO, CO_2 and H_2 Interactions with (0001) and (001) Tungsten Carbide Surfaces: Importance of Carbon and Metal sites. *J. Phys. Chem. C* 2019, **123**, 8871-8883

6 Y. Bai, B. W. J. Chen, G. Peng and M. Mavrikakis, Density Functional Theory Study of Thermodynamic and Kinetic Isotope Effects of H_2/D_2 Dissociative Adsorption on Transition Metals, *Catal. Sci. Technol.* 2018, **8**, 3321-3335.

7 C. Zhi, Q. Wang, B. Wang, D. Li and R. Zhang, Insight into the Mechanism of Methane Synthesis from Syngas on a Ni(111) Surface: a Theoretical Study. *RSC Adv.* 2015, **5**, 66742-66756.

8 L. C. Grabow, A. A: Gokhale, S. T: Evans, J. A. Dumesic and M. Mavrikakis, Mechanism of the Water Gas Shift Reaction on Pt: First Principles, Experiments, and Microkinetic Modeling. *J. Phys. Chem. C* 2008, **112**, 4608-4617.

Appendix C: Supporting information to “Room Temperature Methane Capture and Activation by Ni Clusters Supported on TiC(001): Effects of Metal-Carbide Interactions on the Cleavage of the C-H Bond”

Supplementary Information

Room Temperature Methane Capture and Activation by Ni Clusters Supported on TiC(001): Effects of Metal-Carbide Interactions on the Cleavage of the C-H Bond

Hèctor Prats[†], Ramón A. Gutiérrez[‡,x], Juan José Piñero[†], Francesc Viñes[†], Stefan T. Bromley,[†§] Pedro J. Ramírez[x], José A. Rodriguez[*,‡] and Francesc Illas[*,†]

[†]Departament de Ciència de Materials i Química Física & Institut de Química Teòrica i Computacional (IQTCUB), Universitat de Barcelona, Martí i Franquès 1-11, 08028 Barcelona, Spain.

[‡]Chemistry Department, Brookhaven National Laboratory, Upton, New York 11973, United States of America.

[x]Facultad de Ciencias, Universidad Central de Venezuela, Caracas 1020-A, Venezuela

[§]Institució Catalana de Recerca i Estudis Avançats (ICREA), Barcelona, Spain

[*] Corresponding authors: José A. Rodriguez (rodriguez@bnl.gov), Francesc Illas (francesc.illas@ub.edu)

Table of contents **Page**

S1. Computational details S2
S2. Adsorption energies on clean TiC S3
S3. Transition state for CH_4 dissociation on clean TiC S4
S4. Adsorption energies on supported Ni clusters S5
S5. Transition states for CH_4 dissociation on supported Ni clusters S10
S5.1 Ni_4/TiC S11
S5.2 Frozen Ni_4/TiC S11
S5.3 Ni_9/TiC S12
S5.4 Ni_{13}/TiC S12
S6. Adsorption energies on the supported Ni nanorod S13
S7. Transition state for CH_4 dissociation on on the supported Ni nanorod S14
S8. Kinetic parameters and free energies S14
S9. Details on the calculation of descriptors for C-H activation S15
References S17

S1. Computational details

Further details of the periodic density functional theory (DFT) calculations follow the discussion in the main text. The valence electron density was expanded in a plane wave basis set with a kinetic energy cutoff of 415 eV, chosen to yield total energy variations below 0.01 eV. The effect of core electrons on the valence electron density was described by the projector augmented wave method (PAW) of Blöchl,[1] as implemented by Kresse and Joubert.[2]

The TiC(001) surface slab model for was built from the pre-optimized bulk unit cell containing four atomic layers, where the bottom two layers were constrained to bulk positions and the uppermost two fully relaxed.[3] To avoid interactions between periodic slab images, a vacuum region of 10 Å perpendicular to the surface was added. All adsorbates and Ni clusters were relaxed to their optimum geometry using a conjugate-gradient algorithm, with convergence criteria for electronic and atomic updates of 10^{-5} eV and 0.01 eV·Å^{-1}, respectively. Optimized geometries were characterized as minima on the potential energy surface by appropriate frequency analysis involving diagonalization of the corresponding block of the Hessian matrix with elements obtained through finite differences of analytic gradients.

The clean TiC(001) model consists of a R45º(3√2×3√2) supercell containing 72 Ti and 72 C atoms. The supported Ni_4 clusters were constructed by placing 4 Ni atoms on the TiC(001) model described above. In a similar way, the Ni_9 and Ni_{13} supported clusters were constructed by placing 9 and 13 Ni atoms, respectively, on a R45º(4√2×4√2) supercell containing 128 Ti and 128 C atoms. Integration in reciprocal space was carried out using **k**-point meshes selected following the Monkhorst-Pack scheme[4] adapted to the model. Thus, 5×5×1 and 3×3×1 **k**-point meshes were used for either pristine or Ni_n-containing TiC(001) R45º(3√2×3√2) or R45º(4√2×4√2) surface models, respectively (see Figure 1 in the main text).

Several initial geometries were tested for each adsorbed Ni_n cluster, and the most stable structure for each size was chosen to study the CH_4 dissociation reaction upon. A more extended Ni particle was represented by means of a nanorod supported on a 6×4 supercell model of the TiC(001) surface. The rod was oriented along the [010] direction and the overall model contains 96 Ti and 96 C atoms plus the 20 Ni atoms forming the rod (see Figure 2 in the main text). The atomic structure of all supported Ni clusters and rod models were fully optimized before including any adsorbates.

The energy of the isolated, gas phase, species (CH_4, CH_3 and H) was calculated by placing them in an asymmetric box of 9×10×11 Å and considering the **Γ**-point only. The initial guess for adsorbate geometries was obtained by placing the adsorbate at different sites (see black dots on Figures S3, S5, and S7). The number of candidate adsorption sites depends on the chosen system: four for the clean TiC surface, eleven for the Ni_4/TiC surface, 15 for the Ni_9/TiC, and Ni_{13}/TiC surfaces, and 5 for the Ni-rod/TiC surface. For the final optimized geometries, adsorption energies $E_{i,ads}$ (i = CH_4, CH_3, or H) were then calculated as:

$$E_{i,ads} = E_{i,slab} - (E_{slab} + E_{i,gas}) + E_{ZPE} \quad (1),$$

where $E_{i,slab}$ is the energy of the species i adsorbed on the corresponding slab model, E_{slab} is the energy of the relaxed naked slab, $E_{i,gas}$ is the energy of an isolated molecule of species i, and E_{ZPE} is the zero-point energy (ZPE) term, calculated considering both gas phase and adsorbed phase within the harmonic approximation.

S2. Adsorption energies on clean TiC

Three non-equivalent sites were tested for each species, namely, top C, top Ti, and four-fold hollow. For CH_4, orientations with a sole H pointing toward the TiC surface were neglected since they were previously found to be overall less favourable.[5] The CH_3 species is found to adsorb with the C atom near the surface and the three H bent slightly upwards forming a plane parallel to the surface. These remarks are true also for CH_4 and CH_3 adsorbed on the Ni clusters.

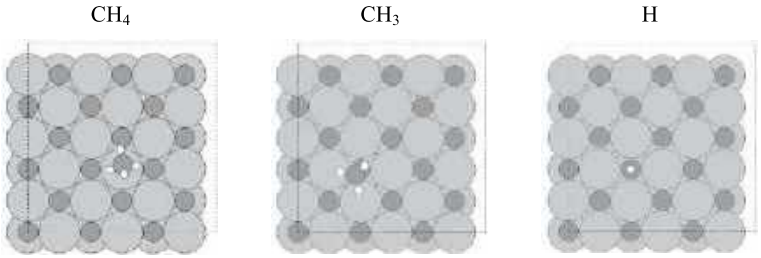

Figure S1. Optimized geometries (top view) for CH_4, CH_3, and H adsorbed on the most stable site on the clean TiC surface. Ti and C atoms are shown as light and dark grey spheres, respectively, and H atoms as white spheres.

S3. Transition state for CH_4 dissociation on TiC

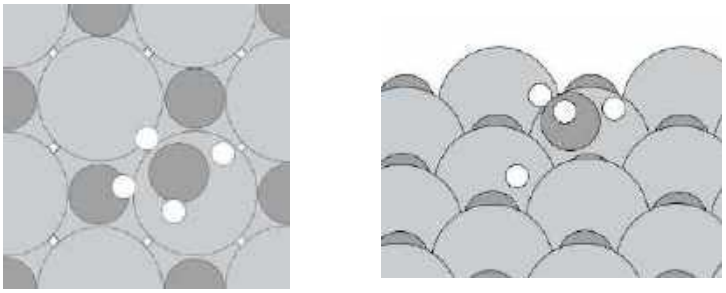

Figure S2. Optimized geometry (top and side views) for the CH_4 dissociation transition state on clean TiC(001) surface surface. Ti and C atoms are shown as light and dark grey spheres, respectively, and H atoms as white spheres.

S4. Adsorption energies on Ni clusters

The top positions of CH_4 are shown, and the corresponding adsorption energies. In many cases, the CH_4 moved to a vicinal adsorption site, and this displacement is shown with a black arrow.

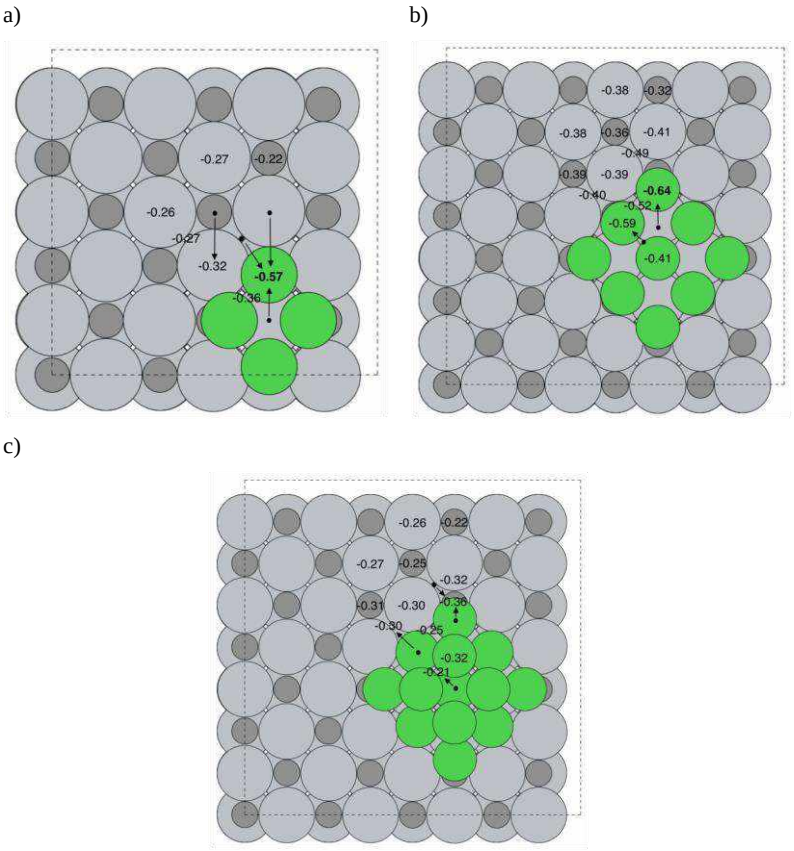

Figure S3. Adsorption energies (in eV) for CH_4 on a) Ni_4, b) Ni_9, and c) Ni_{13} clusters supported on the TiC(001) surface. Dots and arrows correspond to calculations were the adsorbate moved during the optimization (*i.e.*, the black dot shows the initial position and the arrow points to the final position). Ti and C atoms are shown as light and dark grey spheres, respectively, and Ni atoms as green spheres. The unit cell is shown in dotted lines.

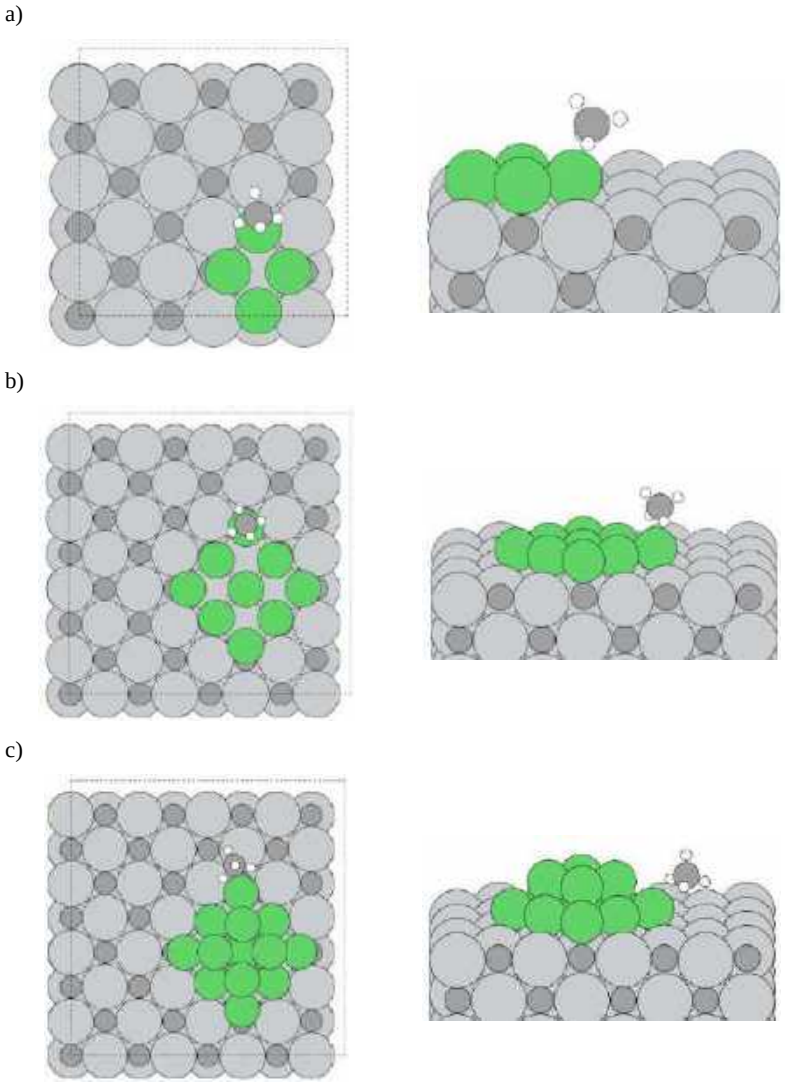

Figure S4. Optimized geometries (top and side views) for CH_4 adsorbed on the most stable site for a) Ni_4, b) Ni_9, and c) Ni_{13} clusters supported on the TiC(001) surface. Ti and C atoms are shown as light and dark grey spheres, respectively, and Ni and H atoms as green and white spheres, respectively. The unit cell is shown in dotted lines.

The CH_3 adsorption sites are shown next.

a) b)

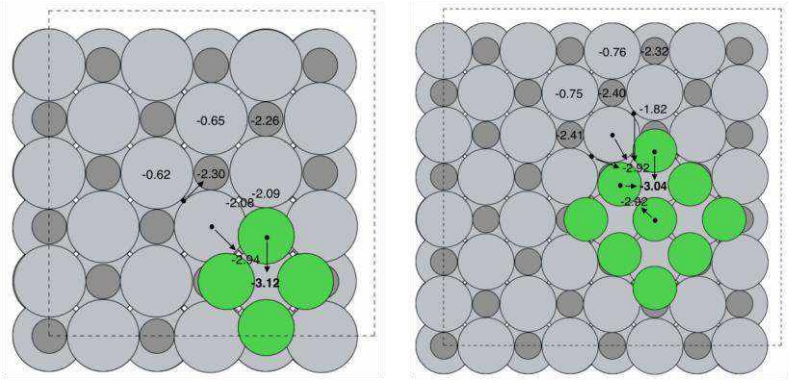

c)

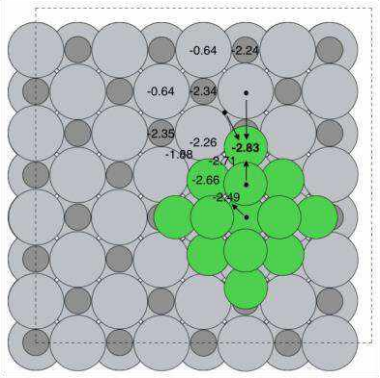

Figure S5. Adsorption energies (in eV) for CH_3 on a) Ni_4, b) Ni_9, and c) Ni_{13} clusters supported on the TiC(001) surface. Dots and arrows correspond to calculations were the adsorbate moved during the optimization (*i.e.*, the black dot shows the initial position and the arrow points to the final position). Ti and C atoms are shown as light and dark grey spheres, respectively, and Ni atoms as green spheres. The unit cell is shown in dotted lines.

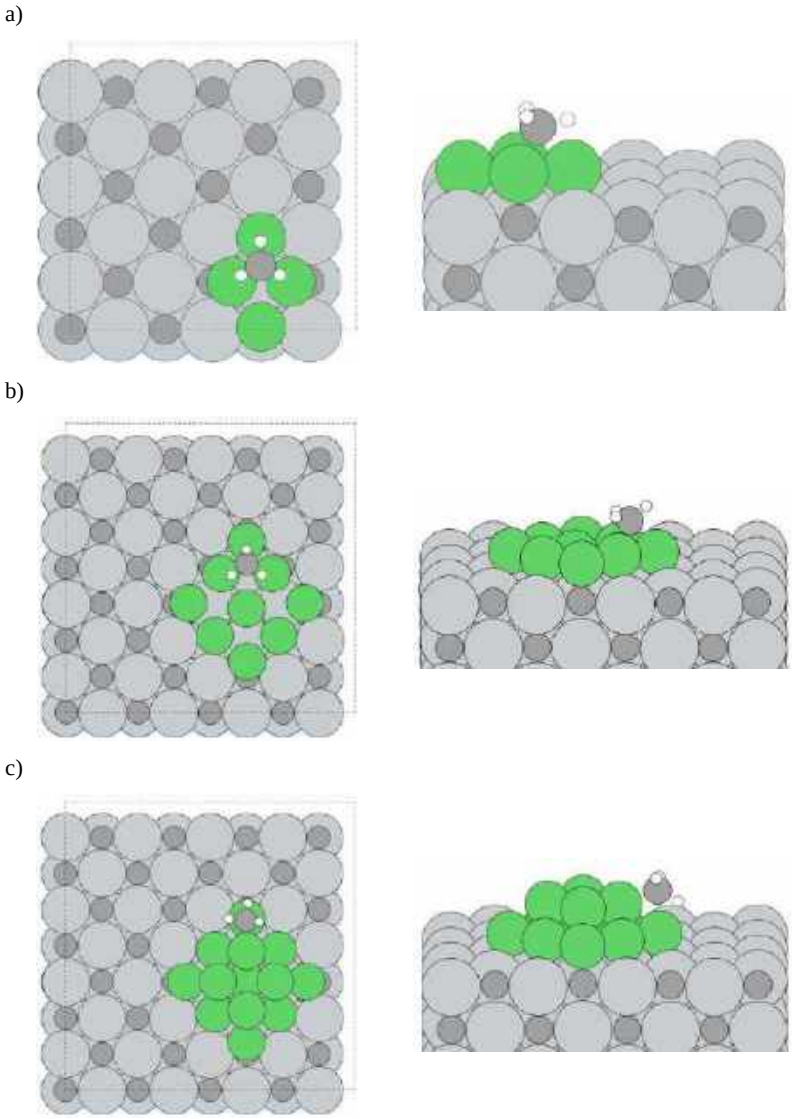

Figure S6. Optimized geometries (top and side views) for CH_3 adsorbed on the most stable site for a) Ni_4, b) Ni_9, and c) Ni_{13} clusters supported on the TiC(001) surface. Ti and C atoms are shown as light and dark grey spheres, respectively, and Ni and H atoms as green and white spheres, respectively. The unit cell is shown in dotted lines.

Finally, the most stable sites for the H adatom are displayed.

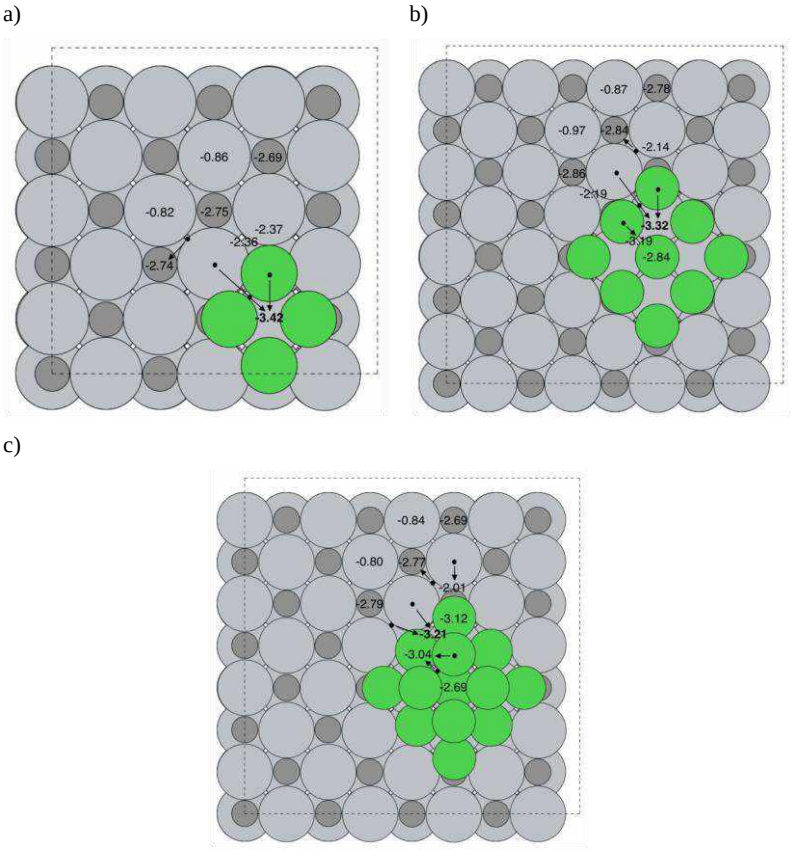

Figure S7. Adsorption energies (in eV) for H on a) Ni_4, b) Ni_9, and c) Ni_{13} clusters supported on the TiC(001) surface. Dots and arrows correspond to calculations were the adsorbate moved during the optimization (*i.e.*, the black dot shows the initial position and the arrow points to the final position). Ti and C atoms are shown as light and dark grey spheres, respectively, and Ni atoms as green spheres. The unit cell is shown in dotted lines.

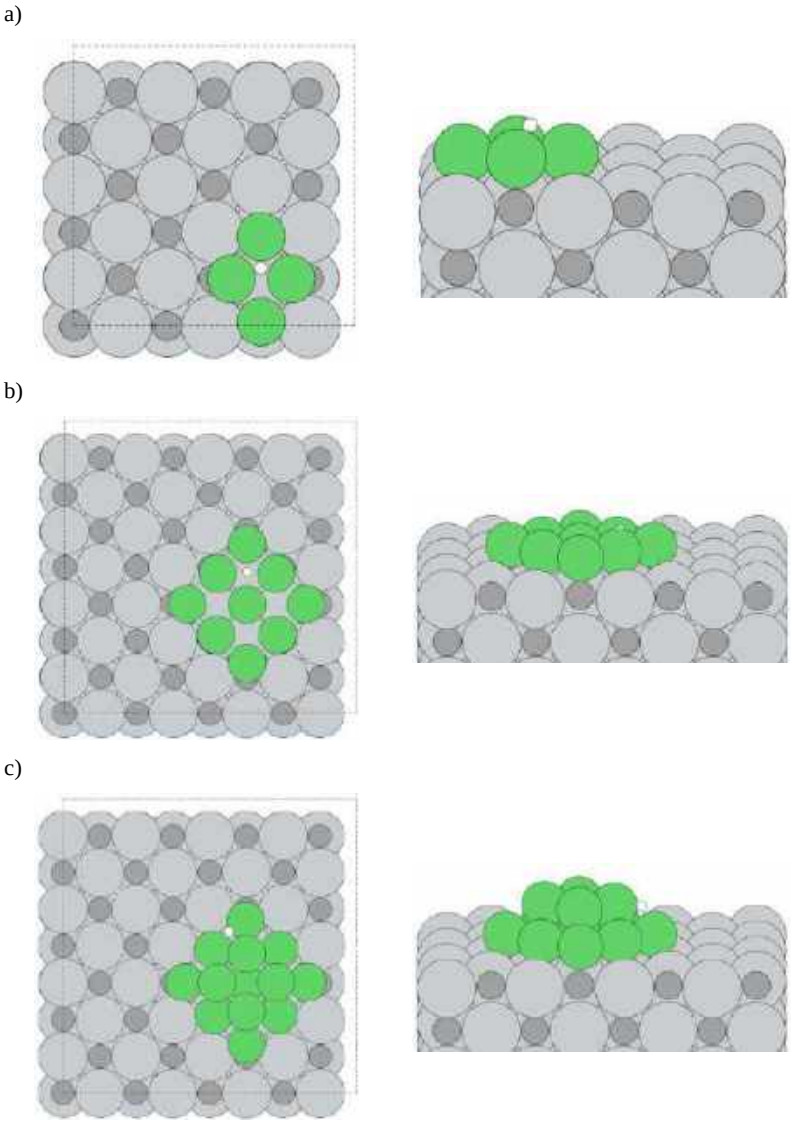

Figure S8. Optimized geometries (top and side views) for H adsorbed on the most stable site for a) Ni_4, b) Ni_9, and c) Ni_{13} clusters supported on the TiC(001) surface. Ti and C atoms are shown as light and dark grey spheres, respectively, and Ni and H atoms as green and white spheres, respectively. The unit cell is shown in dotted lines.

S5. Transition state for CH_4 dissociation on Ni clusters

S5.1 Ni_4/TiC(001)

Initial state TS Final state

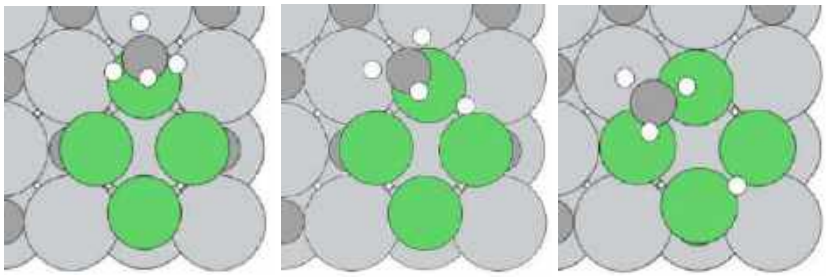

Figure S9. Optimized geometries (top view) for the reactant, transition state and product configurations. Ti and C atoms are shown as light and dark grey spheres, respectively, and Ni and H atoms as green and white spheres, respectively.

S5.2 Frozen Ni_4/TiC(001)

TS^{2*} (frozen cluster)

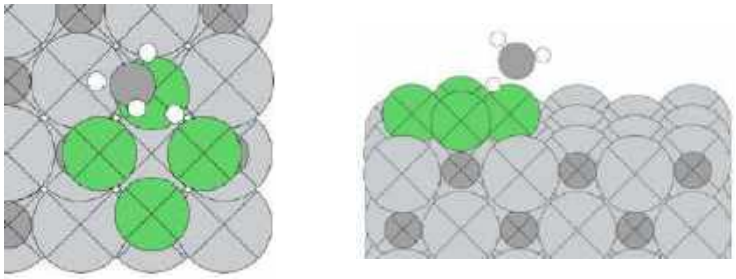

Figure S10. Optimized geometry (top and side views) for the transition state for CH_4 dissociation on Ni_4/TiC(001) when both the surface atoms and the cluster Ni atoms are frozen to the most stable configuration for the clean cluster. Ti and C atoms are shown as light and dark grey spheres, respectively, and Ni and H atoms as green and white spheres, respectively. Black crosses mark the atoms that have been frozen.

S5.3 Ni_9/TiC(001)

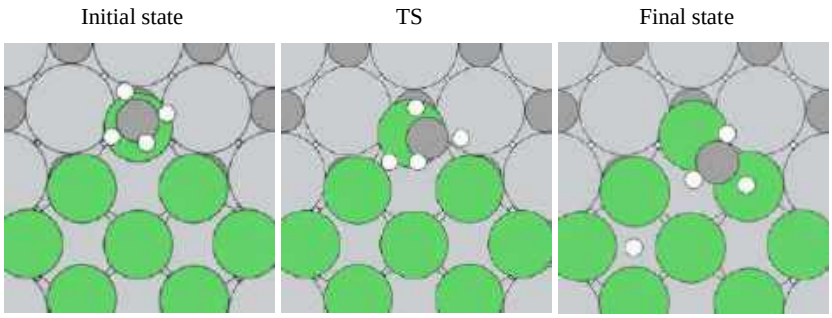

Figure S11. Optimized geometries (top view) for the reactant, transition state and product configurations. Ti and C atoms are shown as light and dark grey spheres, respectively, and Ni and H atoms as green and white spheres, respectively.

S5.4 Ni_{13}/TiC(001)

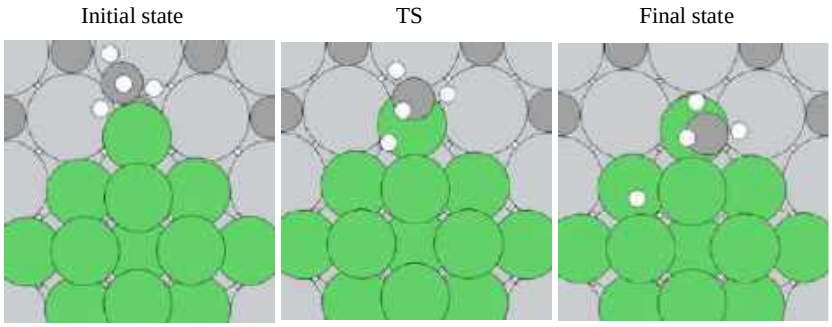

Figure S12. Optimized geometries (top view) for the reactant, transition state and product configurations. Ti and C atoms are shown as light and dark grey spheres, respectively, and Ni and H atoms as green and white spheres, respectively.

S6. Adsorption energies on Ni-rod

a)

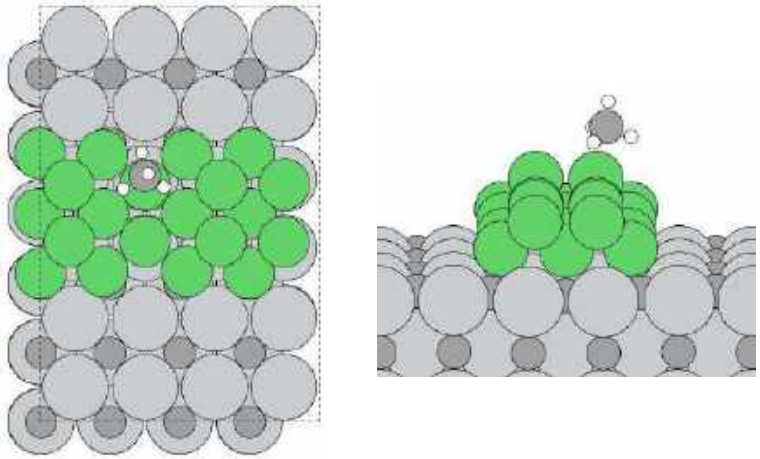

b)

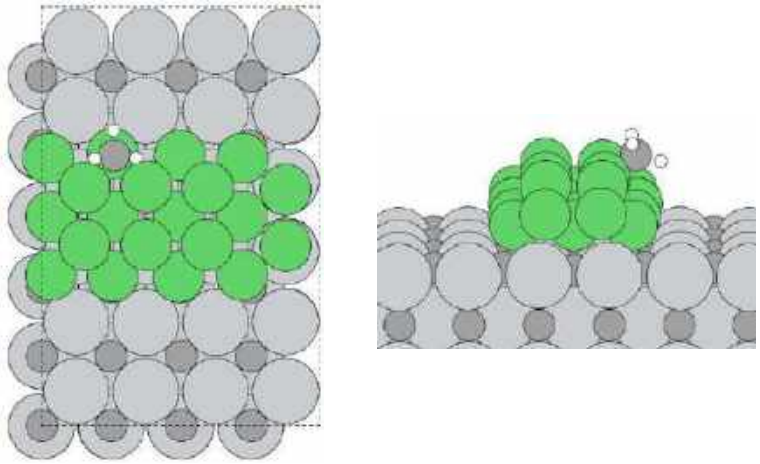

Figure S13. Optimized geometries (top and side views) of a) CH_4 and b) CH_3 adsorbed on the most stable site for Ni-rod/TiC(001) surface. Ti and C atoms are shown as light and dark grey spheres, respectively, and Ni and H atoms as green and white spheres, respectively.

S7. Transition state for CH_4 dissociation on Ni-rod

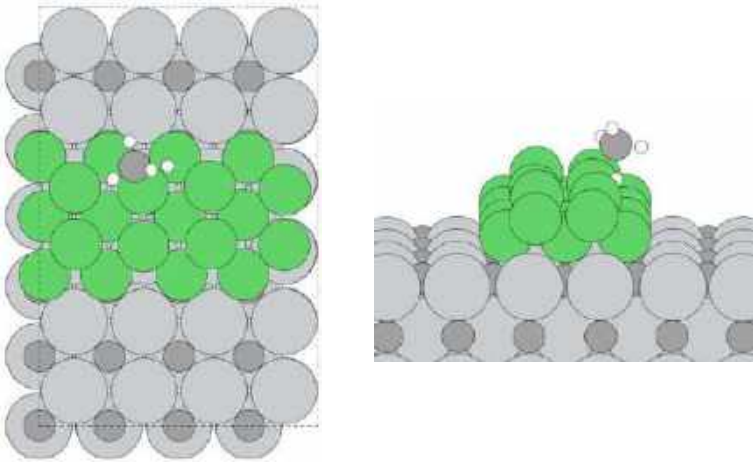

Figure S14. Optimized geometries (top and side views) for the CH_3-H transition state on Ni-rod/TiC(001). Ti and C atoms are shown as light and dark grey spheres, respectively, and Ni and H atoms as green and white spheres, respectively.

S8. Kinetic parameters and free energies

The reaction rate of a surface elementary process, defined as the number of times the process occurs per site and time unit, can be calculated by using either the harmonic transition state theory (TST) or the collision theory (CT).[6,7] Methane adsorption on Ni_n/TiC clusters is assumed to be non-activated (E_b = 0 eV). In that case, one assumes an early 2D gas-like transition state, and therefore, the corresponding rates for adsorption and desorption simplify to:

$$r_{ads}^{non-act.} = S_{st}\frac{P_{CH_4}A_{site}}{\sqrt{2\pi m_{CH_4}k_BT}} \quad (2)$$

$$r_{des}^{non-act.} = S_{st}\frac{k_BTQ_{trans2D,CH_{4(g)}}\cdot Q_{rot,CH_{4(g)}}\cdot Q_{vib,CH_{4(g)}}}{h\,Q_{vib,CH_4}}e^{-\Delta E_{ads}^0/k_BT} \quad (3)$$

where P_{CH_4} is the partial pressure of CH_4, A_{site} is the area of a single adsorption site, m_{CH_4} is the mass of the CH_4 molecule, k_B and T are the Boltzmann constant and temperature, respectively, S_{st} is the sticking coefficient,[8] $Q_{rot,CH_{4(g)}}$ and $Q_{vib,CH_{4(g)}}$ are the rotational and vibrational gas-phase partition functions, respectively, Q_{vib,CH_4} is the

vibrational partition function for adsorbed CH_4, and finally $Q_{trans2D,CH_{4(g)}}$ is the 2D translational partition function over the unit cell:

$$Q_{trans2D,CH_{4(g)}} = A_{site}\frac{2\pi m_{CH_4} k_B T}{h^2} \quad (4)$$

Reaction rate values can also be used to determine the standard free energies for adsorption and dissociation (*i.e.*, ΔG^{o}_{ads} and $\Delta G^{o,\neq}_{dis}$, respectively) as:

$$\Delta G^{o}_{ads} = -k_B T \cdot \ln[K_{eq}] = -k_B T \cdot \ln\left[\frac{r^{non-act.}_{ads}}{r^{non-act.}_{des}}\right] \quad (5)$$

$$\Delta G^{o}_{dis} = E_b - k_B T \cdot \ln\left[\frac{Q^{\neq}_{vib,TS}}{Q_{vib,CH_4}}\right] \quad (6)$$

Assuming S_{st} = 1 and using a value of 4.50 Å^2 for A_{site} the following results are obtained:

	Ni_4/TiC	Ni_9/TiC	Ni_{13}/TiC
r_{ads} (s^{-1})	$1.7\cdot10^{8}$	$1.7\cdot10^{8}$	$1.7\cdot10^{8}$
r_{des} (s^{-1})	$1.3\cdot10^{6}$	$1.4\cdot10^{4}$	$2.1\cdot10^{9}$
K_{eq}	$1.3\cdot10^{2}$	$1.2\cdot10^{4}$	$8.4\cdot10^{-2}$
ΔG^{o}_{ads} (eV)	-0.13	-0.24	0.06
$\Delta G^{o,\neq}_{dis}$ (eV)	0.09	0.16	0.25

Table S1. Kinetic and thermodynamic parameters for the three studied Ni_n/TiC clusters calculated at 300 K and 1 atm.

S9. Details on the calculation of descriptors for C-H activation

Values used to construct the BEP plot in Figure 10 and formation energies used in Figure 11 are reported on Table S2.

	E_b (eV)	E_{re} (eV)	E_H^f(eV)	E_{TS}^f(eV)
Ni_4/TiC	0.30	-1.25	-1.15	-0.27
Ni_9/TiC	0.39	-1.00	-1.05	-0.25
Ni_{13}/TiC	0.51	-0.95	-0.94	0.15
Ni_{rod}/TiC	0.80	-0.60	-0.77	0.31
Ni(111)	1.18[a]	0.13[a]	-0.66	1.10[b]

Table S2. Calculated values at PBE-D3 level of energy barriers (E_b), reaction energies (E_{re}) and formation energies for H (E_H^f) and the CH_3-H TS (E_{TS}^f). Values do not include the ZPE term. [a] PBE values obtained from Ref. [9]. [b]Value obtained from Ref. [10] using the OptPBE functional.

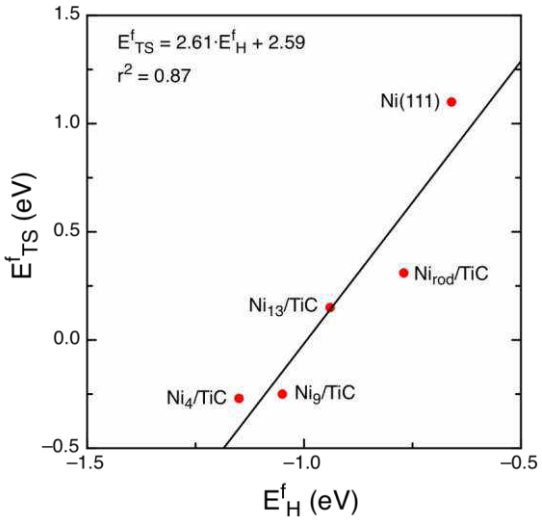

Figure S15. Plot of the formation energy of the TS versus the formation energy of adsorbed hydrogen for CH4 dissociation on the Ni/TiC systems and on Ni(111).

References

[1] Blöchl, P. E. Projector Augmented-Wave Method. *Phys. Rev. B* **1994**, *50*, 17953–17979.

[2] Kresse, G.; Joubert, D. From Ultrasoft Pseudopotentials to the Projector Augmented-Wave Method. *Phys. Rev. B* **1999**, *59*, 1758–1775.

[3] Kunkel, C.; Viñes, F.; Illas, F. Transition metal carbides as novel materials for CO_2 capture, storage, and activation. *Energy Environ. Sci.* **2016**, *9*, 141–144.

[4] Monkhorst, H. J.; Pack, J. D. Special Points for Brillouin-Zone Integrations. *Phys. Rev. B* **1976**, *13*, 5188–5192.

[5] Kunkel, C.; Viñes, F.; Illas, F. Biogas Upgrading by Transition Metal Carbides. *ACS Appl. Energy Mater.* **2018**, *1*, 43–47.

[6] Prats, H.; Álvarez, L.; Illas, F.; Sayós, R. Kinetic Monte Carlo Simulations of the Water Gas Shift Reaction on Cu(111) from Density Functional Theory Based Calculations. *J. Catal.* **2016**, *333*, 217–226.

[7] Prats, H.; Gamallo, P.; Illas, F.; Sayós, R.; Comparing the Catalytic Activity of the Water Gas Shift Reaction on Cu(321) and Cu(111) Surfaces: Step Sites Do Not Always Enhance the Overall Reactivity. *J. Catal.* **2016**, *342*, 75–83.

[8] Laidler, K. J. Chemical Kinetics, Harper & Row Publishers, New York, US A, 1987.

[9] Liu, H.; Yan, R.; Zhang, R.; Wang, B.; Xie, K. A DFT Theoretical Study of CH4 Dissociation on Gold-Alloyed Ni(111) Surface. *J. Nat. Gas Chem.* **2011**, *20*, 611–617.

[10] González, S.; Viñes, F.; García, J. F.; Erazo, Y.; Illas, F. A DF-VdW Study of the CH4 Adsorption on Different Ni Surfaces. *Surf. Sci.* **2014**, *625*, 64–68.